GENEVIÈVE CAUCHON-VOYER

MORPHO-SÉDIMENTOLOGIE ET MOUVEMENTS DE MASSE AU LARGE DE LA RIVIÈRE BETSIAMITES, ESTUAIRE DU SAINT-LAURENT, QUÉBEC

Mémoire présenté
à la Faculté des études supérieures de l'Université Laval
dans le cadre du programme de maîtrise en Sciences de la Terre
pour l'obtention du grade de maître ès sciences (M.Sc.)

DÉPARTEMENT DE GÉOLOGIE ET DE GÉNIE GÉOLOGIQUE
FACULTÉ DES SCIENCES ET DE GÉNIE
UNIVERSITÉ LAVAL
QUÉBEC

AVRIL 2007

Résumé

Une géomorphologie complexe avec d'importantes structures de mouvements de masse sous-marins a été mise en évidence lors de levés géophysiques dans l'estuaire du St-Laurent entre Betsiamites et Rimouski, Québec. Cette étude présente une description morpho-sédimentologique du secteur, une analyse spatio-temporelle des mouvements de masse et finalement une chronologie proposant l'âge pour certaines des ruptures de pente répertoriées. Les structures observées sont associées à au moins quatre épisodes de mouvement de masse. Un premier mouvement de masse paraglaciaire daterait de 9 ka BP. Un second aurait causé de larges couloirs de glissement sur le plateau ainsi qu'un cône de sédiments dans le Chenal laurentien et daterait de 7.25 ka cal BP. Un troisième événement plus récent aurait été causé par le séisme de 1663 AD (M~7) et serait associé au glissement subaérien identifié sur la côte. Finalement une dernière coulée daterait de l'an 1860 AD ou 1870 AD.

Avant-Propos

Mes travaux de recherche s'inscrivent dans le cadre des activités du projet COSTA-Canada pour l'étude de la stabilité des pentes continentales. La réalisation de cette étude a été rendu possible grâce au soutient financier du Conseil de Recherche en Sciences Naturelles et en Génie du Canada (CRSNG).

Je remercie mon directeur de recherche et mon co-directeur, M. Jacques Locat et M. Guillaume St-Onge, pour leur support tout au long de mon projet. Spécifiquement, je veux remercier M. Jacques Locat pour l'encadrement fourni au sein du Laboratoire d'études des risques naturels (LERN) et la confiance que celui-ci m'a octroyée en m'incorporant à plusieurs de ses projets de recherche et par le fait même, me permettant de bénéficier de sa vaste expérience dans le domaine des risques naturels. Je veux remercier M. Guillaume St-Onge pour son aide précieuse lors de mes séjours à Rimouski et pendant les missions d'échantillonnage mais surtout pour son enthousiasme scientifique qu'il sait si bien partager. La partie principale de ce mémoire consiste en un article scientifique réalisé sous la supervision de M. Jacques Locat et M. Guillaume St-Onge et ceux-ci seront co-auteurs lors de la publication de l'article.

Je veux par la suite remercier ma famille, mon père André à qui je dois cet amour du savoir et de la rigueur scientifique, ma mère Hélène qui m'a toujours inconditionnellement supporté dans mes projets, et finalement, mon frère Philippe, qui depuis ma naissance, a toujours si bien su me stimuler intellectuellement.

Je remercie André Godin anciennement au Centre Interdisciplinaire de Développement en Cartographie des Océans (CIDCO), Richard Sanfaçon du Service hydrographique de l'Institut Maurice Lamontagne, Pierre Therrien et Patrick Lajeunesse de l'Université Laval, Roger Urgeles et Ben DeMol de l'Université de Barcelone, Bassam Ghaleb du GEOTOP UQAM-McGill, Mathieu Duchesne de la Commission Géologique du Canada, l'INRS-ETE, ainsi qu'Hydro-Québec Pétrole et Gaz pour des données du projet Énergie des Appalaches de l'Initiative géoscientifique ciblée, les membres d'équipage et les participants scientifiques aux missions du F.G. Creed et du Coriolis II et finalement je remercie mes amis du 5eme, Ariane, Christiane, Dominique, Luc, Mylène, Pascal et Sueng Won.

Table des matières

Résumé i

Avant-Propos ii

Table des matières iii

Liste des tableaux et des figures v

Introduction 1

Morpho-sedimentology and submarine mass movements of the Betsiamites area, Lower St. Lawrence Estuary, Quebec, Canada 4

ABSTRACT 5

RÉSUMÉ 6

1. INTRODUCTION 7

2. REGIONAL SETTING 9

2.1. St. Lawrence Estuary 9

2.2. Subaerial environment 9

3. DATA AND METHODS 12

3.1. Bathymetry 12

3.2. Seismic data 12

3.3. Sediment sampling and core analyses 12

4. OBSERVATIONS AND RESULTS 15

4.1. Morphology 15
4.1.1. Bedrock lineaments 15
4.1.2. Mass movement morphologies 15
4.1.3. Paleochannel 19
4.1.4. Pockmarks 20

4.2. Stratigraphic analysis 21
4.2.1. Ice contact sediments – Unit 1 21
4.2.2. Ice proximal sediments – Unit 2 21

4.2.3. Ice distal sediments – Unit 3 22
4.2.4. Paraglacial sediments – Unit 4 22
4.2.5. Postglacial sediments – Unit 5 23
4.2.6. Debris flow – Facies 6 23

4.3. Mass movements spatio-temporal sequence 25
4.3.1. Paraglacial event (a) 25
4.3.2. Landslide channel event (b) 25
4.3.3. Recent Landslides (c and d) 26

5. DISCUSSION 28

5.1. Chronology of mass movement events 28

5.2. Triggering and hazard 30

6. CONCLUSIONS 32

ACKNOWLEDGEMENTS 34

REFERENCES 35

FIGURES 42

Conclusion 64

ANNEXE A : Résultats des analyses au ^{210}Pb 66

ANNEXE B : CAT-Scan, propriétés physiques et sédimentologiques des carottes sédimentaires des missions COR0307, COR0503 et COR0602 pour le secteur Betsiamites 69

ANNEXE C : Courbes granulométriques cumulatives 172

Liste des tableaux et des figures

Tableau 1. Sampling locations and core characteristics 14

Tableau 2. Summary of seismic attributes of the seismostratigraphic units 24

Figure 1. Location map of the Betsiamites - Rimouski study area in the St. Lawrence Estuary. 42

Figure 2. Bathymetric coverage of the study area and localization of Figures 11 and 14 and the MD99-2220 coring station. 43

Figure 3 Outline of the subaerial landslide and adjoining submarine morphology. 44

Figure 4. Location of the 15 sediment sampling stations and positions of the high resolution seismic reflection profiles presented in this paper. 45

Figure 5. Bathymetric chart of the study area with outline of the bedrock controlled lineaments 46

Figure 6. Bathymetric map of the Betsiamites submarine area and geomorphological interpretations. 47

Figure 7. Shaded bathymetry relief and high resolution seismic profile of the landslide channels and central butte 1 48

Figure 8. Shaded bathymetry relief of the outrunner blocks in the landslide channels and enlargement on the surface of butte 1. 49

Figure 9. Bathymetric images of the rugged area 50

Figure 10. Seismic reflection profile across the rugged area 51

Figure 11. Bathymetric image and high resolution seismic profile of the slope landslides 52

Figure 12. Bathymetric image and high resolution seismic profile of the buried debris fan in the Laurentian Channel 53

Figure 13. Bathymetric image, high resolution seismic profile and geomorphologic interpretatations of the paleochannel 54

Figure 14. Bathymetric image of the Laurentian Channel pockmarks. 55

Figure 15. CAT-scan image of piston 06-BE17-06PC sampled in a large pockmark in the Laurentian Channel. 56

Figure 16. Typical seismostratigraphic sequence for the study area 57

Figure 17. Sedimentological attributes for core 06-BE18-07BC showing typical sediment sequence. 58

Figure 18. Sedimentological attributes for core 05-BE02-02TWC showing debris 59

Figure 19. Sedimentological attributes and ^{210}Pb measurements for box core 05-BE05-05BC sampled in the paleochannel 60

Figure 20. Sedimentological attributes for core 03-BE02-43PC showing shallow sand bed in the Laurentian Channel 61

Figure 21. Sedimentological attributes and ^{210}Pb measurements for box core 05-BE02-02BC sampled in landslide channel West 62

Figure 22. Seismic correlations between the debris flow fan and the age model for core MD99-2200 63

Introduction

Problématique

L'étude des mouvements de masse sous-marins dans le but d'évaluer la stabilité des pentes est requise lors de la détermination des risques naturels en milieu marin. Avec le développement des activités humaines en mer et le long des côtes, il est essentiel de bien comprendre les facteurs qui contrôlent la stabilité des pentes et ceux qui déclenchent des mouvements de masse. En fait, une gestion efficace des activités humaines en milieu marin, par exemple lors de la réalisation de projets d'exploration ou du déploiement d'infrastructures pour l'exploitation de ressources pétrolières et minérales, exige une compréhension des risques naturels de ce milieu. La situation est d'autant plus importante près des côtes à cause de la forte densité de population et des diverses activités économiques qui y sont concentrées.

L'instabilité des pentes sous-marines est habituellement causée par l'érosion, la sédimentation forte ou rapide, la transformation des hydrates de gaz, les tremblements de terre, les glaciations et/ou l'action des vagues (Locat et Lee 2002, Prior 1984). Ces instabilités peuvent générer d'importants mouvements de masse et occasionnellement causer des tsunamis qui peuvent endommager les infrastructures humaines, tels le bris de câbles de télécommunications (Hampton *et al.,* 1996), ou encore mettre en péril la sécurité civile comme dans le cas du glissement sous-marin des Grands Bancs de Terre-Neuve qui avait causé la mort de 27 personnes (Piper *et al.,* 1985).

Au Québec, les glissements sous-marins ont principalement été étudiés dans le Fjord du Saguenay (St-Onge *et al.,* 2004; Locat 2002; Urgeles *et al.,* 2002). Dans l'estuaire du St-Laurent, Hart et Long (1996), Duchesnes *et al.,* (2003), Syvistki et Praeg (1989) et finalement Massé (2001) ont identifié des évidences de mouvements de masse dans le cadre de leurs travaux respectifs. Cependant, aucune étude n'a encore été réalisé avec l'objectif premier de comprendre les mouvements de masse sous-marins dans l'Estuaire. Dans le cadre du projet COSTA-Canada (COntinental slope STAbility) (Locat et Mienert, 2003) pour l'étude de la stabilité des pentes continentales, l'exploration sous-marine dans la région de l'Estuaire située entre les rivières Betsiamites et Manicouagan a été entreprise.

Des instabilités de pente sur la côte dans les dépôts quaternaires émergés de la Côte-Nord avaient déjà été répertoriées sur la côte (Bergeron, 1982), faisant du secteur sous-marin un environnement propice aux mouvements de masse. Allard (1982) avait identifié dans le secteur d'étude, un large glissement de terrain subaérien dans les dépôts postglaciaires émergés sur la côte à l'ouest de l'embouchure de la rivière Betsiamites. Cet amphithéâtre, cicatrice d'un glissement rétrogressif et possiblement d'une coulée de débris dans les dépôts meubles serait associé au séisme de 1663 (Bernatchez, 2003).

Une analyse préliminaire de la zone sous-marine de l'Estuaire en face du glissement subaérien, à l'aide de levés multifaisceaux et de sismiques réflexion, a mis en évidence d'importantes cicatrices de mouvements de masse sous-marins et plusieurs structures associées à la déposition des débris (Locat *et al.,* 2004). Cependant, plusieurs questions quant aux détails de la morphologie sous-marine du secteur, à la nature des matériaux présents, à la description des mouvements de masse et des structures résultantes, ainsi qu'à leur âge et récurrence sont restées sans réponse. La description du territoire permettra d'identifier les structures qui attestent des événements ayant modifié le paysage sous-marin de ce secteur de l'estuaire du Saint-Laurent. De plus, l'étude détaillée de tels mouvements sous-marins est requise en raison des risques importants qu'ils représentent pour les infrastructures et activités humaines de la Côte-Nord et de la Rive-Sud dans l'éventualité d'un tsunami déclenché par un glissement de terrain. La compréhension de ces mouvements de masse sous-marins prend donc toute son importance dans un contexte d'évaluation des risques naturels au Québec.

Objectifs de l'étude

Cette étude propose une description détaillée de la morpho-sédimentologie sous-marine d'un secteur d'environ 500 km^2 afin de comprendre les structures associées aux mouvements de masse. Les objectifs spécifiques de l'étude sont les suivants : 1) faire la description morpho-sédimentologique du secteur ; 2) établir la séquence spatio-temporelle des mouvements de masse ; et 3) proposer des dates pour l'occurrence des ruptures de pente et évaluer l'aléa.

Organisation du mémoire

La partie principale de ce mémoire consiste en un article scientifique réalisé selon les critères de la revue *Marine Geology*. Une conclusion générale des travaux ainsi que des annexes complètent le mémoire. La conclusion rappelle les travaux effectués et présente les résultats pertinents qui découlent de l'analyse. Des recommandations sont faites afin d'orienter les travaux futurs qui seront effectués dans le secteur. Les annexes présentent divers résultats obtenus sur les échantillons de sédiments récupérés dans le secteur de Betsiamites.

Morpho-sedimentology and submarine mass movements of the Betsiamites area, Lower St. Lawrence Estuary, Quebec, Canada

ABSTRACT

A complex submarine geomorphology was revealed from multibeam bathymetry and seismic reflection surveys conducted between 2001 and 2006 in the Lower St. Lawrence Estuary between the Betsiamites River and Rimouski, Quebec. In this paper, we describe the submarine morpho-sedimentology of an area of about 500 km^2 with focus on the various mass movement features observed. A spatio-temporal sequence for the occurrence of the mass movements and a chronology suggesting ages for the failures are established. Four main geomorphological features were mapped within the three physiographic regions of the area: bedrock lineaments, mass movement morphologies, paleochannels, and pockmarks. Four of the observed mass movement deposits were dated. The Paraglacial event is dated at 9 kyr BP. The Landslide Channels event left a major landslide scar characterized by two large channels on the shelf and a large sediments fan in the Laurentian Channel. These two features are related to one another as sediments source and sink. The Landslide Channels event is dated around 7.25 kyr cal BP. Morphological observations and sediment core analyses allow us to identify a least two different recent (*i.e.* less than 1 kyr BP) debris flow deposits on the shelf and in the Laurentian Channel. Two different ^{210}Pb-dated debris flow deposits were identified and associated to two recent earthquake episodes: (1) the AD 1663 (M~7) earthquake and (2) AD 1860 (M~6) or AD 1870 (M~6.5) earthquakes. The 1663 debris flow deposit is associated with a subaerial landslide observed on shore. In addition to a complex geomorphology influenced by mass movements, we have identified several regions on the shelf and on the Laurentian Channel with evidences of pockmarks which could potentially influence submarine slope stability in the Estuary.

RÉSUMÉ

Une géomorphologie complexe avec d'importantes structures de mouvements de masse sous-marins a été mise en évidence à l'aide de levés bathymétriques aux multifaisceaux et de sismique réflexion à haute définition entre 2001 et 2006 dans l'estuaire du St-Laurent entre Betsiamites et Rimouski, Québec. Cette étude propose une description détaillée de la morpho-sédimentologie sous-marine d'un secteur d'environ 500 km^2 en mettant l'accent sur les structures associées aux mouvements de masse. Une analyse spatio-temporelle des mouvements de masse et une chronologie proposant l'âge pour certaines des ruptures de pente répertoriées sont aussi présentées. Quatre groupes d'éléments géomorphologiques ont été cartographiés à l'intérieur des trois provinces physiographiques du secteur: des linéaments du substratum rocheux, des morphologies associées aux mouvements de masse, des paléo-chenaux et des évents de gaz. Quatre dépôts associés à des mouvements de masse ont été datés. Un premier événement paraglaciaire daterait de 9 ka BP. Le second événement a laissé une cicatrice majeure qui est caractérisée par deux larges couloirs de glissement sur le plateau et un large cône de sédiments dans le Chenal laurentien. Ces deux structures sont directement reliées l'une avec l'autre. L'événement des couloirs de glissement daterait de 7.25 ka cal BP. Des observations morphologiques et des analyses sédimentologiques ont permis d'identifier les traces d'au moins deux mouvements de masse récents (*i.e.* moins de 1 ka BP) sur le plateau et dans le Chenal laurentien. Les débris de ces mouvements de masse ont été datés à l'aide du ^{210}Pb. Cette analyse indique que les débris seraient reliés à deux séismes différents : (1) 1663 AD (M~7) et (2) 1860 AD (M~6) ou 1870 AD (M~6.5). Les débris de 1663 seraient associés au glissement subaérien observé sur la côte. En plus de la géomorphologie influencée par les mouvements de masse, nous avons identifié plusieurs régions sur le plateau et dans le Chenal laurentien ayant des évents de gaz, ce qui pourrait potentiellement influencer la stabilité des pentes sous-marines.

1. INTRODUCTION

Investigating submarine mass movements in order to evaluate slope stability for a region is required when carrying out risk assessment related to natural hazards. With the development of coastal and offshore activities such as the exploration and exploitation of oil and mineral resources, there is an essential need to improve our understanding of the factors controlling slope stability and triggering mass movements. This has major implications on the coastal environment as we know that most of the human and economical activities are gathered around the coasts. Slope instability is generally caused by erosion, sedimentation, gas hydrate, earthquake, diapirism, and/or wave action (Locat and Lee 2002; Prior 1984) and can generate submarine landslides which occasionally results in tsunamis. Such consequences of slope instability can both damage man-made infrastructures, *i.e.* the rupture of submarine telecommunication cables (Hampton *et al.,* 1996) and influence public safety (Piper *et al.,* 1985).

Submarine mass movements are widespread geomorphological processes found in many different oceanographic settings (Canals *et al.,* 2004; Locat and Lee 2002). In Quebec, comprehensive analyses of submarine mass movements have mostly been carried out in the Saguenay Fjord (Levesque *et al.,* 2006; St-Onge *et al.,* 2004; Locat *et al.,* 2003; Urgeles *et al.,* 2002,). In the St. Lawrence Estuary (Fig. 1b), Duchesnes *et al.* (2003), Hart and Long (1996) have presented geomorphological and geophysical evidences of slope instability for the Outardes Bay deltaic system, whereas Syvistki and Praeg (1989) and Massé (2001) have identified several local failures in high resolution seismic reflection profiles. However, no exhaustive study has been undertaken with the primary goal of understanding submarine mass movements in the Estuary. As part of the COSTA-Canada project (COntinental slope STAbility) (Locat and Mienert, 2003), intensive field work was carried out in the St. Lawrence Estuary between the Betsiamites and Manicouagan deltaic systems. This led to the recognition of significant evidence of submarine mass movements west of the Betsiamites River mouth (Figs. 2 and 3).

In order to account for the evolution of the submarine area influenced by mass movements between Betsiamites River and Rimouski, we must integrate the work previously done with

purpose of describing the morphology and stratigraphy in the area. In the St. Lawrence Estuary, Syvistki and Praeg (1989) established a seismostratigraphic sequence of (5) five units related to the advance and retreat of the Laurentide Ice Sheet and will be used thereafter in our analysis. In addition, the work of St-Onge *et al.* (2003) on the Holocene magnetic and sedimentological sequences of the St. Lawrence Estuary will provide bases for our mass movement event chronology. On shore, Bernatchez (2003) established a regional relative sea-level (RSL) curve for the last 11 kyr BP and described the Holocene coastal stratigraphy of the area. Many significant subaerial mass movements were previously identified on shore (Bernatchez 2003; Allard 1982) and with one large landslide scar associated with some of the structures we observe underwater.

The glaciation and deglaciation cycles and the geological history of the area are expected to have caused a complex geomorphology in the area. In addition, considering the amount of historical earthquakes known to have disturbed the landscape across Eastern Canada since deglaciation (Levesque *et al.,* 2006, Maslin *et al.,* 2004; St-Onge *et al.,* 2004; Aylsworth *et al.,* 2000; Shilts et Clague 1992; Smith 1962) and the extent of the regional disturbance observed in the Betsiamites – Rimouski area (Fig. 2), it would be expected to identify that more than one failures occurred in the area. Therefore, morphological, sedimentological, and seismostratigraphic analyses of the seafloor integrated with results of two studies presenting radiocarbon dates (St-Onge 2004; Bernatchez 2003) will provide support for our spatio-temporal sequence for the occurrence of the mass movements and for our chronology suggesting ages for the related failures between Betsiamites River and Rimouski in the St. Lawrence Estuary.

2. REGIONAL SETTING

2.1. St. Lawrence Estuary

The study area is located along the North Shore of the Lower St. Lawrence Estuary, Quebec, Canada, 400 km northeast of Québec City (Fig. 1). The regional morphology of the Estuary can be divided into three physiographic regions: the shelf (SH), slope (SL), and the Laurentian Channel (LC) (Fig. 2). The water depth in the study area ranges from the shoreline to depth down to 375 m in the Laurentian Channel. The shelf at the mouth of the Betsiamites River is a sub-horizontal surface and has an average width of 10 km and a maximum slope of 2°. The shelf break occurs between 150 and 200 m water depth and its outline is controlled by bedrock lineaments (Fig. 5). The slope has a height of 200 m. The Laurentian Channel is a long U-shaped glacial valley (Loring and Nota, 1973) and has a maximal water depth of 375 m and a width of 45 km in the study area. The topography of the Laurentian Channel is generally uniform and leveled, with local variations due to landslide debris and pockmarks (Locat *et al.,* 2004). The underlying bedrock in this part of the Estuary is likely made up of Cambrian–Ordovician sedimentary rocks of the St. Lawrence Lowlands. Up to 200 m of Quaternary sediments are present in the study area (Syvitski and Praeg, 1989).

2.2. Subaerial environment

Deglaciation of the coastal sector of the study area is established to have taken place at 11.7 kyr BP (Shaw *et al.,* 2006; Bernatchez, 2003). After ice retreat, this area has been shaped by the Betsiamites River deltaic system. This river, along with the Manicouagan and Outardes Rivers, was an important outlet for meltwater during deglaciation of Quebec and Labrador, accounting for the great volume of paraglacial sediments accumulated in the Estuary (Syvitski and Praeg, 1989). Bernatchez (2003) established a regional relative sea-level curve for the last 11 kyr BP in this area and described the Holocene coastal stratigraphy of the area: emerged marine, prodeltaic, deltaic, fluvial and littoral deposits. The Betsiamites River deltaic system has been formed during and after a post-glacial

relative sea-level fall of at least 150 m and the present sea level was reached around 7.5 kyr BP (Bernatchez, 2003). Glacio-isostatic rebound was significant in this area between 11 ka and 8 kyr BP with an average annual rate of 47 mm and as fast as 94 mm/yr between 11 and 10 kyr BP (Bernatchez, 2003).

A subaerial landslide scar with an area of 6.5 km^2 can be observed on shore, west of the Betsiamites River (Fig. 3). The landslide scar has a maximum width and length of 2000 m and 3280 m, respectively. Its head scarp is located in a marine terrace at 60 m above sea level and the debris reaches the tidal flat, which is composed of deformed prodeltaic silt with incorporated and sporadic pockets of organic matter and wood (Bernatchez, 2003). The lowermost section of the subaerial landslide scar is made of hills of 5 to 15 m high and depressions filled with standing water. These hills are interpreted as large rafted and tilted blocks of well-preserved or intact stratified prodeltaic sediments mobilized by the landslide (Bernatchez, 2003). With an area of 6.5 km^2 and a volume of more than 300 millions m^3 it is one of the biggest historical subaerial landslides that occurred in Québec, comparable to the 1663 Saint-Jean-Vianney landslide (Lasalle and Chagnon, 1968). Bernatchez (2003) suggested, according to three ^{14}C dates and from Jesuits writings (Thwaites, 1959), that this landslide was triggered by the major earthquake that shook the province of Québec on February 5th 1663 (Smith, 1962). A well preserved conifer tree branch with remaining bark was found among other landslide debris within the prodeltaic silt of the tidal flat and was dated at 310 ± 60 years BP (UL-1922). This provides the best radiocarbon dating evidence to relate this landslide to the earthquake of 1663. The Jesuits, who had been living in the area since the early 1600s, recall in their documents details that support this hypothesis and indicate that many landslides were triggered by the 1663 earthquake, as they comment on the amount of sediments in suspension in the St. Lawrence River : "*and our great river Saint Lawrence appeared all whitish as far as the neighborhood of Tadoussacq – a prodigy truly astonishing and fitted to surprise those who know the volume of water carried by this great stream below the Island of Orleans, and how much matter it must have taken to whiten it.*". In the area of Betsiamites, the Jesuits Fathers observed debris flowing from the Betsiamites River: "*We saw in passing the ravages wrought by the Earthquake in the rivers of Port neuf; the water coming therefrom is all yellow, and it retains this color far into the great rivers, as does that of the Bersiamites* [Betsiamites]. *The Savages could no longer*

navigate these two rivers". Although the Jesuits provided valuable descriptions of the extent, magnitude, and outcomes of the 1663 earthquake and resulting landslides in the province of Quebec, they unfortunately do not directly link the 1663 earthquake to the landslide scar we observe today west of the Betsiamites river mouth (Fig. 3). Nevertheless, the existing published dates obtained from the debris of the subaerial landslide and the mention of the Betsiamites River in the Jesuits writings provide reasonable evidence to link this landslide to the 1663 earthquake. However, a much more detailed and rigorous investigation must be undertaken to demonstrate their association.

3. DATA AND METHODS

3.1. Bathymetry

High-resolution bathymetric data were acquired using a SIMRAD EM1000 multibeam echosounder system mounted on board of the Canadian Hydrographic Service vessel FG Creed. The data used for this study were acquired between 2000 and 2003 (Fig. 2). The system operated at a frequency of 95 kHz with 60 beams spaced at 2.5° for a total coverage of 150° (Hughes Clarke *et al.,* 1996). The data are positioned using differential GPS. All grids shown in this paper have a cell size of 10 m. Data visualization and shaded relief bathymetric images were obtained with Generic Mapping Tool (GMT) and Fledermaus 6.1.5.

3.2. Seismic data

Most of the seismic reflection profiles used in this study were obtained with an EG&G chirp system mounted on the Coriolis II research vessel with frequencies ranging from 2 to 12 kHz. 600 km of seismic profiles were acquired during three cruises between 2003 and 2006. 40 km of profiles from an EG&G sparker source (peak frequency of 250 Hz) acquired as part of the Targeted Geoscience Initiative Appalachian Energy project (TGI 2003-2005) (Lavoie *et al.,* 2004) were also integrated in this study. Sound wave velocity for time-depth conversion was estimated at 1500 m/s. All depth values are hence approximated and represent minimal depths in sediments. Integrations of both types of subsurface data were done with the Kingdom Suite software package.

3.3. Sediment sampling and core analyses

10 box cores, 6 Lehigh gravity cores, 8 trigger weight cores, and 9 piston cores were recovered during three cruises (COR0307, COR0503, and COR0602) between 2003 and 2006 on board of the R/V Coriolis II at 15 sampling stations (Table 1, Fig. 4). Core positioning was obtained using the acoustic tracking system Trackpoint II. Low field

volumetric magnetic susceptibility (k) and wet bulk density and porosity derived from gamma ray attenuation were measured on board using a GEOTEK MSCL (Multi sensor core logger) system at 1 cm intervals. Immediately after recovery a few grams of sediments were sampled at all section ends in order to measure water content for geotechnical purpose and later assess core preservation. Digital X-ray images of all cores were obtained with computerized co-axial tomography (CAT-Scan) with a pixel resolution of 1 mm. The resulting grey scale images allow us to extract profiles of tomographic intensity: darker and lighter zones representing lower and higher X-ray attenuation, respectively (*e.g.,* St-Onge *et al.,* in press). 9 cores were split, described and photographed. Grain size measurements were made using a Beckman Coulter LS 13 320 laser diffraction particle size analyzer for the sediment fraction smaller than 2000 µm. The grain size data were processed with the Gradistat program and calculations of grain size statistics were done with the geometric method of moments (Blott and Pye, 2001). Sedimentation rates were derived from ^{210}Pb measurements within sediments of two box cores (05-BE02-02BC, 05-BE05-05BC). The measurements were obtained after chemical treatment, purification and deposition on a silver disk and alpha counting of the daughter ^{210}Po following routine procedures at the GEOTOP-UQAM-McGill research center (*e.g.,* Zhang, 2000).

Table 1: Positions of the sampling stations and length of the sediment cores recovered in the Betsiamites area. The first two digits of the stations number refer to the year of the sampling cruise, 03 for cruise COR0307 in 2003, 05 for cruise COR0503 in 2005 and 06 for cruise COR0602 in 2006. Water depth vales correspond to depth to the seafloor at sampling time.

Station	Core type and sample length (cm)				Feature targeted	Latitude (N)	Longitude (W)	Water Depth (m)
	Piston	Trigger weight	Lehigh gravity	Box				
03-BE01	505	101	-	44	Shelf edge	48°48.742	68°40.374	192
03-BE02	724	131	-	52	Laurentian Channel - debris fan	48°44.812	68°39.318	347
03-BE03	501	-	-	49	Lower Landslide channel East	48°50.309	68°42.143	123
03-BE12	-	-	134	48	Upper Landslide channel East	48°52.687	68°43.030	54
05-BE01	776	95	-	-	Laurentian Channel	48°43.585	68°39.123	352
05-BE02	-	127	-	40	Upper Landslide channel West	48°50.725	68°44.064	97
05-BE04	-	-	30	37	Central butte – (1)	48°51.568	68°43.351	73
05-BE05	-	-	-	38	Paleomeander	48°51.886	68°39.179	129
05-BE06	-	-	205	32	Slope landslide	48°51.628	68°31.867	320
05-BE07	-	-	-	43	Rugged surface – (1)	48°48.430	68°43.230	165
06-BE15	592	13	128	-	Central butte – (2)	48°51.359	68°43.803	73
06-BE16	708	-	90 & 235	-	Rugged surface – (2)	48°47.960	68°43.250	151
06-BE17	882	262	-	-	Laurentian Channel pockmark	48°45.578	68°28.444	370
06-BE18	597	33	-	-	Middle Landslide channel West	48°48.908	68°42.355	169
06-BE19	501	6	-	39	West shelf	48°49.700	68°46.440	85

4. OBSERVATIONS AND RESULTS

4.1. Morphology

A wide variety of landforms are revealed from seafloor investigation (Fig. 6). Combination of morphological, seismostratigraphic, and sedimentological analysis within the three physiographic regions allows us to define three (4) types of morphologies: bedrock lineaments, mass movement morphologies, paleochannels, and pockmarks. In this section, we describe the morpho-sedimentology of the area. The features are presented with regards to the physiographic regions within which they are observed, from the shelf to the Laurentian Channel.

4.1.1. Bedrock lineaments

The regional morphology of the study area is influenced by longitudinal outcrops of basement rock with associated perpendicular faults or fractures (Tremblay *et al.,* 2003; Massé 2001). The orientation of the slope scarp is controlled by structural bedrock lineaments (Fig. 5). A careful analysis of the position of bedrock lineaments within the study area allows us to recognize two main groups of orientations (Fig. 5). Group A has an average SSW-NNE orientation (N22°) and the western flank has a WSW-ENE orientation (N82°). These structural lineaments influence many of the features we describe.

4.1.2. Mass movement morphologies

On the shelf, an area of 70 km^2 is modified by mass movements (Fig. 6). It stretches for 10 km from the shoreline to the shelf break. It is characterized by four distinctive features: (a) a landslide scar with two large channels, (b) buttes of remnant deposits, (c) recent and shallow landslide debris and finally (d) an area with a rugged surface and erosional gullies. The main area modified by mass movements is located west of the Betsiamites River mouth, away from its actual discharge; therefore the river has not had any direct effect on the morphology of the landslide scar.

Two large channels, West and East, separated by a butte of remnant stratified deposits make up the upper sector of the landslide scar (Fig. 7). As it will be presented below, the channels are interpreted as landslide channels. The West landslide channel has a width ranging from 2 to 3 km and a length of 5 km. The slope of the West landslide channel floor is 1°. The western flank heights of the West landslide channel ranges from 12 to 18 m, with average slope of 12°. For the eastern flank, heights range between 10 to 20 m with average slopes of 5°. The western flank has a regular level and curves as it gets downslope to become more or less parallel to the shoreline. The East landslide channel width varies from 2 to 4 km, has a length of 5 km, and a floor slope of 1°. The morphology of the eastern flank of the East landslide channel is irregular due to various mass wasting processes (*i.e.* mass movements and erosion). Sequential analysis of the seismic configuration of the reflectors at the base of the channels allows us to interpret them as having being formed synchronously.

Two buttes with steep flanks and flat tops are observed within the landslide scar (1 and 2 on Figs. 6 and 7). They are remnant deposits of stratified sediments. A continuous stratified sequence is interpreted on the seismic profiles (Fig. 7) of butte 1 (Fig. 6), implying that it was kept mostly intact when the landslide channels formed. Butte 1 is the largest one and is located in the center of the landslide scar marking the separation between the landslide channels. It extends over 5 km^2 with a maximal length and width of 4.5 km and 1.6 km, respectively (Fig. 7). The average slope of the top of butte 1 is 1°. Butte 2 was kept within the lower section of the landslide scar (Fig. 6). We interpret the high amplitude seismic reflectors and the similar uninterrupted seismic sequence in the buttes and in the deposits outside the landslide scar to be correlated (Fig. 7). This therefore implies that these buttes are neither bedrock-controlled features nor gliding blocks and indeed remnant deposits. In addition, the surface of the central butte is coated with few outrunner blocks with sizes up to 2x10x20 m. The flow of the blocks left groves up to 1.5 m in the surface of the butte (Fig. 8).

The floor of landslide channels East and West adjacent to the shoreline is covered with a chaotic layer having a rough surface and transparent seismic attributes (Figs. 7 and 8). It is interpreted as a debris flow. The East landslide channel appears to be a continuity of the

subaerial landslide (Fig. 3). It is covered by large outrunner blocks impeding seismic penetration (Fig. 7) with sizes of up to 20x60x150 m (Fig. 8b). The blocks extend downslope 8 km from the shoreline (Fig. 3). Attempts to sample sediments from one targeted debris block led to the recovery of coarse sand and gravel which contrasts with the finer silty clay sediments between the blocks. These observations are coherent with the seismic interpretation as the seismic signal is totally attenuated right below the blocks (Fig. 7). The characteristics of the submarine debris are consistent with those of the subaerial debris identified by Bernatchez (2003) on shore. Small wood branches with bark and peat were found in the sediments recovered from the submarine debris, hence attesting their subaerial provenance. In addition to debris flows, mud flow sediments drape parts of the East and West landslide channels. In the channels, mudflow deposits differ from debris flow deposits by their acoustic attributes and surface morphology; mudflows being transparent with a uniform tone and a crenulated surface without apparent outrunner blocks. Smaller channels are observed among the debris and mudflow deposits and are interpreted as preferential pathways for downslope transport of the fluidized portion of the mass movement (Figs. 6 and 8).

The lowermost portion of the landslide scar has an irregular rugged surface incised by subparallel gullies (Fig. 9). It has an area of 17 km^2. This area is localized at the bottom of a drop in the relief of the West landslide channel and ends at the shelf break a bedrock ridge (Fig. 9b). There is an apparent limit between the rugged area and the leveled hemipelagic sediments on the surface of the shelf (Fig. 9b). Gullies have a parallel drainage pattern and an orientation more or less perpendicular to the axis of the West landslide channel. The largest gullies have depths up to 2 meters on the seafloor (Fig. 10b). This surface is observed in a confined depression of the bedrock (Fig. 10c). In fact, sediments draping unplanned bedrock relief leads to the seismic reflection interpretations that faults could be present in the area. However conformable sedimentation through all seismostratigraphic units in the sequence leads us to interpret them as inactive since deglaciation. The same profiles lead us also to interpret a buried debris flow which extent correlates with the rugged area on the seafloor (Fig. 10). A disturbed deposit below an average of 30 ms (20 m) of sediments influences the signal creating artefacts and acoustic wipe-out. This buried irregular topography is translated up to the seafloor through conformable sedimentation,

indicated by the continuous parallel internal seismic reflectors (Fig. 10b). A shallow high amplitude reflector (S1 on Fig. 10) is interpreted at about 1 ms (75 cm) below seafloor and correlates to a sandy layer sampled in all long cores from the area. This reflector is also conformable on the rugged morphology and drapes the gullies, implying that they are not currently active. In a piston core (06-BE16-05PC) recovered from the rugged area, we can identify 3 sand layers (30 cm, 380 cm, 530 cm). The sand layer at 30 cm is interpreted as the reflector S1. However the sediment sequence in the rugged area does not have a characteristic debris flow facies, indicating that the uppermost 7 meters of this area on the shelf has not been covered by thick debris of a landslide as seen upslope.

The Estuary slope shows also evidence of slope failure (Fig. 11). The largest landslide scar of the area, across seismic line C-C' on Figure 11, is found at water depths ranging from 180 m at the head scarp to 340 m at its toe. The failure plane has an average slope of about 7°. The landslide scar has a maximal width and length of 1200 m and 1700 m, respectively, extending over an area of 1.8 km^2. The head scarp has a horseshoe shape and is on average 16 m high. The volume of displaced material is estimated at 13.8 millions m^3. The failure plane was interpreted on the seismic reflection profiles has a high amplitude reflector within the highly stratified sediments of the shelf (Fig. 11d). Debris is interpreted on the seismic reflection profiles (Fig. 11c) and are buried downslope under 5.0 m and 11 m of hemipelagic sediments, from the slope to the edge to the depositional lobe.

The Laurentian Channel was also influenced by the events given that we can observe accumulations of debris on the seafloor and within the seismostratigraphic sequence, therefore acting as sink for mass movements in the area. In the study area, a large sediment fan is observed at a water depth of 350 m (Fig. 12). This fan has its apex downslope from the break in the shelf edge where the lineaments in the bedrock meet (Fig. 5). The fan has an area of 115 km^2 and a maximal diameter of 15 km. The outer edge of the fan has a lobated shape. Seismic reflection profiles allow us to interpret this fan as a result of an important accumulation of debris following a major event (Fig. 12c). This large debris flow is buried under an average of 15 meters of postglacial hemipelagic sediments, which implies that the fan is currently inactive. The postglacial hemipelagic sediments sequence is interrupted only by one high amplitude reflector at 1.5 ms (1 m) in the sediments (S1 on

Fig. 12). The acoustic signature of the buried debris flow is variable, either acoustically transparent or incoherent with diffraction hyperboles which are common seismic attributes of debris flows. Due to acoustic masking caused by the debris, it is practically impossible to evaluate if older events also occurred. With an average thickness of 9 m, the debris flow has an estimated volume of 1 km^3. A high amplitude seismic reflector (S2 on Figs. 12 and 22) is interpreted as the upper boundary of the chaotic debris flow deposit. This strong reflector extends also out of the limit of the debris fan. The central portion of the fan is completely masked.

4.1.3. Paleochannel

A paleo-submarine channel and its meander are identified on the shelf east of the landslide scar (Figs. 6 and 13). This submarine channel is not currently related to the modern Betsiamites River discharge (Fig. 2). The meander length, measured along the center of the meander between point A and B (Fig. 13), is 3.4 km. The linear distance between point A and B is 1.9 km. The channel meander has depths of 20 m and 35 m and widths of 280 m and 545 m at points A and B, respectively. The water depth in the meander at point A is 130 m and 170 m at point B. This represents a gradient of 2% for this section of the paleochannel. Terraces are seen on both sides of the meander on the bathymetric images and seismic interpretation reveals conformable stratifications on buried terrace levels. Upslope from the meander, cross-sections of buried submarine channels can be interpreted in the sediment deposits, implying that the channel base level shifted in time and that prodeltaic and hemipelagic sediments have draped the inactive channel after its erosive stage. Interestingly, the position of the upper part of the paleochannel corresponds more of less to the eastern edge of the landslide scar (Fig. 7). Seismic reflection configurations observed on the seismic profiles of the paleochannel meander and sequential analysis of the seismostratigraphic units reveal that this paleochannel is probably a vestige of the progradation of the deltaic system during the last regressive phase (Hart and Long, 1996). In addition, sediments recovered (station 05-BE05, Fig. 19) from the meander present no sedimentary structures with frequent traces of bioturbation, which imply an inactive channel and hemipelagic sedimentation.

4.1.4. Pockmarks

Pockmarks were identified on the bathymetric data and seismic profiles of the shelf and Laurentian Channel regions. On the shelf, they are mostly concentrated in defined areas at water depths around 140 m (Fig. 9). Their diameters range between 50 and 75 m and depths from 2 to 4 m. In the Laurentian Channel, the pockmarks are significantly larger, some of them having diameters up to 400 meters with a depth of 12 m (Fig. 14). Smaller pockmarks are observed at the surface of the buried debris fan but the largest are located outside the extent of this fan. Core samples of surface sediments recovered above the buried debris fan (station 03-BE02) show very little gas disturbance on the CAT-Scan images, indicating that the debris act like an impermeable layer to gas escape. All piston cores recovered outside of the boundaries of the debris flow (station 05-BE01) have gas disturbance and gas lenses on the CAT-Scan images. Station 06-BE17 was chosen in order to sample sediments from a large pockmark. With size of 400 and depth of 12 m in addition to use of the acoustic tracking system Trackpoint II, it was possible to successfully target this feature. The sediments recovered were very disturbed when raised to ambient condition due to degassing. An important amount of shell (Fig. 15) was also observed within the sediment core. These observations are consistent with other descriptions of pockmarks (Hovland *et al.*, 2002).

4.2. Stratigraphic analysis

A seismostratigraphic analysis and core data were integrated to describe the stratigraphy of the Betsiamites – Rimouski area. Five distinct seismo-stratigraphic units previously identified by Syvitski and Praeg (1989) were observed our study area: (1) ice-contact sediments; (2) ice-proximal sediments; (3) ice-distal sediments; (4) paraglacial sediments; and (5) postglacial sediments (Table 2, Fig. 16). This sequence is interpreted on both the shelf and in the Laurentian Channel. The geological interpretations presented in this paper are drawn from the work of Syvitski and Praeg (1989). A facies of debris flow (6) was also added to this sequence. This seismostratigraphic analysis was done in order to temporally correlate observed morphological features and establish a time sequence for the mass movement events. For each seismostratigraphic unit inner reflectors (R), bedding style and stratifications (S), seismic tone (T), and attributes of the lower transition (L) between units were defined. The characteristic of each seismostratigraphic unit are described below and summarized in Table 2. In addition, core data are also integrated into this analysis when recognized useful for our understanding of the morphology and stratigraphy of the area. In fact, analysis of the physical properties (density and CAT-Scan images), magnetic susceptibility, sedimentological properties (grain size, detailed visual descriptions) were taken into considerations for our morpho-sedimentological interpretations.

4.2.1. Ice contact sediments – Unit 1

This unit is acoustically uniform with a moderate to strong tone and rare weak reflectors. Unit 1 overlies bedrock, which is visible only when this unit is thin (Fig. 10). When visible, the lower boundary of Unit 1 is a strong reflector and is interpreted as the bedrock top with a variable relief and acoustic masking below this reflector. Such acoustic attributes and position within the seismostratigraphic sequence lead us to interpret this unit as ice contact sediments. This unit was not sampled.

4.2.2. Ice proximal sediments – Unit 2

This unit is a thin sequence of strong and closely packed reflectors with an alternating tone from low to medium. It is highly conformable on Unit 1. In fact, almost everywhere in our

study area we can recognize two reflectors conformable on Unit 1, the upper reflector marking the sharp transition between Unit 2 and Unit 3. Unit 2 was not sampled.

4.2.3. Ice distal sediments – Unit 3

This unit is thick with a distinctive very low tone, weak reflectors, and punctual reflections. A few thin and weak reflectors are visible and conformable with Unit 2. The upper and lower transitions are sharp. It is interpreted as ice-distal sediments and the punctual reflections are interpreted as ice rafted blocks. Ice-distal sedimentation is interpreted as the accumulation of glaciomarine sediments. This unit was sampled at station 06-BE18 (Figs. 4 and 17). The sediment consists of homogenous light gray clays without apparent structures and with few small ice rafted debris. In comparison with the other units within this core, the measured properties of the sediments of Unit 3 have a lower variability. Bulk density values increase slightly and constantly with burial, with an average of 1.65 g/cm^3 and standard deviation of 0.026 g/cm^3. This trend of low variability is observed within the CAT-Scan intensity profile as it averages 1068 with a standard deviation of 6.52. This low variability in sediment bulk density measured with the MSCL and in CAT-Scan intensity is consistent with the seismic attributes observed (low tone and weak reflection) which imply homogenous material.

4.2.4. Paraglacial sediments – Unit 4

Unit 4 is characterized by the alternation of low and high amplitude reflectors. It has dense stratifications conformable with Unit 3. The tone of this unit varies between low and strong. The transition between Unit 3 and Unit 4 is sharp and is mostly recognized by the contrast in tone. Unit 4 is interpreted as paraglacial sediments. Paraglacial sedimentation occurs when high volumes of sediments are transport from land to the sea. This unit was sampled within piston core (06-BE18-07PC) and consists of a light grey laminated facies. Horizontal and parallel laminations are visible on the CAT-Scan image (Fig. 17). Bulk density values within this core average 1.73 g/cm^3, with a standard deviation of 0.049 g/cm^3. Bulk density values are measured as higher in Unit 4 than in Unit 3 (Fig. 17) in this core and is opposed to our expectation of increase bulk density with burial due to consolidation. Higher values are hence results of changing sediment compositions, grain

size, or water content and imply a change in the sedimentary, which is consistent with the geological interpretations. The characteristics of Unit 3, finer ice-distal sediments, and Unit 4, coarser paraglacial sediments discharged from fluctuating glacial plumes, are coherent with the observed seismic attributes.

4.2.5. Postglacial sediments – Unit 5

Unit 5 makes up the uppermost sediments of the study area and is interpreted as post-glacial sediments. The seismic attributes of the unit consists of a body of medium to strong tone with few weak and thin reflectors. The transition between Unit 4 and Unit 5 is gradational. Unit 5 also contains few high amplitude reflectors sharply contrasting with the lower tone background. These reflectors are interpreted as rapidly deposited layer (RDL). This unit was sampled in many cores recovered from the study area and can be divided into two subunits with main difference being sediment homogeneity. Subunit 5a consists mostly of homogenous, dark massive silty clays with few thin sand layers. It is mostly undisturbed but contains few shell fragments and rock. Frequent traces of bioturbation were identified. Subunit 5b consists of heterogeneous sediments, often interrupted by sand layers and traces of bioturbation. CAT-Scan images indicate also a great variability in materiel density (Fig. 17) that is noticeable by the differences in pixel intensity.

4.2.6. Debris flow – Facies 6

Facies 6 was not defined as a seismostratigraphic unit as it appears in the sequence regardless of the position within this succession of units. Facies 6 has highly variable seismic attributes, ranging from seismically transparent to acoustically impermeable (Figs. 7, 10, 11, and 12). It is often recognized on the seismic profiles by the chaotic character of its upper boundary. Stratification is absent. This unit was sampled in cores recovered from the debris area of the upper shelf (Fig. 18). Abundant wood and shells fragments were found within these very poorly sorted sediments. When core sampling allowed recovery of overlying and underlying units, the lower and upper contacts are sharp. Bulk density and magnetic susceptibility of this facies are usually much higher with average density of 2.0 g/cm^3. Sand content (Fig. 18) is also much higher in this facies than all other units.

Table 2: Summary of seismic attributes of the seismostratigraphic units and facies. R refers to inner reflectors, S to bedding style and stratifications, T to seismic tone, and L to the attributes of the lower transition of the units.

Seismostratigraphic sequence and geological interpretations	**Seismic attributes**
Unit 5 Postglacial sediments	R: Weak reflectors with few strong internal reflectors S: When apparent, conformable with Unit 4 T: Medium to strong tone L: Gradation from Unit 4 to Unit 5
Unit 4 Paraglacial sediments	R: Strong high amplitude reflectors S: Dense stratifications, conformable with Unit 3 T: Alternating low to strong tone L: Sharp transition from Unit 3 to Unit 4
Unit 3 Ice distal sediments	R: Weak reflectors with punctual reflections S: When apparent, stratifications conformable with Unit 2 T: Very low tone L: Sharp transition from Unit 2 to Unit 3
Unit 2 Ice proximal sediments	R: Strong and closely packed reflector S: Stratifications conformable with Unit 1 T: Alternating low to medium tone L: Sharp transition from Unit 1 to Unit 2
Unit 1 Ice contact sediments	R: Poor or absent reflectors, acoustic masking S: Absent stratifications T: Medium to strong tone L: When visible, strong reflector (interpreted as the bedrock), with a variable relief and acoustic masking below this reflector
Facies 6 Debris flow	Highly variable seismic attributes, from seismically transparent to acoustically impermeable S: Absent stratification L: When visible, sharp transition with lower unit

4.3. Mass movements spatio-temporal sequence

Bathymetric data, seismic reflection surveys, and sediment core data reveal that at least 4 major non-synchronous landslide events have shaped the area. In this section, we describe morphologic and stratigraphic evidence for the occurrence of the landslides and expose the seismic interpretations that lead us to define a spatio-temporal sequence for these events.

4.3.1. Paraglacial event (a)

The oldest debris flow interpreted on the seismic profiles of the study area is located below the central butte 1 (Fig. 7). The debris flow is acoustically transparent or acoustically opaque when thick. The upper reflector of the deposit has an irregular relief. It is stratigraphically below the base level of the landslide channels, implying that this event is not related with the landslide channels. More than 26 m (35 ms) of sediments with strong reflector of dense stratifications was deposited conformable on the debris flow deposits. As described in section 4.2, the sediments overlying the debris flow are interpreted as paraglacial prodeltaic sediments (seismostratigraphic Unit 4).

4.3.2. Landslide channel event (b)

A second event, with greatest magnitude in the study area, caused the formation of the two large landslide channels on the shelf. The main observation that allows us to say that the event is not recent, *i.e.* not linked to the event of 1663, is that the sediments remobilized by the landslide deposited downslope are interpreted in the sediment fan of the Laurentian Channel. The debris are buried under 15 m (Fig. 12) of hemipelagic sediments, which would represent at least 5300 years of sedimentation if we simply assume the constant ^{210}Pb derived sedimentation rate of 0.28 cm yr^{-1} determined by St-Onge *et al.* (2003) on box core AH00-2220 recovered from the location of the MD99-2200 (48°38.32N/68°37.93W) coring site (Fig. 2), about 15 km to the southwest. The landslide left clear flanks in the highly stratified deposits, (seismostratigraphic Unit 4), which implies that the event occurred after that phase of prodeltaic paraglacial sedimentation.

The position of the paleochannel may have influenced the spatial extension of the landslide scar since the remnant of the paleochannel appears to be the eastern limit of the East landslide channel (Fig. 7). Evans (1994) made the same observation for the South River Nation subaerial slide in the Ottawa region as that the area of the landslide was confined between two creeks. The paleochannel incised paraglacial prodeltaic sediments (seismostratigraphic Unit 4) indicated by the letter P on Figure 13c. Closely packed reflectors (C on Fig. 13c) interpreted also as paraglacial sediments are conformable on the truncated reflector (P) and on the abandoned meander. The lower portion of the paleochannel before the shelf edge follows a lineament (Fig. 5)

4.3.3. Recent Landslides (c and d)

Morphological observations and high resolution seismic interpretations led us to establish that more than one recent landslide (*i.e.* less than 1000 years old) have occurred in the area. Debris, gullies, and blocks are identified on the surface of both landslide channels. Analysis of the sediment properties recovered from a box core (05-BE05-05BC) sampled in the meander area (Fig. 13) led to the identification of recent homogenous hemipelagic sedimentation (Unit 5a) and sand bed associated to a debris flow (Facies 6) (Fig. 19). The hemipelagic unit within this box core is composed of homogenous sediments lacking apparent sedimentary structures and is observed between 0 and 30 cm depth. The density and magnetic susceptibility values are stable across the profiles: average magnetic susceptibility of 350 x 10^{-5} SI and average density of 1.8 g/cm^3, indicating fairly stable hemipelagic sedimentary conditions in the meander. The mean grain size in the hemipelagic sediments is 25 μm with 10 % of clay, 60 % of silt and 30 % of sand. ^{210}Pb activity was measured within this box core and results indicate that the uppermost 15.5 cm of the sedimentary column contains unsupported ^{210}Pb. Three different horizons can be identified in the ^{210}Pb activity profile of core 05-BE05-05BC (Fig. 19): the active mixing upper horizon, the central radioactive decay and the background horizons. These observations imply that this 15.5 cm of sediments were deposited in the last 100 years (Appleby and Oldfield 1978, Koide *et al.,* 1972) and that hemipelagic sedimentation is active in the paleomeander. A sharp transition occurs between the hemipelagic sediments

and the sand bed at 30 cm. Layer of organic matter, most likely peat, and sand were identified in the laboratory and are clearly visible on the CAT-Scan at 30 cm depth (Fig. 19). They are associated with a recent event of mass movement.

Evidence of recent events is also observed within the sediments of the Laurentian Channel. In fact, a high amplitude reflector was interpreted at an average depth of 1.5 ms (1 m) in the sediments (S1 on Fig. 12). The layer was also sampled with gravity coring at station 03-BE02 and was clearly identified on the CAT-Scan images of core 43PC (Fig. 20) based on change in grayscale from dark gray for the lighter background sediments to the white for the denser sand layer. This layer is about 5 cm thick and by the examination of the density and pixel intensity profiles presented in Fig. 20, we can see that this layer show a peak in the profiles of density (average1.5 g/cm^3) and CT number (average 1055).

In the West channel, morphological observations allow us to identify more than one recent superficial mass movements occurred in the area. In fact the landslide debris was subsequently eroded by another landslide that produced the shallow channels seen at the surface (Letter C on Fig. 7). ^{210}Pb measurements were done on the sediments of a box core recovered within the uppermost eroded channel, most likely eroded by the last landslide event of the area, in the West Channel at station 05-BE02 (Figs. 7 and 21). Background values were reached at 22.5 cm. Similarly to the box core sampled in the meander area, these measurements indicate that this 22.5 cm of sediments were deposited in the last 100 years.

5. DISCUSSION

5.1. Chronology of mass movement events

Bernatchez (2003), in its effort to reconstitute the Holocene evolution of the Betsiamites delta area, established from sedimentological observations and ^{14}C dates a chronology of deposition of the emerged sediments. For our submarine seismostratigraphic analysis, his work is considered to set boundary dates for the deposition of the seismostratigraphic units previously described in order to estimate dates for the mass movement events. As we do not have datable material, a correlation between our observations and the chronology of Bernatchez is the only way to estimate a date for the Paraglacial event. For our purpose in the submarine environment, Bernatchez (2003) analysis can be summarized by a phase of predominantly marine sedimentation between 11 and 9 kyr BP, a phase of prodeltaic sedimentation between 9 and 8 kyr BP and the present sea level was reached around 7.5 kyr BP with fluctuations in the order of 10 m were after observed (Dionne, 2001). As previously described, the Paraglacial event is thought to have occurred during a stage of prodeltaic paraglacial sedimentation because more than 26 m of highly stratified prodeltaic sediments are deposited on top of the debris (Fig. 7). A date of 9 kyr BP can hence be estimated for this first Paraglacial event. Following this same analysis, a minimal age of 8 kyr BP can be proposed for the Landslide Channel event since most of the paraglacial prodeltaic (Unit 4) is truncated by the event (Fig. 7).

In addition to this seismostratigraphic analysis to date the older events, a correlation to date this event can be done with the work of St-Onge *et al.* (2003) who established from 17 AMS ^{14}C dates an age model for core MD99-2220 sampled in the Laurentian Channel, only about 15 km from the study area (Fig. 2). The seismic reflector S2 interpreted as the upper boundary of the debris flow deposits can be mapped to the sampling location of core MD99-2220 in the Laurentian Channel. This reflector is observed at a depth of 1100 cm, leading to an age estimate of about 7250 cal BP (Fig. 22). This age estimate is consistent with many observations linking isostatic rebound and earthquake triggered landslide. In the Saguenay Fjord, St-Onge *et al.* (2004) suggested that at least 4 rapidly deposited layers,

possibly caused by earthquakes, occurred between 6800 and 7200 cal BP. Similarly, Aylsworth *et al.* (2000) associated observations of very disturbed terrain in a flat erosional plain in the Ottawa Valley to earthquake deformations and liquefaction of sensitive clays and estimate the date of occurrence of this large earthquake to ca. 7060 yr BP.

For the recent events, the age estimates were obtained from sedimentation rates derived from ^{210}Pb measurements (Figs. 19 and 21). As described previously, many landslides elsewhere in Quebec are related to the AD 1663 earthquakes (Saguenay Fjord, Levesque *et al.,* 2006 and St-Onge *et al.,* 2004; Saint-Jean Vianney, Lasalle and Chagnon, 1968) as it is also suggested for the Betsiamites subaerial landslide (Bernatchez, 2003). For core 05-BE05-05BC sampled in the paleomeander (Figs. 13 and 19), the debris flow was clearly identified at 30 cm. However, 5 cm of compaction was recorded when the core was sampled, implying that the debris flow at this location is buried under a minimum of 35 cm of hemipelagic sediments. Using the sedimentation rate of 0.11 cm yr^{-1} calculated from the slope of the ln ($^{210}Pb_{excess}$) (Fig. 19), the debris flow buried under 35 cm is dated at about AD 1685, suggesting it could have been triggered by the 1663 earthquake.

The rapidly deposited layer (S1 on Fig. 12) identified in the Laurentian Channel presented above can also be related to the AD 1663 event. It is buried at an average depth of 1.5 ms (1 m) in the sediments and using the ^{210}Pb derived sedimentation rate of 0.28 cm yr^{-1} determined by St-Onge *et al.* (2003) on box core AH00-2220 13 km from our coring station (Fig. 4), we can estimate a date of occurrence at AD 1646, which can reasonably be linked to the AD 1663 earthquake. The work of Filion *et al.* (1991) in the Rivière du Gouffre in the Charlevoix region, 200 km southwest from our study area also supports the hypothesis that some of the observed recent landslides were triggered by the AD 1663 earthquakes. In fact, Filion *et al.* (1991) established a radiocarbon-based chronology of landslide activity from tree trunks buried in debris flow material. The radiocarbon dates indicate that most landslides were triggered before 600 yr BP. In addition, tree-ring dating allowed them to conclude that two large landslides in the area were caused by the AD 1663 earthquake.

For station 05-BE02 in the West Channel, the debris flow was not identified in the 40-cm long ^{210}Pb-dated box core 05-BE05-05BC. It would have required a longer box core from the same station to identify the depth of the debris and date the flow identified in the West

Channel. Nevertheless, the debris flow is identified within the trigger weight core 05-BE02-02TWC of this same coring station at a depth of 30 cm, indicating some loss due to sampling associated with the gravity coring. We can not determine precisely the depth of the debris flow sediments in the trigger weight core. However, based on the sedimentation rate estimated at this station on the box core 05-BE05-05BC (0.29 cm yr^{-1}, Fig. 21) a depth of 40 cm would lead to AD 1872 for the event whereas a depth of 45 cm to AD 1855.. Despite the fact that we can not provide a precise date, it nevertheless discards the hypothesis that this last event is associated with the AD 1663 earthquake. In fact, with an average sedimentation rate of 0.29 cm yr^{-1}, the debris flow would have to be buried under at least 100 cm of hemipelagic sediments to be dated around AD 1663, which is too far from the minimum estimated depth of 40 cm in the trigger weight core of this coring station. Dates for submarine landslides that do not all correlate with the AD 1663 event was also observed by Levesque *et al.* (2006) in the Saguenay Fjord. They have compiled many ^{210}Pb dated landslides and concluded that not all landslides can be associated with the AD 1663 event. Furthermore, two significant earthquakes were recorded in the Charlevoix Seismic Zone (CSZ) (Smith, 1962): a first one on October 17, 1860 (M~6) and a second one on October 20, 1870 (M~6.5). The epicenters for the 1860 and 1870 events are evaluated at 180 km and 200 km from the Betsiamites area, respectively.

5.2. Triggering and hazard

The recurrence of slope instability within the Betsiamites – Rimouski area could be attributed to seismic activity due to glacio-isostatic rebound. Since the area is located within the Lower St. Lawrence Seismic Zone (LSZ) and close to the Charlevoix Seismic Zone (CSZ), it is expected that seismicity will influence the occurrence of slope instability. However, other factors reducing slope stability such as highly stratified deposits, groundwater seepage, and possible gas escape are found in the Estuary. In combination with earthquakes they cumulate to create a less stable environment. As seen in Figure 7, the failure plan of the landslide channel is interpreted in a unit of dense stratified seismic reflectors. These highly variable seismic attributes could indicate different sediments composition, such as the alternation of silty and sandy layers. The layer identified by R3 in

Figure 7 could have developed in a weak layer which would undergo liquefaction when subject to an earthquake and thus will result in slope failure. Such liquefaction has likely occurred for the slide in the East landslide channel (Fig. 7) and for the slide presented on Figure 11, as little sediments remained on the failure plane. Finally, possible destabilization of gas hydrates due to change in relative-sea level could have also impacted slope stability in the Laurentian Channel. In most cases for reported submarine mass movements linked to gas hydrate destabilization (Locat and Mienert, 2003), it has been speculated that they occurred after a time of relative low sea level which could potentially initiate gas hydrate dissociation. For the study area in the St. Lawrence Estuary this relative low level was reached around 7 kyr BP, after rapidly dropping from 150 m to present relative sea level (Bernatchez, 2003). As described above, pockmarks identified on seismic profiles and bathymetric surveys as well gas disturbance observed within the recovered sediments (Figs. 14 and 15) could have seriously impacted slope stability in the study area.

6. CONCLUSIONS

The main objective of this study was to define a framework accounting for the evolution of the morpho-sedimentology observed in the Betsiamites –Rimouski area in the St. Lawrence Estuary. This was done by presenting a geomorphological map of the area and by proposing a spatio-temporal sequence for the occurrence of the mass movements. Finally, we proposed a chronology suggesting ages for the related failures in the area.

Four main geomorphological features were identified in the area: bedrock lineaments, mass movement morphologies, paleochannels, and pockmarks. This paper demonstrates also that more than one failure events have influenced the morphology of the area during the Holocene. At least (4) four events remobilized massive volumes of sediments which created the complex geomorphology observed in the area. The first paraglacial event, estimated to have occurred 9 kyr BP, left buried traces in the deposits of the shelf. The second event is dated at ca. 7.25 kyr cal BP had the greatest outcomes in the area. In fact, we attribute to this event the large landslide scar characterized by the two landslide channels and the buried debris fan of the Laurentian Channel. The third event, of more recent occurrence, is linked to the AD 1663 (M~7) earthquake. ^{210}Pb-dated subaerial landslide debris were identified and related to a subaerial event dated on shore (Bernatchez, 2003). Our results lead us to link the submarine and the subaerial events to one another and support the hypothesis that the subaerial event, or at least part of it, occurred following the AD 1663 earthquake. Debris flow deposits associated to the AD 1663 event are also identified in the Laurentian Channel. Finally, morphological observations indicate that a smaller landslide is subsequent to the 1663 event. In fact, ^{210}Pb analyses and considerations of historical earthquakes in Eastern Quebec allow us to estimate that this event could be related to the AD 1860 (M~6) or AD 1870 (M~6.5) earthquakes.

In our chronology we were able to link 4 main events (9000 BP, 7250 cal BP, AD 1663 and AD 1860 or AD 1870) to slope instability (*i.e.*, not to catastrophic river discharge), and to

differentiate them from one another based on a sequential stratigraphy point of view and on ^{210}Pb or radiometric dates. Our analysis has raised many other questions such as the tsunamigenic potential of these events and the treat of future similar events elsewhere in the Estuary. There is thus a need to pursue our research to clearly define the mechanisms responsible for slope failures and to describe post-failure behavior in order to assess slope stability in the St. Lawrence Estuary. Investigating bedrock faults influence and gas escape on sediment stability will also lead to a better understanding of the area.

ACKNOWLEDGEMENTS

The authors wish to thank the NSERC for their financial support for the Costa-Canada project and for ship time allocation. Many thanks to André Godin and Richard Sanfaçon (Services hydrographique de l'Institut Maurice Lamontagne), Christiane Levesque, Pierre Therrien, Patrick Lajeunesse (Université Laval), Roger Urgeles and Ben DeMol (University of Barcelona), Bassam Ghaleb (GEOTOP UQAM-McGill), Mathieu Duchesne (CGS-Quebec and INRS-ETE), and Hydro-Québec Pétrole et Gaz for data of the Targeted Geoscience Initiative Appalachian Energy project, and finally for all the crew members aboard the F.G. Creed and Coriolis II.

REFERENCES

Allard, J.-D., 1984. Zones exposées aux mouvements de terrain, région de Chutes-aux-Outardes, Ministère de l'Énergie et des Ressources, Québec, 42 pp.

Appleby, P.G. and Oldfield, F., 1978. The calculation of lead-210 dates assuming a constant rate of supply of unsupported ^{210}Pb to the sediment. CATENA, 5(1): 1-8.

Aylsworth, J.M., Lawrence, D.E. and Guertin, J., 2000. Did two massive earthquakes in the Holocene induce widespread landsliding and near-surface deformation in part of the Ottawa Valley, Canada? Geology, 28(10): 903-906.

Bernatchez, P., 2003. Évolution littorale holocène et actuelle des complexes deltaiques de Betsiamites et de Manicouagan-Outardes : synthèse, processus, causes et perspectives, Université Laval, Sainte-Foy, 460 pp.

Bernatchez, P., Dubois, J.-M.M. and Dionne, J.C., 1999. Les dépôts coquilliers (faluns) holocènes de Baie-Comeau, Côte-Nord de l'estuaire du Saint-Laurent, Québec. Canadian Journal of Earth Sciences, 36(4): 519-531.

Blott, S.J. and Pye, K., 2001. GRADISTAT: A grain size distribution and statistics package for the analysis of unconsolidated sediments. Earth Surface Processes and Landforms, 26(11): 1237-1248.

Boespflug, X., Long, B.F.N. and Occhietti, S., 1995. Cat-Scan in Marine Stratigraphy - a Quantitative Approach. Marine Geology, 122(4): 281-301.

Boyer-Villemaire, U., Gagné, H., 2005. Analyses granulométriques de carottes sédimentaires de la mer de Beaufort et analyses au MSCL et au CAT-scan des carottes sédimentaires de la mission COR0503. Technical report ISMER, 86 pp.

Brown, L.F. and W.L, F., 1980. Principles of seismic stratigraphic interpretation. AAPG, Austin, Texas, 125 pp.

Brunsden, D. and Prior, D.B. (Editors), 1984. Slope instability. Wiley, New York, 620 pp.

Canals, M., *et al.*, 2004. Slope failure dynamics and impacts from seafloor and shallow sub-seafloor geophysical data: case studies from the COSTA project. Marine Geology, 213 (1-4): 9-72

Clet-Pellerin, M. and Occhietti, S., 2000. Pleistocene palynostratigraphy in the St. Lawrence Valley and middle Estuary. Quaternary International, 68: 39-57.

Cojan, I. and Renard, M., 2003. Sédimentologie. Dunod, Paris, 418 pp.

Cremer, J.F., Long, B., Desrosiers, G., de Montety, L. and Locat, J., 2002. Application de la scanographie à l'étude de la densité des sédiments et à la caractérisation des structures sédimentaires : exemple des sédiments déposés dans la rivière Saguenay (Québec, Canada) après la crue de juillet 1996. Canadian Geotechnical Journal, 39(2): 440-450.

Cruden, D.M. and Varnes, D.J., 1996. Landslide Types and Processes. In: A.K. Turner and R.L. Schuster (Editors), Landslides Investigation and Mitigation. Transportation Research Board, Washington DC, pp. 36-75.

Damuth, J.E., 1980. Use of High-Frequency (3.5-12 Khz) Echograms in the Study of near-Bottom Sedimentation Processes in the Deep-Sea - a Review. Marine Geology, 38(1-3): 51-75.

d'Anglejan, B., 1990. Recent sediments and sediment transport processes in the St. Lawrence Estuary. In: M.I.a.S. El-Sabh, N. (Editor), Oceanography of a Large-Scale Estuarine System-The St. Lawrence. Springer-Verlag, New York, pp. 109-129.

d'Anglejan, B. and Brisebois, M., 1974. First Subbottom Acoustic Reflector and Thickness of Recent Sediments in Upper Estuary of St-Lawrence River. Canadian Journal of Earth Sciences, 11(2): 232-245.

Dionne, J.C., 1977. La Mer de Goldthwait au Québec. Géographie physique et Quaternaire, 16(1-2): 61-80.

Dionne, J.C., 1988. Holocene Relative Sea-Level Fluctuations in the St Lawrence Estuary, Quebec, Canada. Quaternary Research, 29(3): 233-244.

Dionne, J.C., 2001. Relative Sea-Level changes in the St. Lawrence Estuary from deglaciation to present day. In: T.K. Weddle and M.J. Retelle (Editors), Deglacial History and Relative Sea-Level Changes, Northern New England and Adjacent Canada. Geological Society of America Special Paper, Boulder, Colorado, pp. 271-284.

Dionne, J.C., 2002. État des connaissances sur la ligne de rivage Micmac de J.W. Goldthwait (Estuaire du Saint-Laurent). Géographie physique et Quaternaire, 56(1): 97-121.

Dredge, L.A., 1976. Quaternary geomorphology of the Quebec North Shore, Godbout to Sept-Iles. Ph.D Thesis, University of Waterloo, Waterloo, 268 pp.

Dubois, J.-M.M., 1977. La déglaciation de la Côte-Nord du Saint-Laurent. Géographie physique et Quaternaire, 16(3-4): 229-246.

Dubois, J.-M.M., 1980. Géomorphologie du littoral de la Côte-Nord du Saint-Laurent : Analyse sommaire. In: S.B. McCann (Editor), The Coasline of Canada. Geological Survey of Canada, pp. 215-238.

Duchesne, M. J. and Bellefleur, G. in press. Processing of single-channel high-resolution seismic data collected in the St. Lawrence Estuary. Current Research, 15 p.

Duchesne, M.J., Long, B.F., Urgeles, R. and Locat, J., 2003. New evidence of slope instability in the Outardes Bay delta area, Quebec, Canada. Geo-Marine Letters, 22(4): 233-242.

Filion, L., Quinty, F. and Begin, C., 1991. A Chronology of Landslide Activity in the Valley of Riviere Du Gouffre, Charlevoix, Quebec. Canadian Journal of Earth Sciences, 28(2): 250-256.

Franconi, A., Sharma, K.N.M. and Laurin, A.F., 1975. Région des rivières Betsiamites (Bersimis) et Moisie, Rapport géologique 162. Québec; Ministère des richesses naturelles, Direction générale des mines, Service de l'exploration géologique, 149 pp.

Fulton, R.J., 1989. Le Quaternaire du Canada et du Groenland. Commission géologique du Canada, Ottawa, 907 pp.

Grondin, G., d'Astous, J., Demers, D. and Dorval, P., L'érosion des berges de la péninsule de Manicouagan et de la région de Ragueneau, Québec, Ministère des Transport du Québec, Québec.

Hampton, M.A., Lee, H.J. and Locat, J., 1996. Submarine landslides. Reviews of Geophysics, 34(1): 33-59.

Hart, B.S., 1987. The Evolution of the Outardes Estuary. M.Sc. Thesis, Université du Québec à Rimouski, Rimouski, 197 pp.

Hart, B.S. and Long, B.F., 1996. Forced regressions and lowstand deltas: Holocene Canadian examples. Journal of Sedimentary Research, 66(4): 820-829.

Hein, F.J., Syvitski, J.P.M., Dredge, L.A. and Long, B.F., 1993. Quaternary Sedimentation and Marine Placers Along the North Shore, Gulf of St-Lawrence. Canadian Journal of Earth Sciences, 30(3): 553-574.

Hovland, M., Gardner J. V., and Judd, A. G., 2002. The significance of pockmarks to understanding fluid flow processes and geohazards. Geofluids 2(2): 127-136.

Hughes Clarke, J.E.H., Mayer, L.A. and Wells, D.E., 1996. Shallow-water imaging multibeam sonars: A new tool for investigating seafloor processes in the coastal zone and on the continental shelf. Marine Geophysical Researches, 18(6): 607-629.

Josenhans, H. and Lehman, S., 1999. Late glacial stratigraphy and history of the Gulf of St. Lawrence, Canada. Canadian Journal of Earth Sciences, 36(8): 1327-1345.

Juichiro, A. (Editor), 1997. Computed tomography scan image analysis of sediments. Proceedings of the Ocean Drilling Program, 156.

Koide, M., Bruland, K. and Goldberg, E., 1973. 228/Th-232 and Pb-210 geochronologies in marine and lake sediments. Geochimica and Cosmochimica Acta, 37: 1171–1181.

Krishnaswamy, S., Lal, D., Martin, J.M. and Meybeck, M., 1971. Geochronology of lake sediments. Earth and Planetary Science Letters, 11(1-5): 407-414.

Lajoie, M., Simard, P., and Boyer-Villemaire, U., 2007. Analyse au MSCL et au CAT-Scan des carottes sédimentaires de la mission COR0602. Fjord du Saguenay, estuaire et golfe du Saint-Laurent. Technical report. ISMER. Université du Québec à Rimouski. pp. 126

Lamontagne, M., Keating, P. and Perreault, S., 2003. Seismotectonic characteristics of the Lower St. Lawrence Seismic Zone, Quebec: insights from geology, magnetics, gravity, and seismics. Canadian Journal of Earth Sciences, 40(2): 317-336.

Lasalle, P., and Chagnon, J.-Y., 1968. An ancient landslide along the Saguenay River, Quebec. Canadian Journal of Earth Sciences, 5(1):548 -549.

Lavoie, D. *et al.*, 2004. The Targeted Geoscience Initiative Appalachian Energy project: a multipartner-multidiscipline approach to defining the hydrocarbon potential of the Appalachian frontier basins. Québec Exploration 2004: abstracts of oral presentations and posters, 38.

Lee, H.J. *et al.*, 2002. Distinguishing sediment waves from slope failure deposits: field examples, including the 'Humboldt slide' and modelling results. Marine Geology, 192(1-3): 79-104.

Levesque, C.L., Locat, J., and Leroueil S., 2006. Dating submarine mass movements triggered by earthquakes in the Upper Saguenay Fjord, Quebec, Canada. Norwegian Journal of Geology, 86: 231-242.

Locat, J., 1977. L'émersion des terres dans la région de Baie-des-Sables/Trois-Pistoles. Géographie physique et Quaternaire, 31: 297-306.

Locat, J. and Lee, H.J., 2002. Submarine landslides: advances and challenges. Canadian Geotechnical Journal, 39(1): 193-212.

Locat, J. *et al.*, 2004. Aperçu des mouvements de masse sous-marins au large de la rivière Betsiamites, estuaire du Saint-Laurent, Québec, Canada, Conférence Canadienne de Géotechnique, Québec.

Locat, J. and Mienert, J. (Editors), 2003. Submarine Mass Movements and their Consequences 1st International Symposium. Kluwer Academic Publishers, Dordrecth, The Netherlands, 540 pp.

Lomas, S.A. and Joseph, P. (Editors), 2004. Confined turbidite systems. Geological Society Special Publications, 222. The Geological Society Publishing House, Oxford, UK, 336 pp.

Loring, D.H. and Nota, D.J.G., 1973. Morphology and Sediments of the Gulf of St. Lawrence, Bulletin of the Fisheries Research Board of Canada 182, Ottawa, 147 pp.

Maslin, M., Owen, M., Day, S. and Long, D., 2004. Linking continental-slope failures and climate change: Testing the clathrate gun hypothesis. Geology, 32(1): 53-56.

Masse, M., 2001. Évolution générale des dépôts quaternaires sous l'estuaire du St-Laurent entre l'Îles aux Lièvres et Rimouski. Mémoire de maîtrise, Université du Québec à Rimouski, Rimouski, 129 pp.

McAdoo, B.G., Pratson, L.F. and Orange, D.L., 2000. Submarine landslide geomorphology, US continental slope. Marine Geology, 169(1-2): 103-136.

McQuillin, R., 1979. Introduction à l'interprétation sismique. SCM, Paris, 195 pp.

Michaud, E. *et al.*, 2003. Use of axial tomography to follow temporal changes of benthic communities in an unstable sedimentary environment (Baie des Ha! Ha!, Saguenay Fjord). Journal of Experimental Marine Biology and Ecology, 285: 265-282.

Mulder, T. and Alexander, J., 2001. The physical character of subaqueous sedimentary density flows and their deposits. Sedimentology, 48(2): 269-299.

Mulder, T. and Cochonat, P., 1996. Classification of offshore mass movements. Journal of Sedimentary Research, 66(1): 43-57.

Occhietti, S. *et al.*, 2001. Late Wisconsian glacial dynamics, deglaciation, and marine invasion in southern Québec. In: T.K. Weddle and M.J. Retelle (Editors), Deglacial History and Relative Sea-Level Changes, Northern New England and Adjacent Canada:. Geological Society of America Special Paper, Boulder, Colorado, pp. 243-270.

Payton, C.E. (Editor), 1977. Seismic stratigraphy : applications to hydrocarbon exploration, AAPG Memoir 26. American Association of Petroleum Geologists, Tulsa, Oklahoma, 516 pp.

Pelletier, M., 1993. Les glissements sous-marins du Bras Nord du Fjord du Saguenay : Aspects géomorphologiques et géotechniques. Mémoire de maîtrise, Université Laval, Ste-Foy, 124 pp.

Piper D.J.W, *et al.*, 2003. The chronology and recurrence of submarine mass movements on the continental slope off southeastern Canada. In: Locat, J. and Mienert, J. (Editors), 2003. Submarine Mass Movements and their Consequences 1st International Symposium. Kluwer Academic Publishers, Dordrecth, The Netherlands, pp 299-305.

Piper, D.J.W., Shor, A.N., Farre, J.A., Oconnell, S. and Jacobi, R., 1985. Sediment Slides and Turbidity Currents on the Laurentian Fan - Sidescan Sonar Investigations near the Epicenter of the 1929 Grand Banks Earthquake. Geology, 13(8): 538-541.

Prior, D.B., Bornhold, B.D. and Johns, M.W., 1984. Depositional Characteristics of a Submarine Debris Flow. Journal of Geology, 92(6): 707-727.

Reading, H.G., 1996. Sedimentary Environments : Processes, Facies, and Stratigraphy. Blackwell Scientific Publications, Oxford, UK, 688 pp.

Sangree, J.B. and Widemier, J.M., 1977. Seismic Stratigraphy and Global Changes of Sea Level, Part 9 : Seismic Interpretation of Clastic Depositional Facies. In: C.E. Payton (Editor), Seismic stratigraphy : applications to hydrocarbon exploration. American Association of Petroleum Geologists, Tulsa, Oklahoma, pp. 165-184.

Sauvé, P. and Lasalle, P., 1968. Notes sur la géologie glaciaire de la région de Manic 2. Le Naturaliste Canadien, 95(6): 1293-1300.

Shaw, J., D.J.W. Piper, G.B.J. Fader, E.L. King, B.J. Todd, T. Bell, M.J. Batterson and D.G.E. Liverman, 2006. A conceptual model of the deglaciation of Atlantic Canada, Quaternary Science Reviews, 25 (17-18), 2059-2081.

Shaw, J., Gareau, P. and Courtney, R.C., 2002. Palaeogeography of Atlantic Canada 13-0 kyr. Quaternary Science Reviews, 21(16-17): 1861-1878.

Sheriff, R.E., 1977. Limitations on Resolution of Seismic Reflections and Geologic Detail Derivable from Them. In: C.E. Payton (Editor), Seismic stratigraphy : applications to hydrocarbon exploration. American Association of Petroleum Geologists, Tulsa, Oklahoma, pp. 3-14.

Shilts, W.W. and Clague, J.J., 1992. Documentation of Earthquake-Induced Disturbance of Lake-Sediments Using Subbottom Acoustic Profiling. Canadian Journal of Earth Sciences, 29(5): 1018-1042.

Smith, J.N. and Schafer, C.T., 1999. Sedimentation, bioturbation, and Hg uptake in the sediments of the Estuary and Gulf of St. Lawrence. Limnology and Oceanography, 44(1): 207-219.

Smith, W., 1962. Earthquakes of eastern Canada and adjacent areas, 1534-1927, 26. Publications of the Dominion Observatory, Ottawa, pp. 271-301.

St-Onge, G. *et al.*, 1999. Caractérisation des sédiments récents du fjord du Saguenay (Québec) à partir de traceurs physiques, géochimiques, isotopiques et micropaléontologiques. Géographie physique et Quaternaire, 53(3): 339-350.

St-Onge, G., Mulder, T., Piper, D.J.W., Hillaire-Marcel, C. and Stoner, J.S., 2004. Earthquake and flood-induced turbidites in the Saguenay Fjord (Quebec): a Holocene paleoseismicity record. Quaternary Science Reviews, 23(3-4): 283-294.

St-Onge, G., Mulder, T., Francus, P., Long, B. *In press*. Continuous physical properties of cored marine sediments. In: C. Hillaire-Marcel et A. de Vernal (Editors.), Proxies in Late Cenozoic Paleoceanographie, Elsevier.

St-Onge, G., Stoner, J.S. and Hillaire-Marcel, C., 2003. Holocene paleomagnetic records from the St. Lawrence Estuary, eastern Canada: centennial- to millennial-scale geomagnetic modulation of cosmogenic isotopes. Earth and Planetary Science Letters, 209(1-2): 113-130.

Syvitski, J.P.M. and Praeg, D., 1989. Quaternary Sedimentation in the St. Lawrence Estuary and adjoining areas, Eastern Canada : an overview based on high resolution seismo-stratigraphy. Géographie physique et Quaternaire, 43(3): 291-310.

Thwaites, R.G. (Editor), 1959. The Jesuit relations and allied documents : travels and explorations of the Jesuit missionaries in New France, 1610-1791 : the original French, Latin, and Italian texts, with English translations and notes. Pageant Book Co, New York.

Tremblay, A., Long, B. and Masse, M., 2003. Supracrustal faults of the St. Lawrence rift system, Quebec: kinematics and geometry as revealed by field mapping and marine seismic reflection data. Tectonophysics, 369(3-4): 231-252.

Urgeles, R., Locat, J., Lee, H.J. and Martin, F., 2002. The Saguenay Fjord, Quebec, Canada: integrating marine geotechnical and geophysical data for spatial seismic slope stability and hazard assessment. Marine Geology, 185(3-4): 319-340.

Zhang, D., 2000. Fluxes of Short-lived Radioisotopes in the Marginal Marine Basins of Eastern Canada. Ph.D Thesis, Université du Québec à Montréal, Montréal, 193 pp.

FIGURES

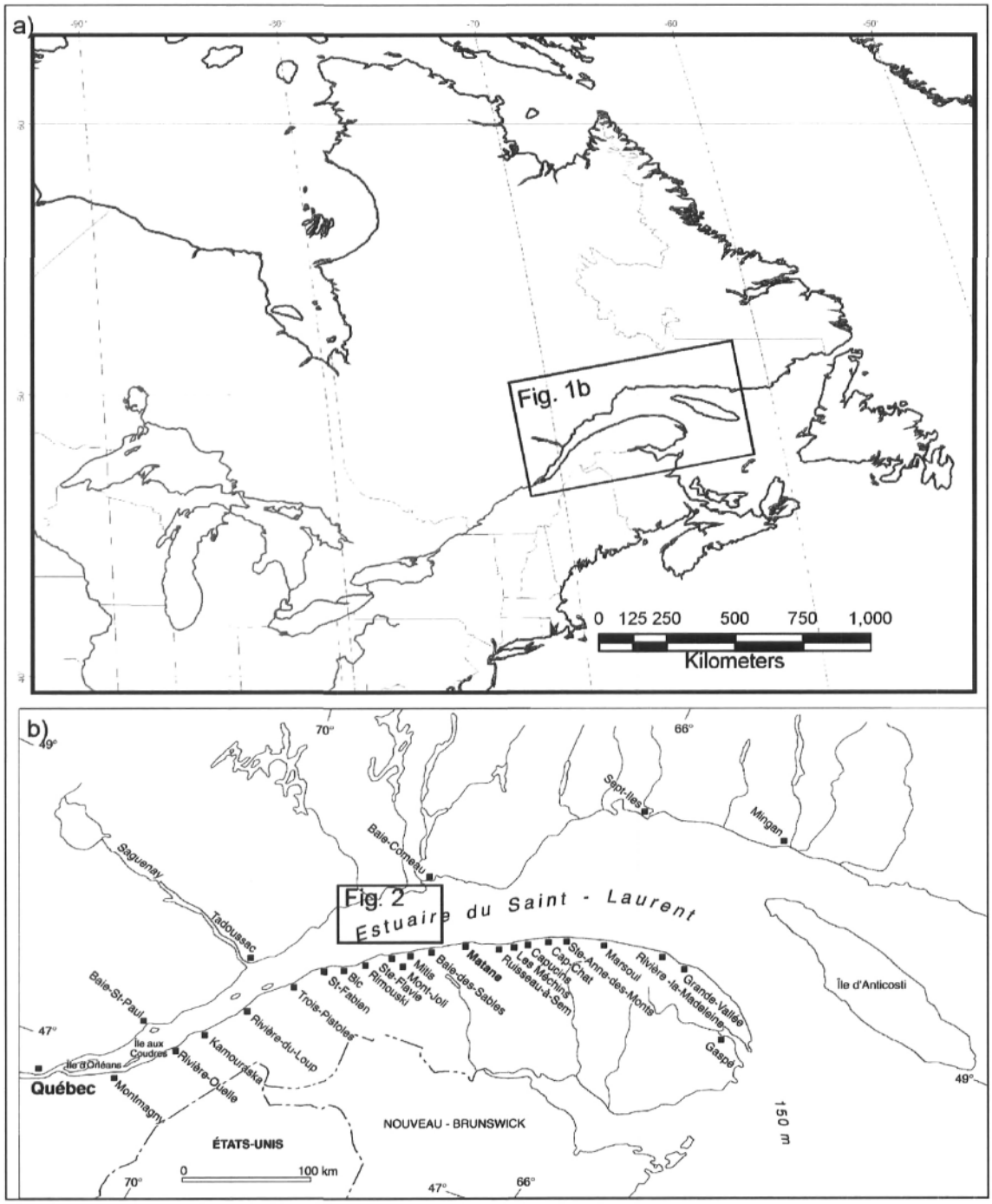

Figure 1. Map of Eastern Canada. Black rectangle indicates location of Figure 1b. (b) Location map of the Betsiamites - Rimouski study area in the St. Lawrence Estuary. Black rectangle indicates location of the study area presented on Figure 2

Figure 2. Bathymetric coverage of the study area and localization of Figs. 11 and 14. The three physiographic regions are indicated: shelf (SH), slope (SL), and Laurentian Channel (LC). Notice the location of the subaerial landslide scar, the Betsiamites River, and the MD99-2220 coring station. The white line corresponds to the position of the high resolution profile I-I' presented in Figure 22.

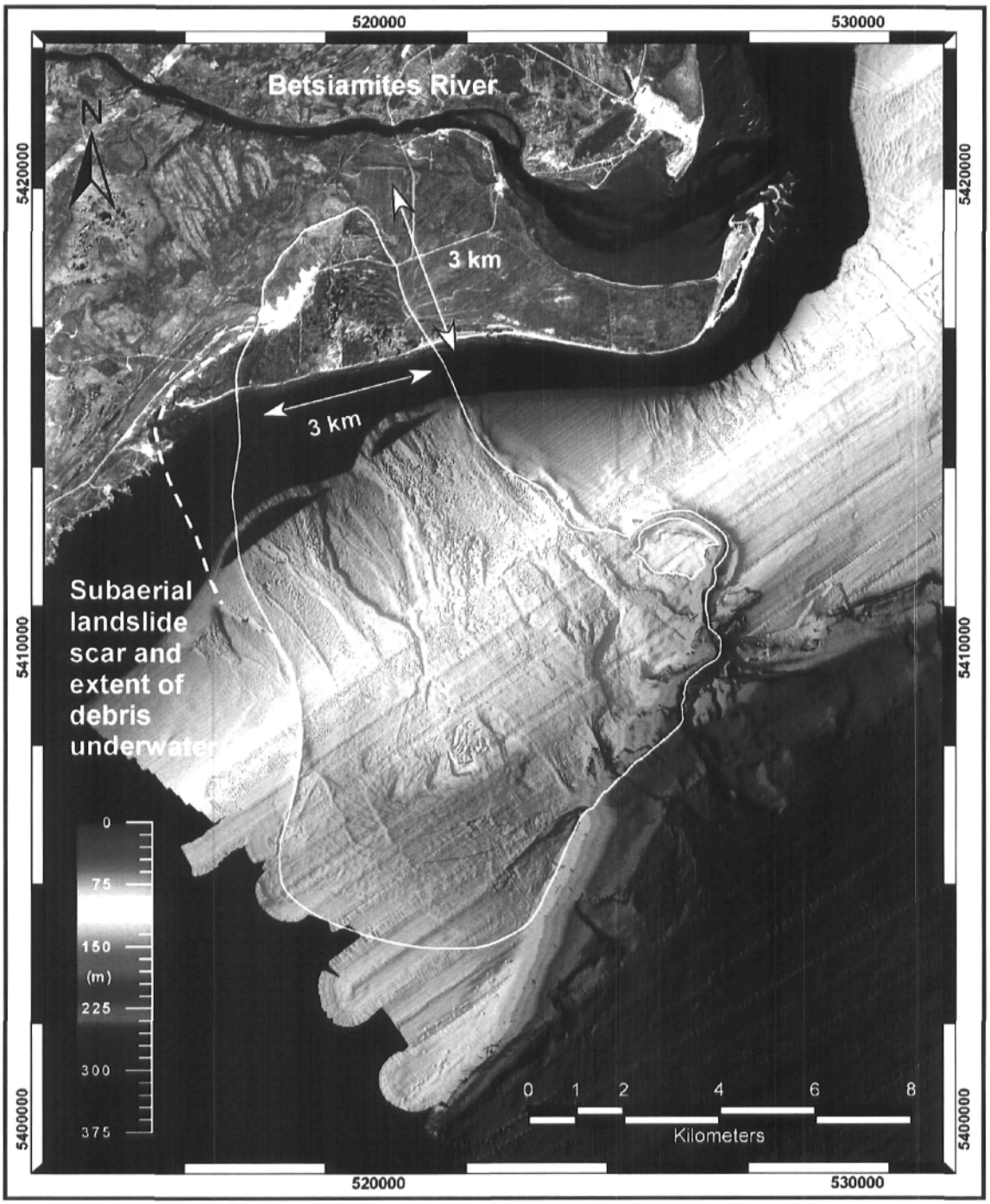

Figure 3 Outline of the subaerial landslide and adjoining submarine morphology. The subaerial landslide scar and the extent of the debris underwater on the shelf are outlined by the white line. The dashed line indicates the link between the subaerial and the submarine landslide structures. Notice the divergence between the extent of the last event on land and the submarine structures.

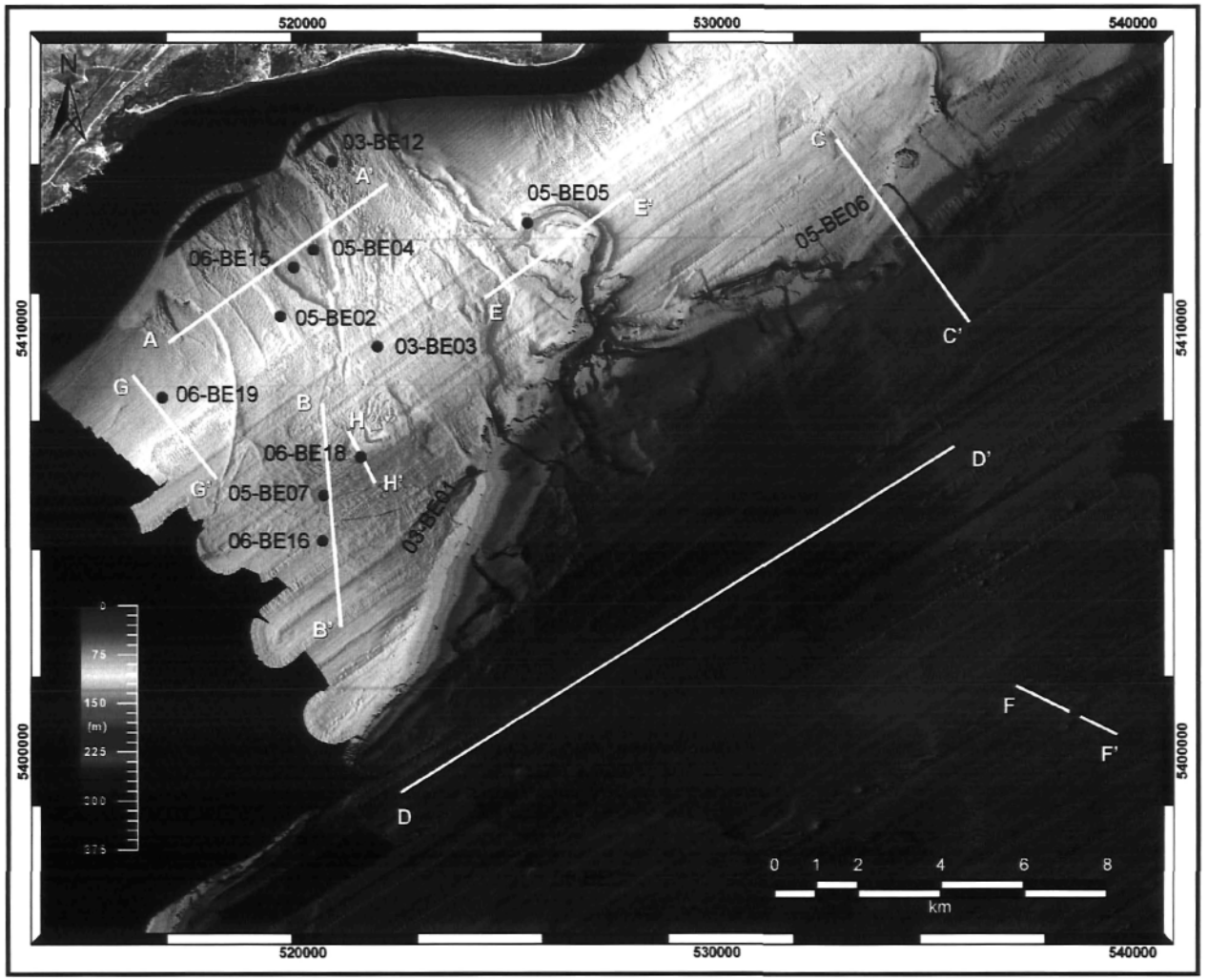

Figure 4. Location of the 15 sediment sampling stations described in Table 1 and positions of the high resolution seismic reflection profiles presented in this study.

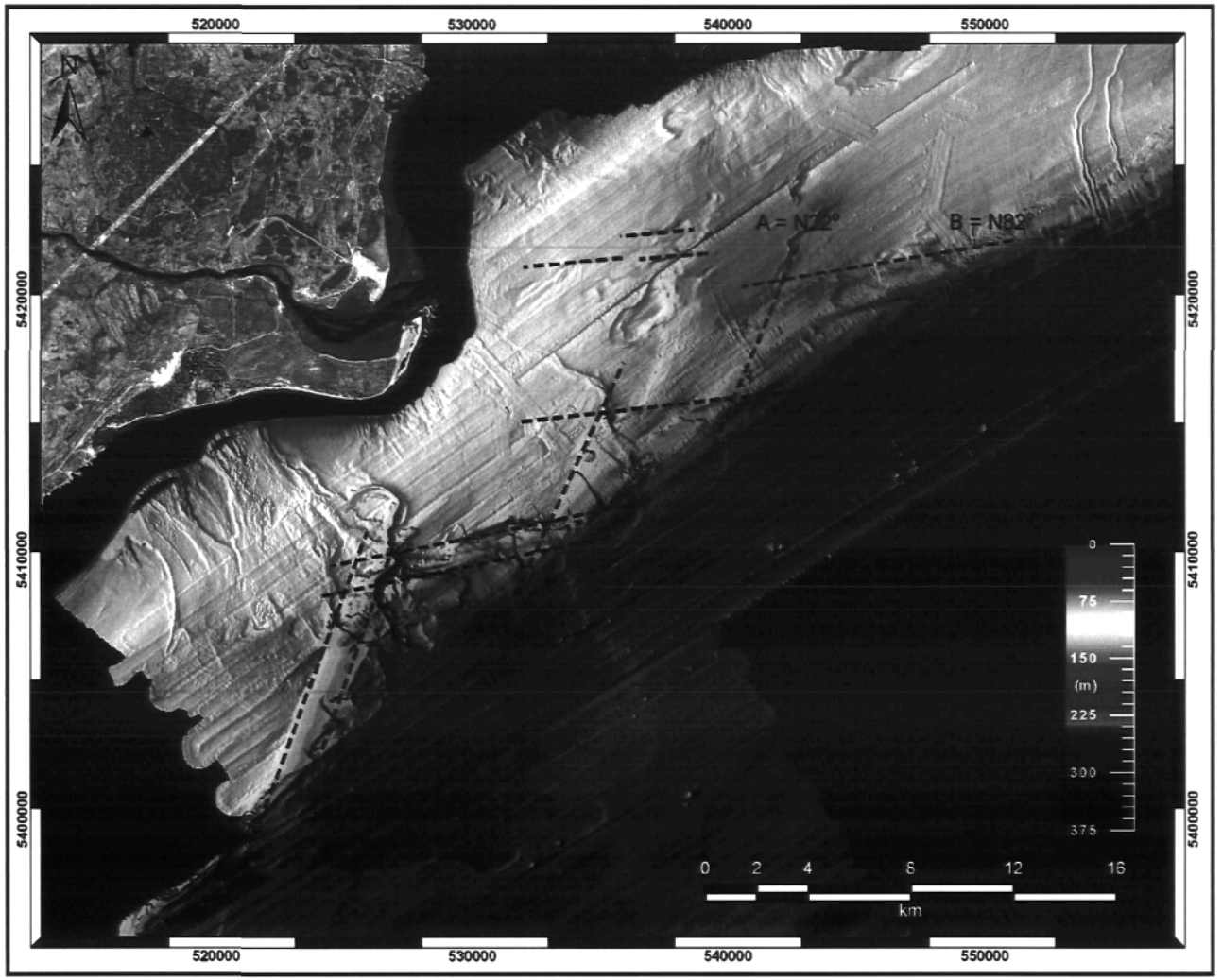

Figure 5. Bathymetric chart of the study area. Dashed lines outline the bedrock controlled lineaments. Notice the two families of orientation A=N22°and B=N82°.

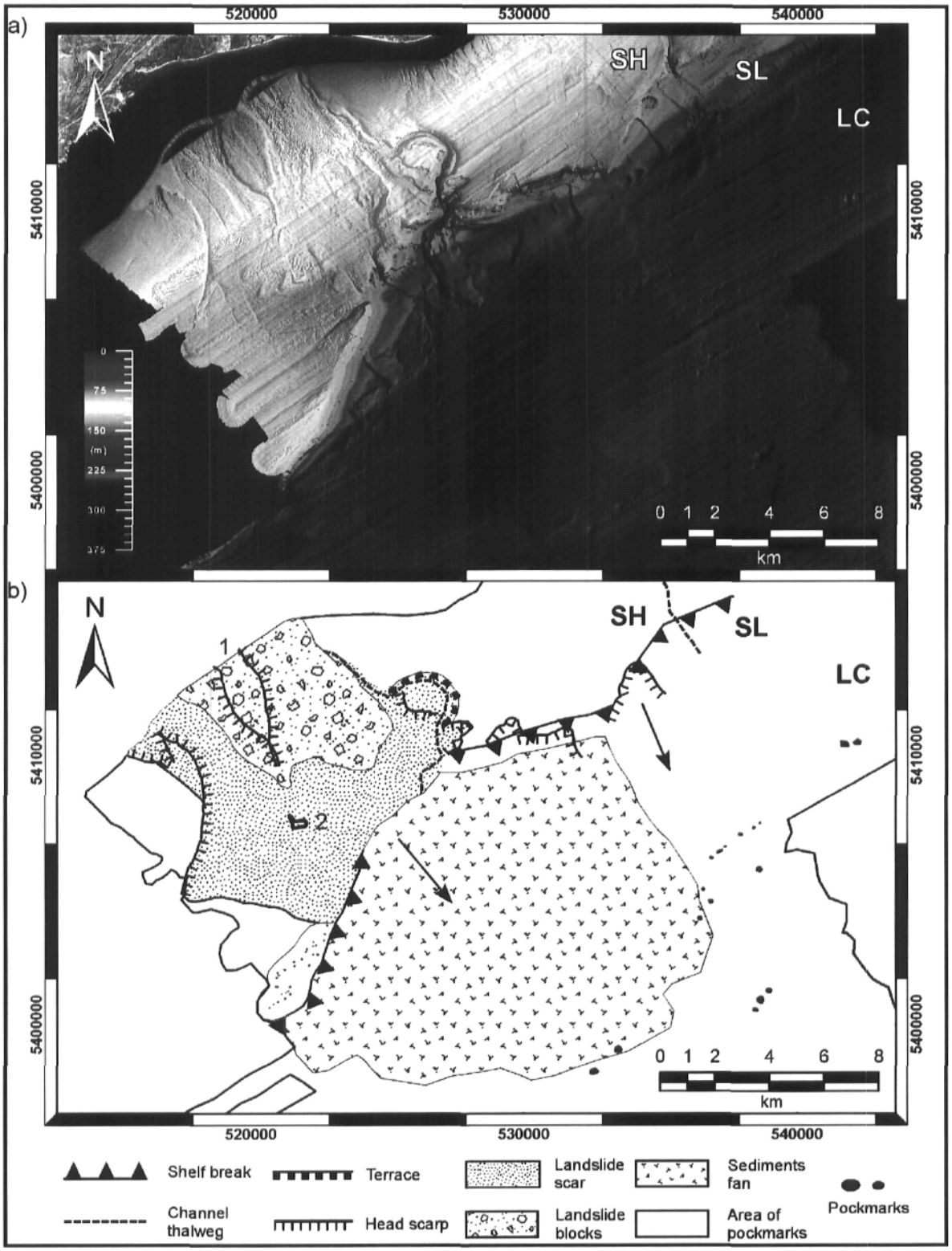

Figure 6. (a) Bathymetric map of the Betsiamites submarine area. SH indicates the shelf, SL the slope, and LC the Laurentian Channel. Water depth ranges from 0 to 375 m. (b) Geomorphological interpretations of the area, with focus on the mass movement morphologies. Arrows indicate landslide flow direction. 1 and 2 refer to the buttes.

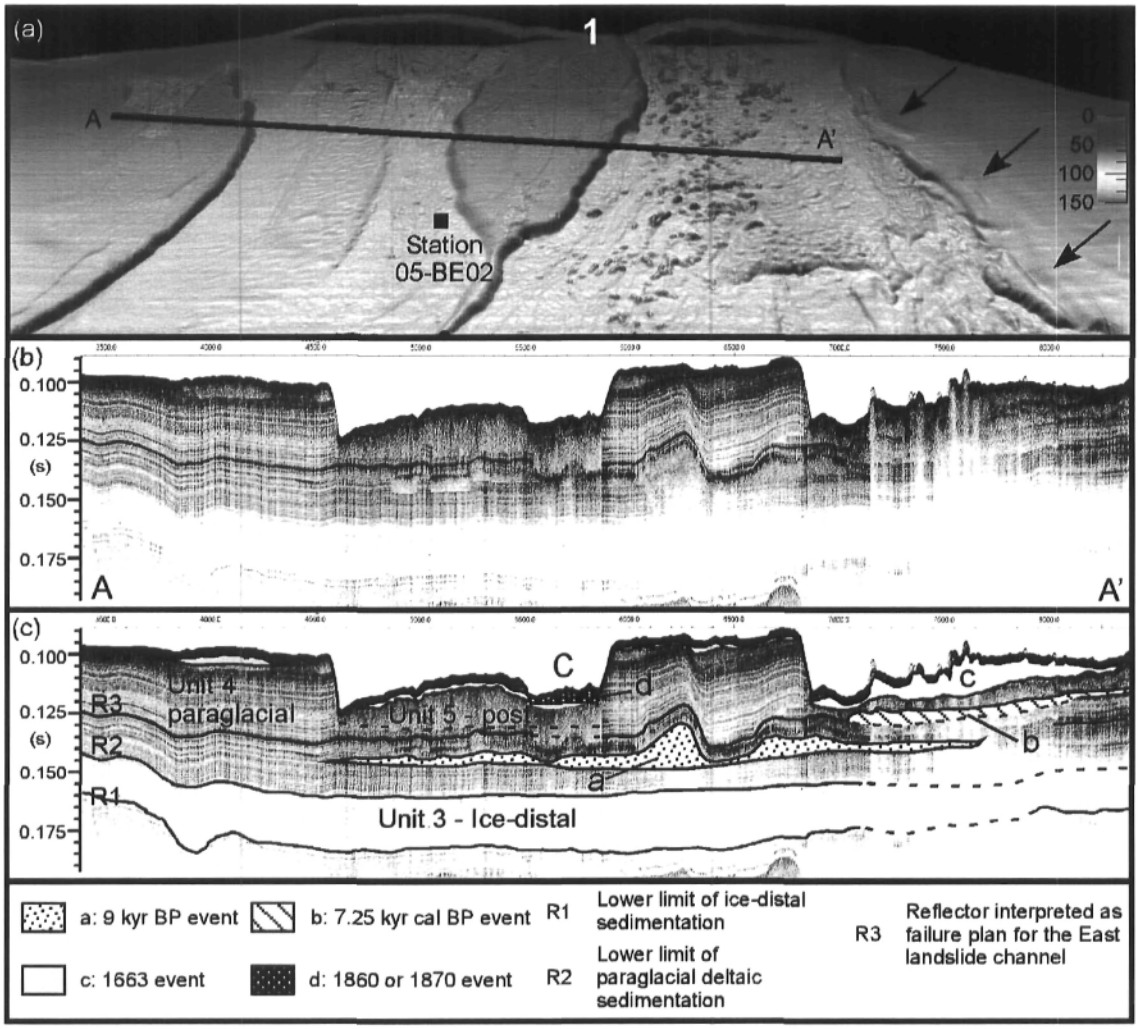

Figure 7. (a) Shaded bathymetry relief of the landslide channels and butte 1. View is looking north-west. Vertical exaggeration is 5x. Position of seismic profile A-A' is shown. Notice the remnants of upper paleochannel, indicated by the 3 arrows.

(b) High resolution seismic across the landslide Channel East and West the Central butte. Profile A-A' has a length of 7.4 km. The vertical exaggeration is 20x. Line be06_111. Scale in seconds, two way travel time. Notice the debris flow blocks which cause acoustic wipe-out.

(c) Interpretations of the seismic reflection profile. Seismostratigraphic Unit 5 (postglacial), Unit 4 (paraglacial sediments), and Unit 3 (ice-distal sediments) are indicated. The transition between Unit 4 and Unit 5 is a dashed line indicating a gradation between both units. Notice the high amplitude reflector R3 interpreted as the lower boundary of the East Landslide channel. Lower case letters refer to the mass movement sequence and chronology, (a) Paraglacial event, (b) Landslide channels Event, (c) 1663 event and (d) 1860-1870 event.

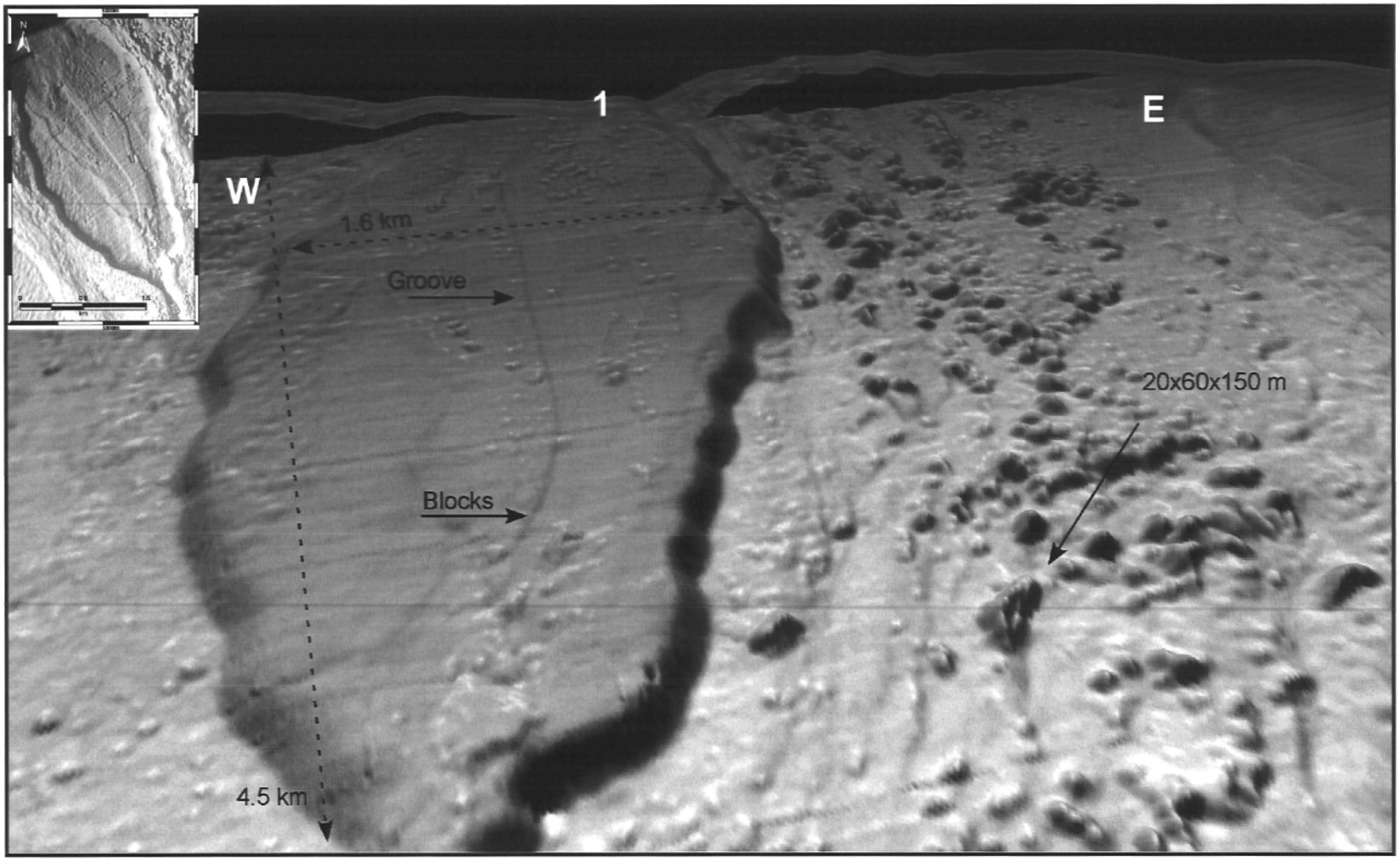

Figure 8. Shaded bathymetry relief of the landslide channels, enlargement on the surface of butte 1 and outrunner blocks. W and E refer to the West and East landslide channels, respectively. View is looking north-east. Vertical exaggeration is 5x. Notice the large outrunner blocks and the resulting grooves on the surface of butte 1.

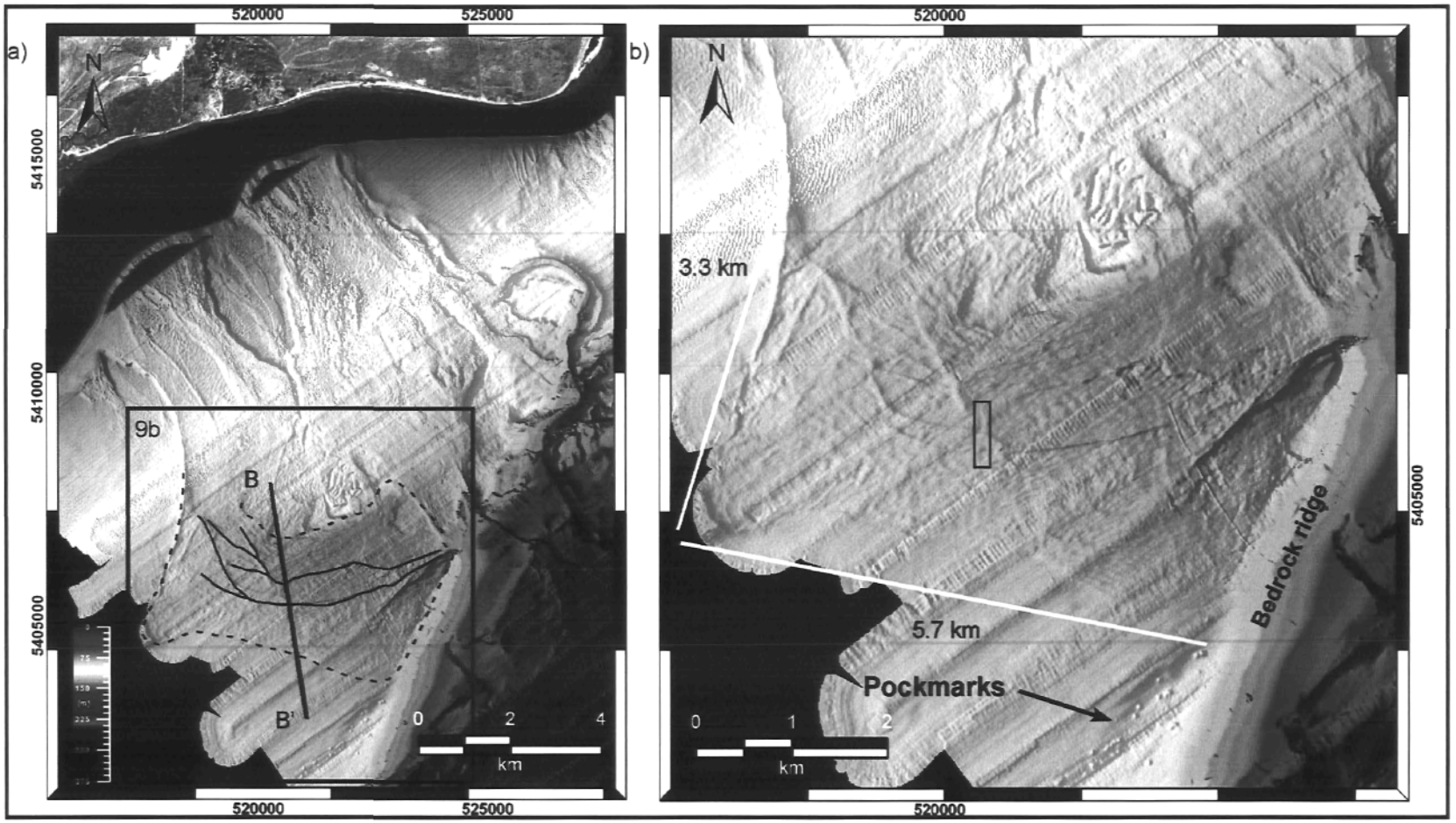

Figure 9. (a) Bathymetric image of the rugged area and the landslide channels with position of seismic profile B-B' presented on Figure 10. White rectangle indicates the enlargement presented in Figure 9b. Dashed line represents the limit between the rugged surface and the leveled sediments. Thin plain lines outline the gullies of the rugged area. Notice the pockmarks located close to the shelf edge. The water depth of the rugged area ranges between 130 and 170 m. (b) Enlargement of the bathymetric image of the rugged area with few interpretations. The rectangle corresponds to the enlargement of the seismic profile shown in Figure 10b.

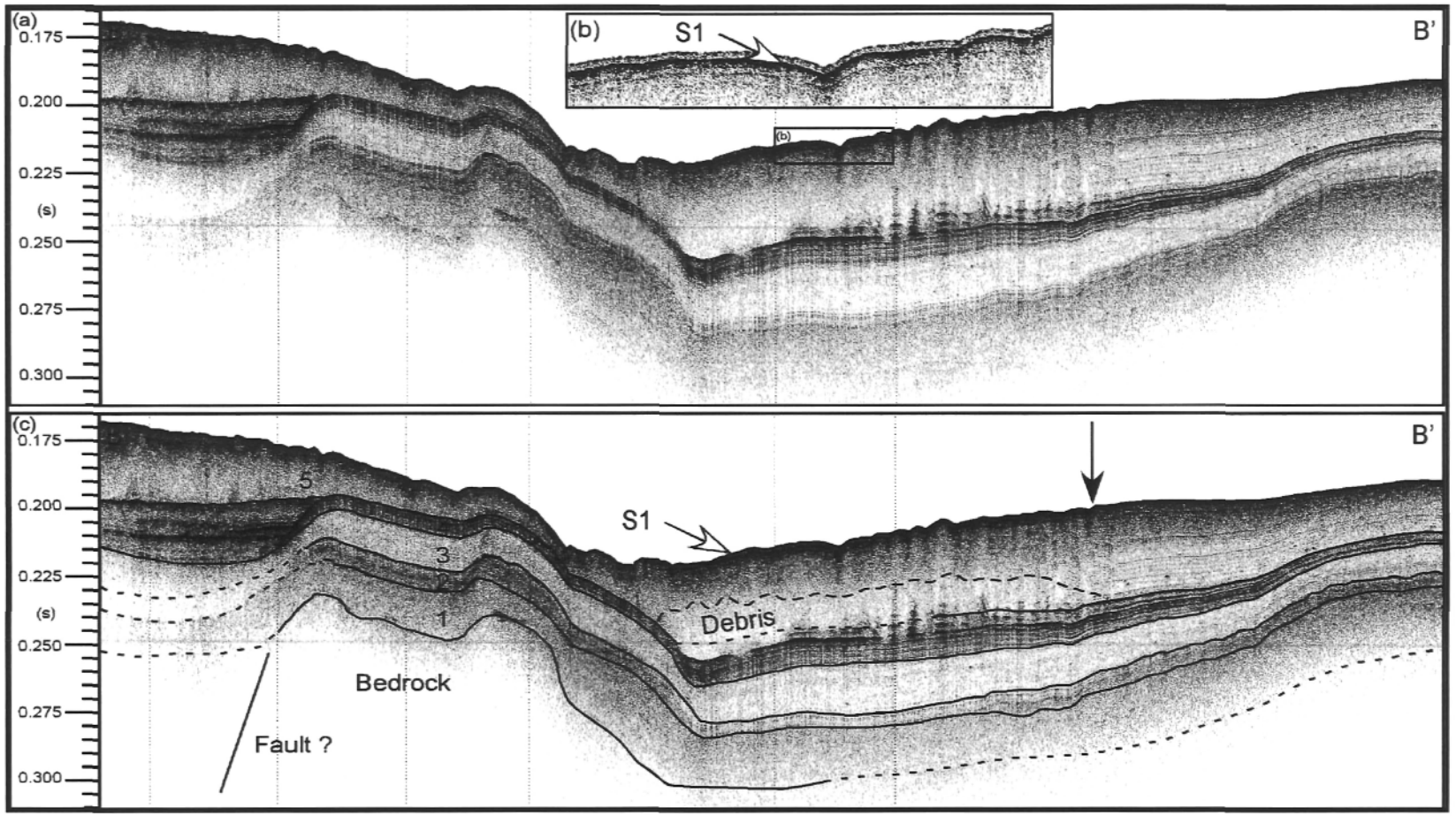

Figure 10. (a) Seismic reflection profile B-B' across the landslide channel west and the rugged area. Line is 5.6 km long. Vertical exaggeration is 15x. Line be06_102. Scale in seconds, two way travel time. (b) Enlargement of surface of the seismic reflection profile. The grove corresponds to the deepest gullies of the rugged area and is indicated by the black rectangle on Figure 9b. S1 is the shallow reflector identified across the study area and associated to the subaerial event. This enlargement also shows high amplitude reflectors implying conformable sedimentation. (c) Interpretations of the seismic reflection profile. Numbers refers to the seismostratigraphic units. Dotted lines indicate possible contact position between units. Arrow points to the limit between the rugged area and the level sediments.

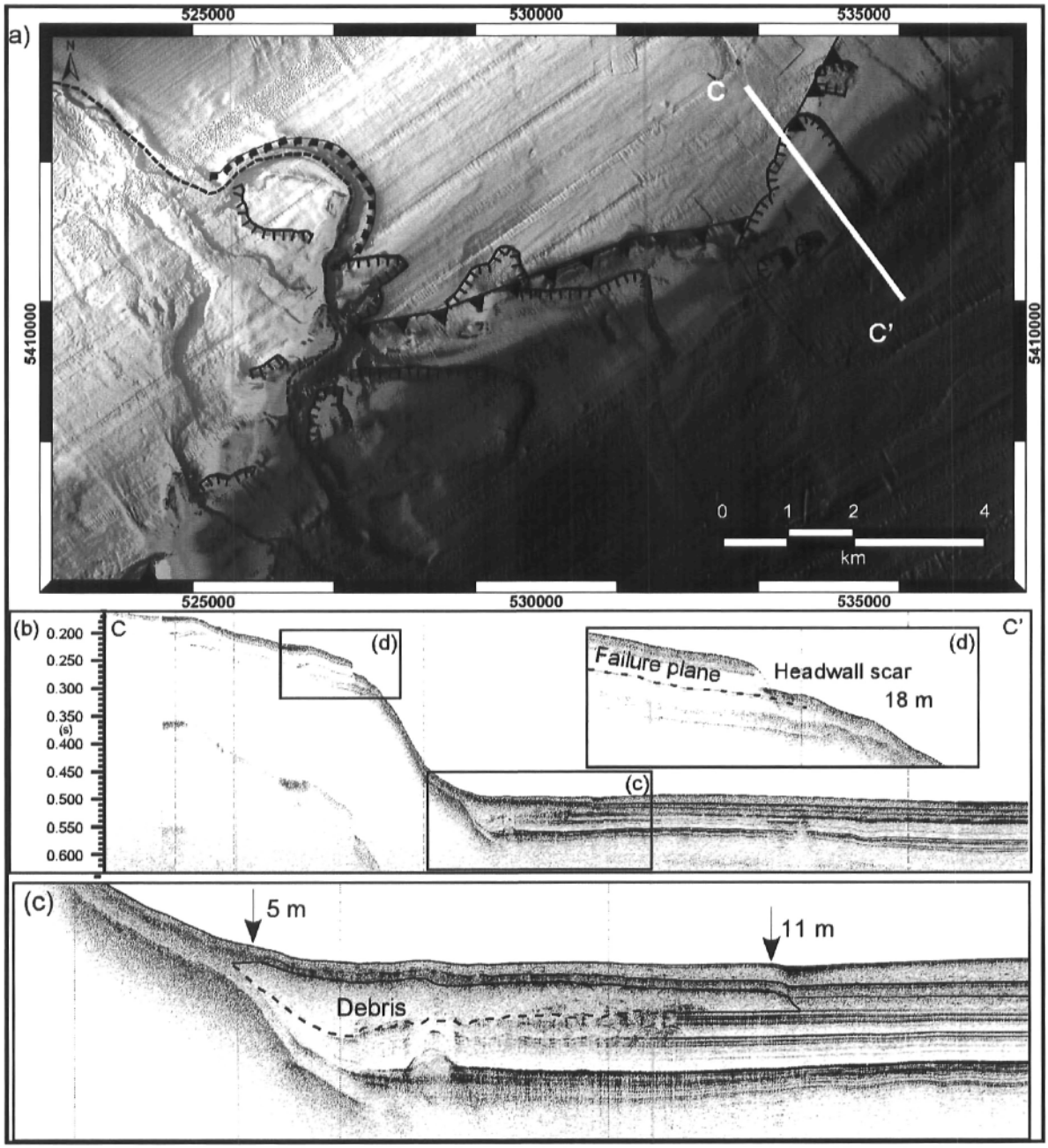

Figure 11. (a) Bathymetric image of the slope and landslides. Refer to Figure 6 for legend. Position of seismic profile C-C' is indicated. (b) Seismic reflection profile C-C' with enlargement of the headwall and the debris. Dotted line indicates the failure plane. Line is km 4.8 long. Vertical exaggeration is 4.5 x. Line bc06_118. Scale in seconds, two way travel time. (c) Enlargement on the debris area. 5 m and 11 m refer to the thickness of hemipelagic sediments draping the debris flow, assuming a sound wave velocity of 1500 m/s. (d) Enlargement of the headwall area, which is 18 m high at this location. The dashed line outlines the interpreted failure plane.

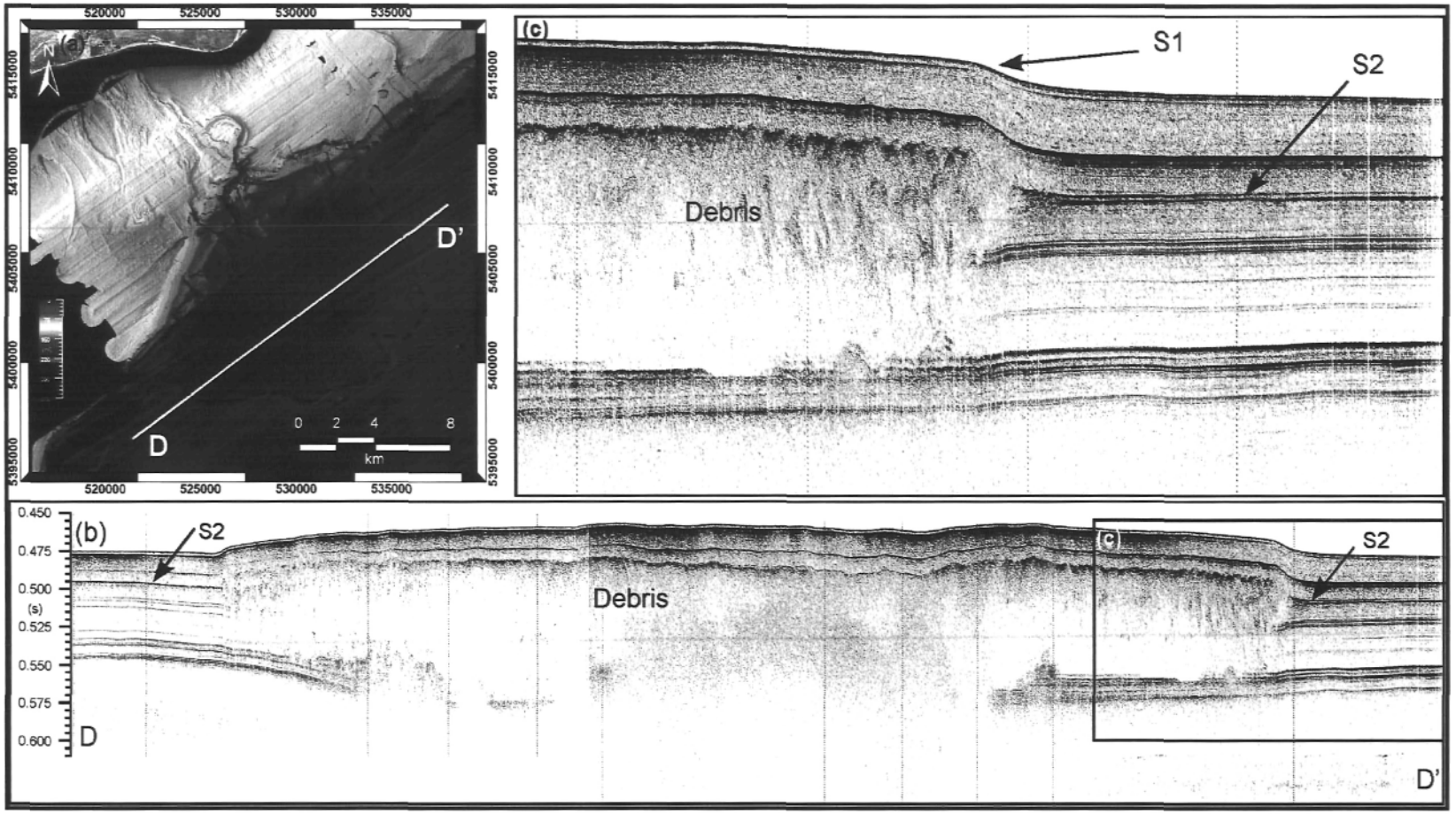

Figure 12. (a) Bathymetric image of the landslide area and the buried debris fan in the Laurentian Channel. Dashed line outlines the buried debris interpreted in the seismic reflection profiles and from raised topography on the bathymetric chart. (b) Seismic reflection profile D-D' across the debris flow fan. Line is 17.8 km long and vertical exaggeration is 30x. Line 03_bet2. Scale in seconds, two way travel time. Notice the debris flow and the resulting acoustic wipe-out, which is greater in the central section of the fan. (c) Enlargement on the outer limit of the debris flow fan. Notice the diffraction hyperbolae resulting from the debris flow.

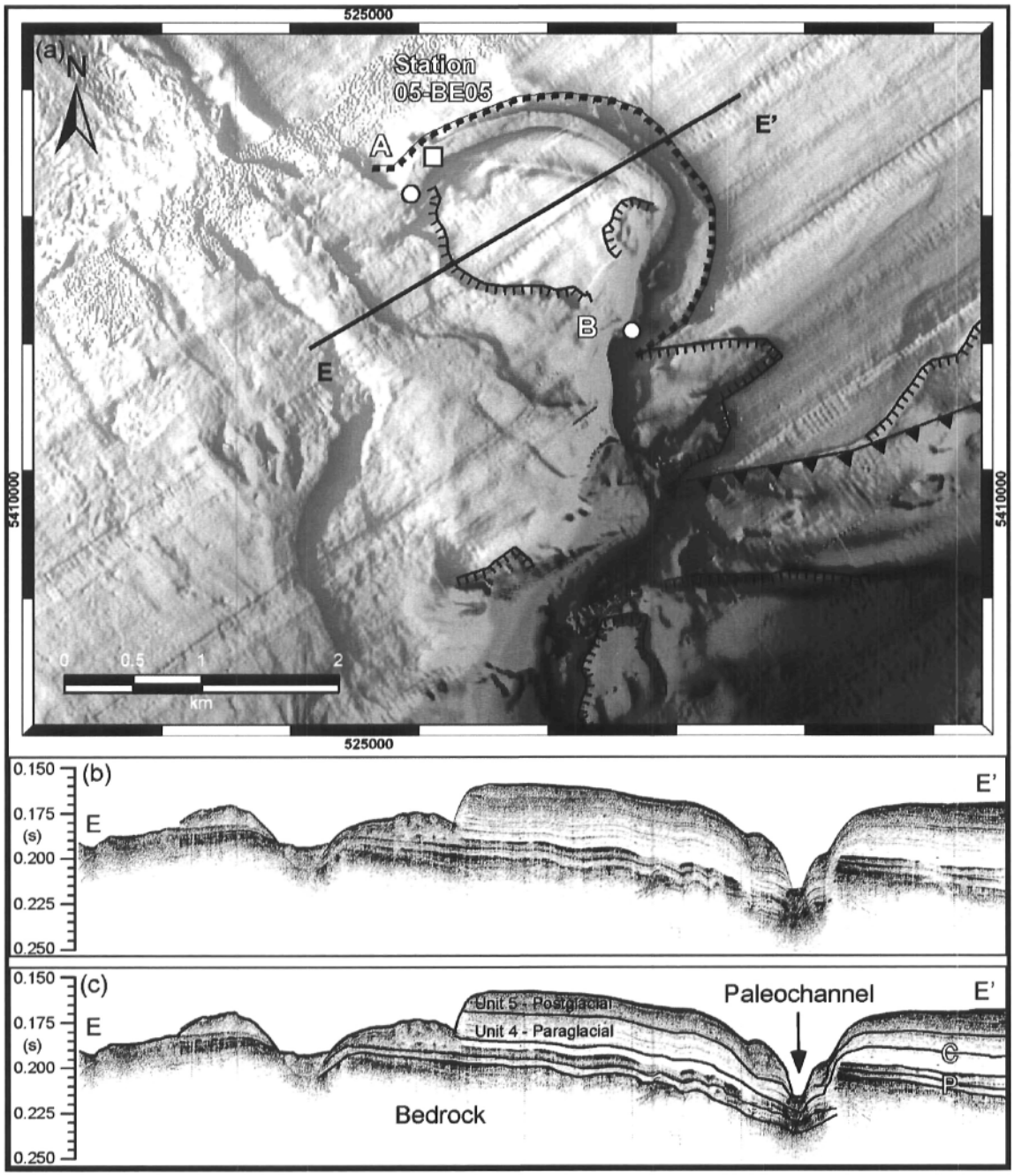

Figure 13. (a) Bathymetric image of the meander and the shelf break. Position of seismic profile E-E'. (b) Seismic profile E-E'. Notice the differences between the truncated and conformable reflector within the deposits of the meander banks. Line is km 4.8 long. Vertical exaggeration is 13x. Line 05_bet_12. Scale in seconds, two way travel time. (c) Interpretations with indication of seismostratigraphic Unit 4 (paraglacial sediments) and Unit 5 (postglacial). P refers to paraglacial reflectors and C to conformable sedimentation.

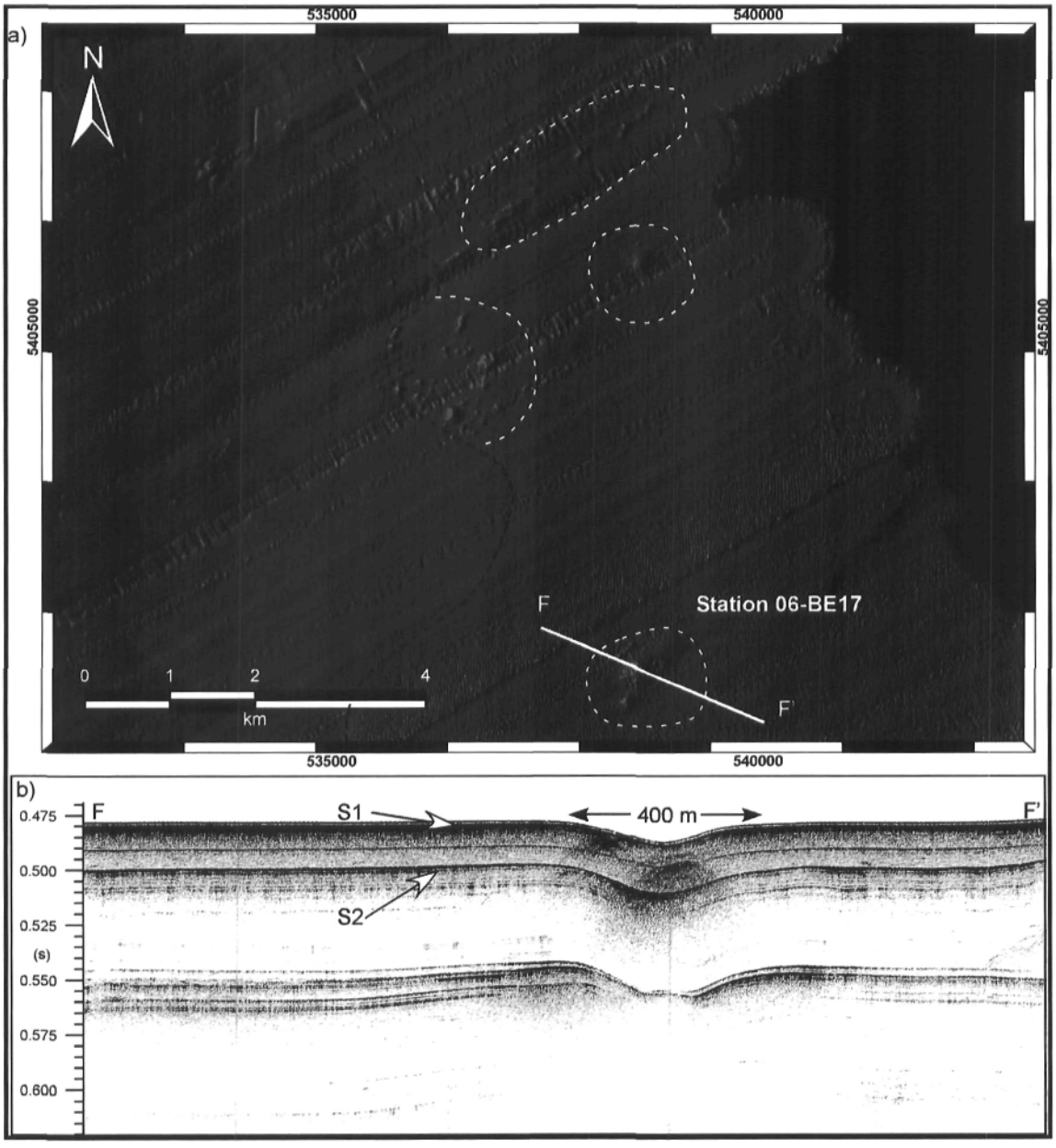

Figure 14. (a) Bathymetric image of the Laurentian Channel pockmarks. The water depth range from 330 to 350 m. Black dashed line outlines the buried debris flow fan. The white dashed lines outline the area with greater density of pockmarks. Notice that more pockmarks are observed outside the debris fan. Station 06-BE17 was not indicated precisely on this figure in order to allow the reader to fully size the pockmark. Refer to Figure 4 and Table 2 for exact position. (b) Seismic reflection profile F-F' across the pockmark. S1, S2 refer to reflectors observed elsewhere in the study area. Line is 3.0 km long. Vertical exaggeration is 9.5 x. Line be06_112. Scale in seconds, two way travel time.

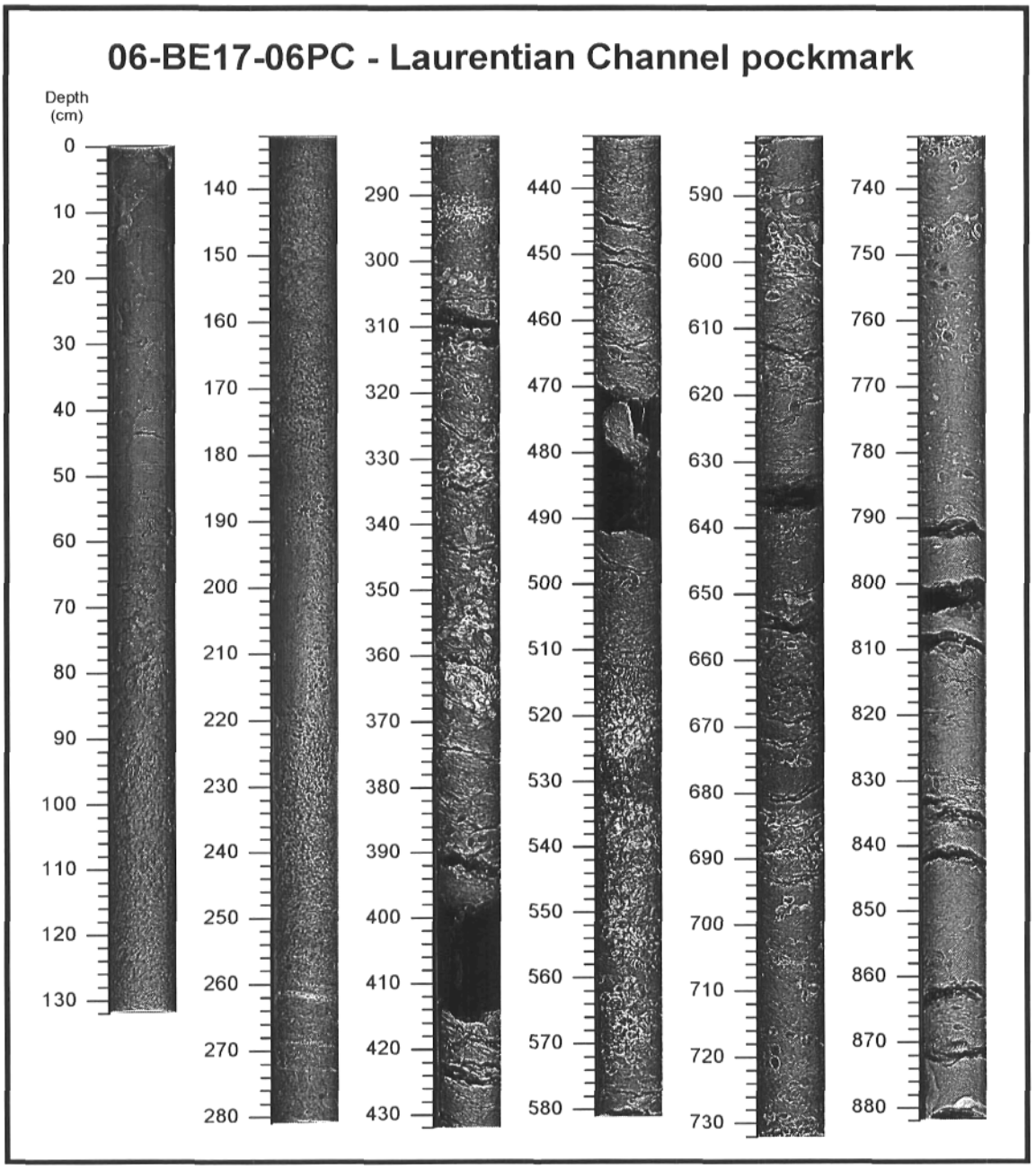

Figure 15. CAT-scan image of piston 06-BE17-06PC sampled in a large pockmark in the Laurentian Channel. Sample position is presented in Figure 14. Notice the substantial gas disturbance and benthic community.

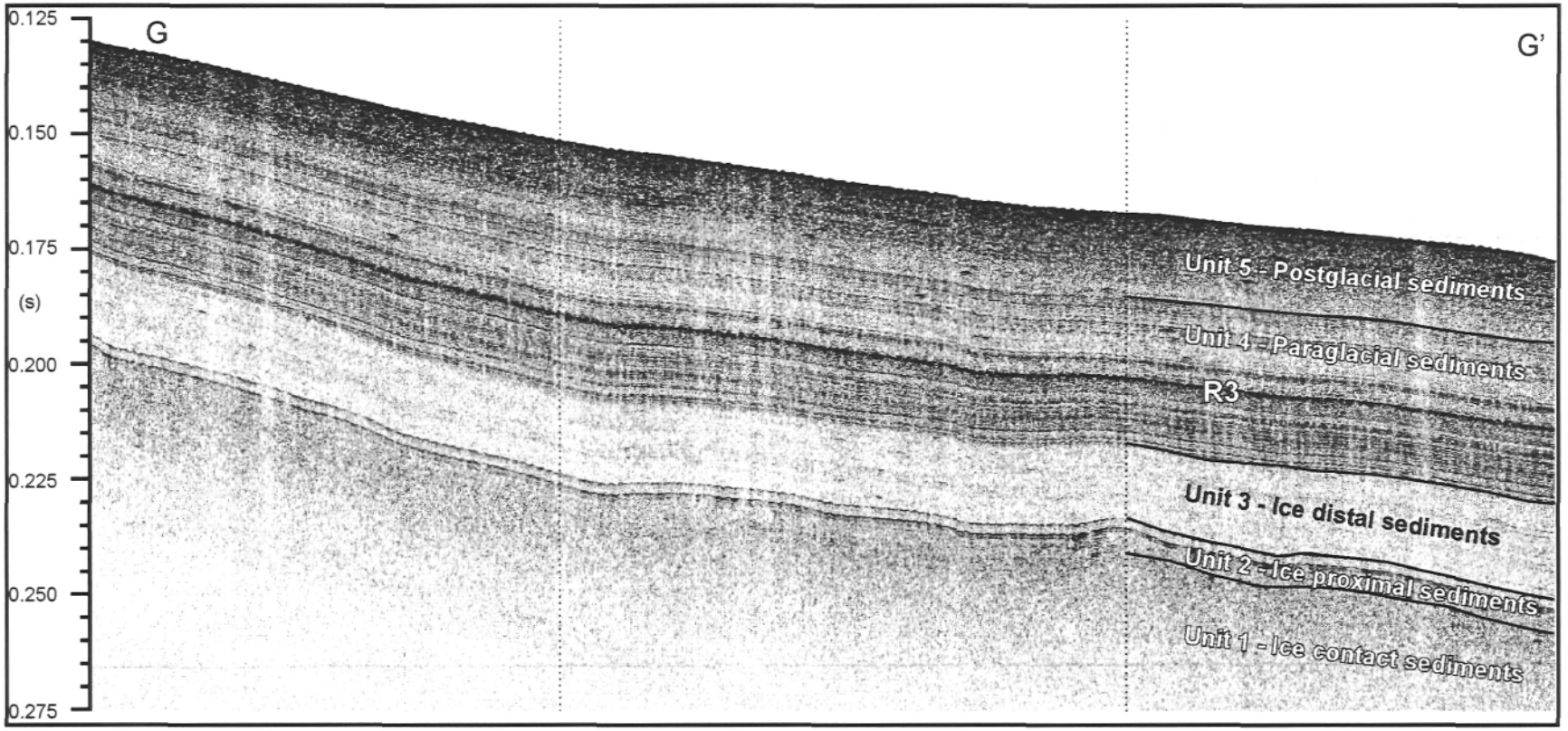

Figure 16. Profile G-G' showing the typical seismostratigraphic sequence for the study area: Unit 5 postglacial sediments, Unit 4 paraglacial sediments, Unit 3 ice distal sediments, Unit 2 ice proximal sediments, and unit 1 Ice contact sediments. R3 refers to the high amplitude reflector interpreted on the shelf as the failure plan for channel East and identified in Figure 7. Location of this section is located on Figure 4. 4 The profile is 1.3 km long. The vertical exaggeration is 5.4 x.

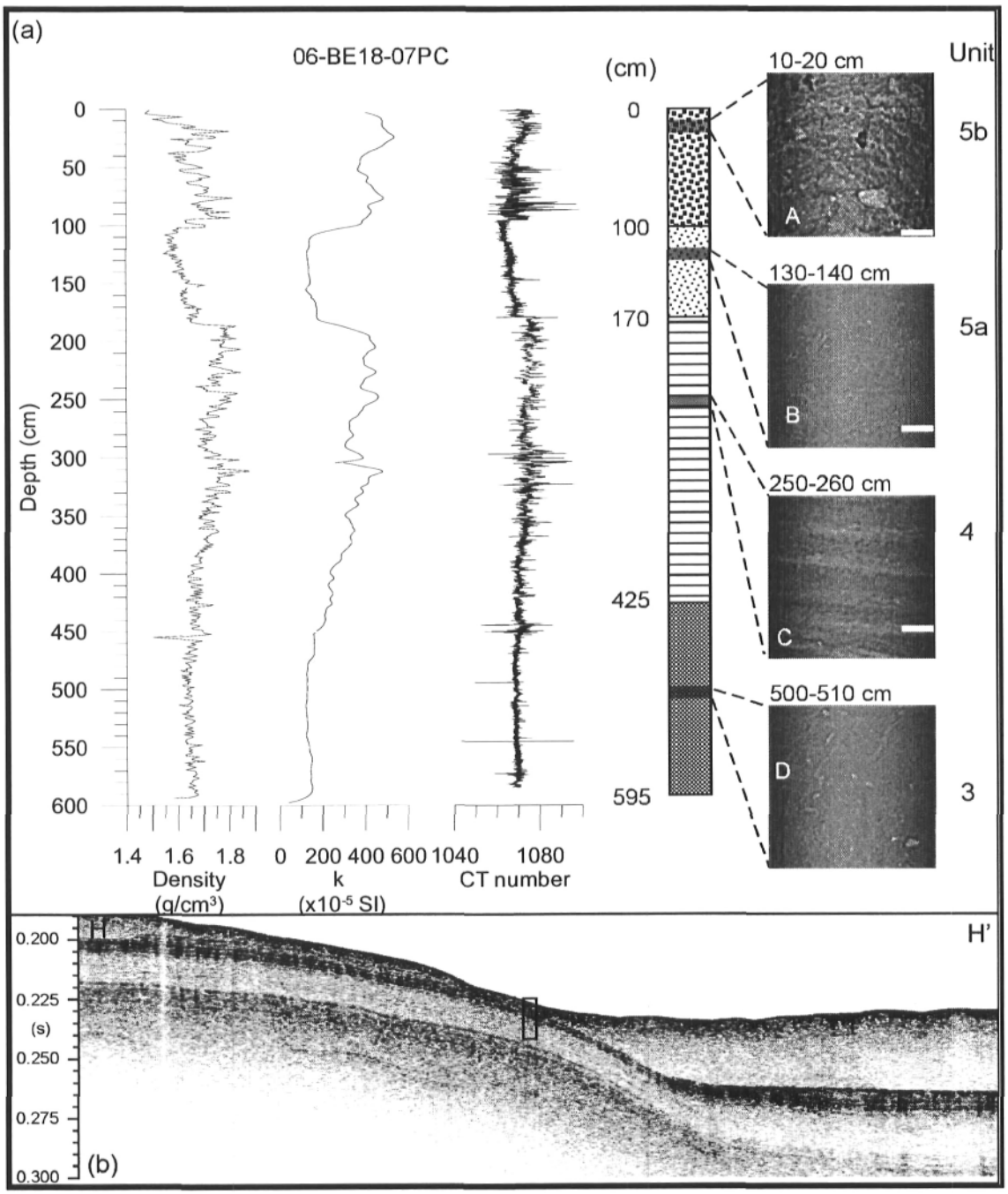

Figure 17. (a) Bulk density, magnetic susceptibility and tomographic intensity profiles for core 06-BE18-07PC. Seismostratigraphic interpretations and CAT-Scan for facies observed within this core. Artefacts on the profiles due to transitions between sections at located at 151, 305, 450 cm. Dark grey areas within facies interpretation sequence indicate position of CAT-Scan images. CAT-Scan images are 10 x 10 cm, white scale bar represents 2 cm. Unit 5b corresponds to heterogeneous post-glacial sediments, 5a to homogenous post-glacial sediments, 4 to paraglacial sediments, and finally 3 to ice-distal sediments. (b) Seismic reflection profile G-G', with indication of piston core sampling location and core depth, assuming sound velocity of 1500 m/s. Length of section is 1.1 km. Vertical exaggeration is 4x. Line be06_102.

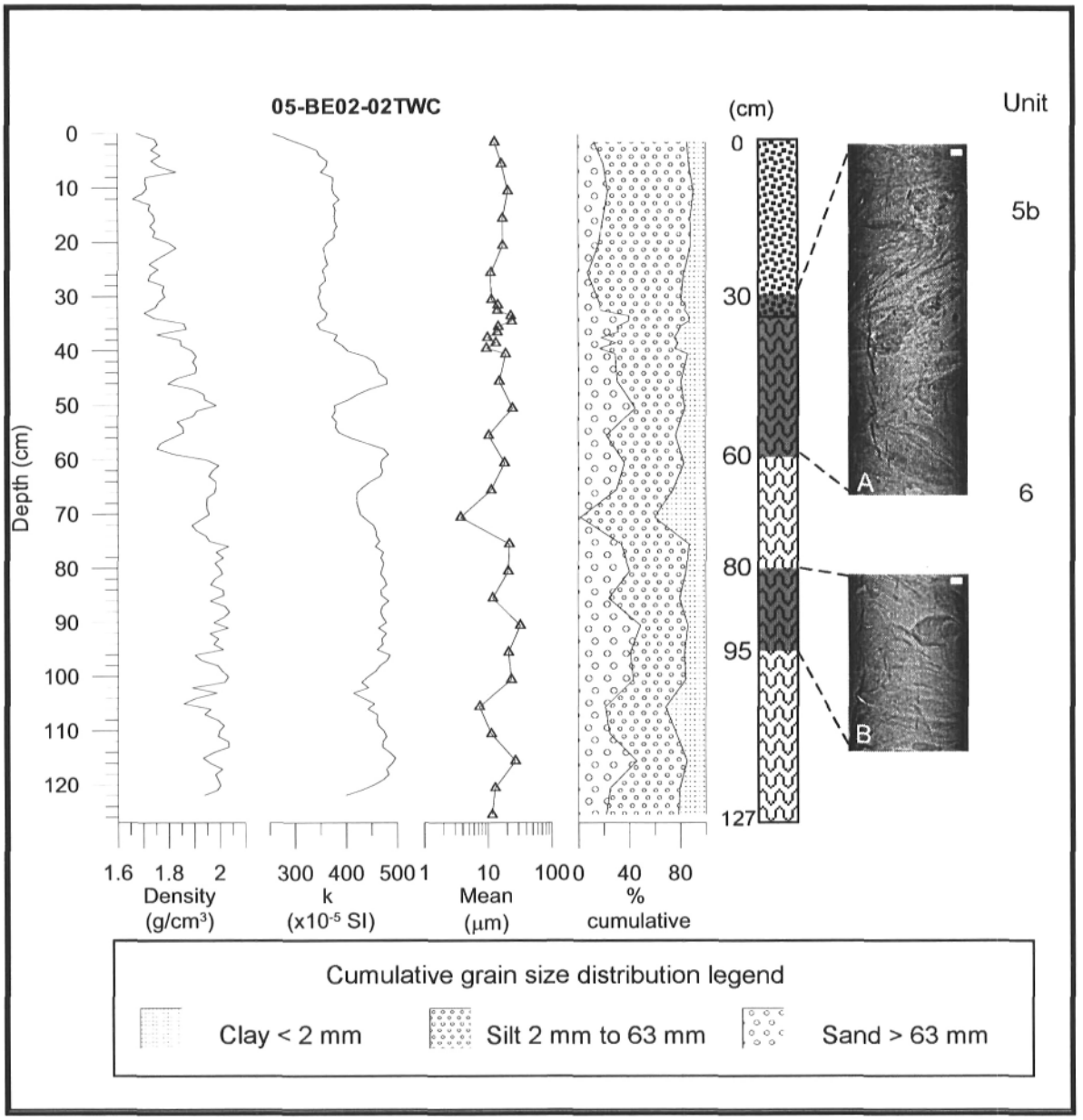

Figure 18. Bulk density, magnetic susceptibility, mean grain size and cumulative fraction for clay, silt and sand size particles for core 05-BE02-02TWC. Debris flow was identified at 30 cm depth. CAT-scan image A is 10 x 30 cm and corresponding to depth between 30 and 60 cm, B is 10 x 15 cm, corresponding to depth between 80 and 85 cm. White scale bar represents 2 cm.

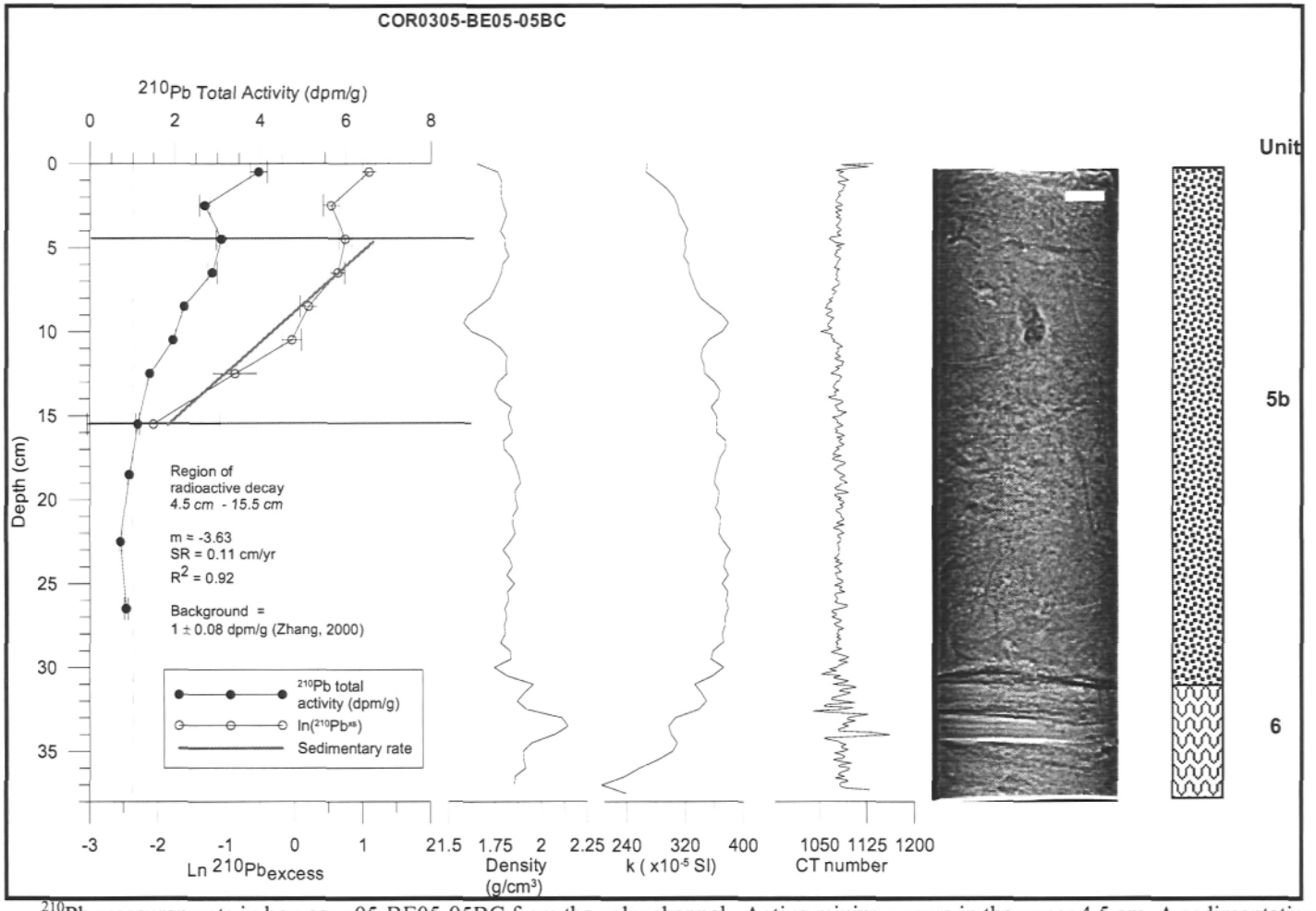

Figure 19. ^{210}Pb measurements in box core 05-BE05-05BC from the paleochannel. Active mixing occurs in the upper 4.5 cm. A sedimentation rate (SR) of 0.11 cm yr^{-1} can be estimated (R^2= 0.92). Regional ^{210}Pb supported value is from Zhang (2000). Bulk density and magnetic susceptibility profiles for box core with lithologic interpretations and CAT-SCAN image. White scale bar represents 2 cm. Notice the sand bed at 30 cm, associated with the 1663 event.

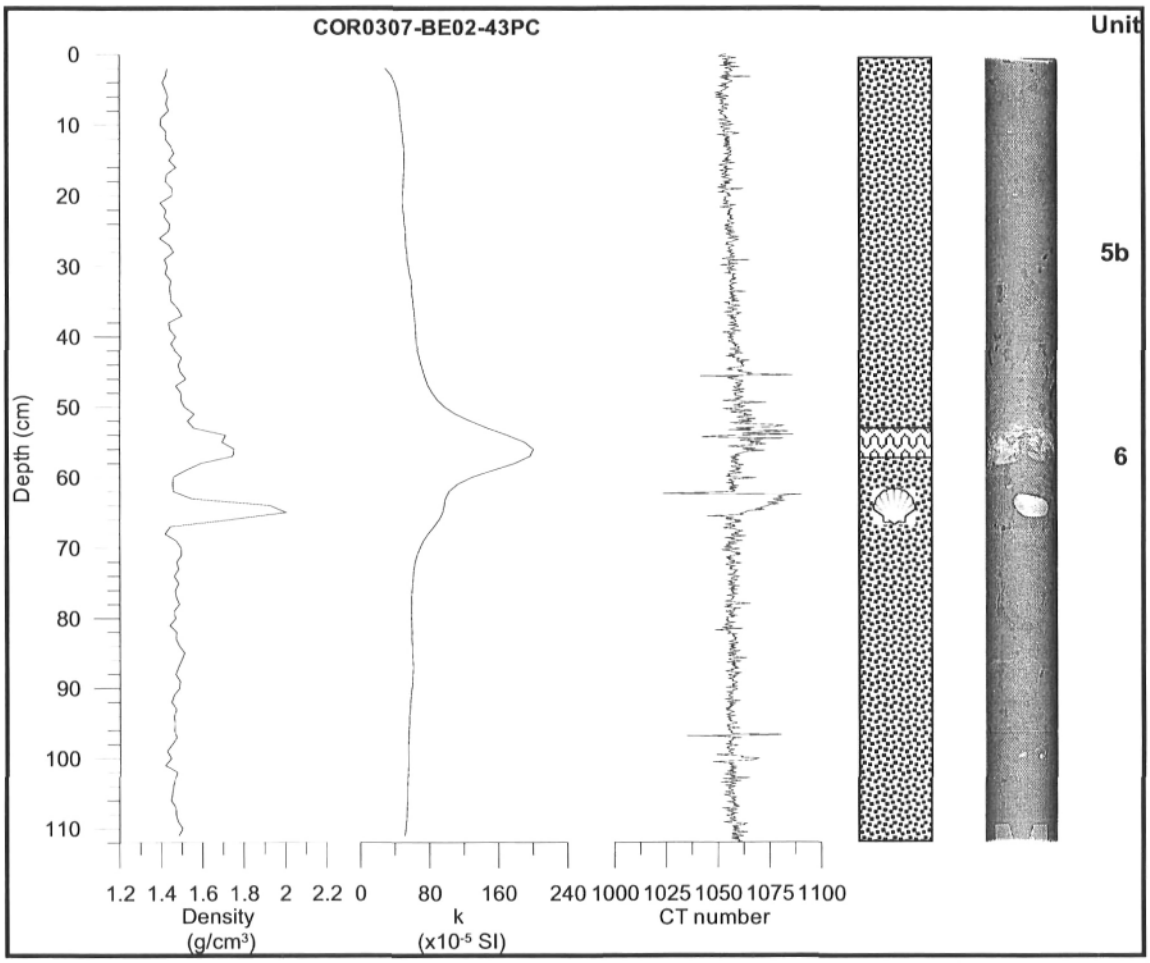

Figure 20. Bulk density, magnetic susceptibility and tomographic intensity profiles for upper section of piston core 03-BE02-43PC, depth ranging from 0 to 112 cm. Lithologic interpretations and CAT-Scan image for facies observed within this core. It is worth noting that a seashell is identified at 65 cm and its datation would provide a more precise age estimate for the deposition of the sand layer. Sand layer at 55 cm is interpreted as the shallow reflector S1.

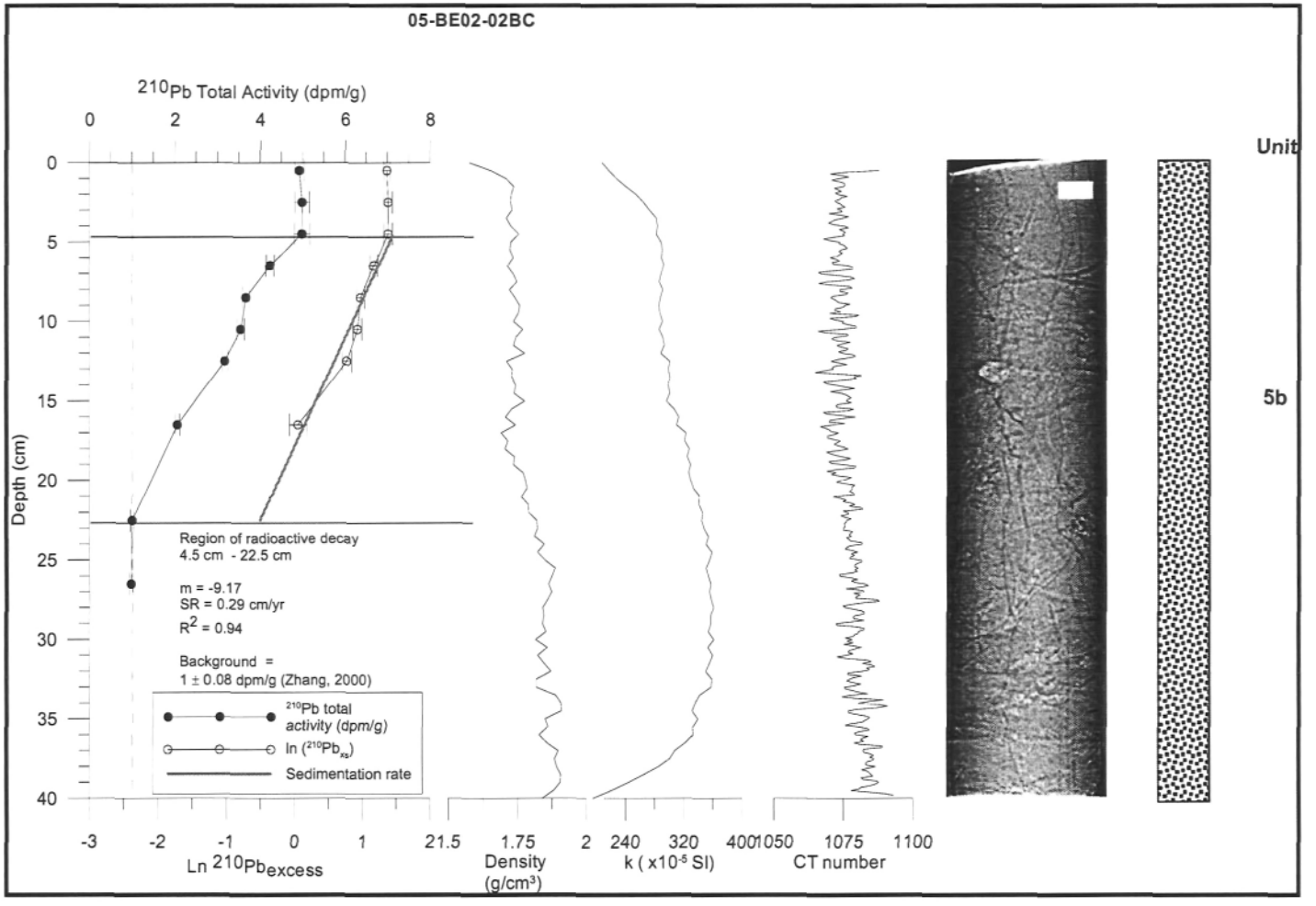

Figure 21. ^{210}Pb measurements in box core 05-BE02-052C sampled in a shallow landslide channel seen at the surface. Figure 7 indicates location of station. Active mixing occurs in the upper 4.5 cm. A sedimentation rate (SR) of 0.26 cm yr^{-1} can be estimated (R^2= 0.94). Bulk density and magnetic susceptibility profiles for box core with lithologic interpretations and CAT-Scan image. White scale bar represents 2 cm.

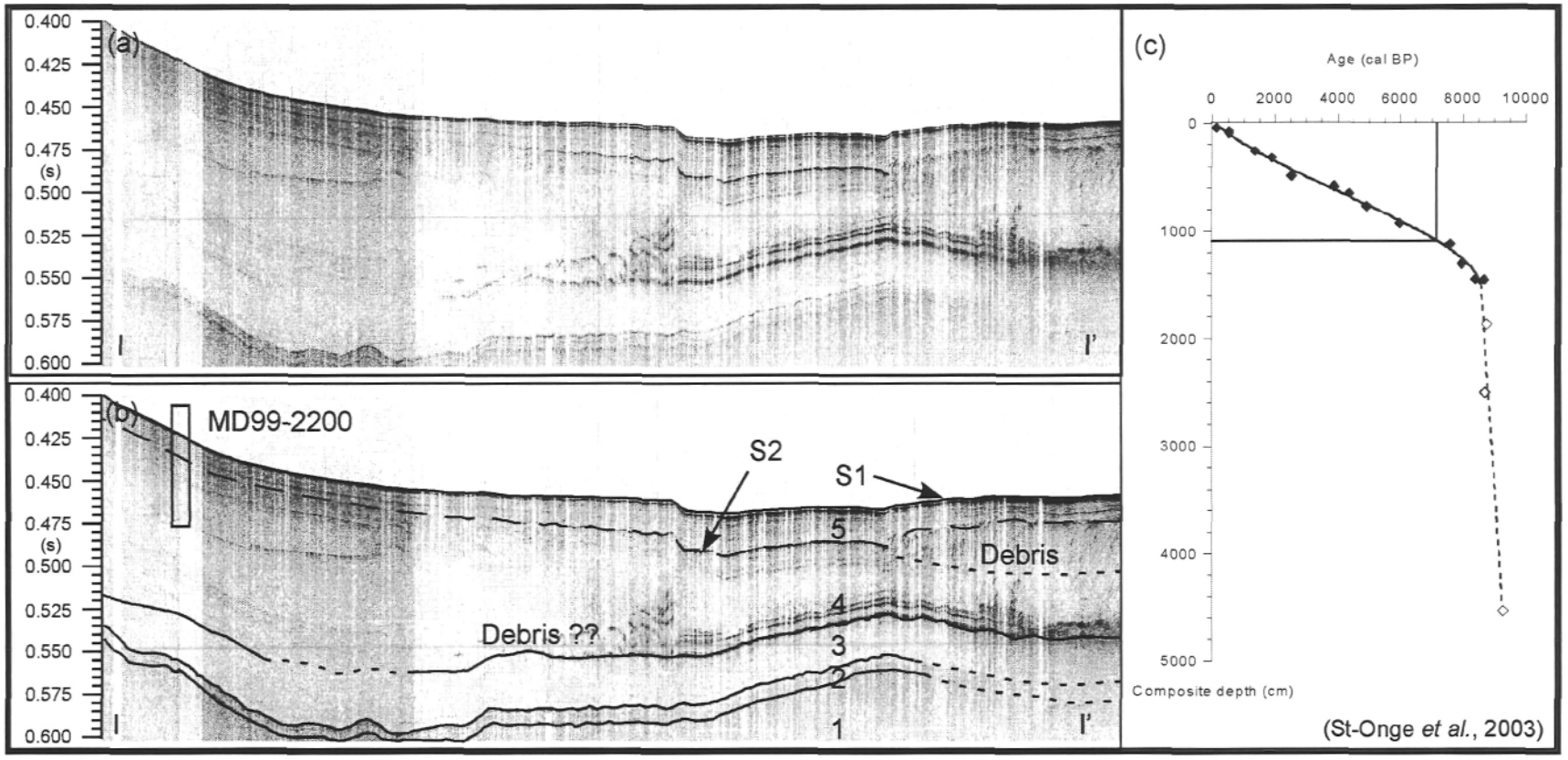

Figure 22. (a) High resolution seismic profile I-I' providing a spatial correlation between the debris flow fan and the location of the MD99-2200 core location. Position of line I-I' is found on Figure 2. The line is 15 km long and the vertical exaggeration is 33x. Line be06_100. Scale in seconds, two way travel time. (b) Seismic interpretations. The blue line indicates position of the reflector S2 that allows us to link the debris flow to the age model. Numbers refers to the seismostratigraphic units. Dotted lines indicate possible contact position between units. Note that the transition between Unit 4 and Unit 5 correspond more or less to the upper boundary of the debris flow. (c) Age model with indication of depth of seismic reflector at 1100 cm and corresponding age of 7250 cal BP (St-Onge *et al.*, 2003).

Conclusion

Le but principal des travaux réalisés dans le cadre de ce projet de maîtrise est de présenter un modèle géologique conceptuel et intégratif décrivant la morpho-sédimentologie sous-marine du secteur entre Betsiamites et Rimouski dans l'estuaire du Saint-Laurent. Cette étude a permis de présenter une cartographie géomorphologique du secteur, d'établir les relations spatio-temporelles entre les événements de mouvement de masse et finalement de proposer des dates pour l'âge des ruptures. Cette analyse morpho-sédimentologique comprend principalement la description des éléments géomorphologiques et de leurs caractéristiques sédimentologiques et intègre à cette analyse des interprétations seismostratigraphiques afin de reconstituer le contexte spatio-temporel des événements survenus dans le secteur. Les éléments géomorphologiques ont été localisés, identifiés et caractérisés selon l'influence que les mouvements de masse ont eue sur ceux-ci.

Nous avons identifié qu'au cours de l'Holocène, au moins quatre (4) épisodes de rupture de pente ont causé des mouvements de masse qui ont façonné la morphologie du secteur. Le premier événement paraglacial daterait de 9 ka BP et aurait perturbé les dépôts du plateau. Les traces de cet événement ont été interprétées sur les profils de sismique réflexion. Le second épisode de mouvements de masse daterait de 7.25 ka cal BP et aurait eu le plus d'impact dans le secteur. En fait, c'est à cet événement que nous associons 1) la large cicatrice sur le plateau caractérisée par les deux couloirs de glissement et 2) le dépôt de débris en forme d'éventail dans le Chenal laurentien. Le troisième épisode discerné dans le secteur est associé au séisme de 1663 AD (M~7) sur la base de la datation de débris du plateau au ^{210}Pb. Ces observations soutiennent l'hypothèse que la cicatrice de glissement de terrain subaérien sur la côte daterait, du moins en partie, de 1663. On a également identifié la présence de débris associés à cet événement dans le Chenal laurentien. Finalement, des observations morphologiques sur le plateau indiqueraient qu'il y aurait un dernier glissement postérieur à l'événement de 1663. L'analyse au ^{210}Pb et la prise en considération des séismes historiques indiqueraient que ce dernier mouvement de masse sous-marin daterait soit de l'an 1860 AD, causé par un séisme de magnitude estimée de 6, ou de l'an 1870 AD lors d'un séisme de magnitude estimée à 6.5. Ce projet de maîtrise décrit les mouvements de masses survenus dans le secteur sous-marin et établit une relation

entre le glissement subaérien et les structures sous-marines adjacentes. Notre étude soulève toutefois d'importantes questions quant au glissement de terrain subaérien sur la côte que notre travail n'a su répondre, n'étant pas dans les objectifs du projet de maitrise. Cependant, les observations connues de ce glissement subaérien suggèrent qu'il s'agit du plus important glissement de terrain de l'histoire récente du Québec et notre travail révèle que ce glissement a eu des conséquences dans le milieu sous-marin. Nous concluons qu'il faut approfondir davantage les connaissances de ce site, autant pour le secteur sous-marin que pour le secteur subaérien, afin d'évaluer adéquatement les risques associés à de tels mouvements sur les personnes et les infrastructures à proximité. Nous recommandons donc une étude complète pour déterminer le ou les mécanismes de rupture, la caractérisation géotechnique des matériaux présents et le comportement lors de la post-rupture, pour établir la possibilité d'événements récurrents et finalement, pour approfondir les corrélations entre les mouvements observés sous l'eau et ceux observés sur terre. De plus, il sera nécessaire de poursuivre les travaux de terrain pour établir si, comme dans le milieu sous-marins, plusieurs mouvements se seraient produits en zone subaérienne. Nous recommandons aussi de poursuivre l'échantillonnage en milieu sous-marin et subaérien afin de récupérer des matériaux datables et d'ainsi établir avec plus de précision l'âge des événements.

ANNEXE A : Résultats des analyses au ^{210}Pb

Tableau 1 : COR0305-BE02-02BC (48°50.725 N, 68°44.064 W)

Profondeur de l'intervalle (cm)	Profondeur moyenne (cm)	$^{210}Pb_{xs+s}$	±	$^{210}Pb_{xs}$	±	$\ln^{210}Pb_{xs}$	±
0-1	0.5	4.9247	0.1047	3.9247	0.1847	1.3673	0.0471
2-3	2.5	4.9861	0.1705	3.9861	0.2505	1.3828	0.0628
4-5	4.5	4.9783	0.1787	3.9783	0.2587	1.3809	0.0650
6-7	6.5	4.2301	0.0943	3.2301	0.1743	1.1725	0.0540
8-9	8.5	3.6656	0.0808	2.6656	0.1608	0.9804	0.0603
10-11	10.5	3.5396	0.0875	2.5396	0.1675	0.9320	0.0660
12-13	12.5	3.1612	0.0711	2.1612	0.1511	0.7707	0.0699
16-17	16.5	2.0579	0.0530	1.0579	0.1330	0.0563	0.1257
22-23	22.5	1.0093	0.0411	0.0093	0.1211	-4.6777	13.0215
26-27	26.5	0.9785	0.0388	-0.0215	0.1188		

Tableau 2 : COR0305-BE05-05BC (48°51.886 N, 68°39.179 W)

Profondeur de l'intervalle (cm)	Profondeur moyenne (cm)	$^{210}Pb_{xs+s}$	±	$^{210}Pb_{xs}$	±	$\ln^{210}Pb_{xs}$	±
0-1	0.5	3.9570	0.2003	2.9570	0.2803	1.0842	0.0948
2-3	2.5	2.6991	0.1188	1.6991	0.1988	0.5301	0.1170
4-5	4.5	3.0990	0.1204	2.0990	0.2004	0.7415	0.0955
6-7	6.5	2.8832	0.1100	1.8832	0.1900	0.6330	0.1009
8-9	8.5	2.2230	0.0666	1.2230	0.1466	0.2013	0.1199
10-11	10.5	1.9565	0.0569	0.9565	0.1369	-0.0445	0.1431
12-13	12.5	1.4212	0.0516	0.4212	0.1316	-0.8646	0.3124
15-16	15.5	1.1273	0.0443	0.1273	0.1243	-2.0612	0.9764
18-19	18.5	0.9233	0.0417	-0.0767	0.1217		
22-23	22.5	0.7260	0.0398	-0.2740	0.1198		
26-27	26.5	0.8524	0.0408	-0.1476	0.1208		

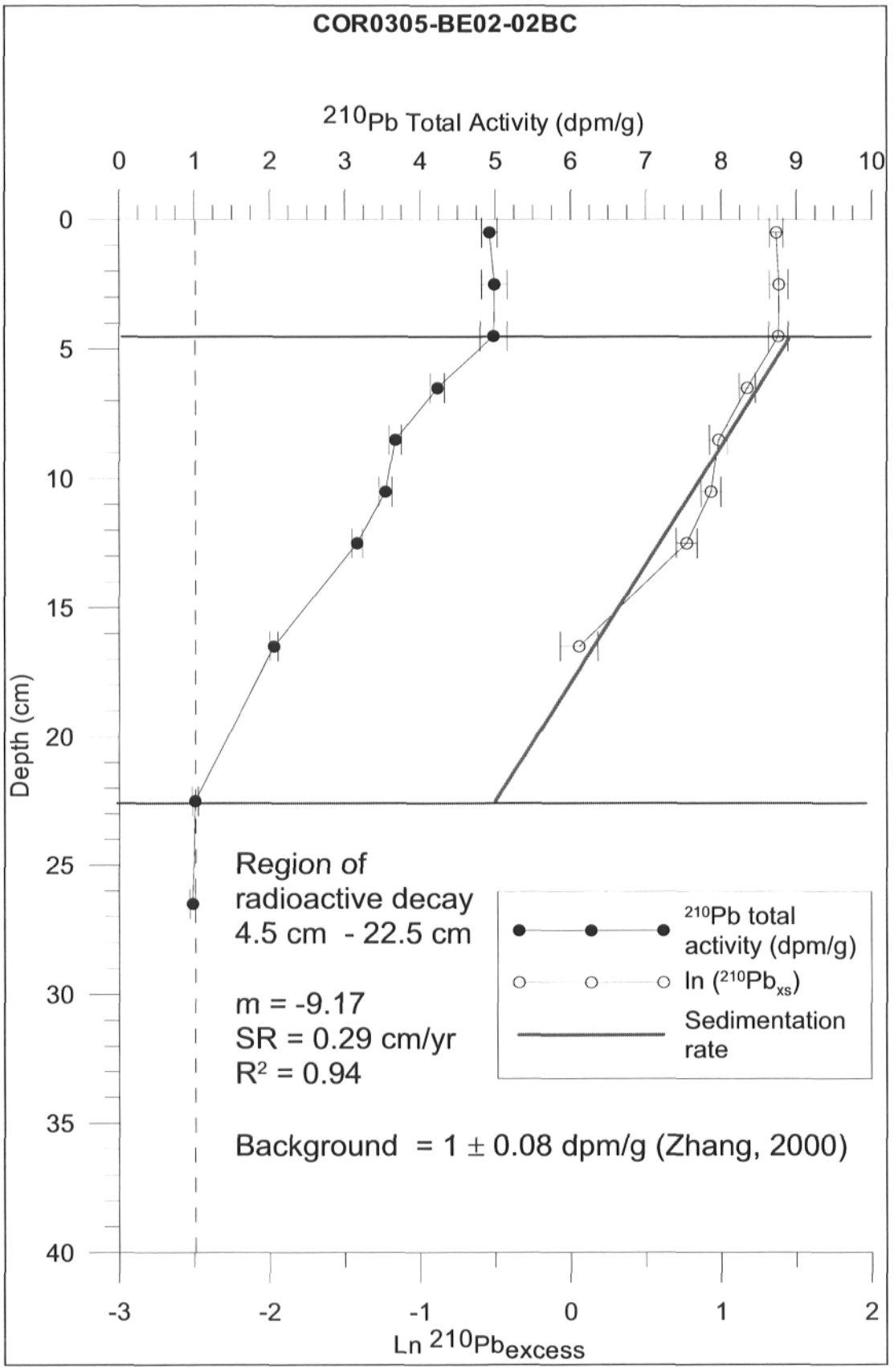
COR0305-BE02-02BC
210Pb Total Activity (dpm/g)
0
1
2
3
4
5
6
7
8
9
10
Depth (cm)
0
5
10
15
20
25
30
35
40
Region of radioactive decay 4.5 cm - 22.5 cm
m = -9.17
SR = 0.29 cm/yr
R2 = 0.94
Background = 1 ± 0.08 dpm/g (Zhang, 2000)
210Pb total activity (dpm/g)
ln (210Pbxs)
Sedimentation rate
-3
-2
-1
0
1
2
Ln 210Pbexcess

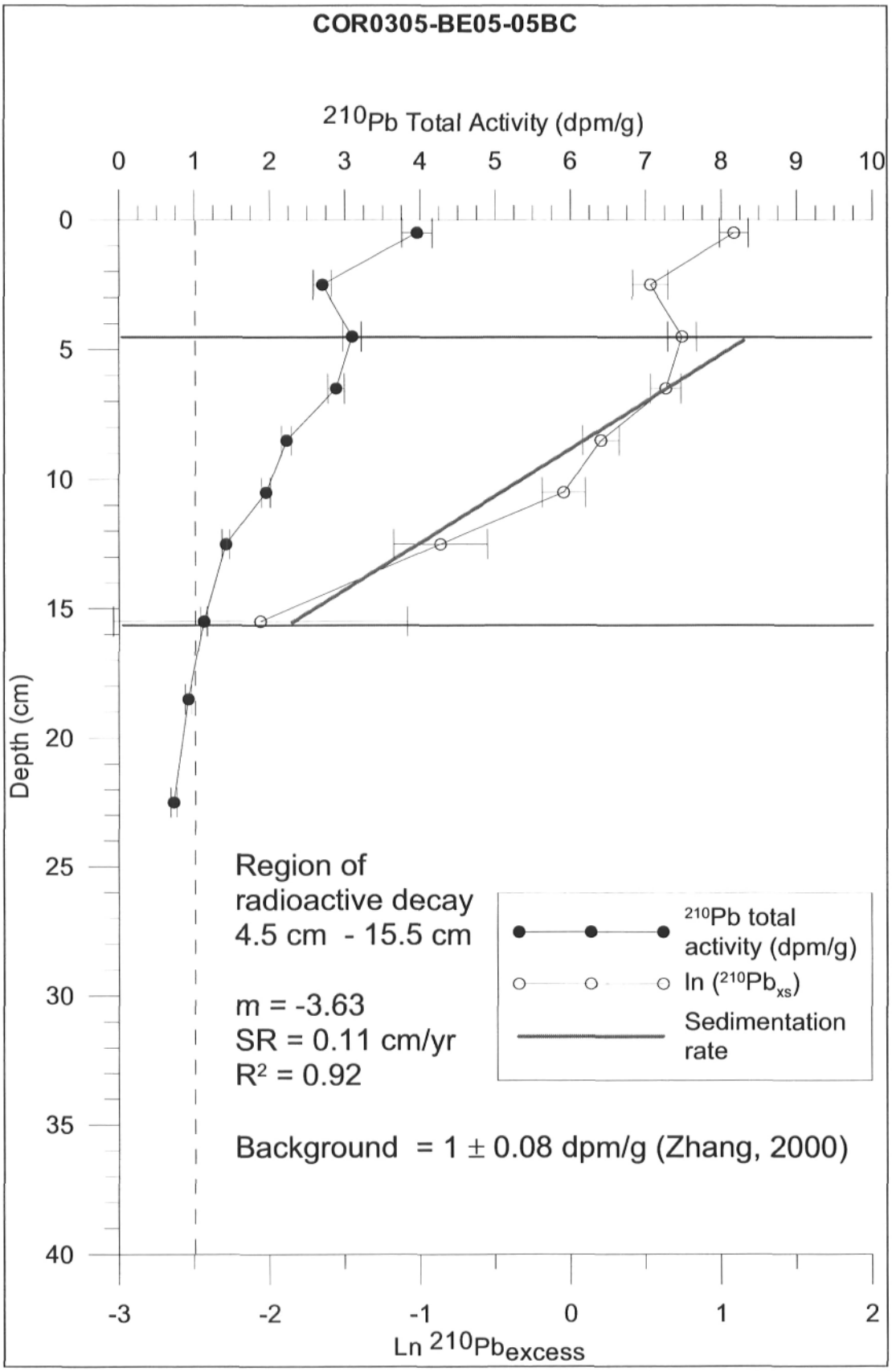
COR0305-BE05-05BC
210Pb Total Activity (dpm/g)
0
1
2
3
4
5
6
7
8
9
10
Depth (cm)
0
5
10
15
20
25
30
35
40
Region of
radioactive decay
4.5 cm - 15.5 cm
m = -3.63
SR = 0.11 cm/yr
R2 = 0.92
Background = 1 ± 0.08 dpm/g (Zhang, 2000)
210Pb total
activity (dpm/g)
ln (210Pbxs)
Sedimentation
rate
-3
-2
-1
0
1
2
Ln 210Pbexcess

ANNEXE B : CAT-Scan, propriétés physiques et sédimentologiques des carottes sédimentaires des missions COR0307, COR0503 et COR0602 pour le secteur Betsiamites

Données	Commentaires
Image Cat-Scan	Topogrammes des carottes sédimentaires
Profiles de MSCL	Profils de densité, susceptibilité magnétique et porosité obtenus à l'aide du GEOTEK MSCL
CT number	Les profils d'intensité tomographique proviennent de : Boyer-Villemaire, U., Gagné, H. 2005. Analyses granulométriques de carottes sédimentaires de la mer de Beaufort et analyses au MSCL et au CAT-scan des carottes sédimentaires de la mission COR0503. ISMER, 86 p. Lajoie, M., P. Simard et U. Boyer-Villemaire. 2007. Analyse au MSCL et au CAT-Scan des carottes sédimentaires de la mission COR0602. Fjord du Saguenay, estuaire et golfe du Saint-Laurent. Rapport technique. Institut des sciences de la mer de Rimouski. Université du Québec à Rimouski. 126 p.
Pixel intensity	Les profils de 2003 ont été obtenus directement à l'aide du logiciel de visualisation OSIRIS
L*	Réflectance spectrale des sédiments
Moyenne granulométrique	Moyenne géométrique des grains obtenue à l'aide du programme GRADISTAT (Blott et Pye, 2001)
% cumulatif	Distribution du pourcentage d'argile, de silt et de sable
Photo	Photographie prise à l'aide d'une caméra numérique en laboratoire
Coquille	Présence ou non de coquille dans la carotte, avec indication de la profondeur
Matière organique	Indication de la présence ou non de matière organique dans la carotte, avec indication de la profondeur
Tableau	Tableau des notes en laboratoire

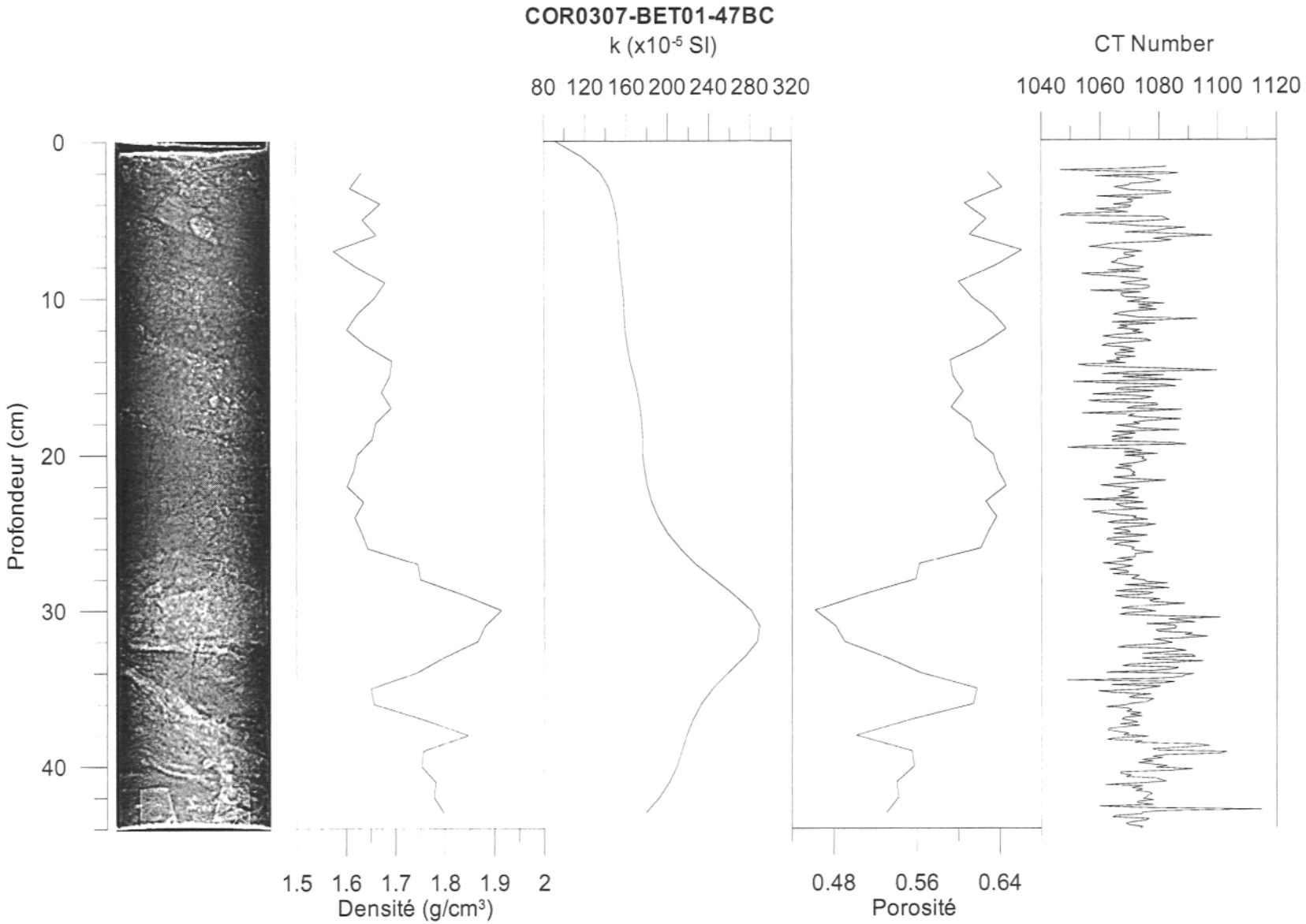
COR0307-BET01-47BC
k (x10-5 SI)
80 120 160 200 240 280 320
CT Number
1040 1060 1080 1100 1120
Profondeur (cm)
0
10
20
30
40
1.5 1.6 1.7 1.8 1.9 2
Densité (g/cm3)
0.48 0.56 0.64
Porosité

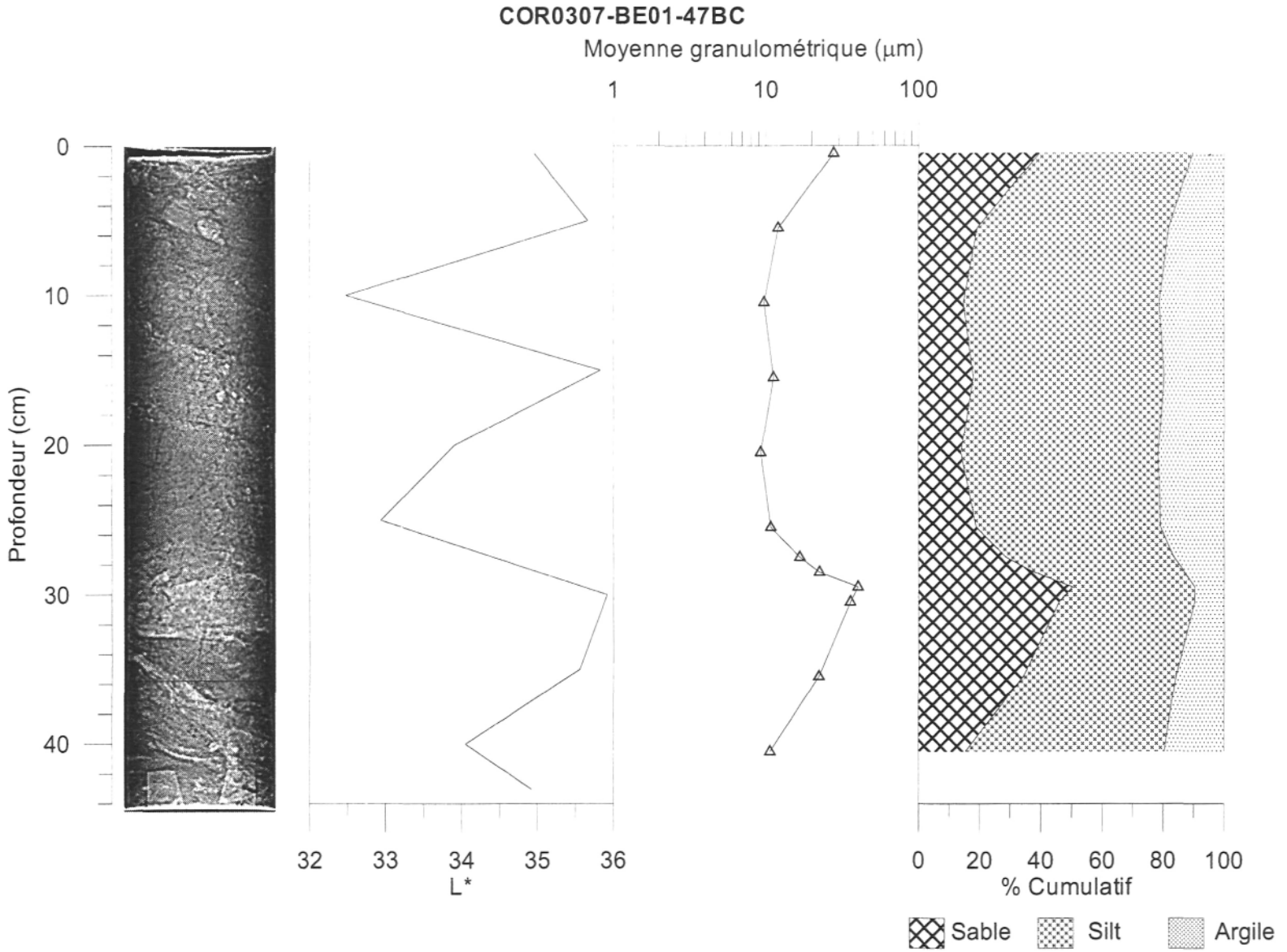
COR0307-BE01-47BC
Moyenne granulométrique (µm)
1
10
100
0
10
20
30
40
Profondeur (cm)
32
33
34
35
36
L*
0
20
40
60
80
100
% Cumulatif
Sable
Silt
Argile

COR0307-BE01-47BC

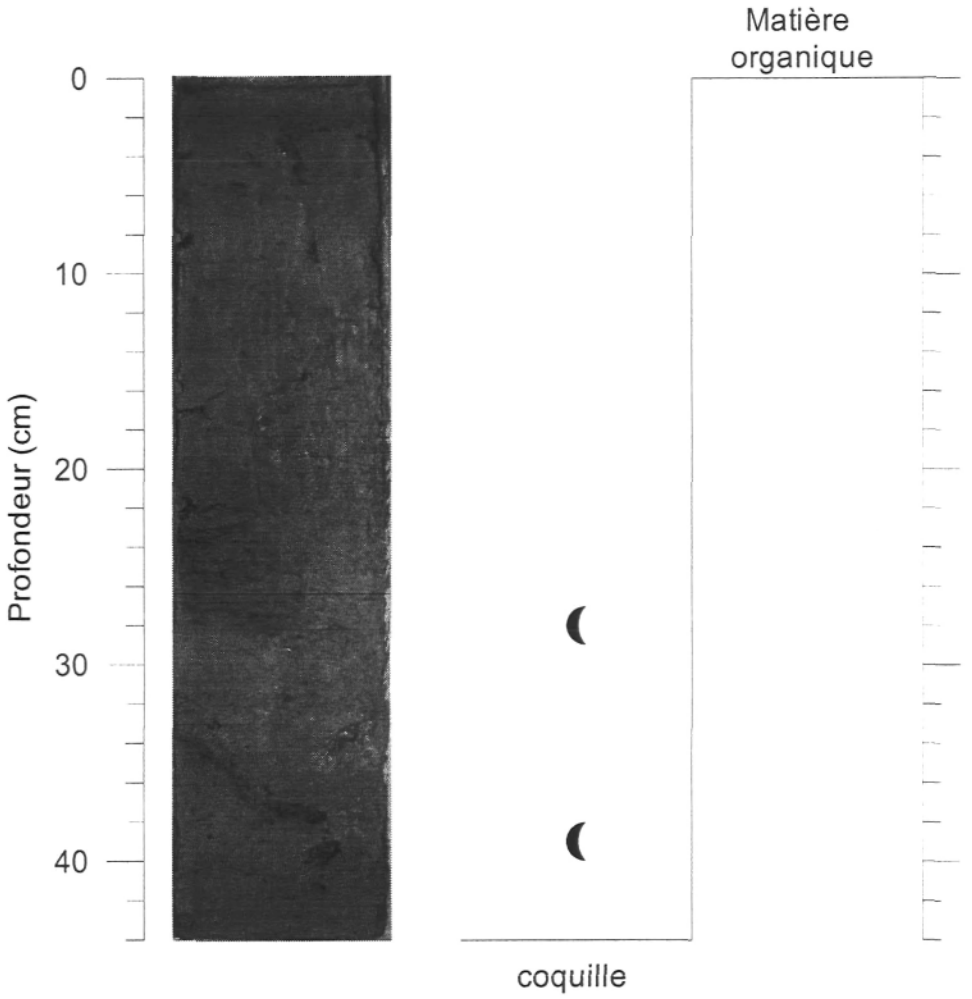

Date: 11/25/2005
Observateurs: GCV G. St-Onge
Échantillon: COR0307-BE01-47BC
Section: AB
Longueur: 44 cm
Profondeur: 0 - 44 cm

Intervalle	Structure	Granulo	Description
0-5		MS	Muddy sand avec gros trou de bioturbation, tubes de ver, gros grains de sable très évidents, poche d'argile avec laminations noires
10-44		Si A	Silt argileux avec présence des lits sable, tous les lits de sables sont parallèles les uns avec les autres, avec le même angle
	11	Sa	Lit de sable
	17	Sa	Lit de sable
	33	Sa	Lit de sable, avec présence de petits gravier
22-27			Pochettes d'argile silteuse avec laminations noires
	27.5		Contact entre argile et sable, possiblement le contact entre le silt argileux normal et la coulée de débris
27-31		Sa	Lit de sable, plutôt diffus et épais
	28		Fragment de coquille, environ 1 cm
	33		Trou de bioturbation, diamètre de 1 cm, plutôt profond
	39		Petite coquille intacte, environ 2 mm, brisée après l'échantillonnage

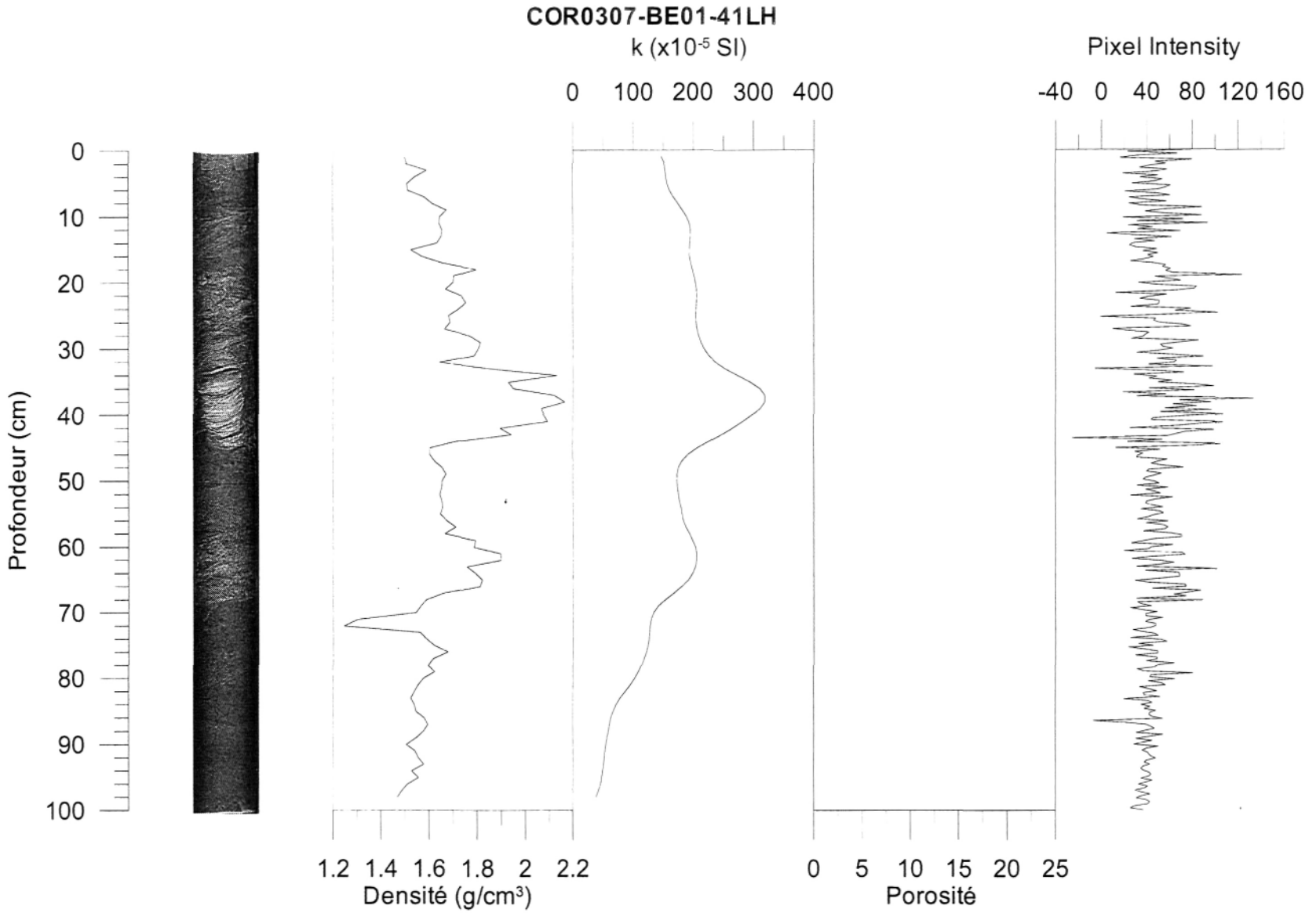
COR0307-BE01-41LH
k (x10-5 SI)
0 100 200 300 400
Pixel Intensity
-40 0 40 80 120 160
Profondeur (cm)
0 10 20 30 40 50 60 70 80 90 100
1.2 1.4 1.6 1.8 2 2.2
Densité (g/cm3)
0 5 10 15 20 25
Porosité

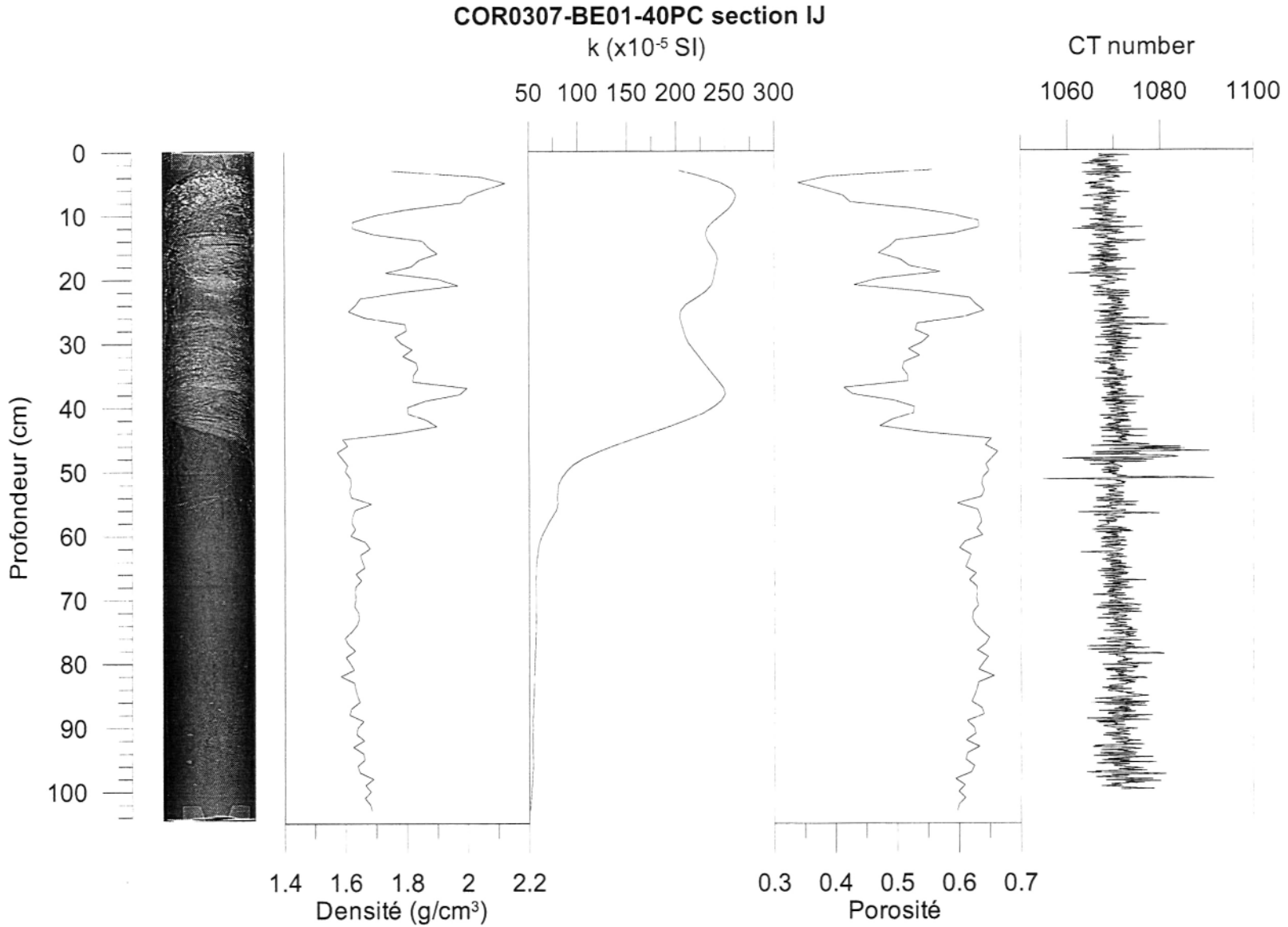
COR0307-BE01-40PC section IJ
k (x10-5 SI)
50 100 150 200 250 300
CT number
1060 1080 1100
Profondeur (cm)
0 10 20 30 40 50 60 70 80 90 100
1.4 1.6 1.8 2 2.2
Densité (g/cm3)
0.3 0.4 0.5 0.6 0.7
Porosité

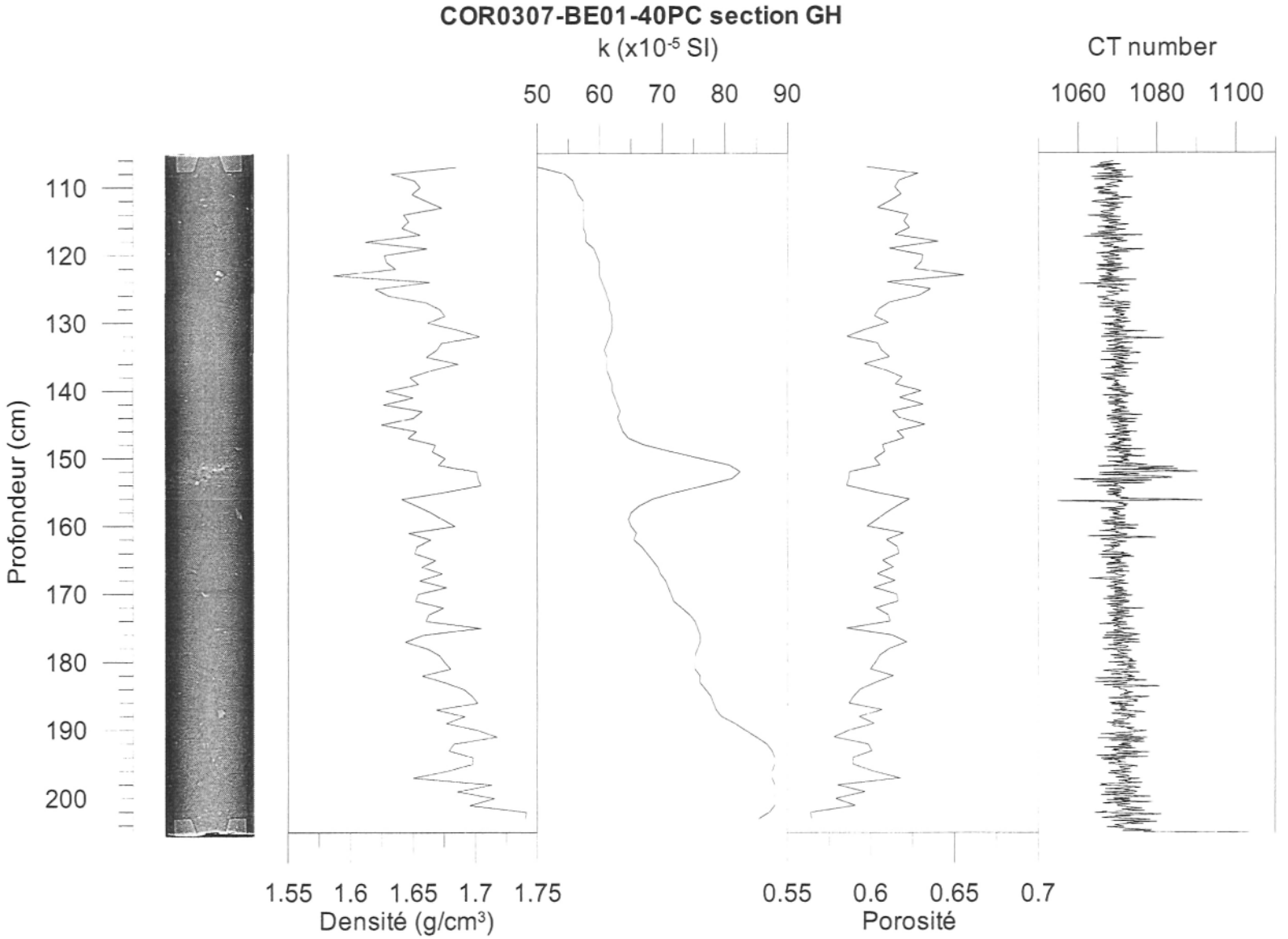
COR0307-BE01-40PC section GH
k (x10-5 SI)
50 60 70 80 90
CT number
1060 1080 1100
Profondeur (cm)
110
120
130
140
150
160
170
180
190
200
1.55 1.6 1.65 1.7 1.75
Densité (g/cm3)
0.55 0.6 0.65 0.7
Porosité

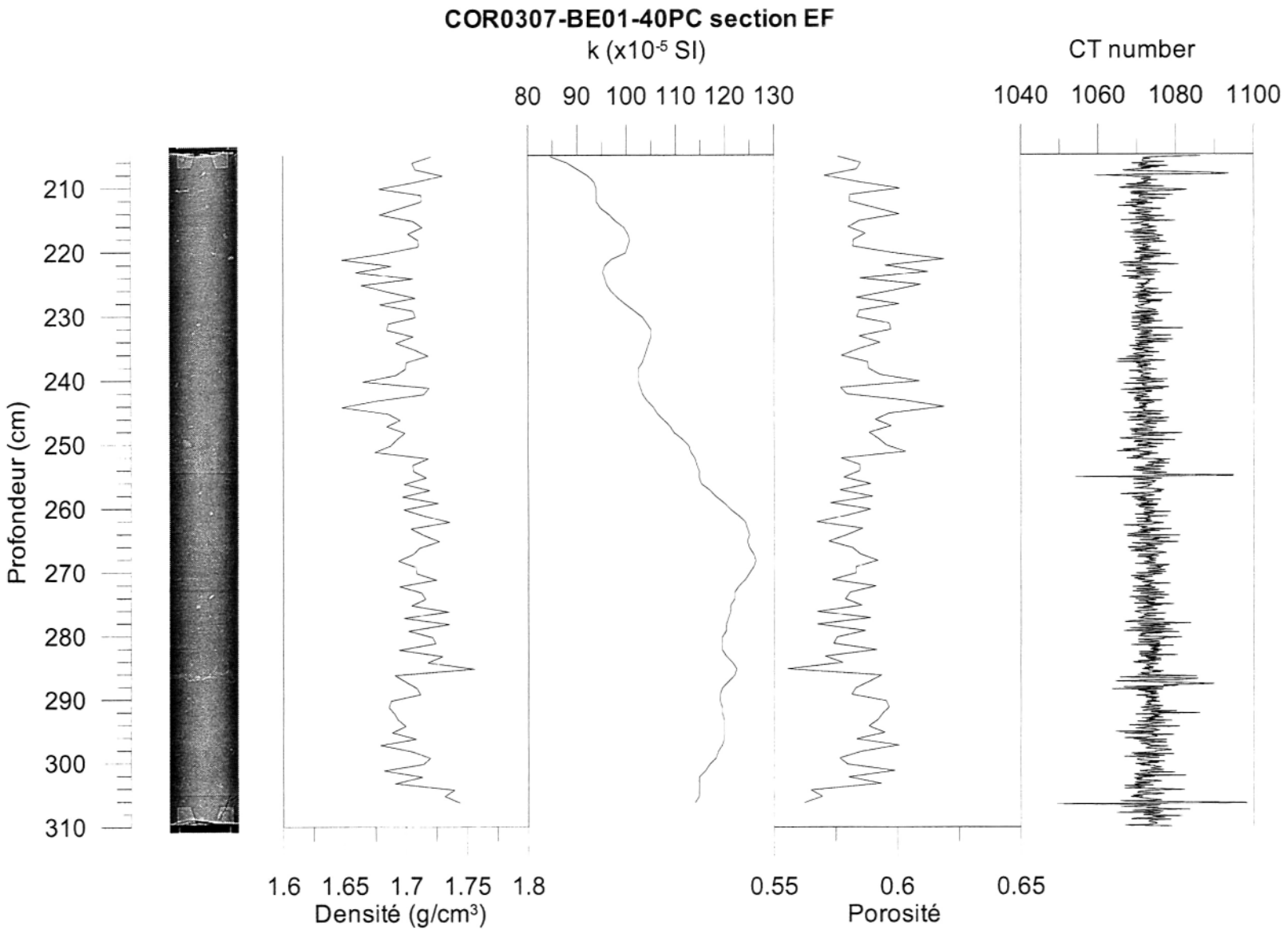
COR0307-BE01-40PC section EF
k (x10-5 SI)
80 90 100 110 120 130
CT number
1040 1060 1080 1100
Profondeur (cm)
210
220
230
240
250
260
270
280
290
300
310
1.6 1.65 1.7 1.75 1.8
Densité (g/cm3)
0.55 0.6 0.65
Porosité

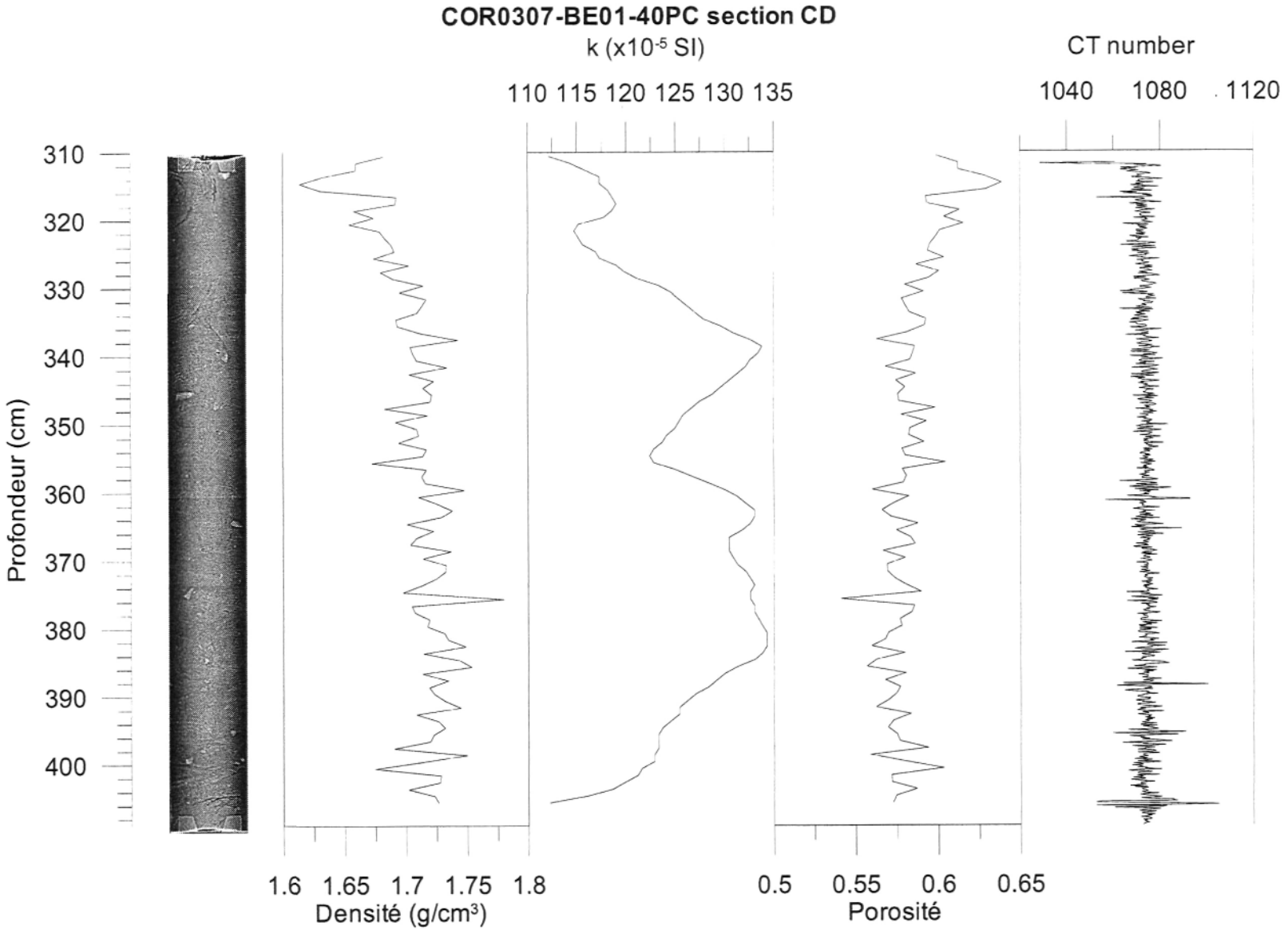
COR0307-BE01-40PC section CD
k (x10-5 SI)
110 115 120 125 130 135
CT number
1040 1080 1120
Profondeur (cm)
310
320
330
340
350
360
370
380
390
400
1.6 1.65 1.7 1.75 1.8
Densité (g/cm3)
0.5 0.55 0.6 0.65
Porosité

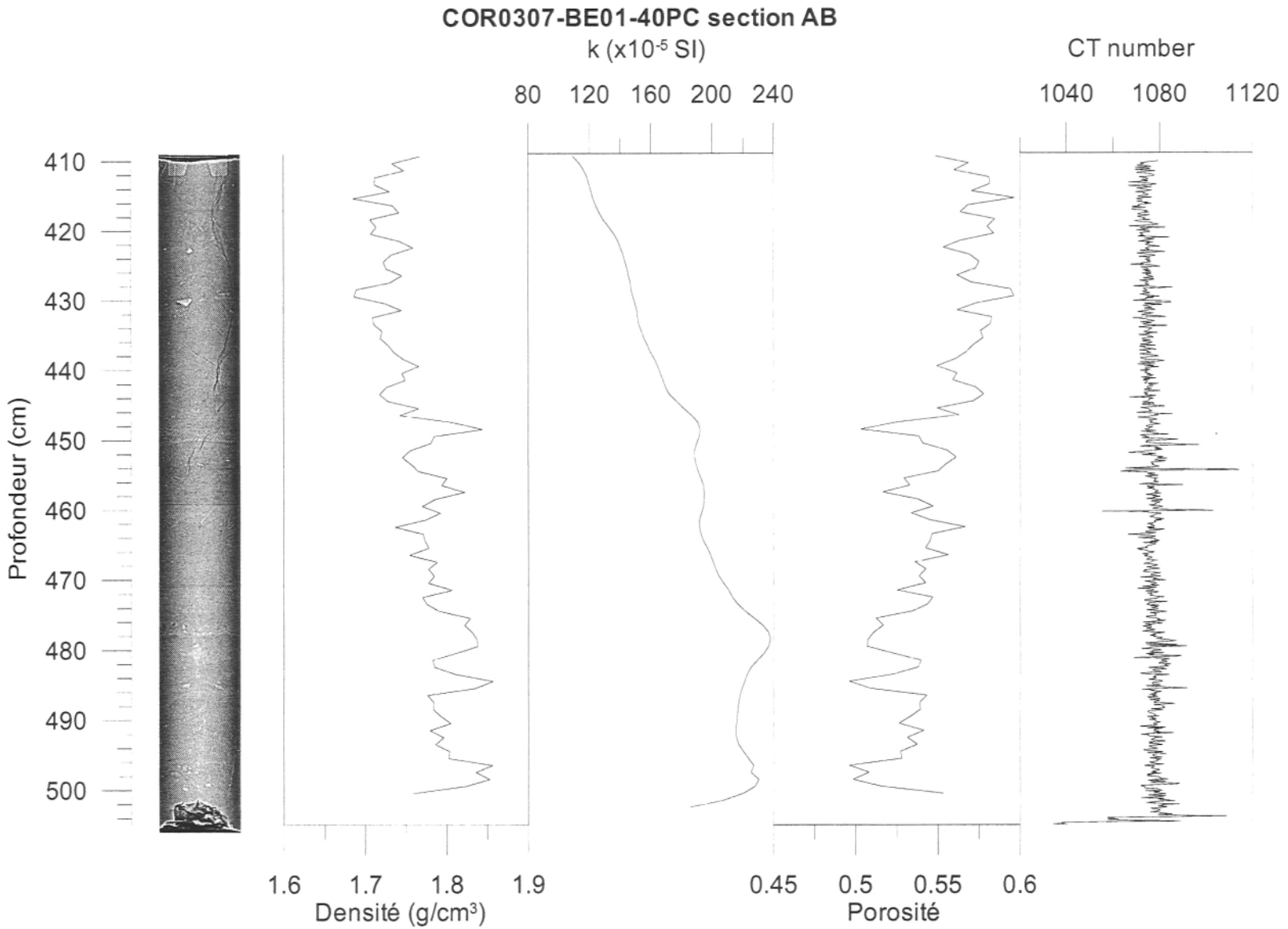
COR0307-BE01-40PC section AB
k (x10-5 SI)
80 120 160 200 240
CT number
1040 1080 1120
Profondeur (cm)
410
420
430
440
450
460
470
480
490
500
1.6 1.7 1.8 1.9
Densité (g/cm3)
0.45 0.5 0.55 0.6
Porosité

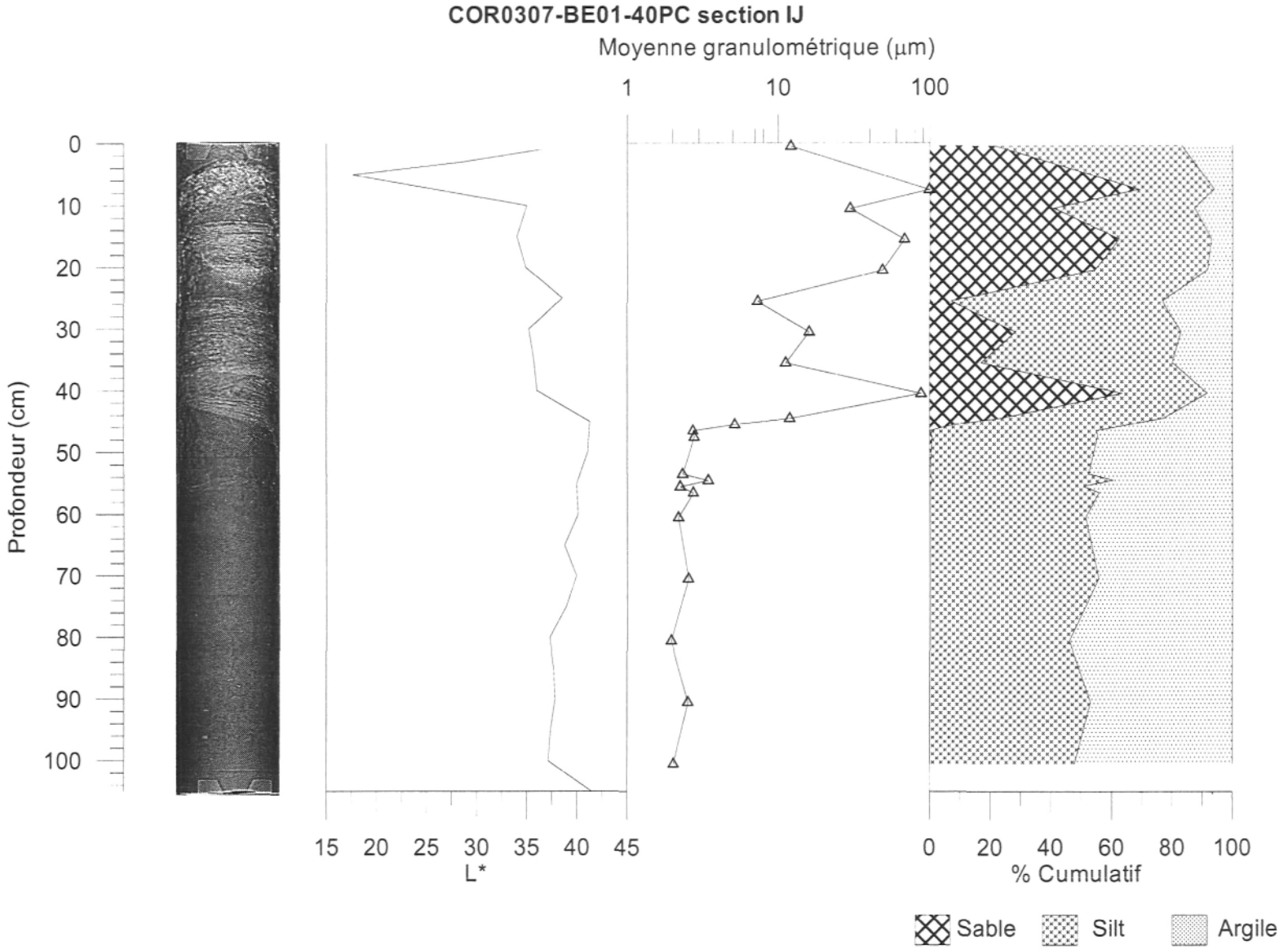
COR0307-BE01-40PC section IJ
Moyenne granulométrique (µm)
1
10
100
Profondeur (cm)
0
10
20
30
40
50
60
70
80
90
100
15
20
25
30
35
40
45
L*
0
20
40
60
80
100
% Cumulatif
Sable
Silt
Argile

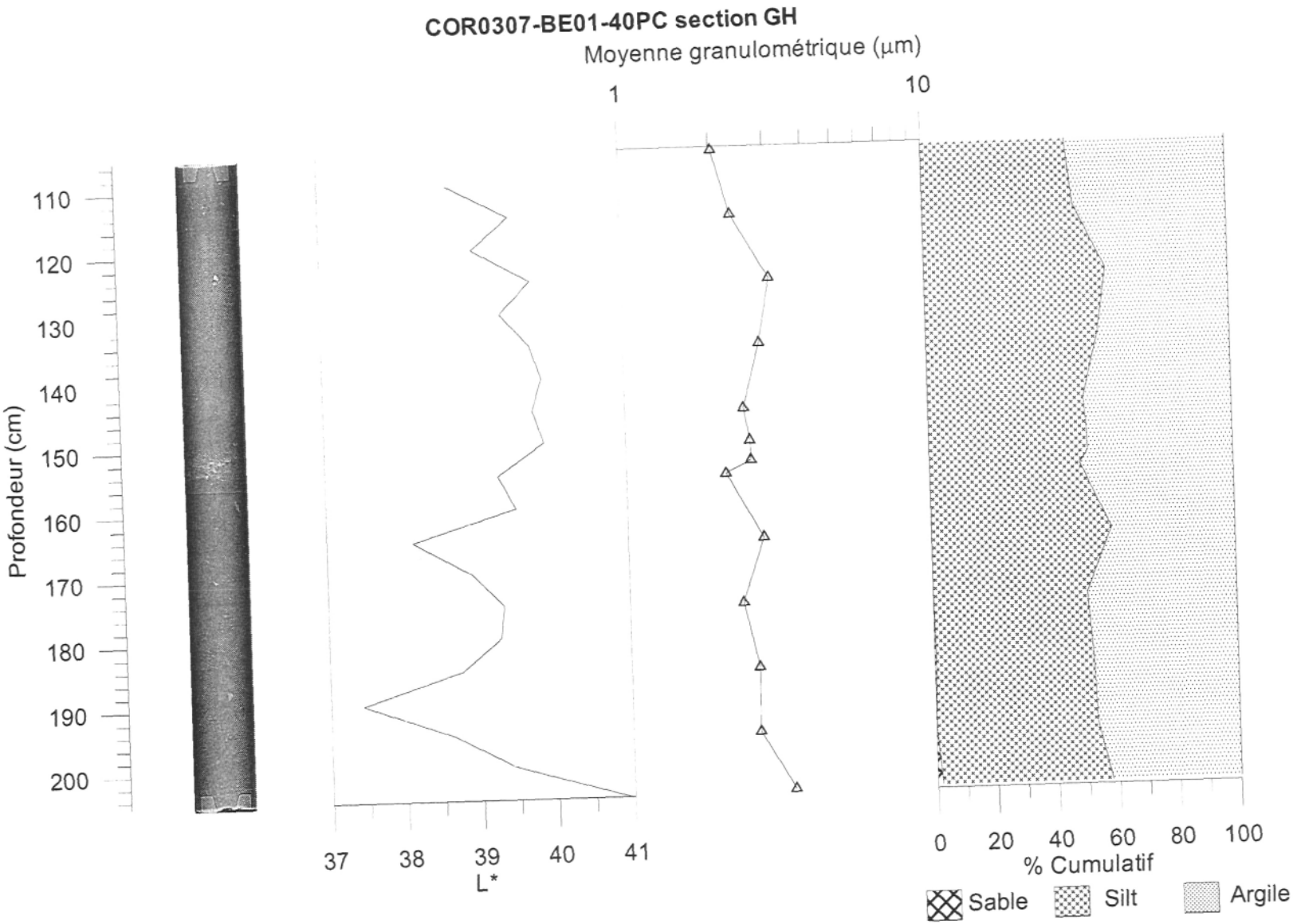
COR0307-BE01-40PC section GH
Moyenne granulométrique (µm)
1
10
Profondeur (cm)
110
120
130
140
150
160
170
180
190
200
37
38
39
40
41
L*
0
20
40
60
80
100
% Cumulatif
Sable
Silt
Argile

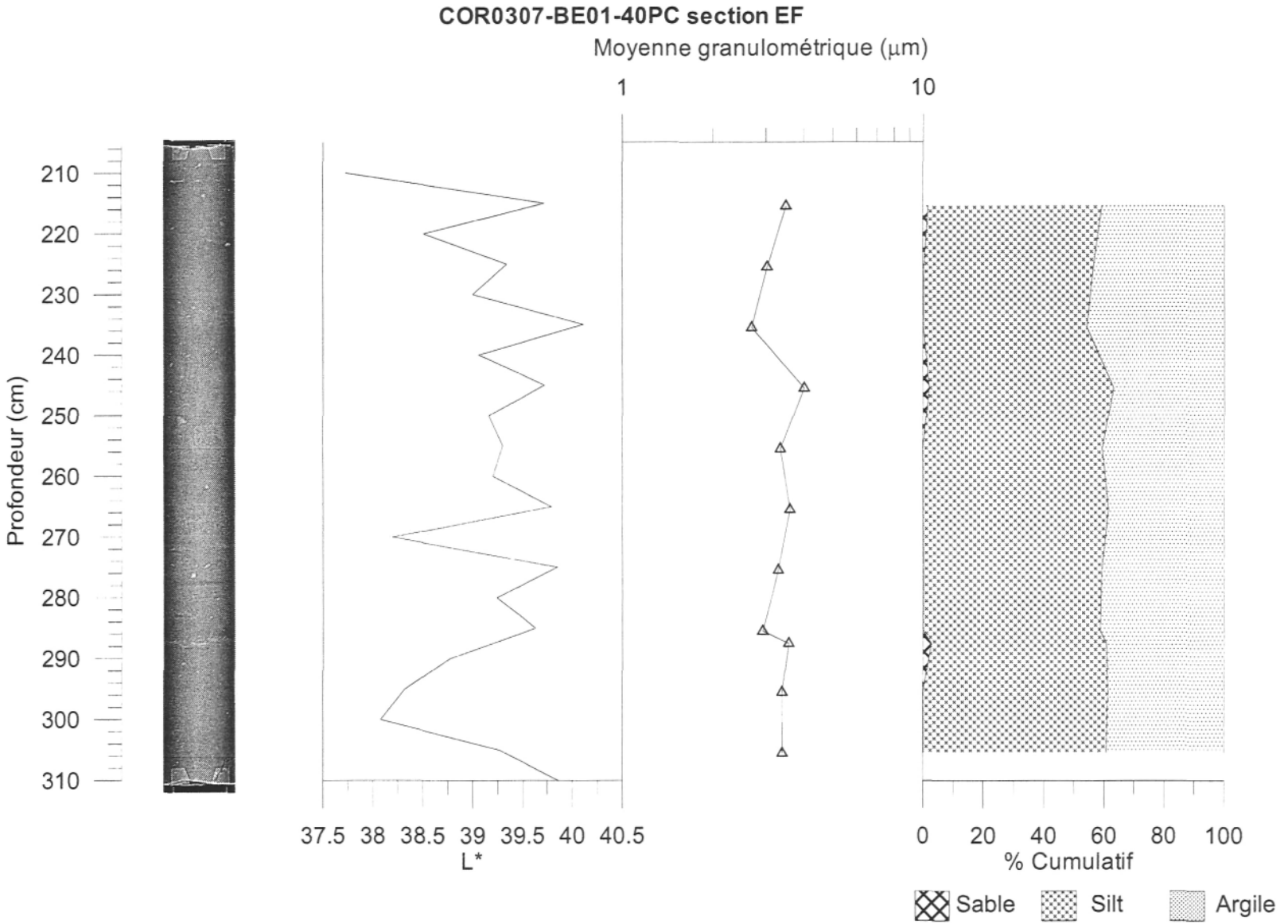
COR0307-BE01-40PC section EF
Moyenne granulométrique (µm)
1
10
Profondeur (cm)
210
220
230
240
250
260
270
280
290
300
310
37.5 38 38.5 39 39.5 40 40.5
L*
0 20 40 60 80 100
% Cumulatif
Sable
Silt
Argile

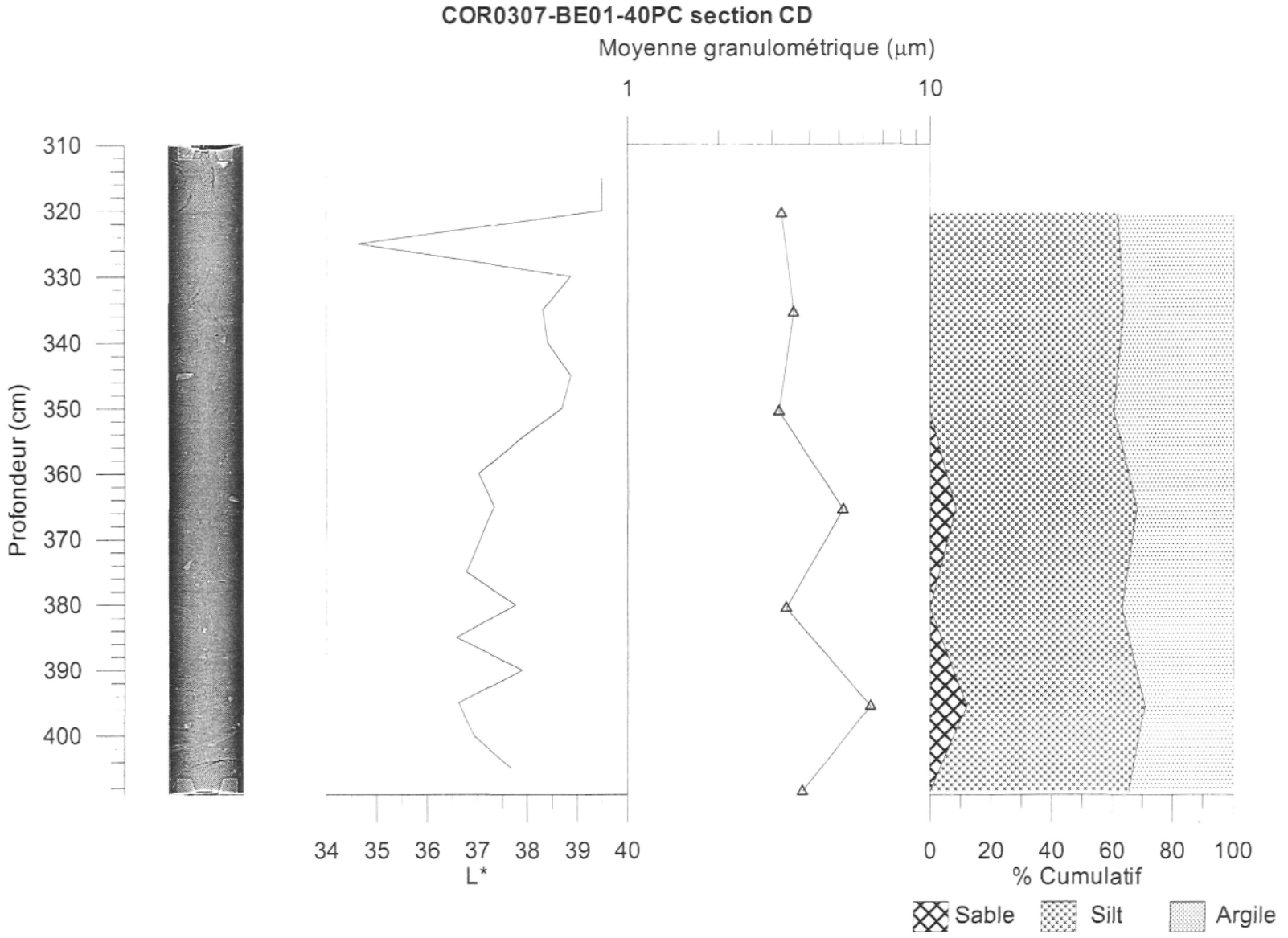
COR0307-BE01-40PC section CD
Moyenne granulométrique (µm)
1
10
Profondeur (cm)
310
320
330
340
350
360
370
380
390
400
34
35
36
37
38
39
40
L*
0
20
40
60
80
100
% Cumulatif
Sable
Silt
Argile

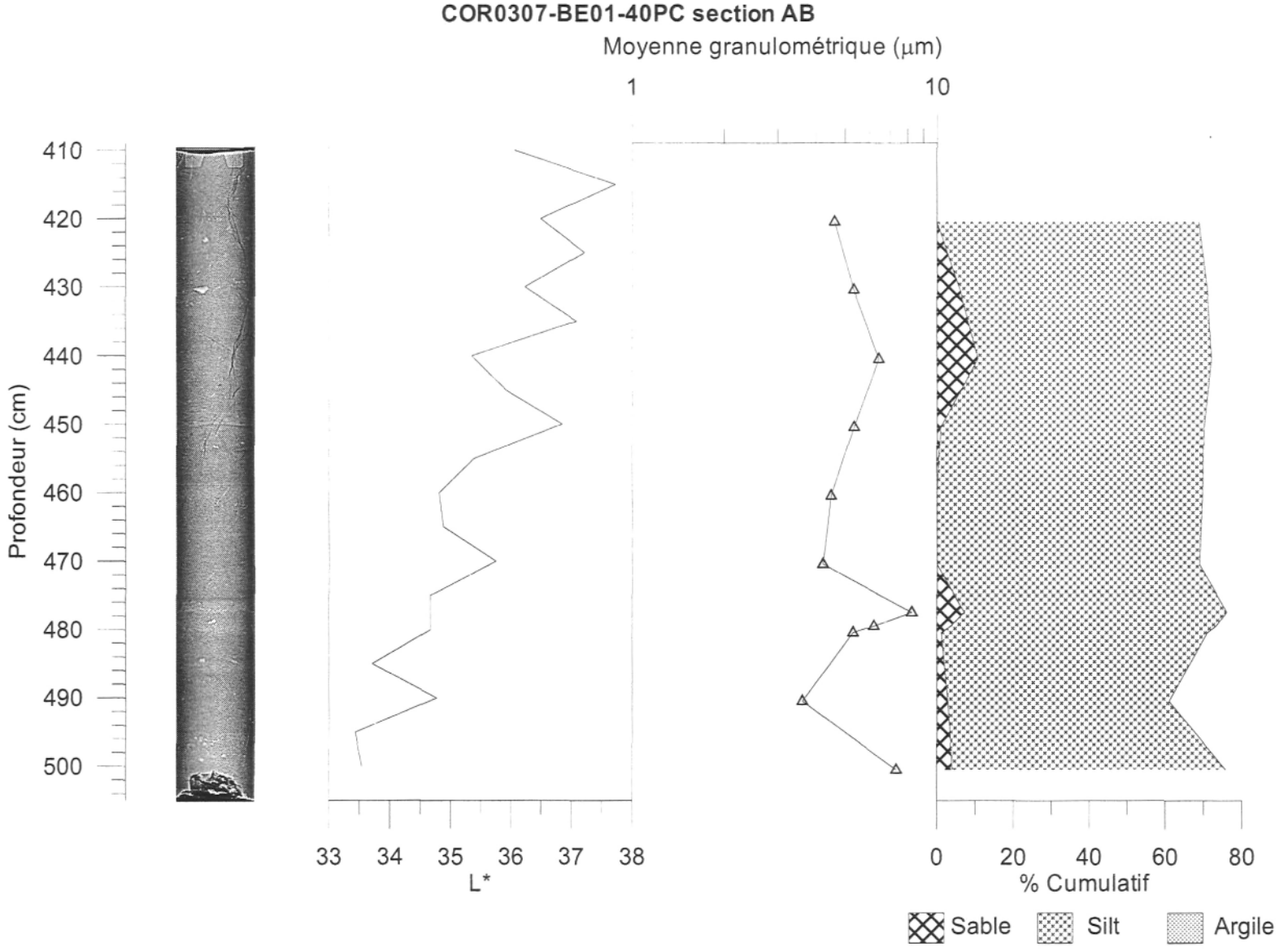
COR0307-BE01-40PC section AB
Moyenne granulométrique (μm)
1
10
Profondeur (cm)
410
420
430
440
450
460
470
480
490
500
33
34
35
36
37
38
L*
0
20
40
60
80
% Cumulatif
Sable
Silt
Argile

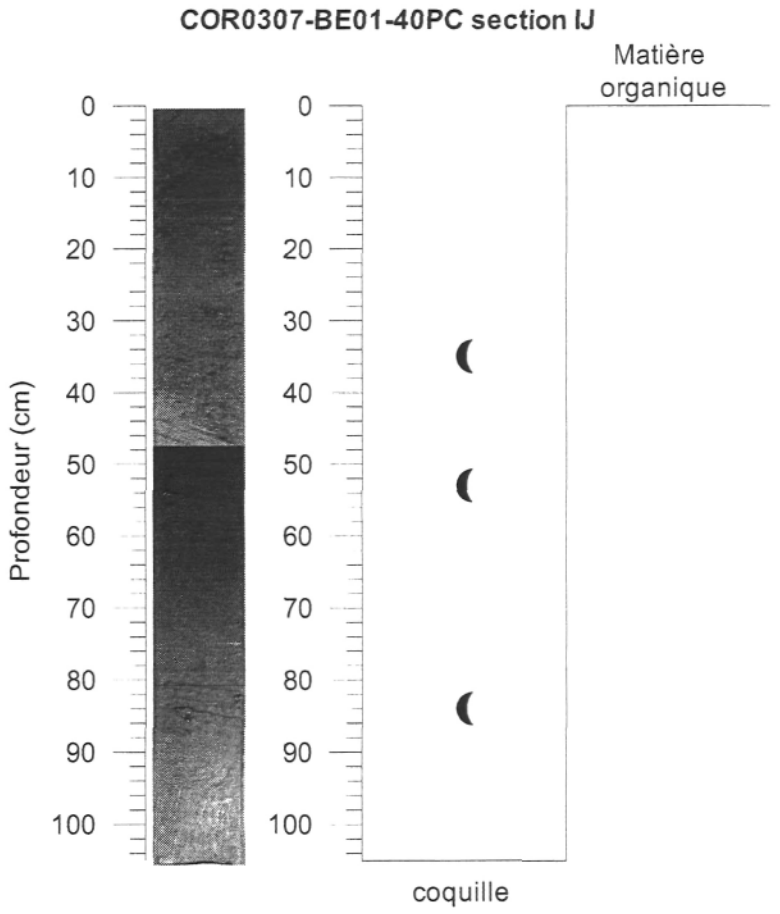

Intervalle	Structure	Granulo	Description
0-3		Si A	Silt argileux homogène avec surface oxidée
3-6		S G	Poche de sable et gravier (arrondis, à subarrondis), roches ignées avec fragment de coquilles,
6-12		MS	Couche de muddy sand
12-20		MS / S	Alternance de lits de muddy sand et de sable. Argile est présente dans les lits de muddy sand, les laminations sont visibles au CAT-SCAN
20-26		A Si	Galet d'argile de forme triangulaire, argile silteuse assez homogène. Petite couche d'argile plus pâle au bas du galet
26-46		MS / S	Alternance de lits de muddy sand et de sable. Contact érosif très distinct oblique entre 39 et 46 cm
	35		Bivalve intact, environ 1 cm
46-55		A	Argile homogène, très faiblement bioturbée, avec de petites lignes/laminations noires
	53		Fragment de bivalve
	55		Algue verte, ou quelque chose du type, filamenteuse
56-105			Argile grise légèrement bioturbée, traces de mouchetures noires, l'argile 56-105 est beaucoup plus raide que l'argile 46-55
	84		Gastéropode intact

Date:11/22/2005
Observateurs: GCV - G. St-Onge
Échantillon: COR0307-BE01-40PC
Section: IJ
Longueur: 105 cm
Profondeur: 0 - 105 cm

COR0307-BE01-40PC section GH

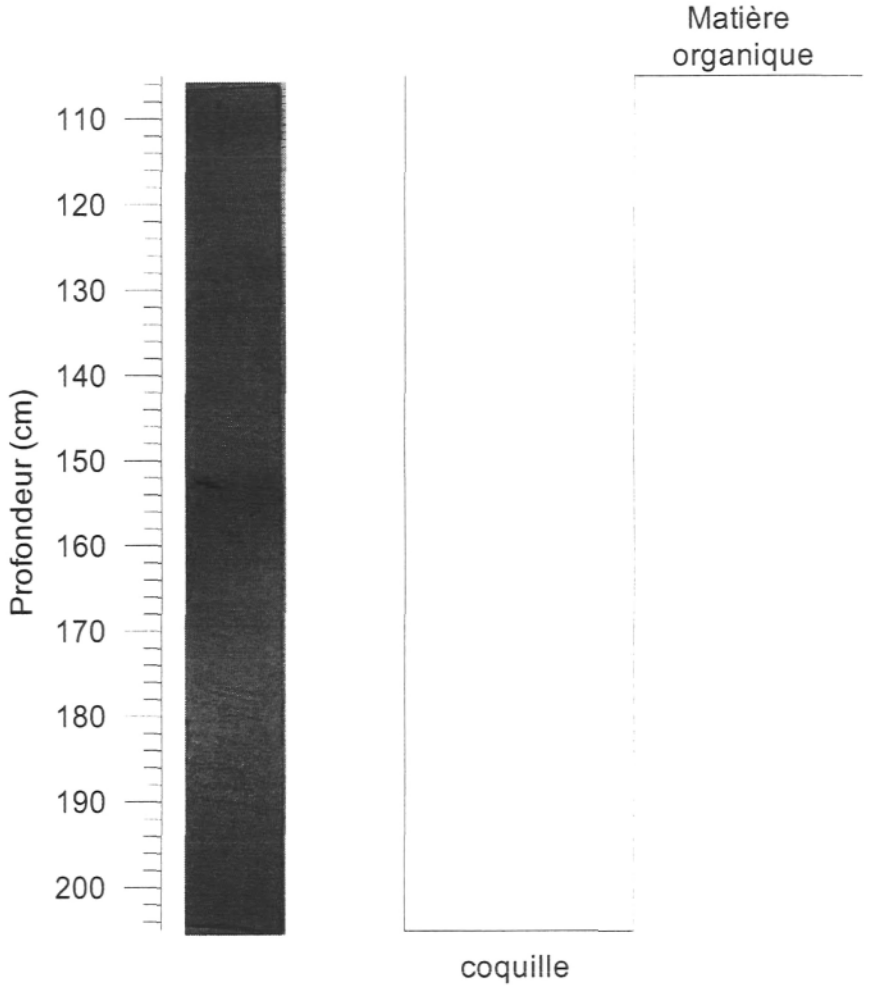

Intervalle	Structure	Granulo	Description
105-205		A	Argile relativement homogène avec mouchetures de bioturbation
	127		Présence de fractures dues à l'échantionnage
	143		Présence de fractures dues à l'échantionnage
151-155		Sa	Lit de sable

Date: 11/22/2005
Observateurs: GCV - G. St-Onge
Échantillon: COR0307-BE01-40PC
Section: GH
Longueur: 100 cm
Profondeur: 105 -205 cm

COR0307-BE01-40PC section EF

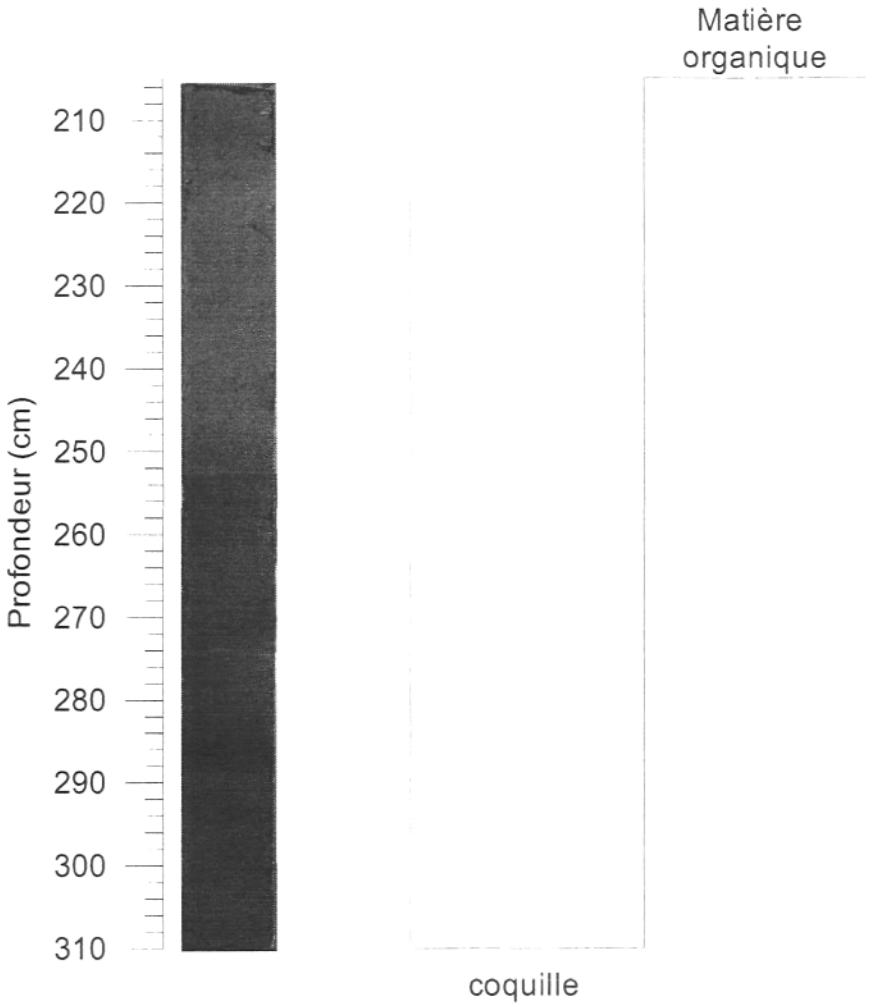

Date: 11/22/2005
Observateurs: GCV - G. St-Onge
Échantillon: COR0307-BE01-40PC
Section: EF
Longueur: 105 cm
Profondeur: 205-310 cm

Intervalle	Structure	Granulo	Description
250-310		A	Argile homogène avec quelques petits grains de silt/sable ici et là. Petites mouchetures de bioturbation
	240		Petite poche de matière organique, 2 mm
	225		Fracture due à l'échantillonnage
	257		Fracture due à l'échantillonnage
	275		Petite roche, 1 cm
287-288		MS	Lit de muddy sable

COR0307-BE01-40PC section CD

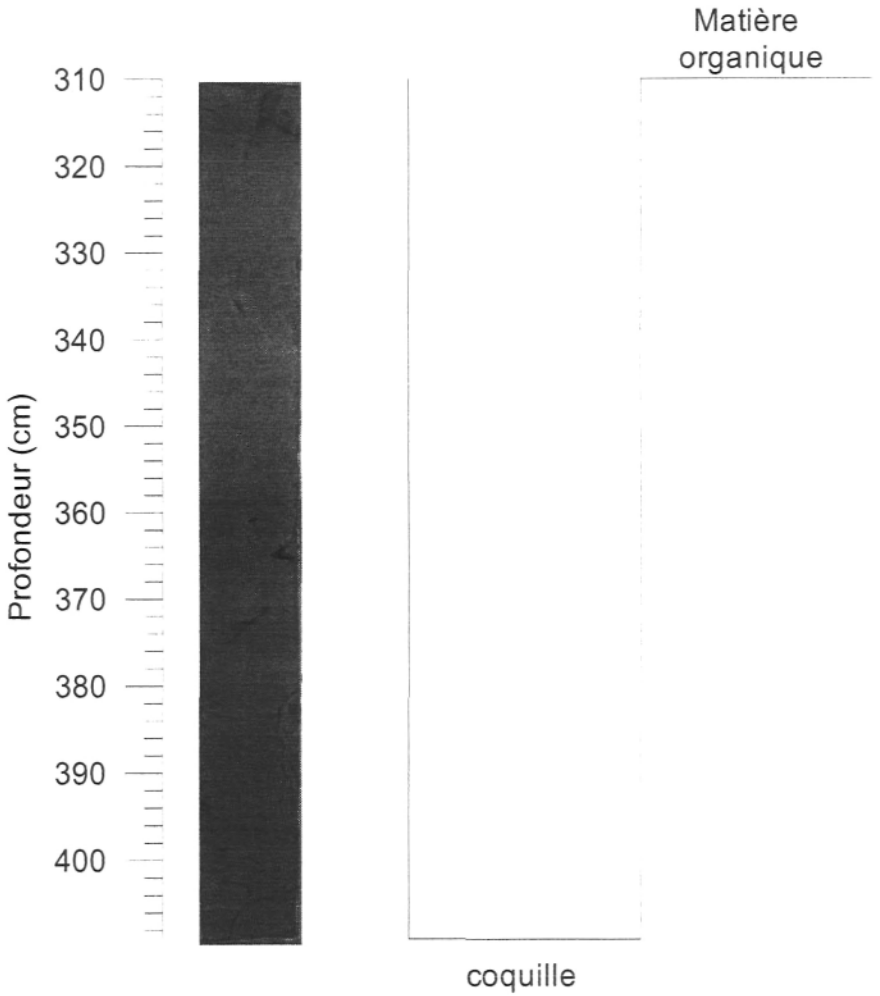

Date: 11/23/2005
Observatrice: GCV
Échantillon: COR0307-BE01-40PC
Section: CD
Longueur: 99 cm
Profondeur: 310 - 409 cm

Intervalle	Structure	Granulo	Description
310-409		A Si	Argile avec quelques grains de silt (mais très peu) Échantillon assez fracturé à cause de l'échantillon, présence d'oxidation autour des fractures, lég;re mouchetures de bioturbation.
	340		Petit fragment de coquille
	364		Roche arrondie (0.70)
	375		Petit fragment de coquille

COR0307-BE01-40PC section AB

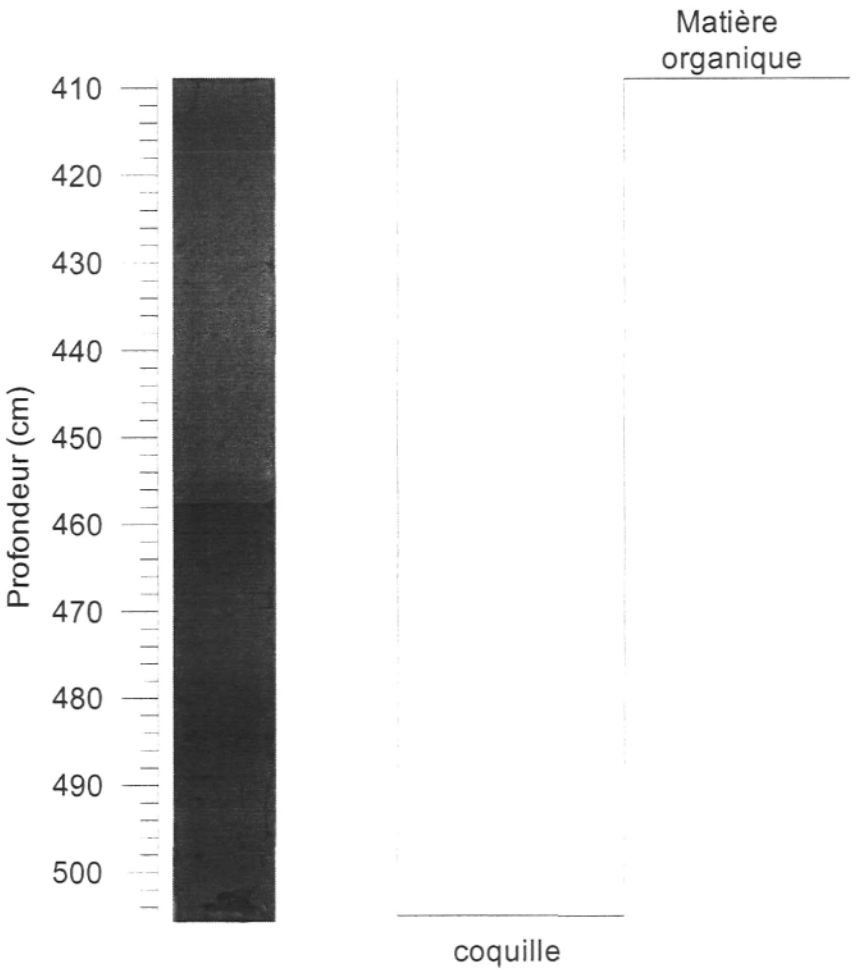

Date: 11/23/2005
Observatrice: GCV
Échantillon: COR0307-BE01-40PC
Section: AB
Longueur: 96 cm
Profondeur: 409-505 cm

Intervalle	Structure	Granulo	Description
409-505		A	Argile grise avec peu de silt, faiblement bioturbée avec mouchetures noires, parties oxidées
	430		Grosse roche métamorphique (avec quartz) assez anguleire, visible sur le Cat-Scan
	454		Fragment de coquille, environ 2 mm
	479		Deux roches de 1 cm sur le même niveau
	491		Petite poche de silt (rosé??)
	498		gravier de 1 cm

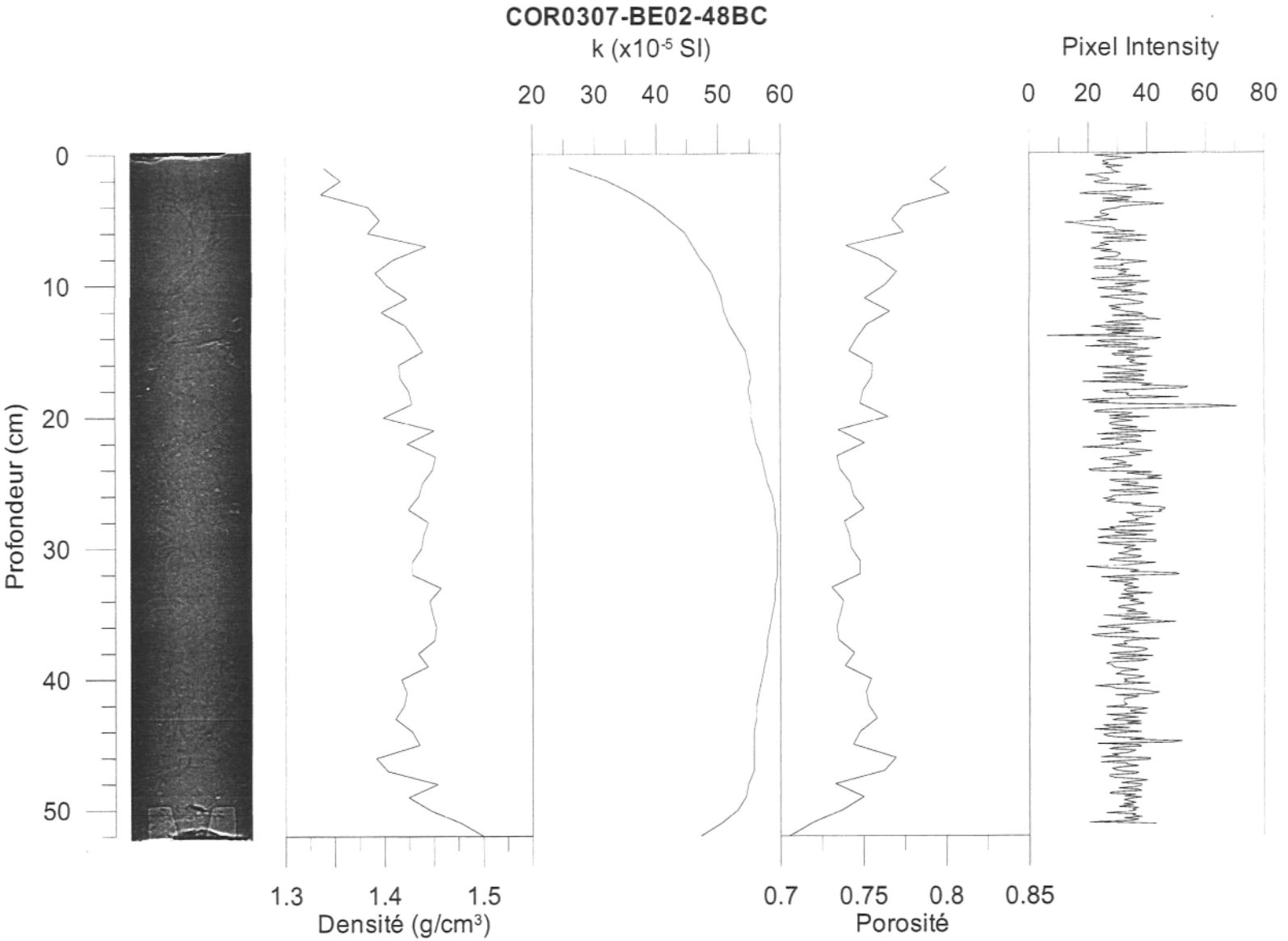
COR0307-BE02-48BC
k (x10-5 SI)
20 30 40 50 60
Pixel Intensity
0 20 40 60 80
Profondeur (cm)
0
10
20
30
40
50
1.3 1.4 1.5
Densité (g/cm3)
0.7 0.75 0.8 0.85
Porosité

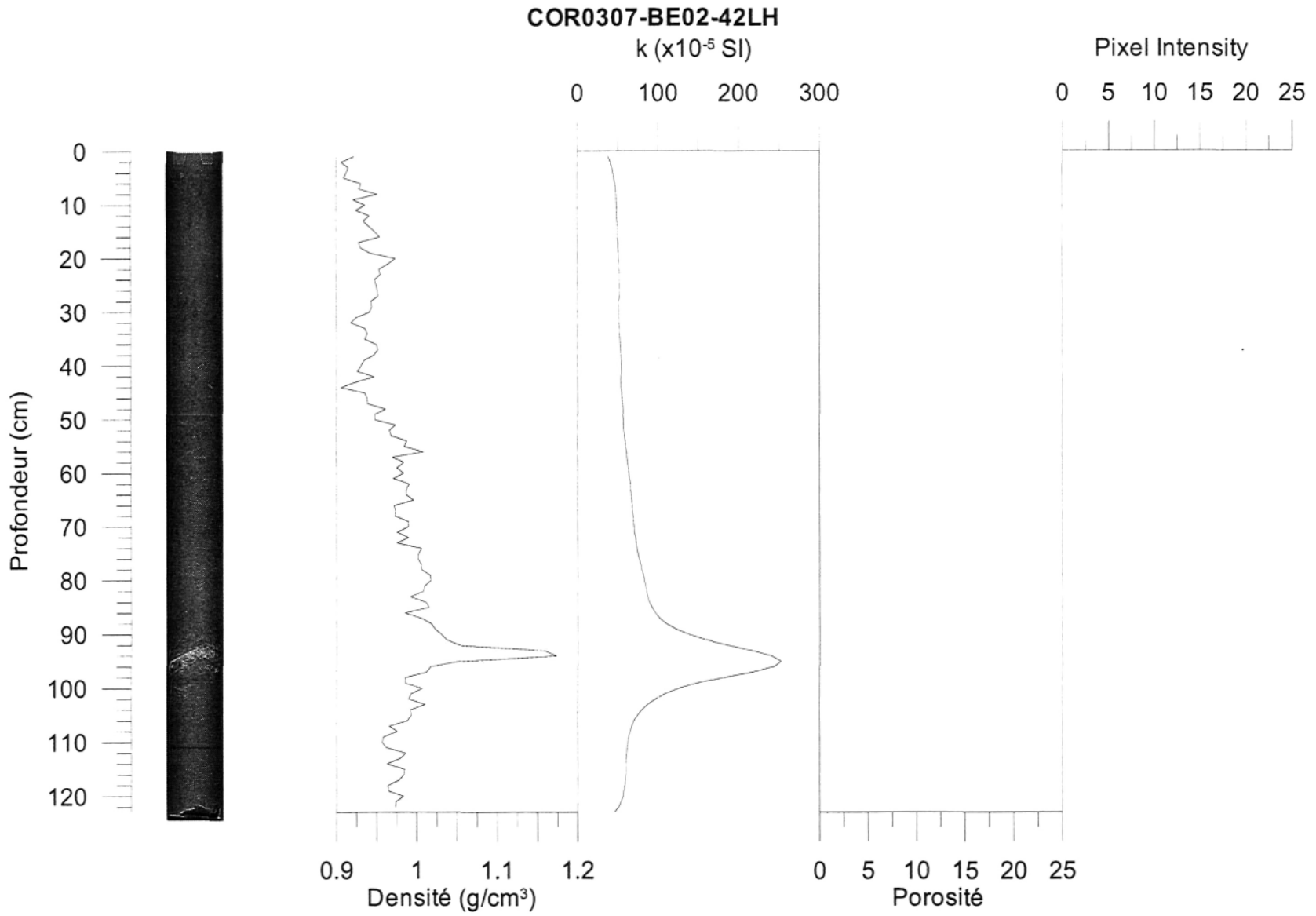
COR0307-BE02-42LH
k (x10-5 SI)
0 100 200 300
Pixel Intensity
0 5 10 15 20 25
Profondeur (cm)
0 10 20 30 40 50 60 70 80 90 100 110 120
0.9 1 1.1 1.2
Densité (g/cm3)
0 5 10 15 20 25
Porosité

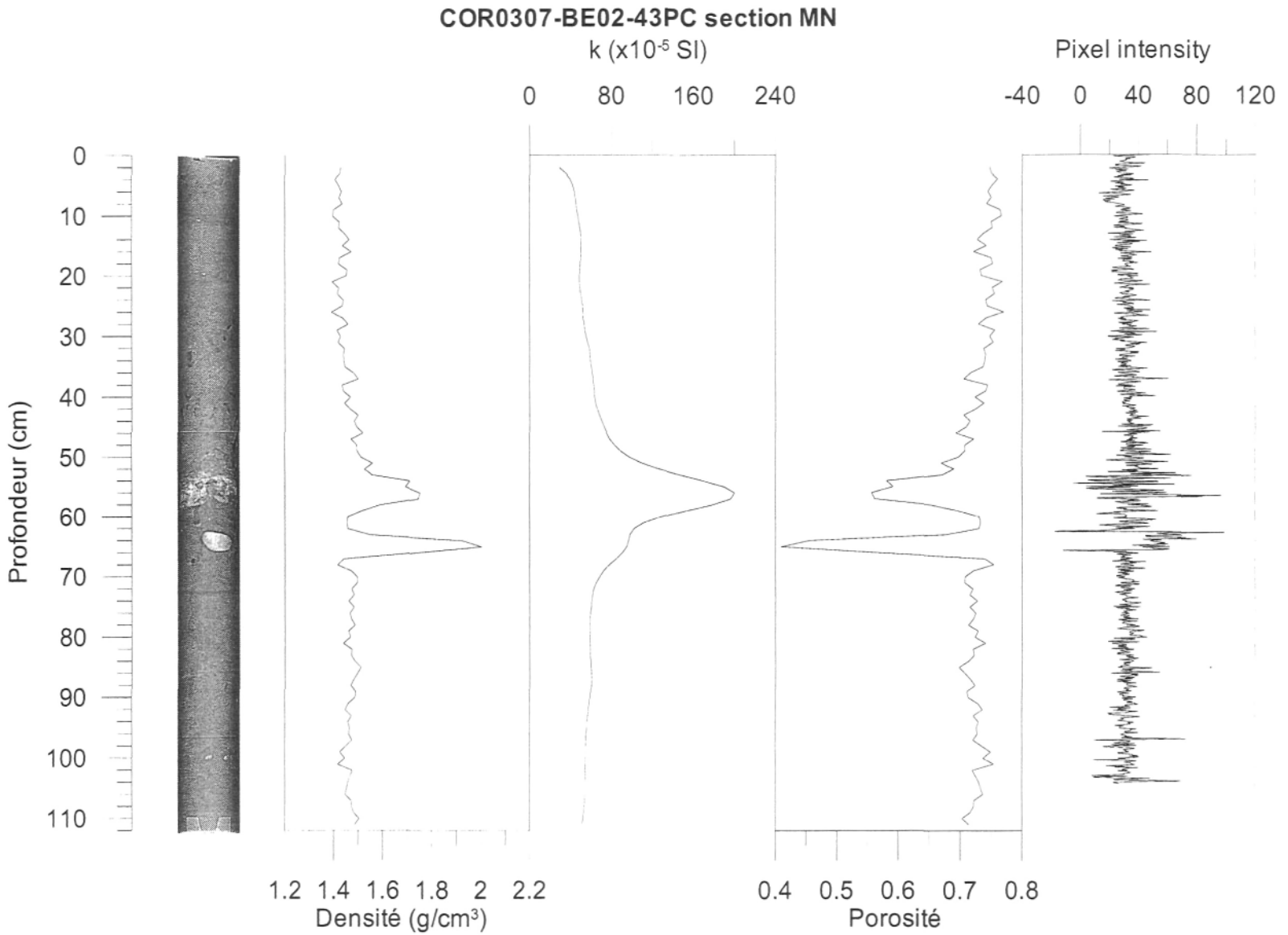
COR0307-BE02-43PC section MN
k (x10-5 SI)
0 80 160 240
Pixel intensity
-40 0 40 80 120
Profondeur (cm)
0 10 20 30 40 50 60 70 80 90 100 110
1.2 1.4 1.6 1.8 2 2.2
Densité (g/cm3)
0.4 0.5 0.6 0.7 0.8
Porosité

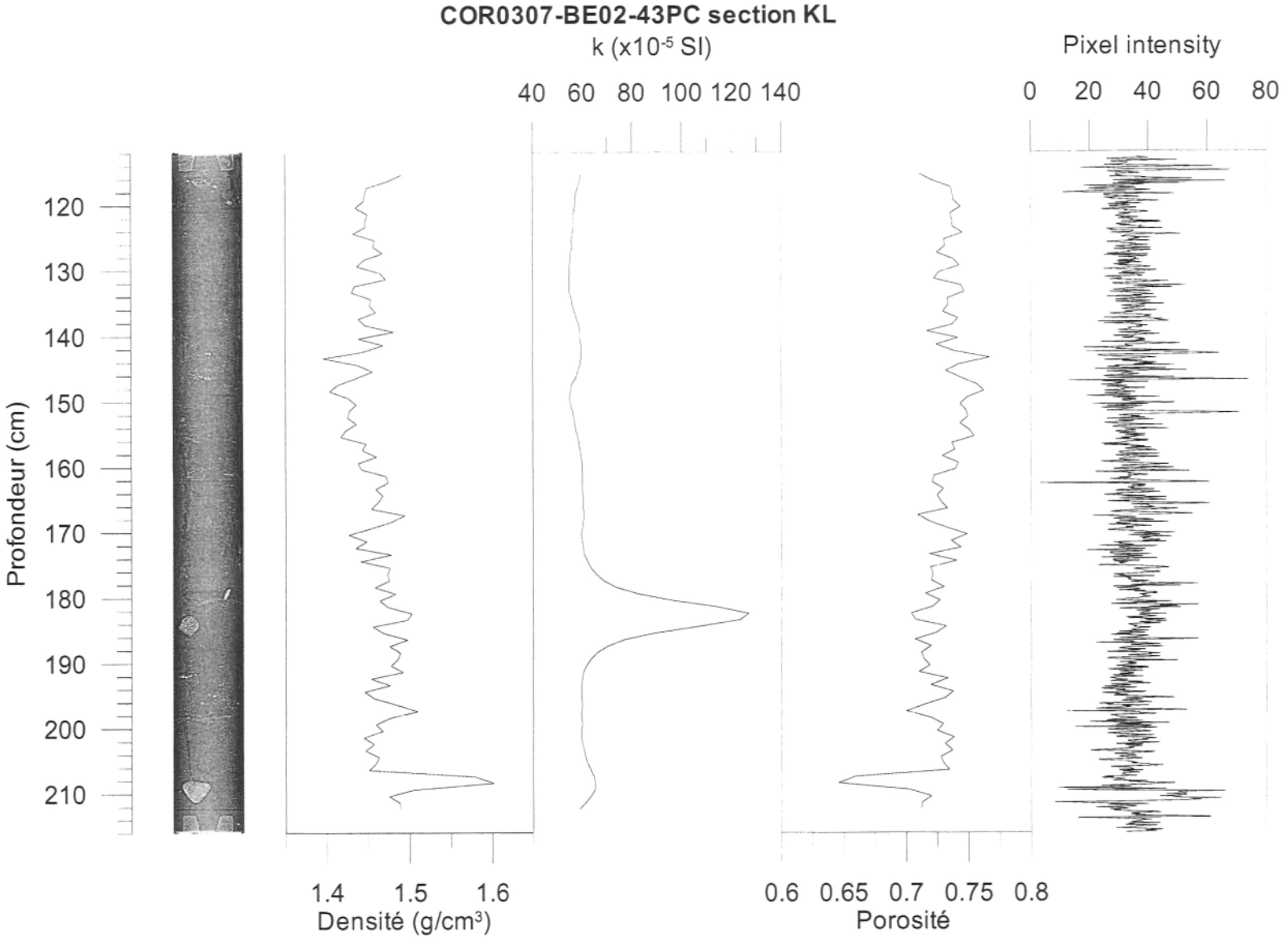
COR0307-BE02-43PC section KL
k (x10-5 SI)
40 60 80 100 120 140
Pixel intensity
0 20 40 60 80
Profondeur (cm)
120
130
140
150
160
170
180
190
200
210
1.4 1.5 1.6
Densité (g/cm3)
0.6 0.65 0.7 0.75 0.8
Porosité

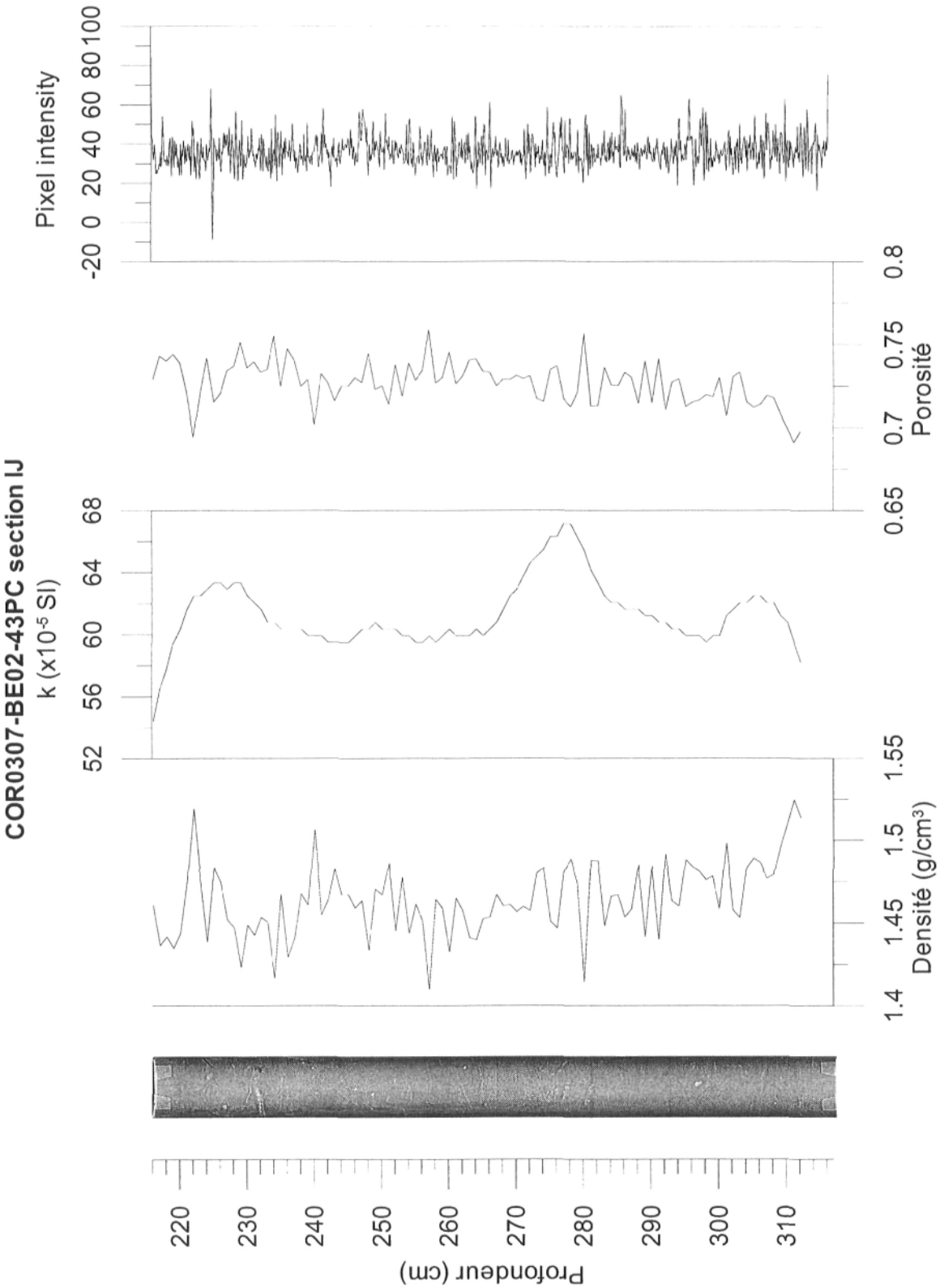
COR0307-BE02-43PC section IJ
Pixel intensity
-20 0 20 40 60 80 100
k (x10-5 SI)
52 56 60 64 68
Porosité
0.65 0.7 0.75 0.8
Densité (g/cm3)
1.4 1.45 1.5 1.55
Profondeur (cm)
220 230 240 250 260 270 280 290 300 310

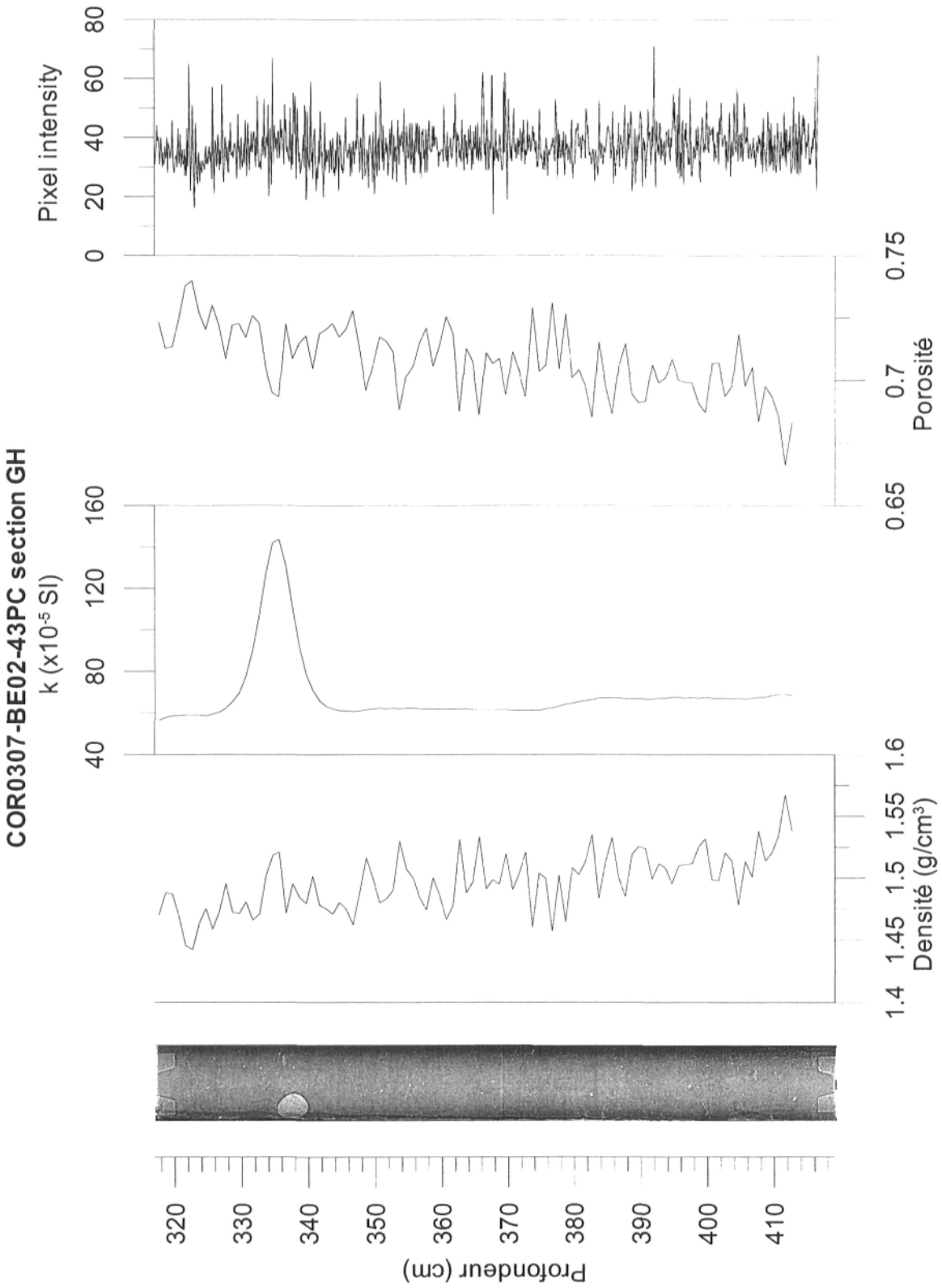
COR0307-BE02-43PC section GH
Profondeur (cm)
320
330
340
350
360
370
380
390
400
410
k (x10-5 SI)
40
80
120
160
Densité (g/cm3)
1.4
1.45
1.5
1.55
1.6
Porosité
0.65
0.7
0.75
Pixel intensity
0
20
40
60
80

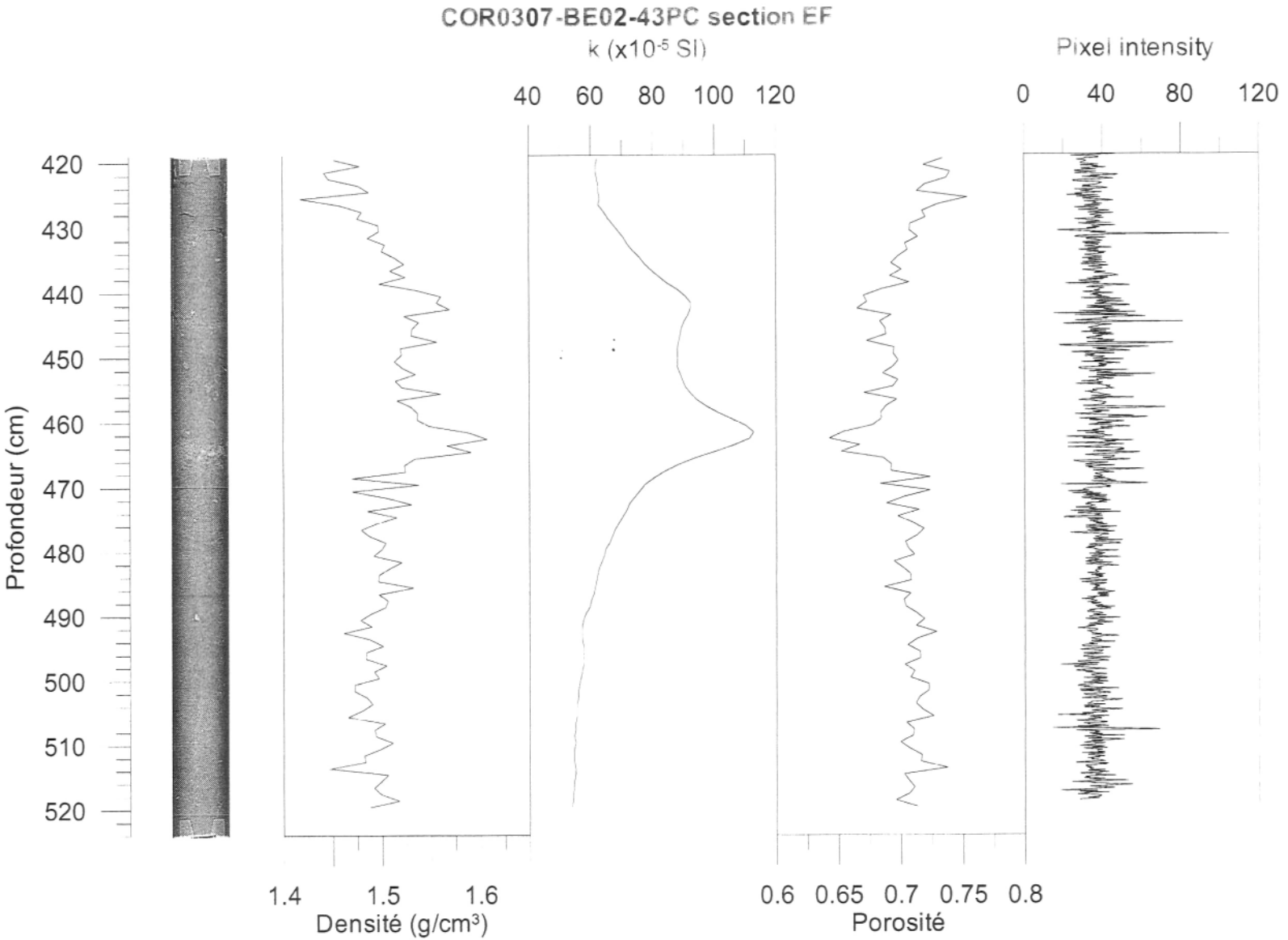
COR0307-BE02-43PC section EF
k (x10-5 SI)
40 60 80 100 120
Pixel intensity
0 40 80 120
Profondeur (cm)
420
430
440
450
460
470
480
490
500
510
520
1.4 1.5 1.6
Densité (g/cm3)
0.6 0.65 0.7 0.75 0.8
Porosité

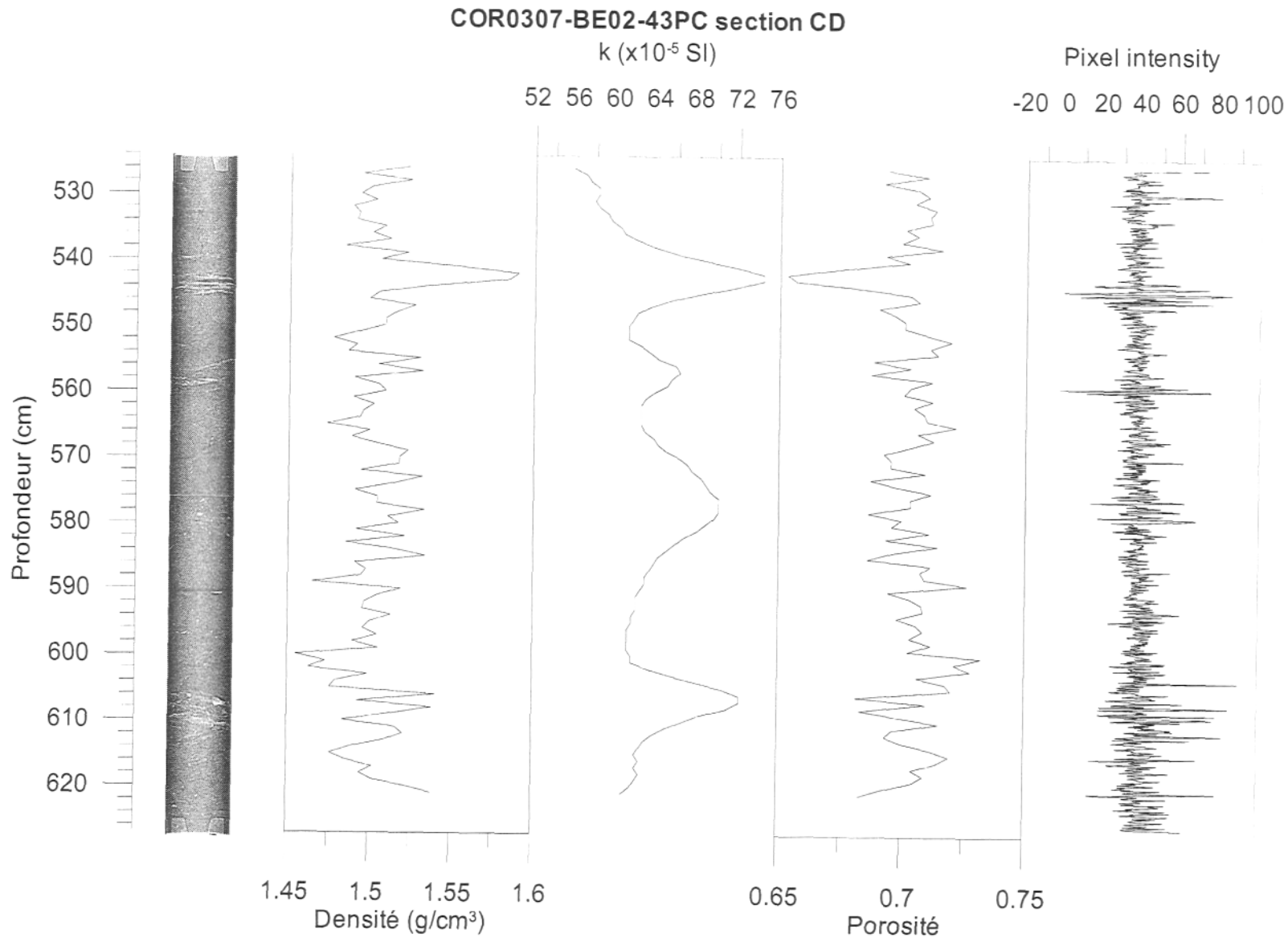
COR0307-BE02-43PC section CD
k (x10-5 SI)
52 56 60 64 68 72 76
Pixel intensity
-20 0 20 40 60 80 100
Profondeur (cm)
530
540
550
560
570
580
590
600
610
620
1.45 1.5 1.55 1.6
Densité (g/cm3)
0.65 0.7 0.75
Porosité

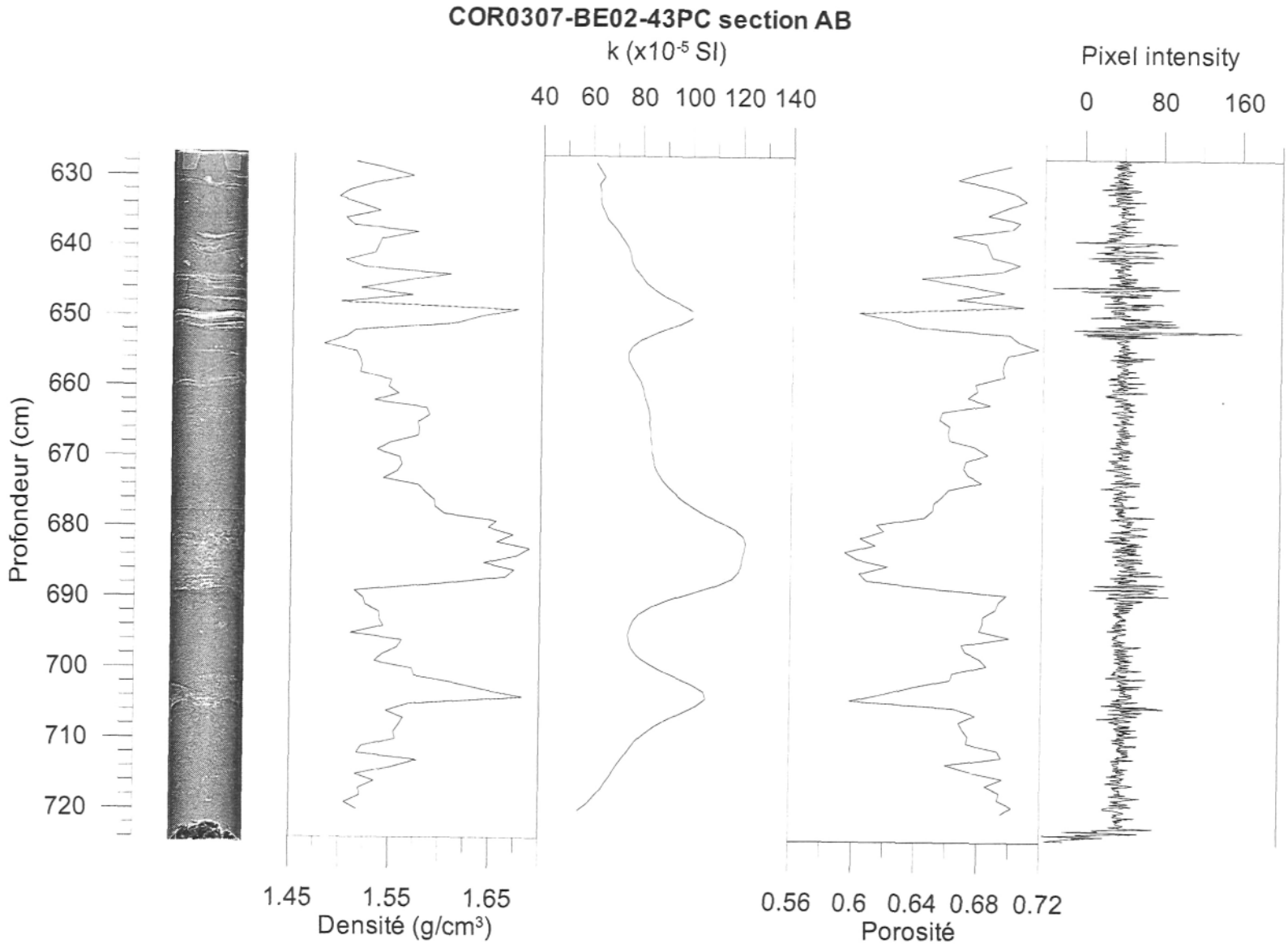
COR0307-BE02-43PC section AB
k (x10-5 SI)
40 60 80 100 120 140
Pixel intensity
0 80 160
Profondeur (cm)
630
640
650
660
670
680
690
700
710
720
1.45 1.55 1.65
Densité (g/cm3)
0.56 0.6 0.64 0.68 0.72
Porosité

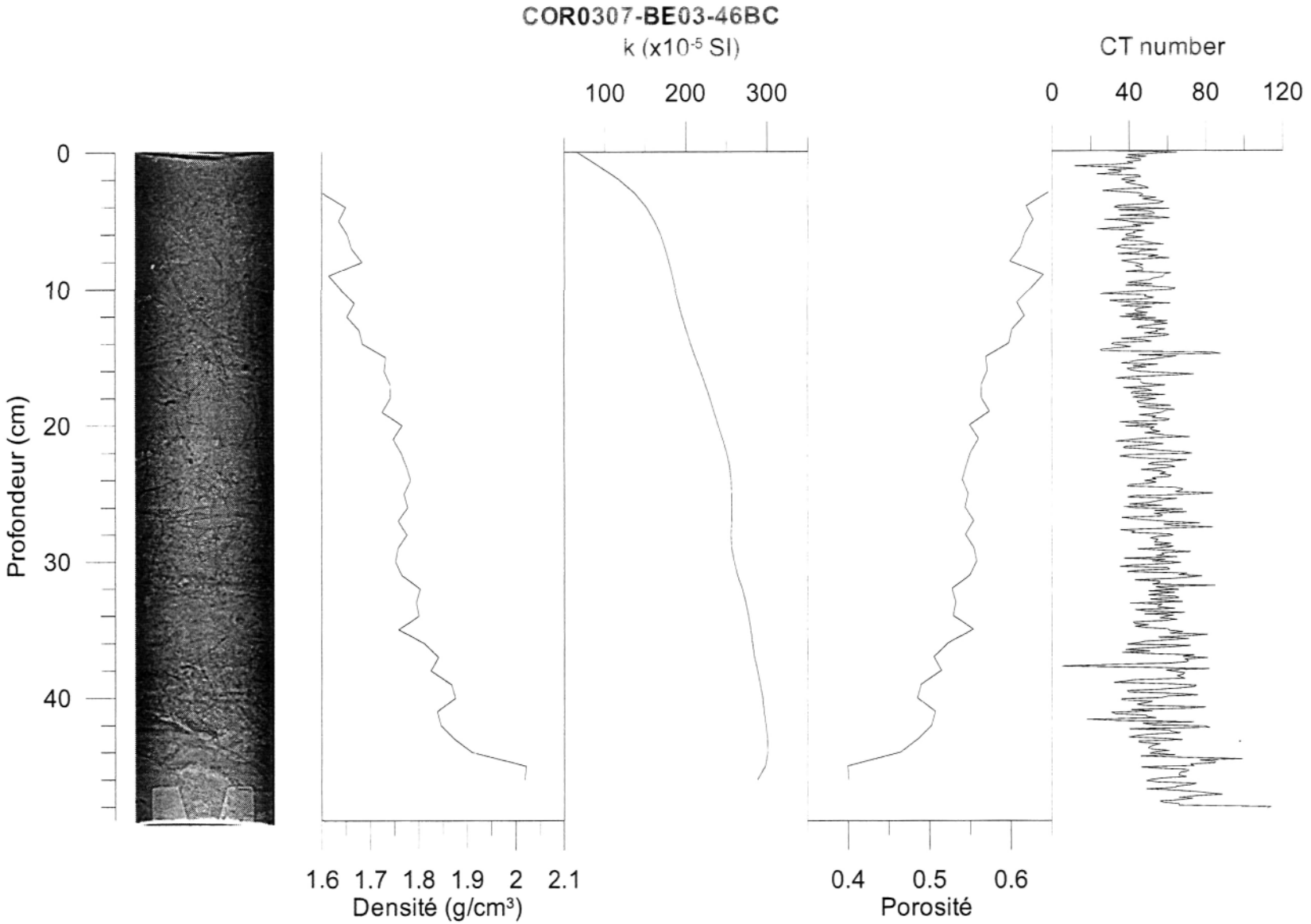
COR0307-BE03-46BC
k (x10-5 SI)
100 200 300
CT number
0 40 80 120
0
10
20
30
40
Profondeur (cm)
1.6 1.7 1.8 1.9 2 2.1
Densité (g/cm3)
0.4 0.5 0.6
Porosité

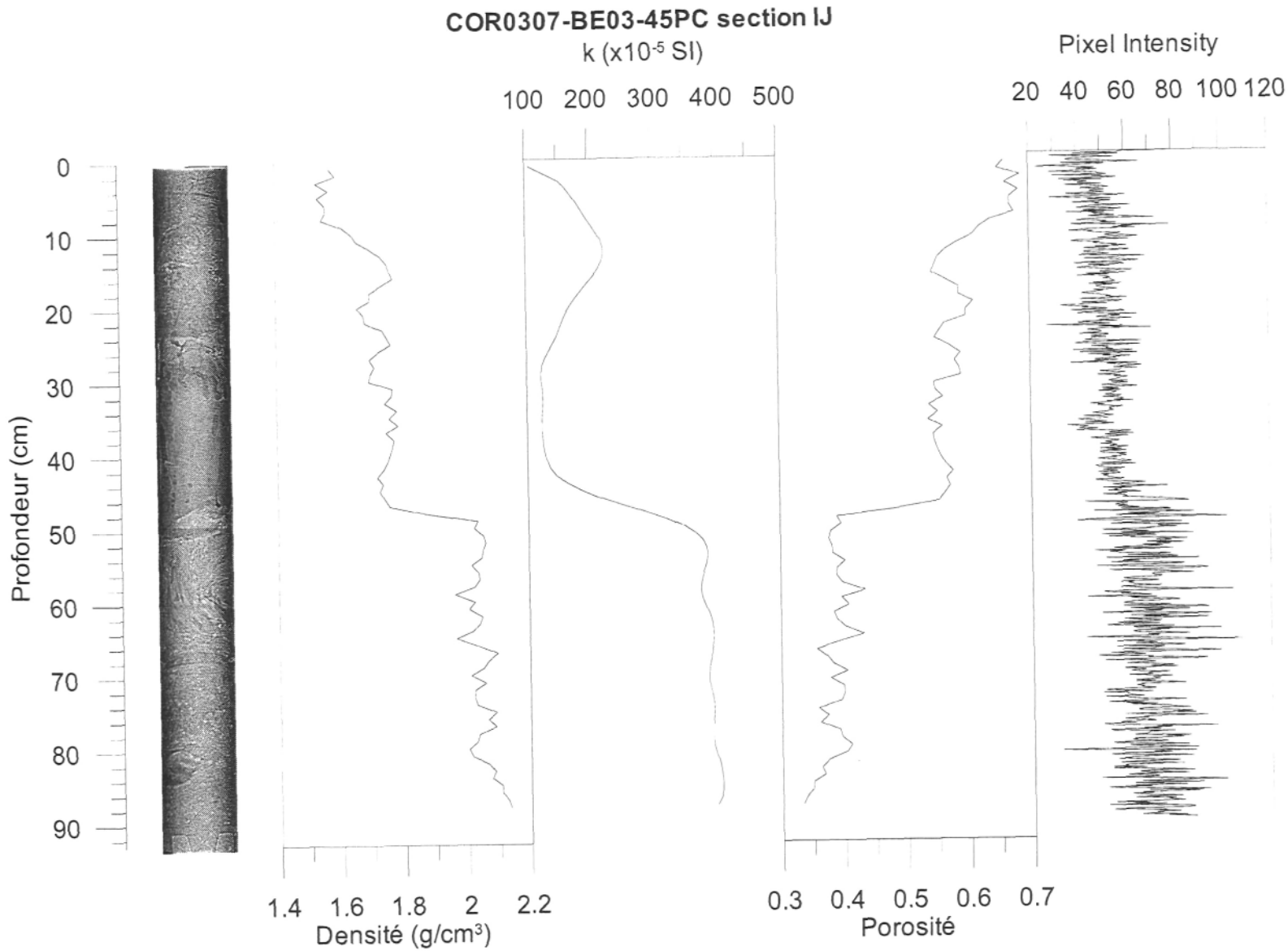
COR0307-BE03-45PC section IJ
k (x10-5 SI)
100 200 300 400 500
Pixel Intensity
20 40 60 80 100 120
Profondeur (cm)
0
10
20
30
40
50
60
70
80
90
1.4 1.6 1.8 2 2.2
Densité (g/cm3)
0.3 0.4 0.5 0.6 0.7
Porosité

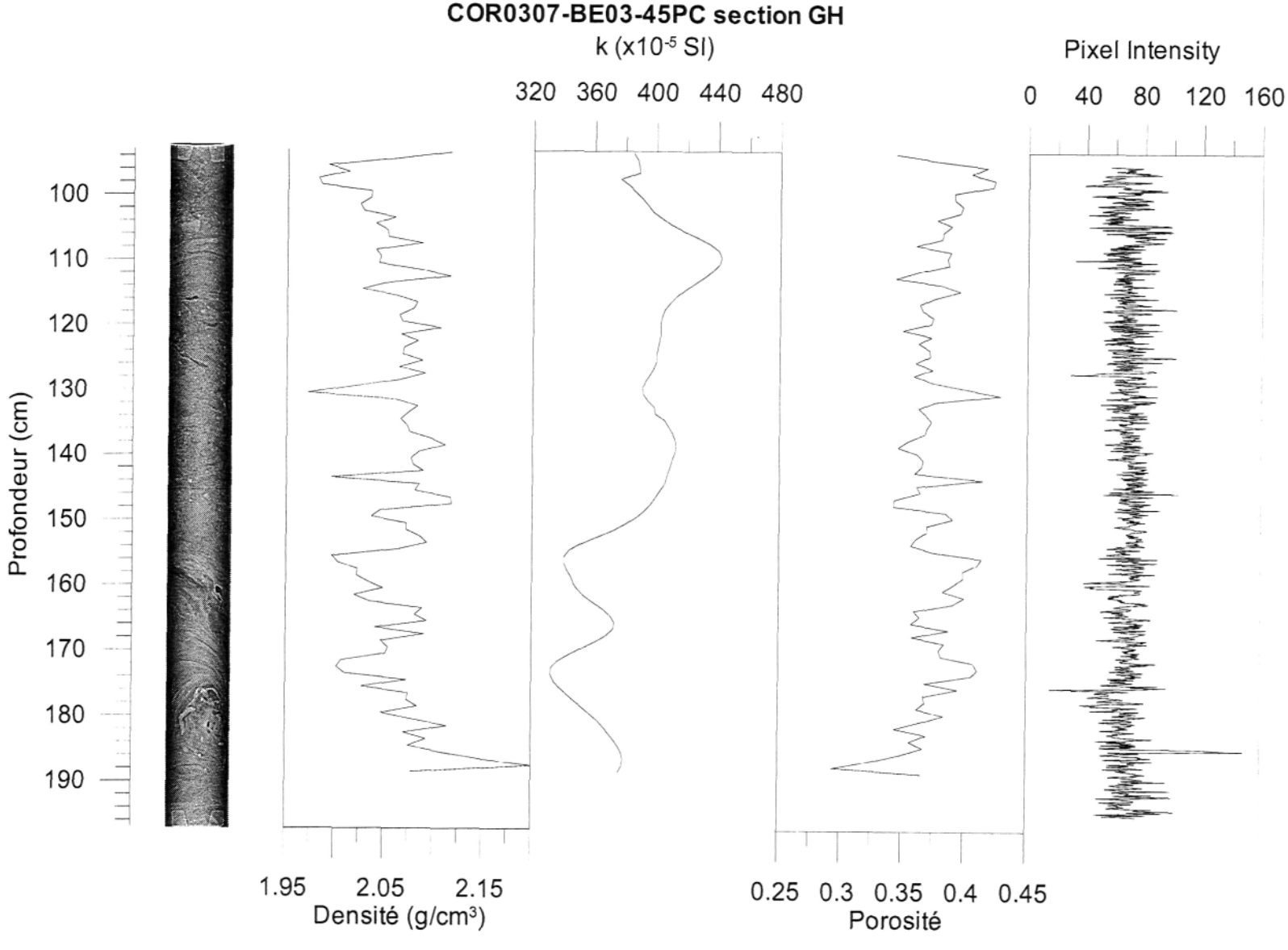
COR0307-BE03-45PC section GH
k (x10-5 SI)
320 360 400 440 480
Pixel Intensity
0 40 80 120 160
Profondeur (cm)
100
110
120
130
140
150
160
170
180
190
1.95 2.05 2.15
Densité (g/cm3)
0.25 0.3 0.35 0.4 0.45
Porosité

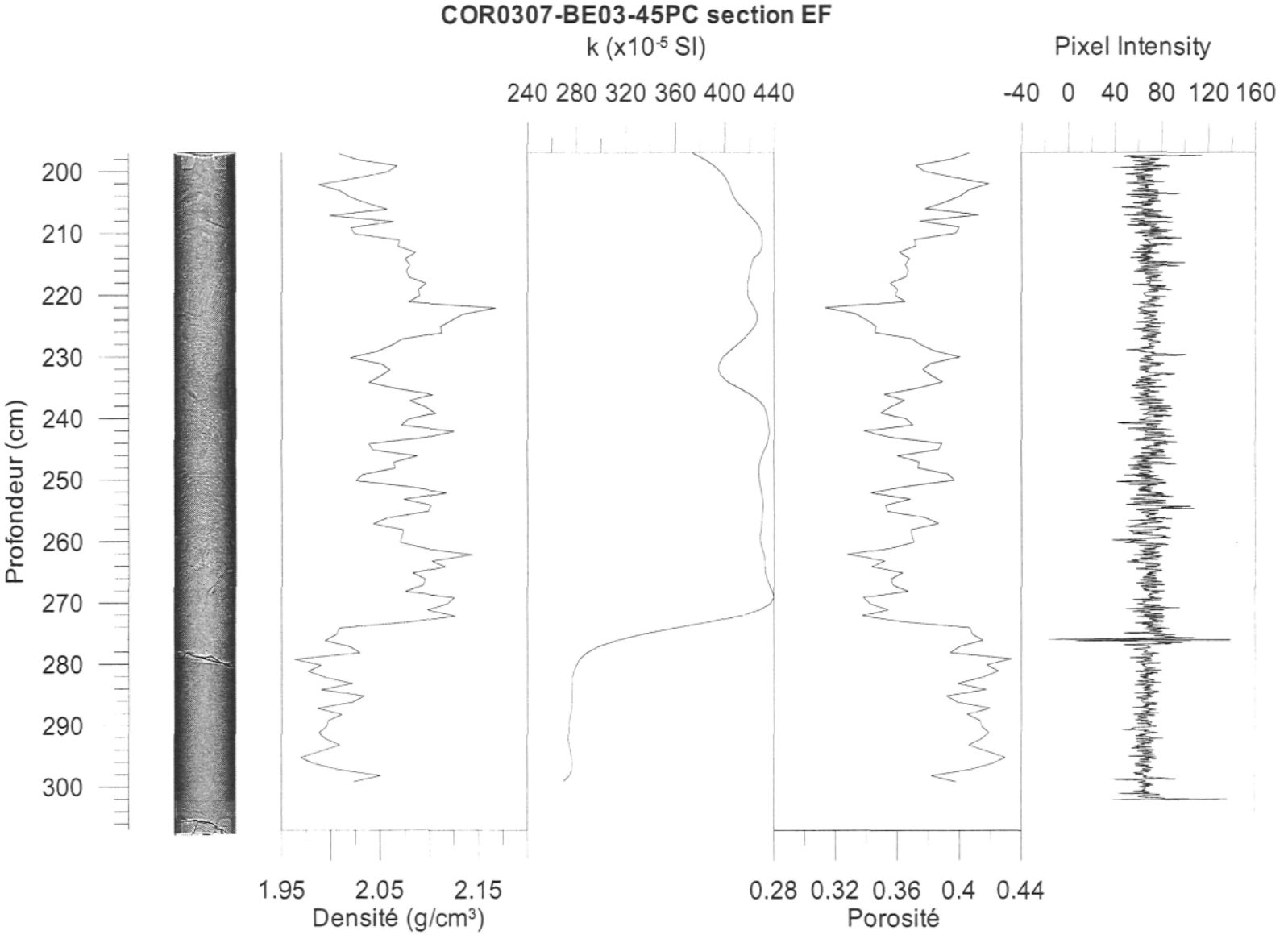
COR0307-BE03-45PC section EF
k (x10-5 SI)
240 280 320 360 400 440
Pixel Intensity
-40 0 40 80 120 160
Profondeur (cm)
200
210
220
230
240
250
260
270
280
290
300
1.95 2.05 2.15
Densité (g/cm3)
0.28 0.32 0.36 0.4 0.44
Porosité

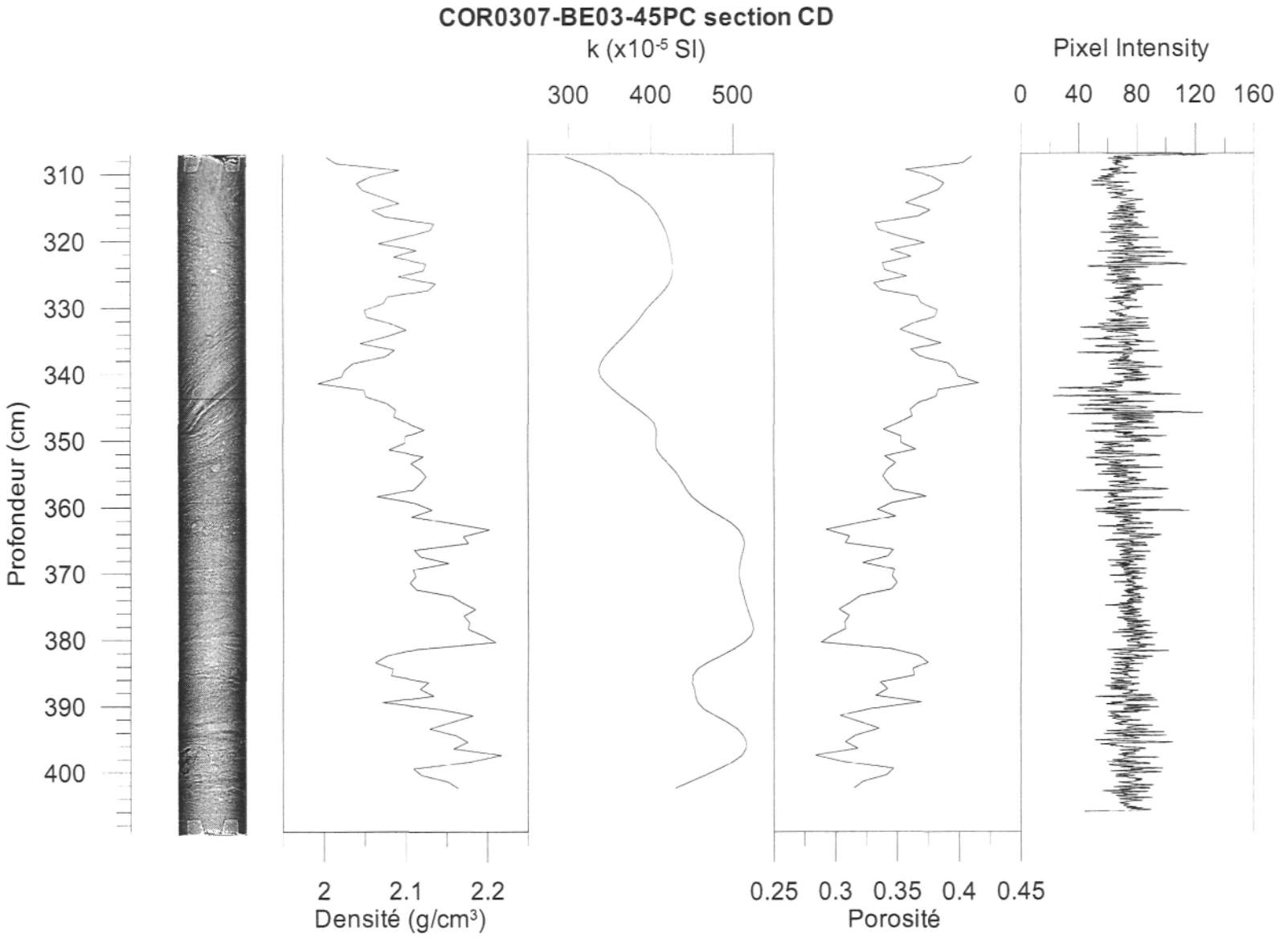
COR0307-BE03-45PC section CD
k (x10-5 SI)
300 400 500
Pixel Intensity
0 40 80 120 160
Profondeur (cm)
310
320
330
340
350
360
370
380
390
400
2 2.1 2.2
Densité (g/cm3)
0.25 0.3 0.35 0.4 0.45
Porosité

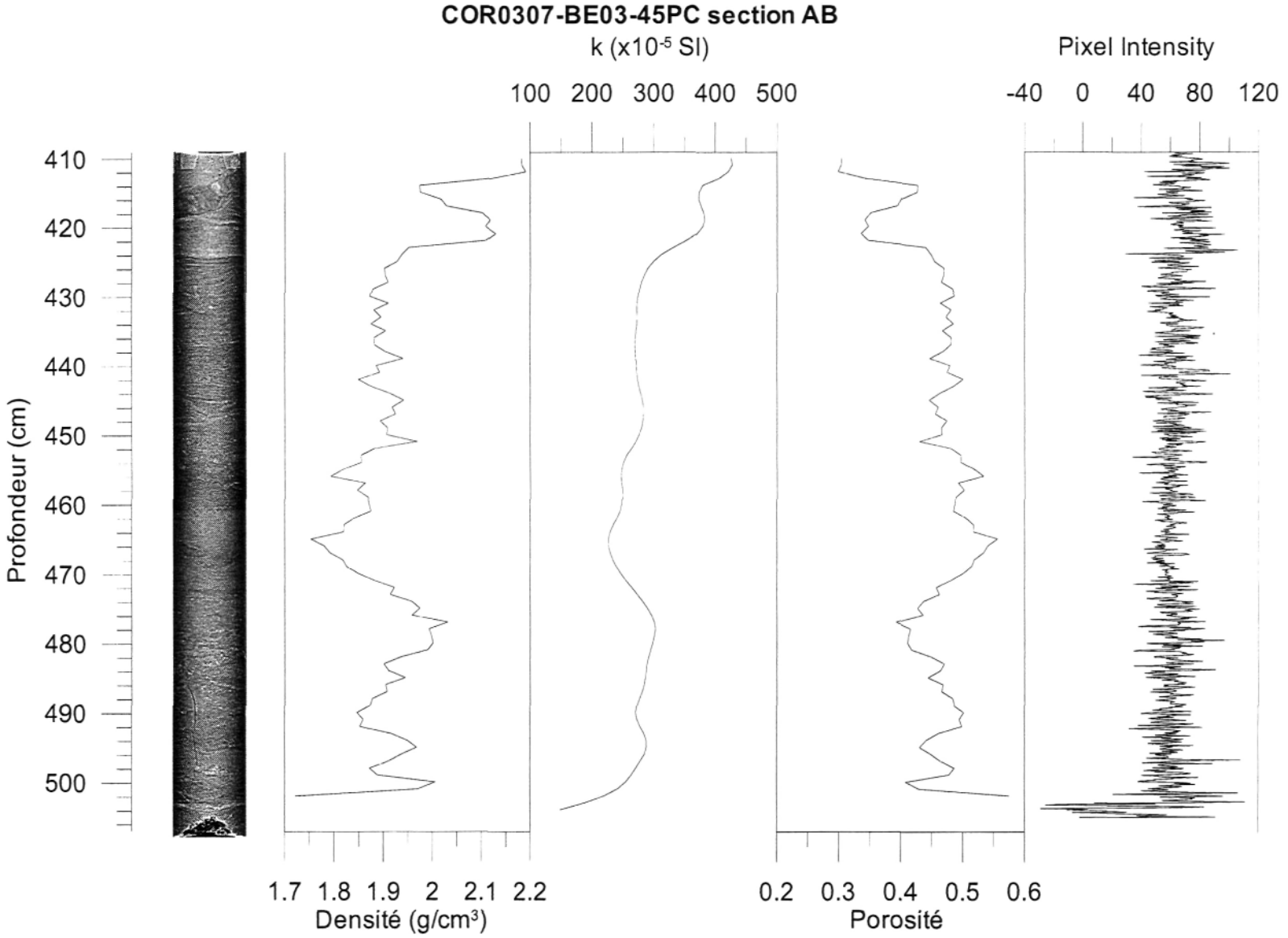
COR0307-BE03-45PC section AB
k (x10-5 SI)
100 200 300 400 500
Pixel Intensity
-40 0 40 80 120
Profondeur (cm)
410
420
430
440
450
460
470
480
490
500
1.7 1.8 1.9 2 2.1 2.2
Densité (g/cm3)
0.2 0.3 0.4 0.5 0.6
Porosité

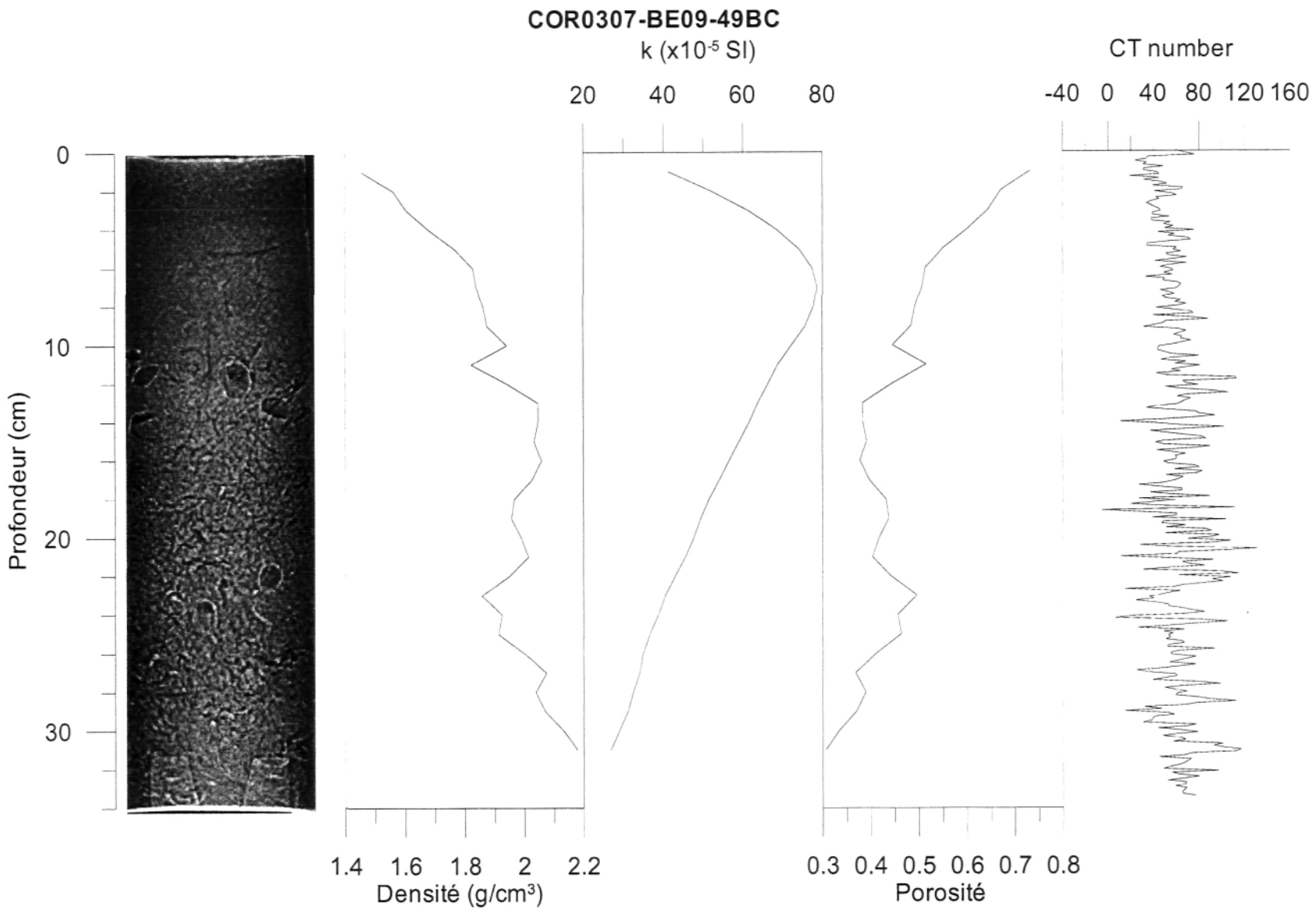
COR0307-BE09-49BC
k (x10-5 SI)
20 40 60 80
CT number
-40 0 40 80 120 160
0
10
20
30
Profondeur (cm)
1.4 1.6 1.8 2 2.2
Densité (g/cm3)
0.3 0.4 0.5 0.6 0.7 0.8
Porosité

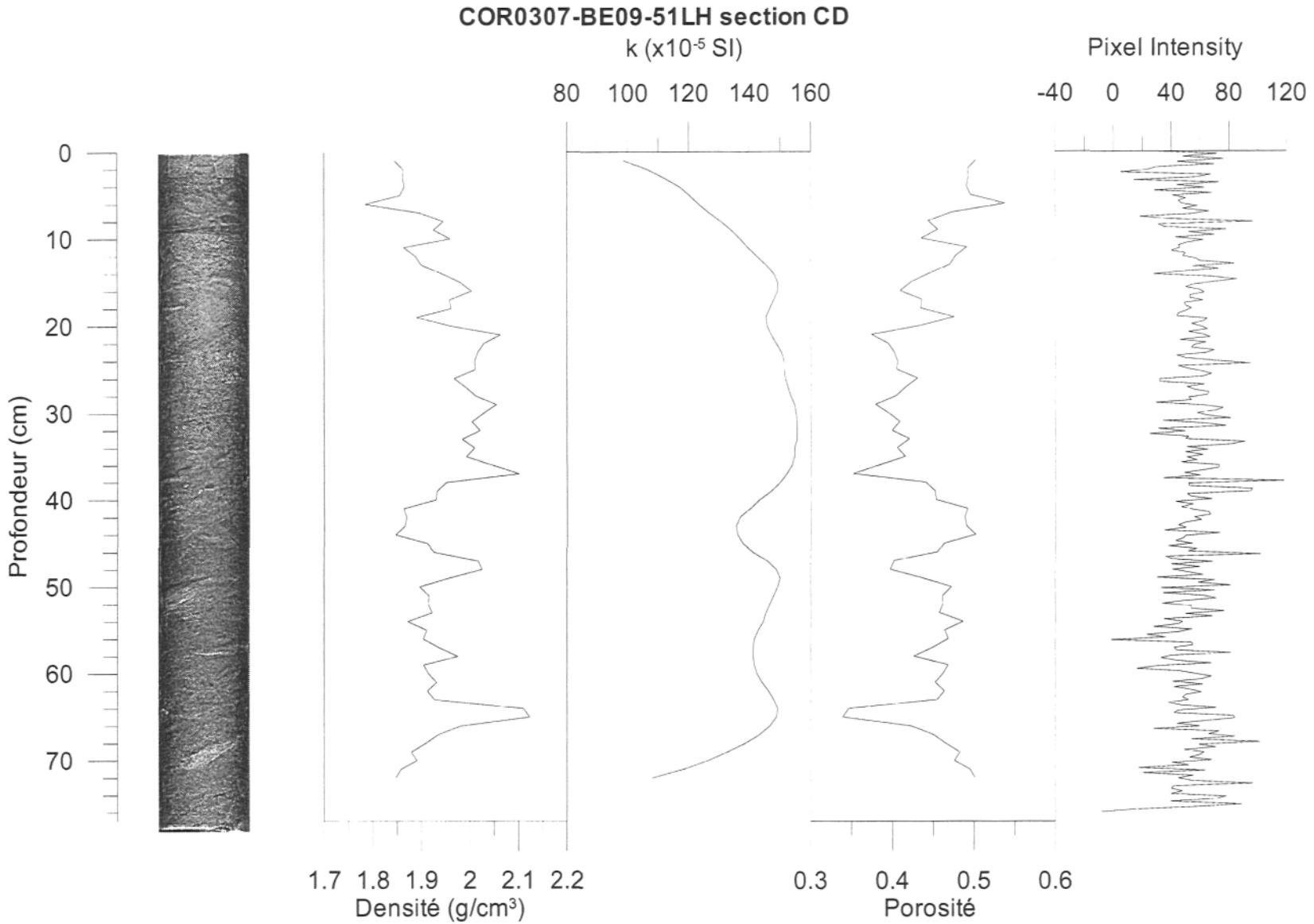
COR0307-BE09-51LH section CD
k (x10-5 SI)
80 100 120 140 160
Pixel Intensity
-40 0 40 80 120
Profondeur (cm)
0 10 20 30 40 50 60 70
1.7 1.8 1.9 2 2.1 2.2
Densité (g/cm3)
0.3 0.4 0.5 0.6
Porosité

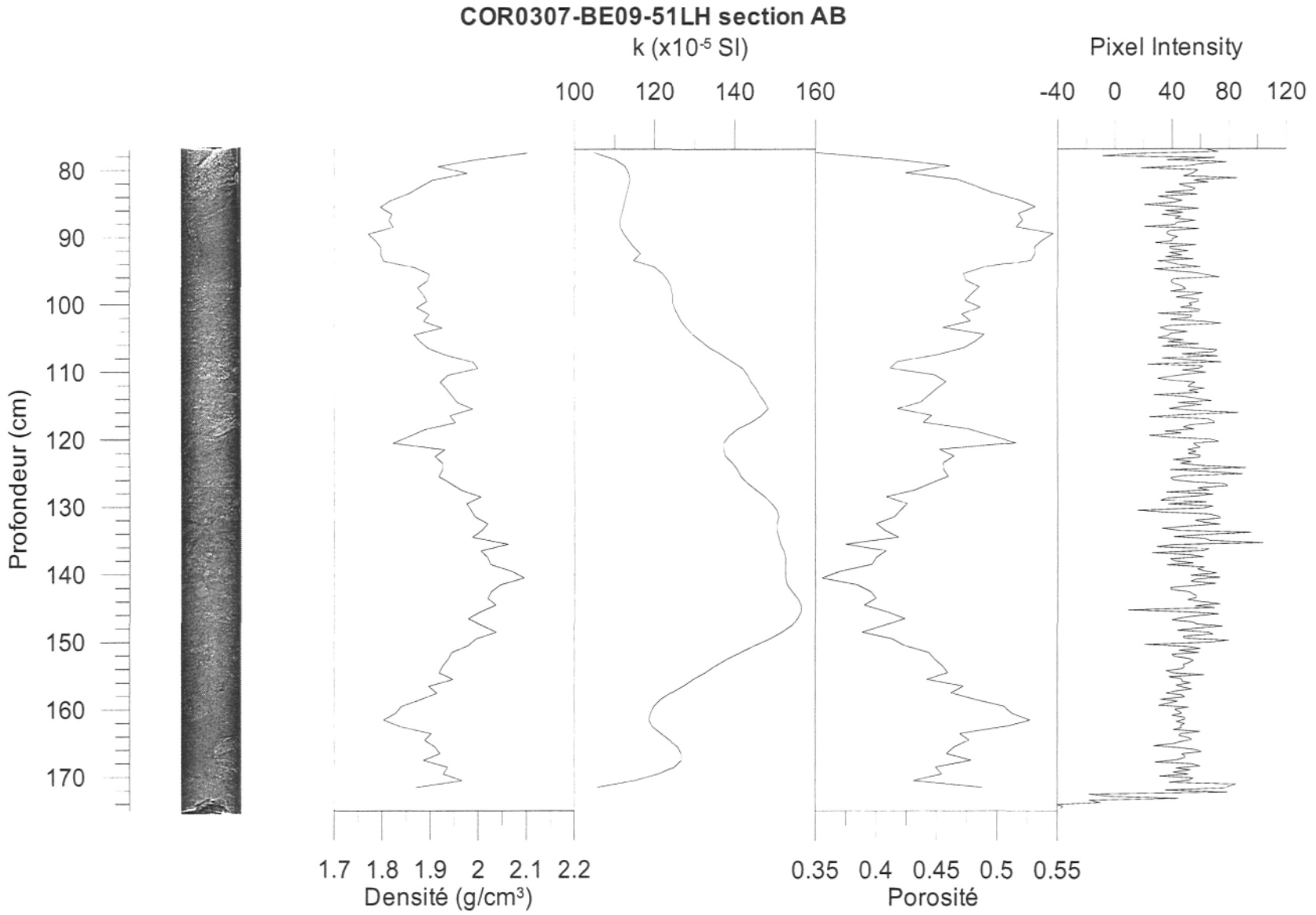
COR0307-BE09-51LH section AB
k (x10-5 SI)
100 120 140 160
Pixel Intensity
-40 0 40 80 120
Profondeur (cm)
80 90 100 110 120 130 140 150 160 170
1.7 1.8 1.9 2 2.1 2.2
Densité (g/cm3)
0.35 0.4 0.45 0.5 0.55
Porosité

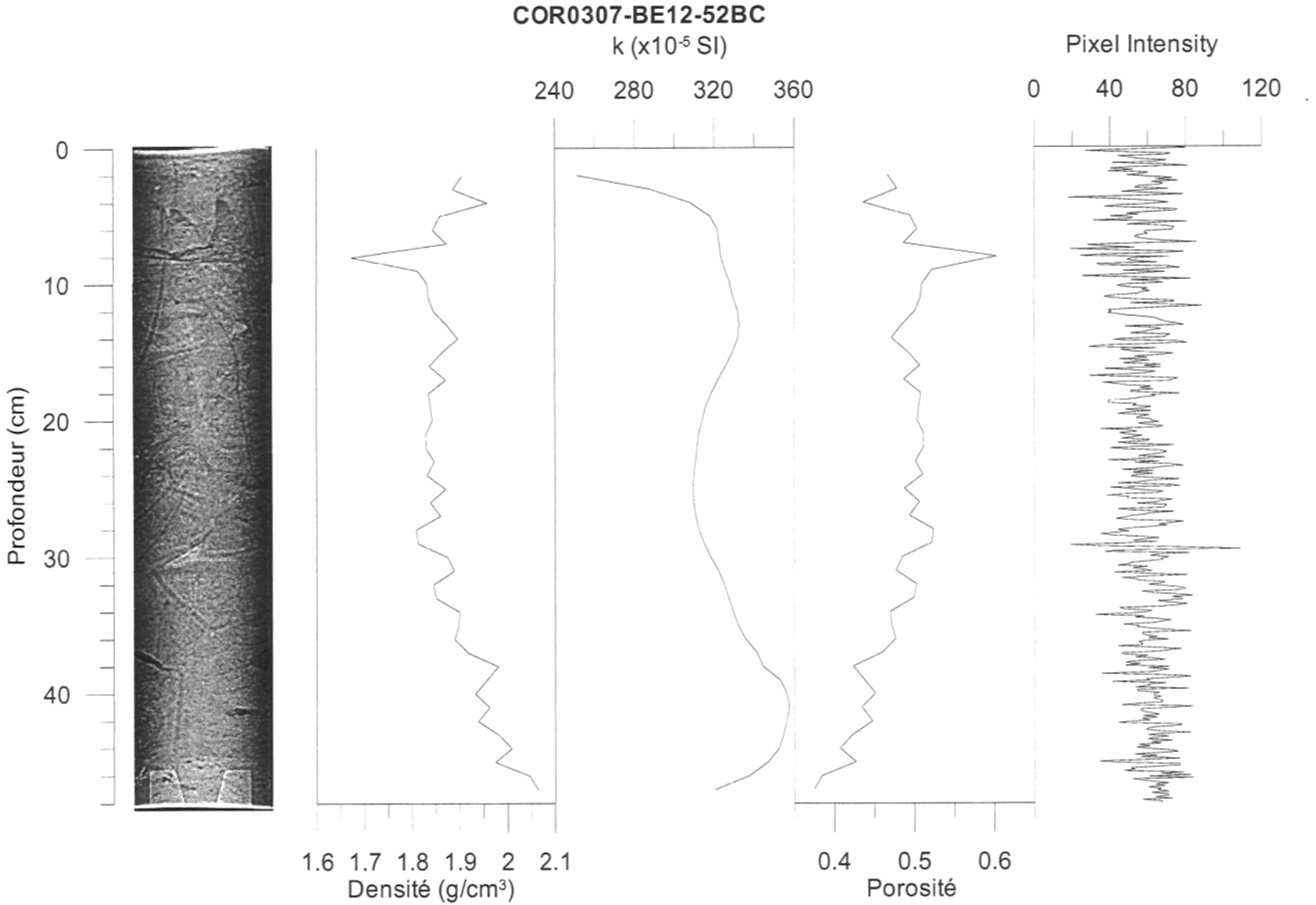
COR0307-BE12-52BC
k (x10-5 SI)
240 280 320 360
Pixel Intensity
0 40 80 120
Profondeur (cm)
0
10
20
30
40
1.6 1.7 1.8 1.9 2 2.1
Densité (g/cm3)
0.4 0.5 0.6
Porosité

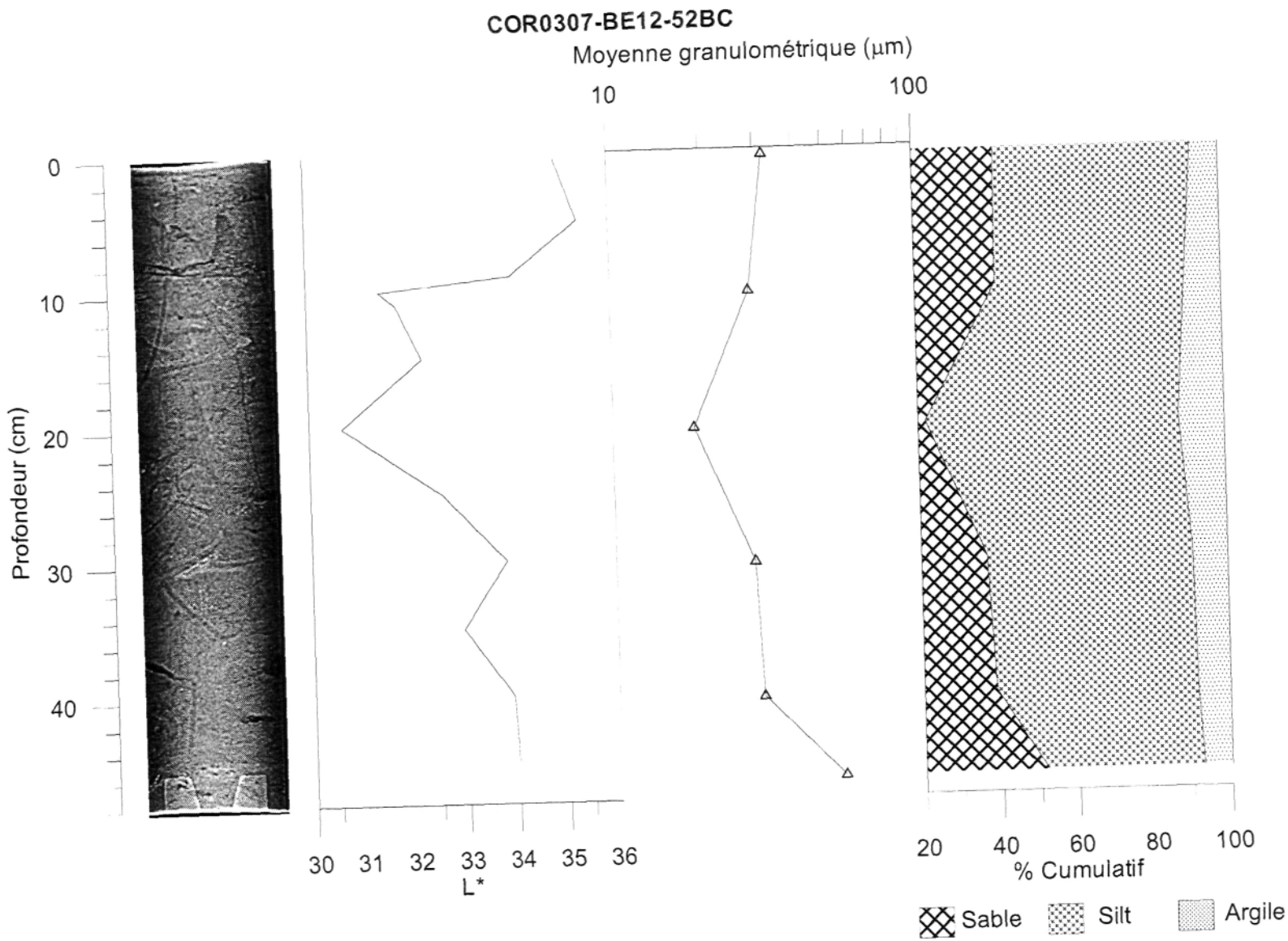
COR0307-BE12-52BC
Moyenne granulométrique (µm)
10
100
0
10
20
30
40
Profondeur (cm)
30
31
32
33
34
35
36
L*
20
40
60
80
100
% Cumulatif
Sable
Silt
Argile

COR0307-BE12-52BC

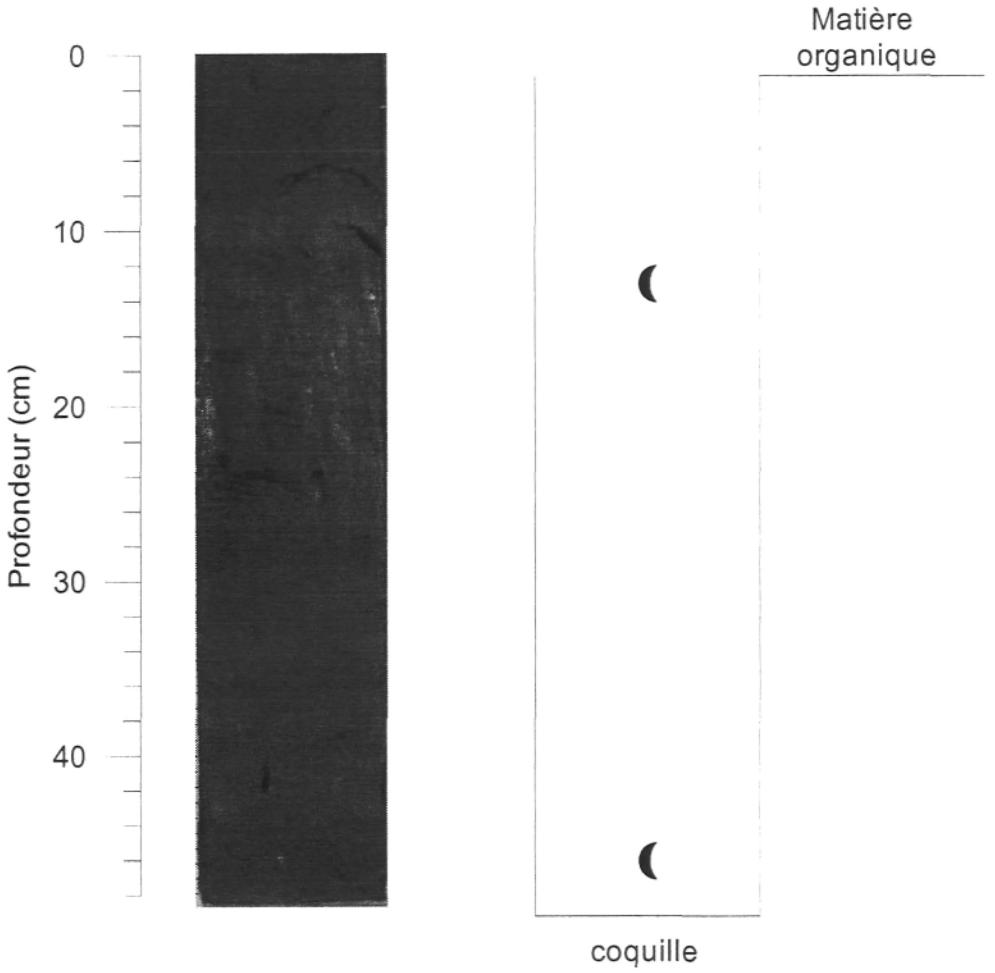

Date: 11/24/2005
Observatrice: GCV
Échantillon: COR0307-BE12-52BC
Section: AB
Longueur: 48 cm
Profondeur: 0-48 cm

Intervalle	Structure	Granulo	Description
0-9		Si A	Silt argileux bioturbé mais sans mouchetures noires, tubes de ver présent, aspect homogène
	13		Très beau gastérode intact, environ 1.5 cm
20-22		A Si	Pochette d'argile silteuse, sur le côté gauche de la carotte
46-47		Sa	Lit de sable avec fragment de coquille
	46		Fragment de coquille, environ 1 cm

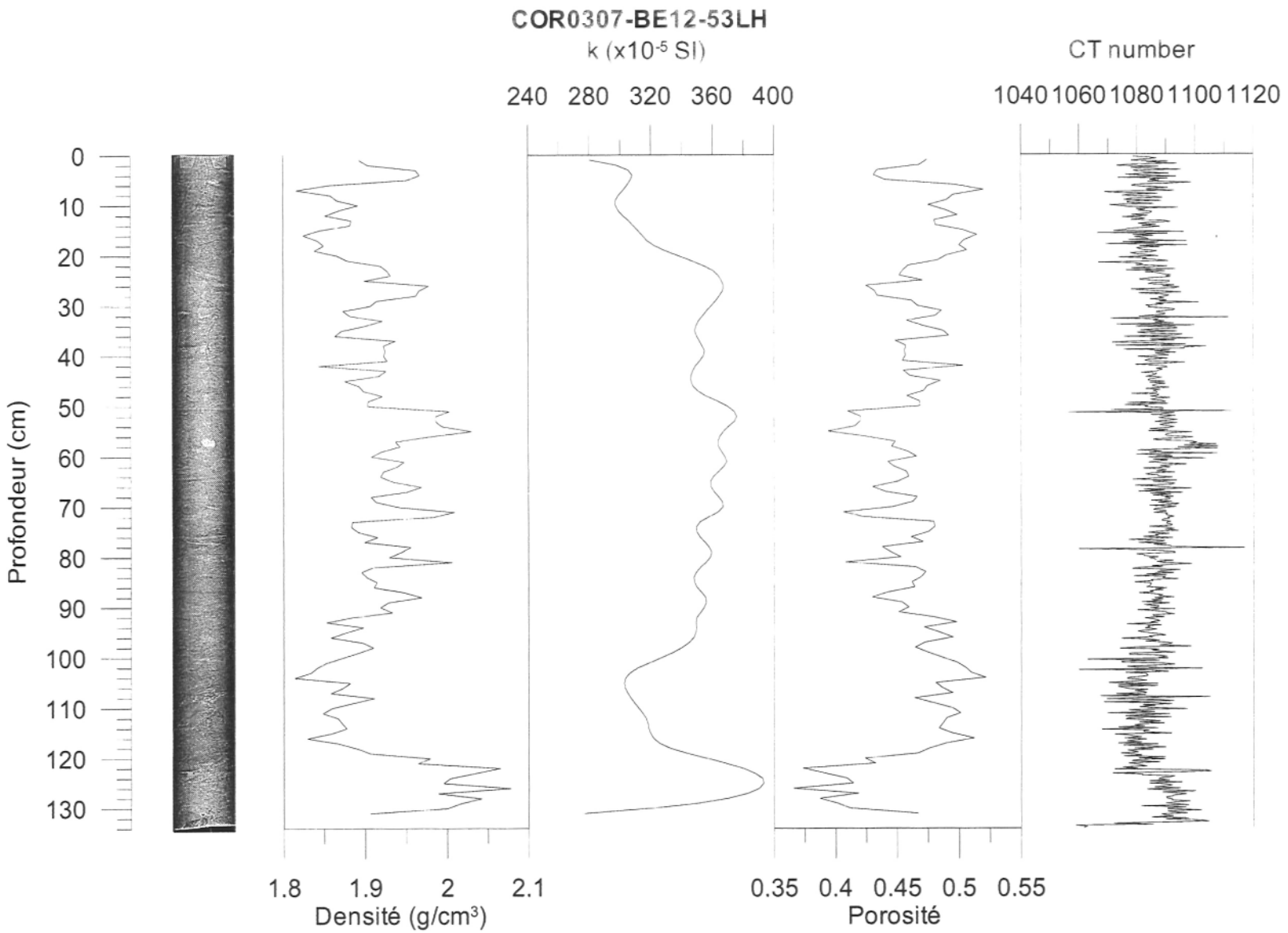
COR0307-BE12-53LH
k (x10-5 SI)
240 280 320 360 400
CT number
1040 1060 1080 1100 1120
Profondeur (cm)
0 10 20 30 40 50 60 70 80 90 100 110 120 130
1.8 1.9 2 2.1
Densité (g/cm3)
0.35 0.4 0.45 0.5 0.55
Porosité

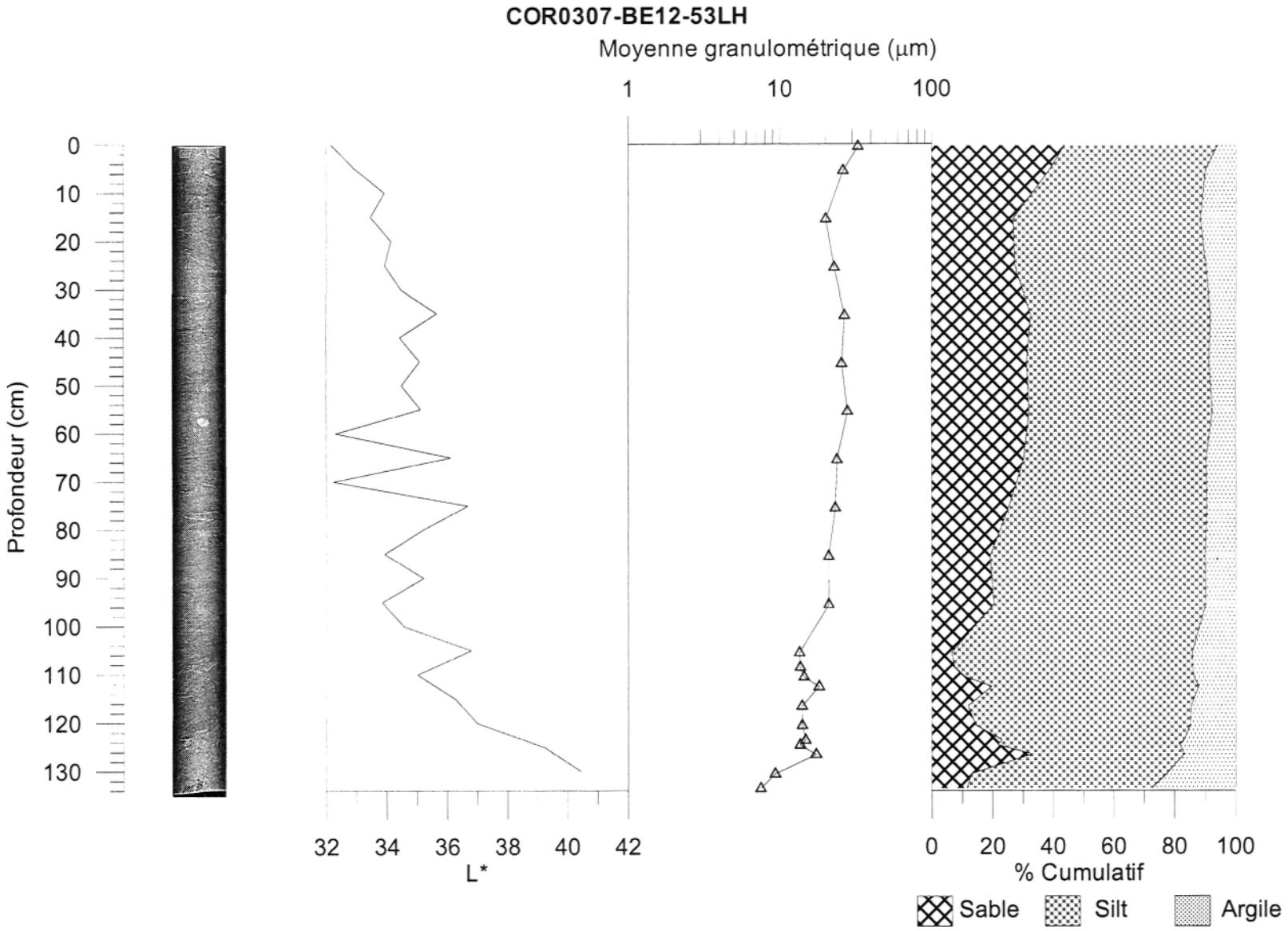
COR0307-BE12-53LH
Moyenne granulométrique (µm)
1
10
100
Profondeur (cm)
0
10
20
30
40
50
60
70
80
90
100
110
120
130
32
34
36
38
40
42
L*
0
20
40
60
80
100
% Cumulatif
Sable
Silt
Argile

COR0307-BE12-53LH

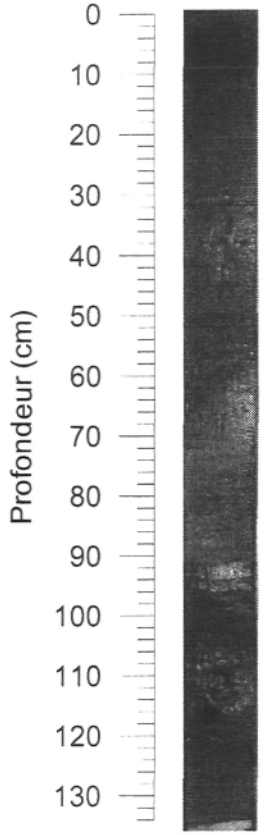

Date: 11/24/2005
Observateurs: GCV - G.St-Onge
Échantillon: COR0307-BE12-53LH
Section: AB
Longueur: 134 cm
Profondeur: 0-134 cm

Intervalle	Structure	Granulo	Description
0-106		Si A	Silt argileux avec minéraux noirs, présence de tube de ver et de bioturbation, légère laminations noires, augmentation du nombre de tubes de ver vers le haut entre 0 et 39 cm, beaucoup de mouchetures de bioturbations entre 39 et 106 cm, plusieurs petites lentilles de avec plus de silt, visible sur le cat-scan
106-122		A Si	Possiblement une coulée, contact assez net, argile silteuse
	108		Petit amas de sable et de petit gravier
	113		Gros morceau de bois (écorce??) environ 2 x 8 cm
	118		morceau de bois, 1 x 4 cm
122-134		MS	Muddy sand, uniforme et homogène, sans structures apparentes
	133	A	Petite pochette d'argile en bas à gauche de la carotte, avec contact franc sur le MS, visible sur le CAT-SCAN

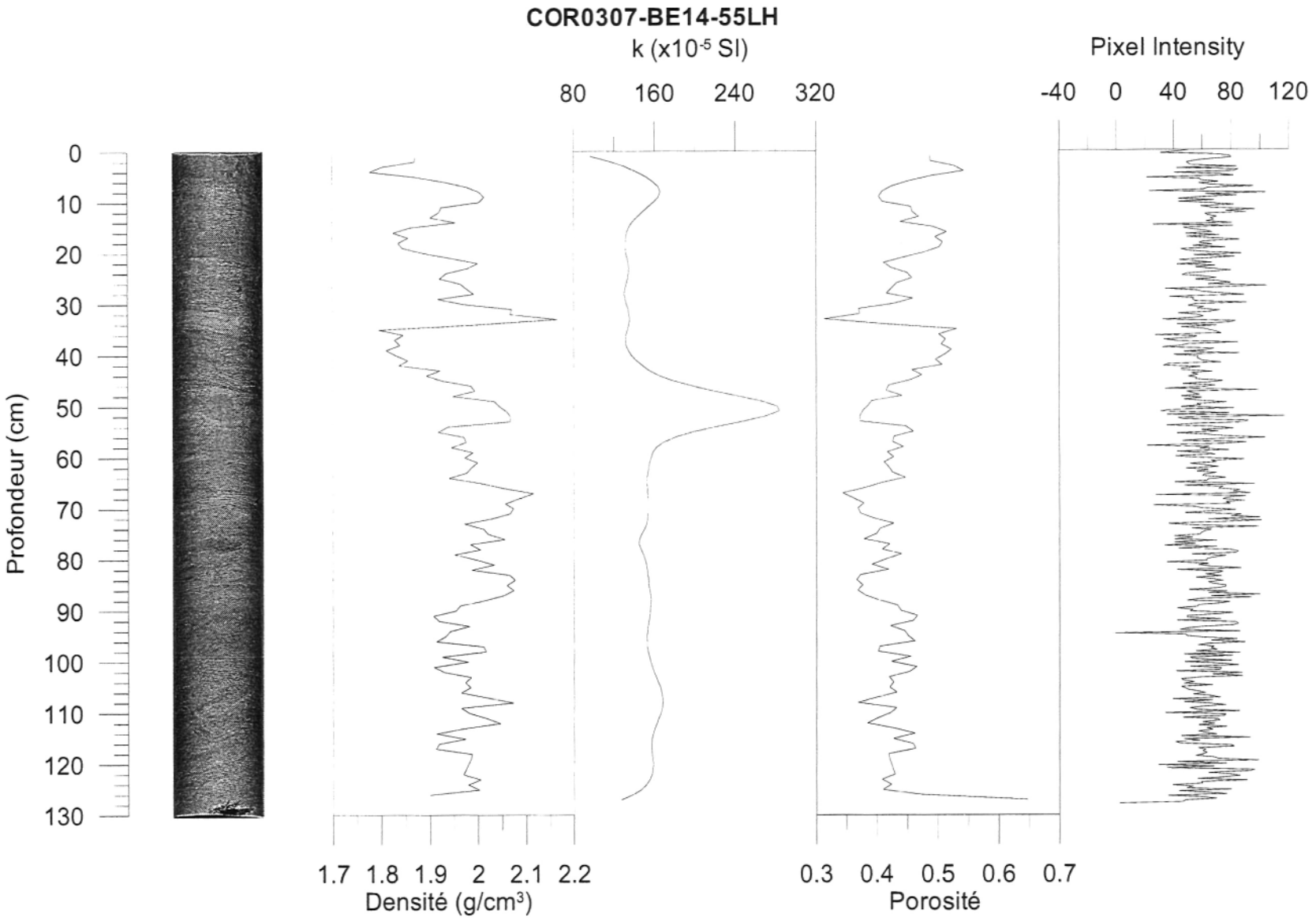
COR0307-BE14-55LH
k (x10-5 SI)
80 160 240 320
Pixel Intensity
-40 0 40 80 120
Profondeur (cm)
0 10 20 30 40 50 60 70 80 90 100 110 120 130
1.7 1.8 1.9 2 2.1 2.2
Densité (g/cm3)
0.3 0.4 0.5 0.6 0.7
Porosité

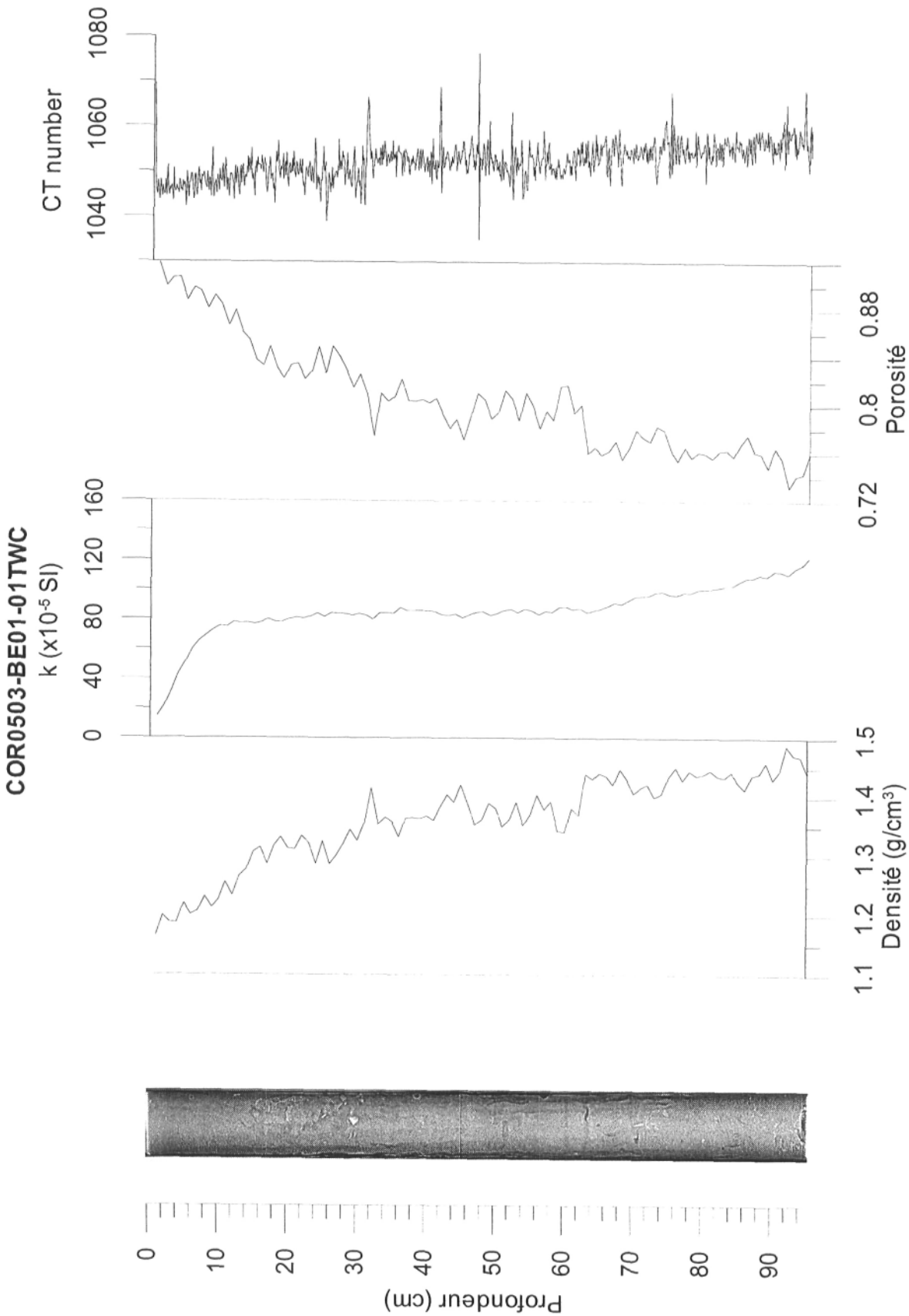
COR0503-BE01-01TWC
CT number
1040
1060
1080
k (x10-5 SI)
0
40
80
120
160
0.72
0.8
0.88
Porosité
1.1
1.2
1.3
1.4
1.5
Densité (g/cm3)
Profondeur (cm)
0
10
20
30
40
50
60
70
80
90

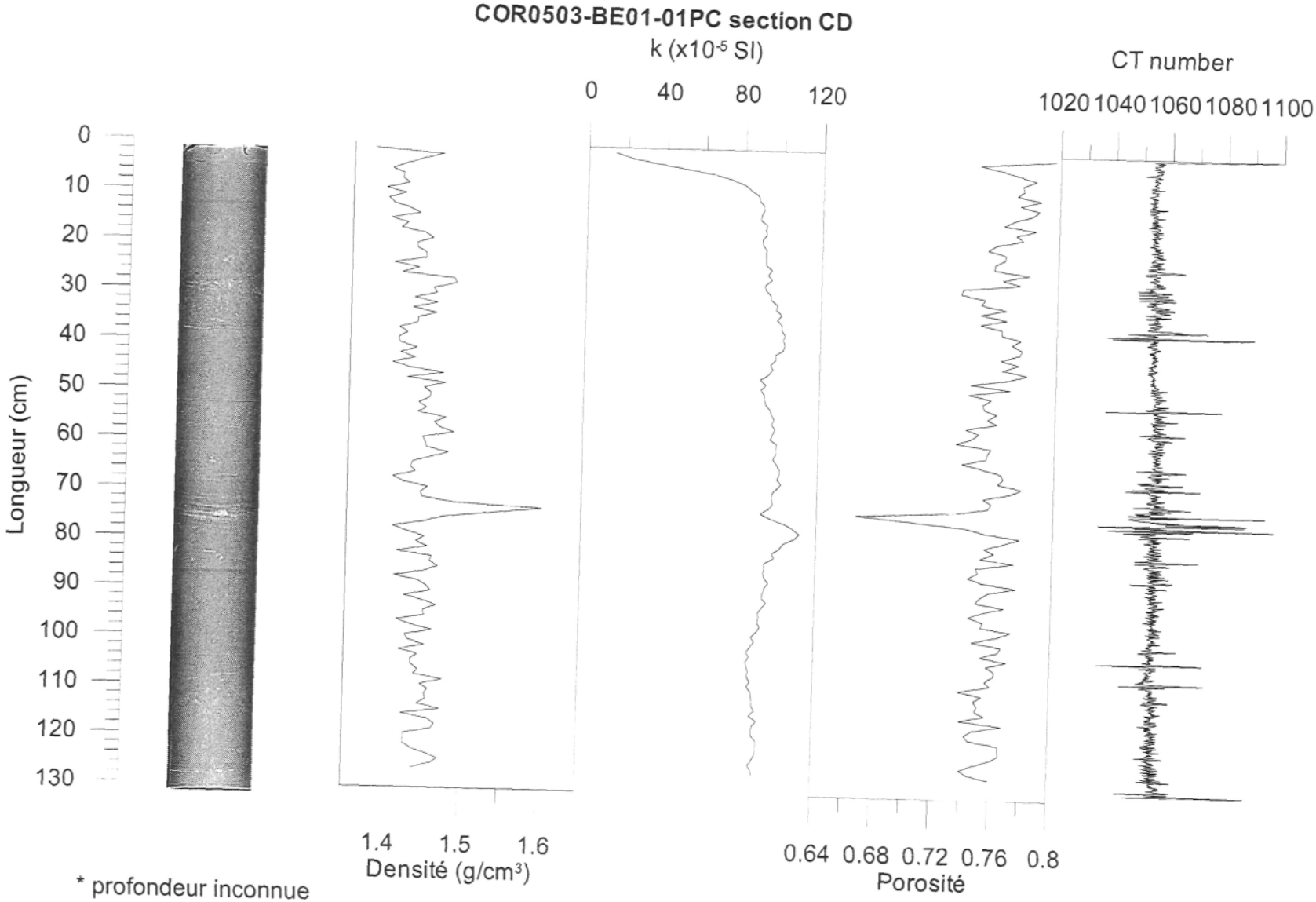
COR0503-BE01-01PC section CD
k (x10-5 SI)
0 40 80 120
CT number
1020 1040 1060 1080 1100
Longueur (cm)
0 10 20 30 40 50 60 70 80 90 100 110 120 130
1.4 1.5 1.6
Densité (g/cm3)
0.64 0.68 0.72 0.76 0.8
Porosité
* profondeur inconnue

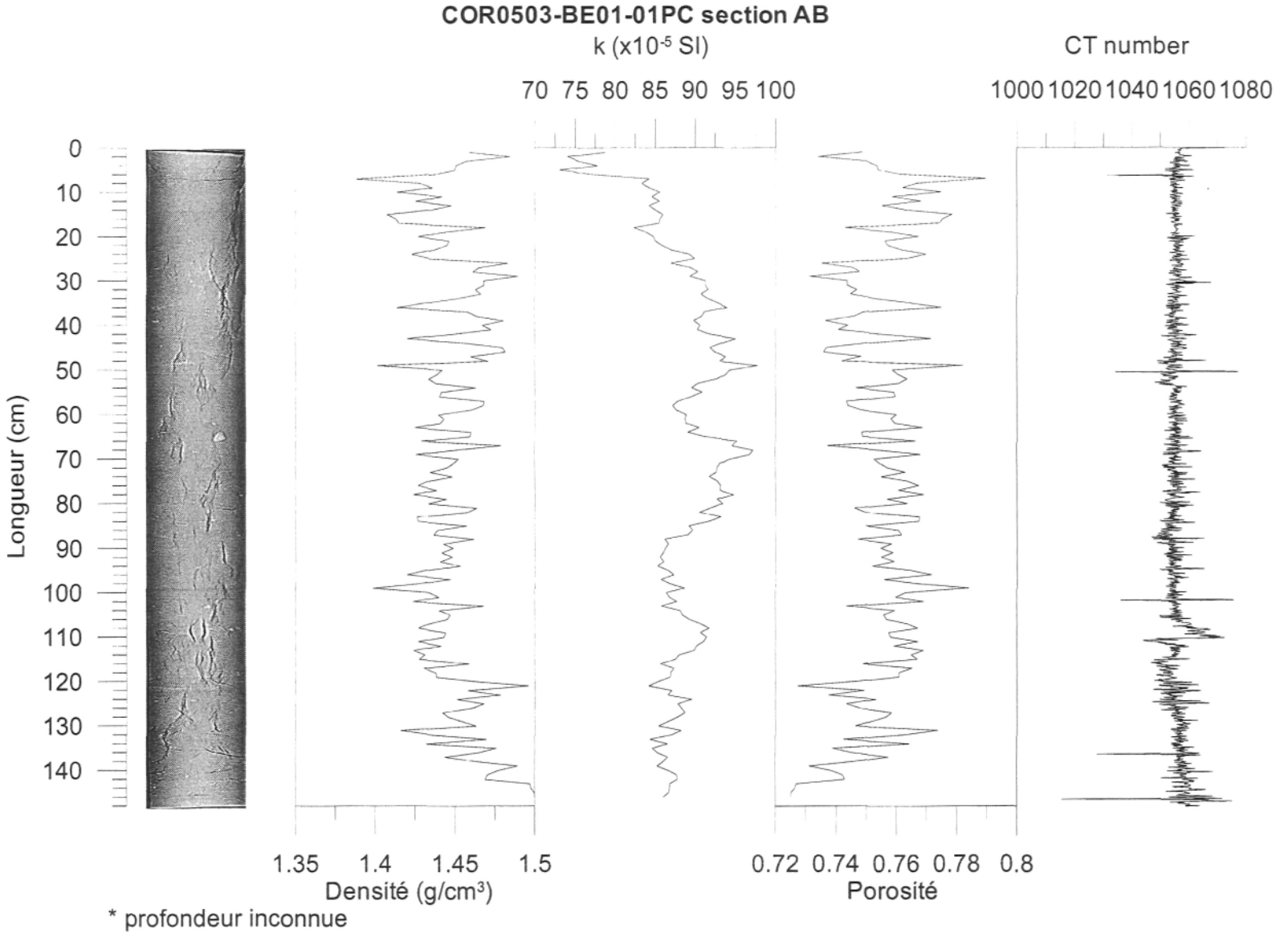
COR0503-BE01-01PC section AB
k (x10-5 SI)
70 75 80 85 90 95 100
CT number
1000 1020 1040 1060 1080
Longueur (cm)
0 10 20 30 40 50 60 70 80 90 100 110 120 130 140
1.35 1.4 1.45 1.5
Densité (g/cm3)
0.72 0.74 0.76 0.78 0.8
Porosité
* profondeur inconnue

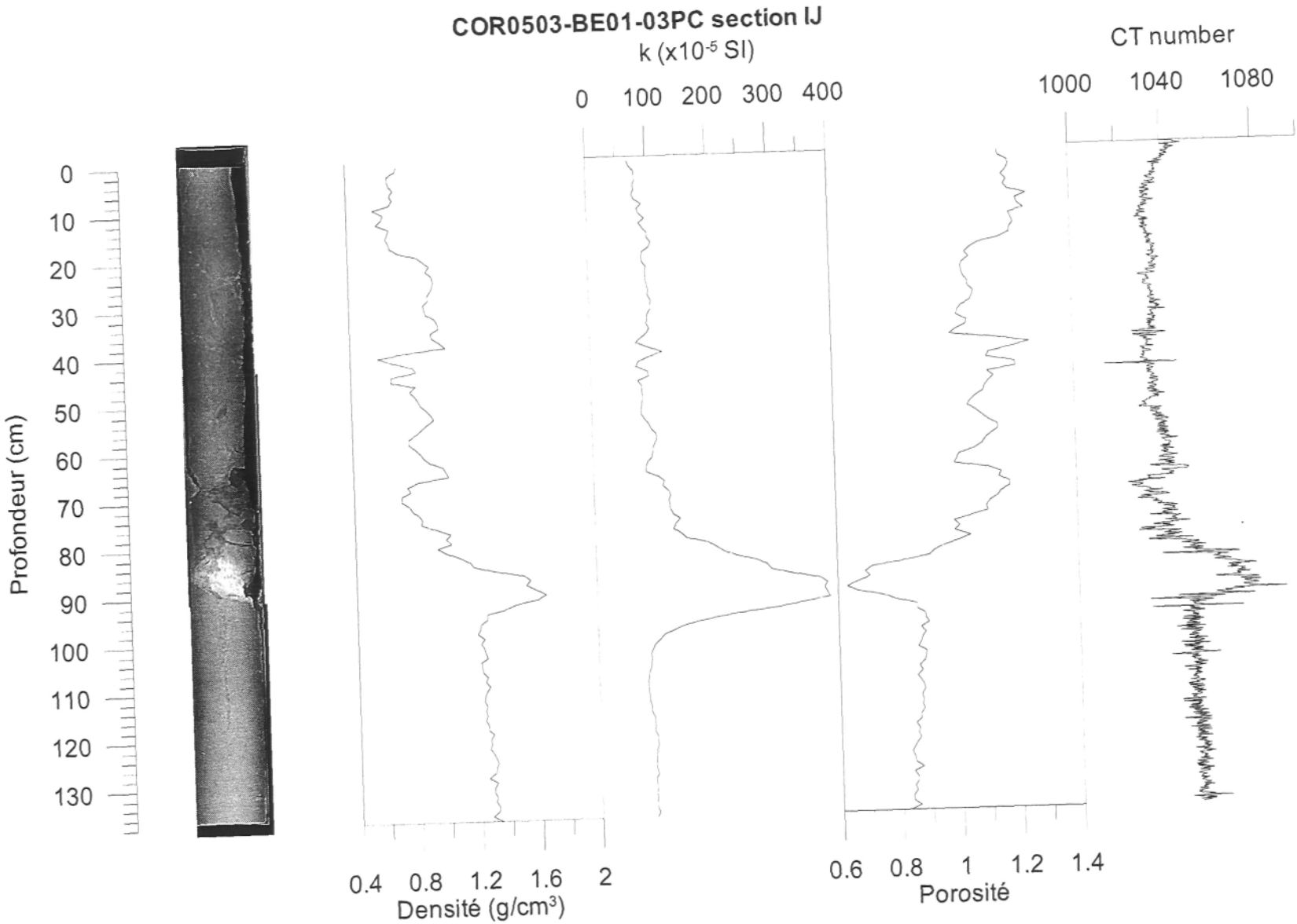
COR0503-BE01-03PC section IJ
k (x10-5 SI)
0 100 200 300 400
CT number
1000 1040 1080
Profondeur (cm)
0 10 20 30 40 50 60 70 80 90 100 110 120 130
0.4 0.8 1.2 1.6 2
Densité (g/cm3)
0.6 0.8 1 1.2 1.4
Porosité

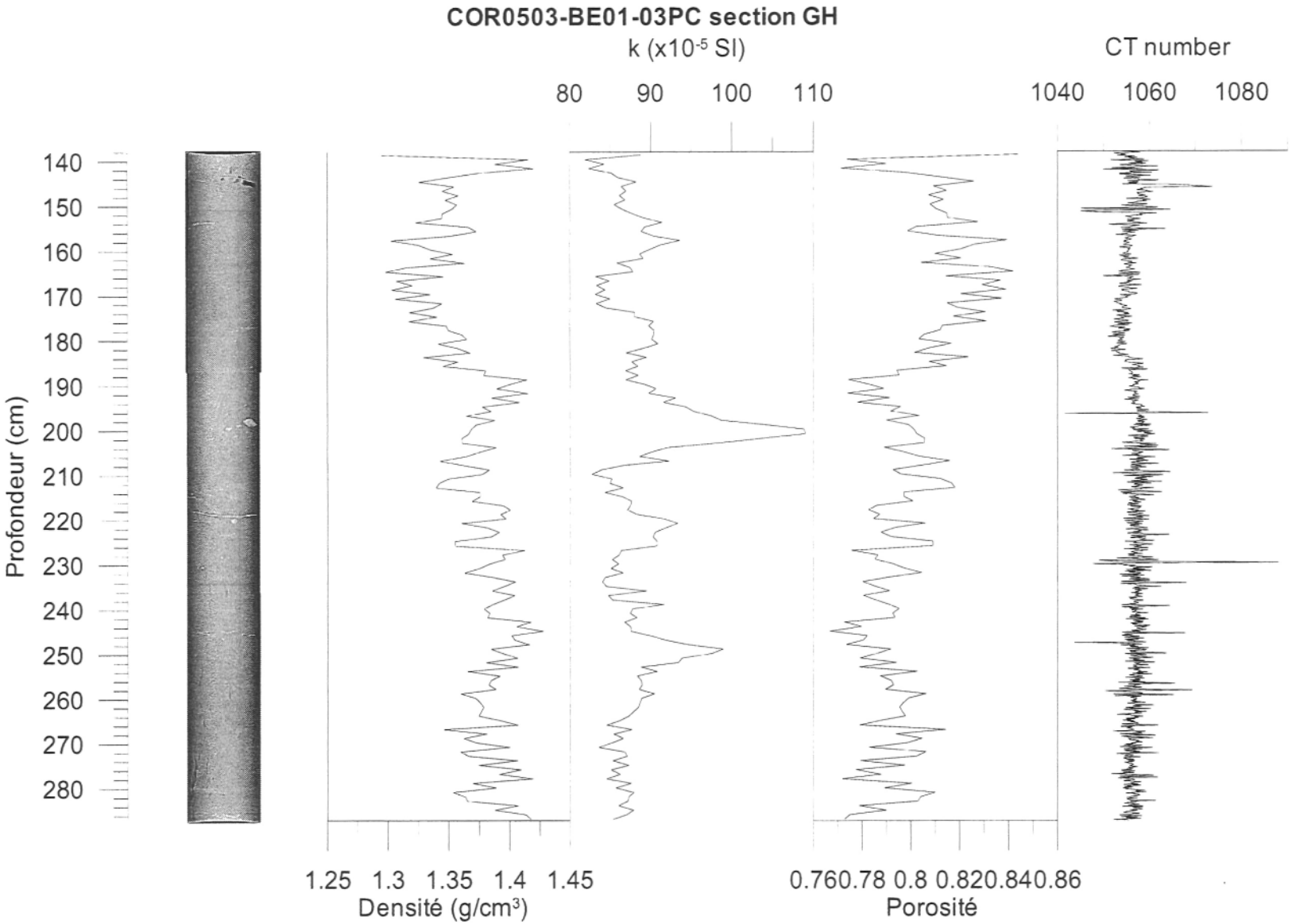
COR0503-BE01-03PC section GH
k (x10-5 SI)
80 90 100 110
CT number
1040 1060 1080
Profondeur (cm)
140 150 160 170 180 190 200 210 220 230 240 250 260 270 280
1.25 1.3 1.35 1.4 1.45
Densité (g/cm3)
0.760.78 0.8 0.820.840.86
Porosité

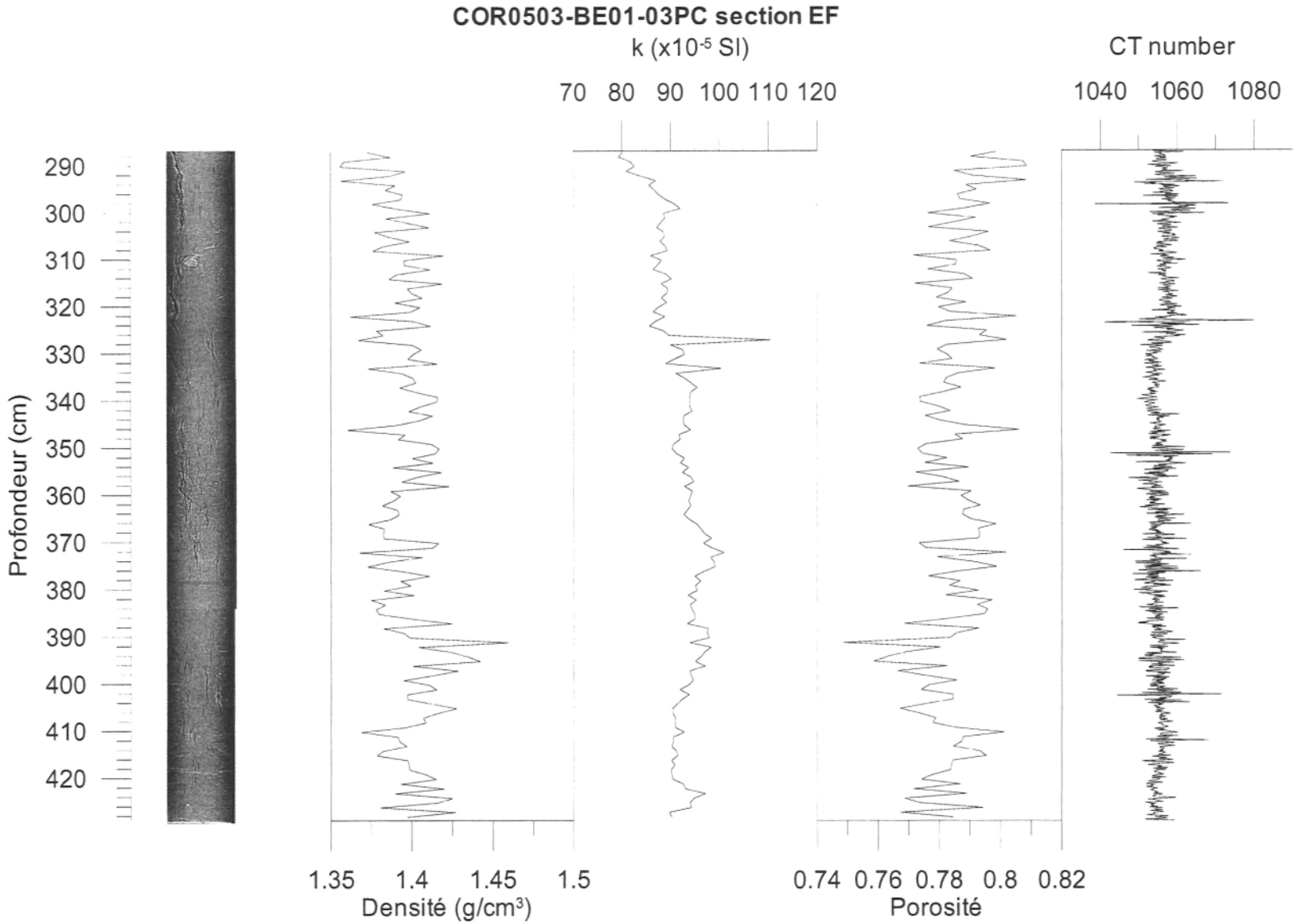
COR0503-BE01-03PC section EF
k (x10-5 SI)
70 80 90 100 110 120
CT number
1040 1060 1080
Profondeur (cm)
290
300
310
320
330
340
350
360
370
380
390
400
410
420
1.35 1.4 1.45 1.5
Densité (g/cm3)
0.74 0.76 0.78 0.8 0.82
Porosité

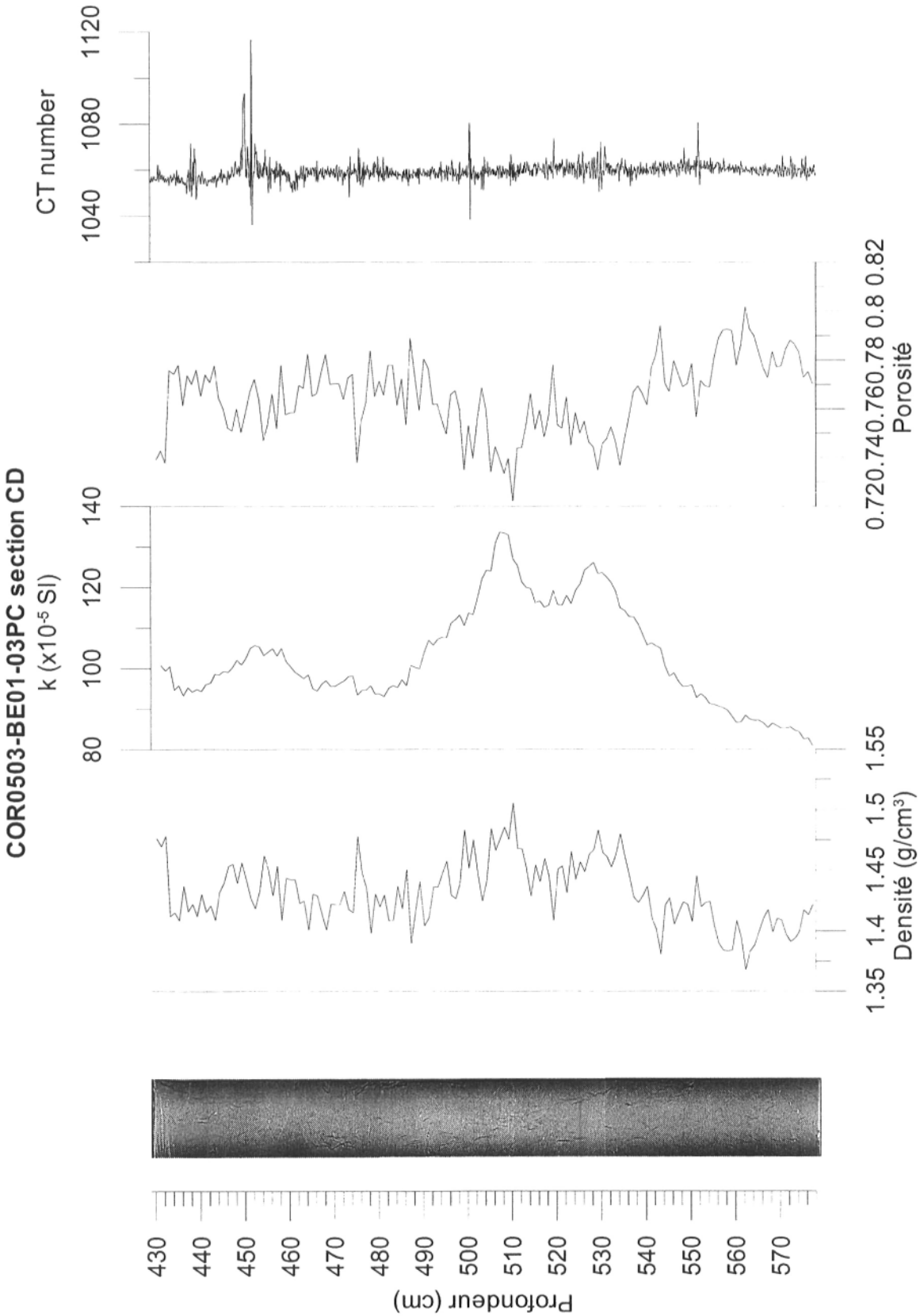
COR0503-BE01-03PC section CD
CT number
1040 1080 1120
k (x10-5 SI)
80 100 120 140
0.72 0.74 0.76 0.78 0.8 0.82
Porosité
1.35 1.4 1.45 1.5 1.55
Densité (g/cm3)
Profondeur (cm)
430 440 450 460 470 480 490 500 510 520 530 540 550 560 570

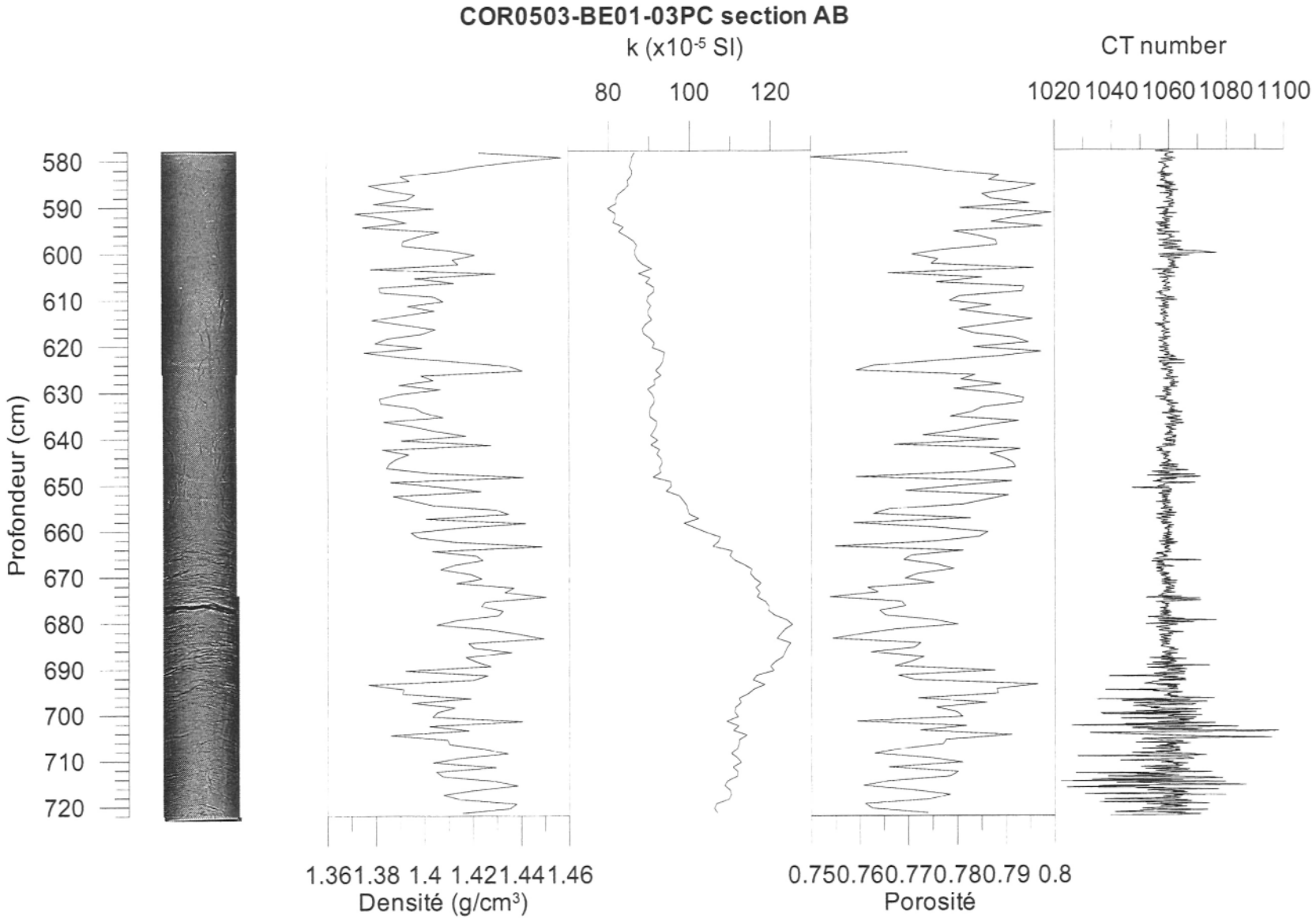
COR0503-BE01-03PC section AB
k (x10-5 SI)
80 100 120
CT number
1020 1040 1060 1080 1100
Profondeur (cm)
580
590
600
610
620
630
640
650
660
670
680
690
700
710
720
1.36 1.38 1.4 1.42 1.44 1.46
Densité (g/cm3)
0.75 0.76 0.77 0.78 0.79 0.8
Porosité

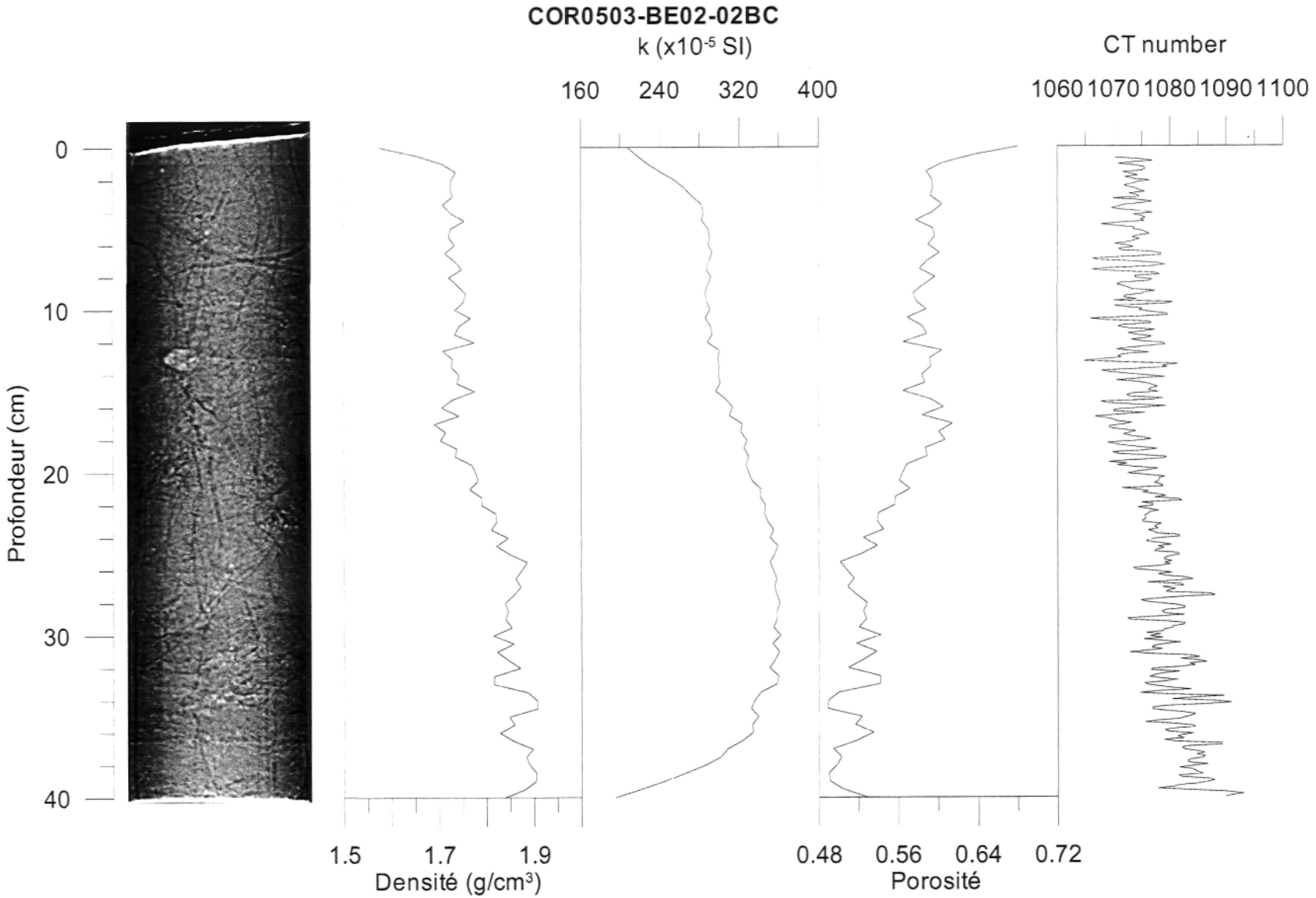
COR0503-BE02-02BC
k (x10-5 SI)
160 240 320 400
CT number
1060 1070 1080 1090 1100
Profondeur (cm)
0
10
20
30
40
1.5 1.7 1.9
Densité (g/cm3)
0.48 0.56 0.64 0.72
Porosité

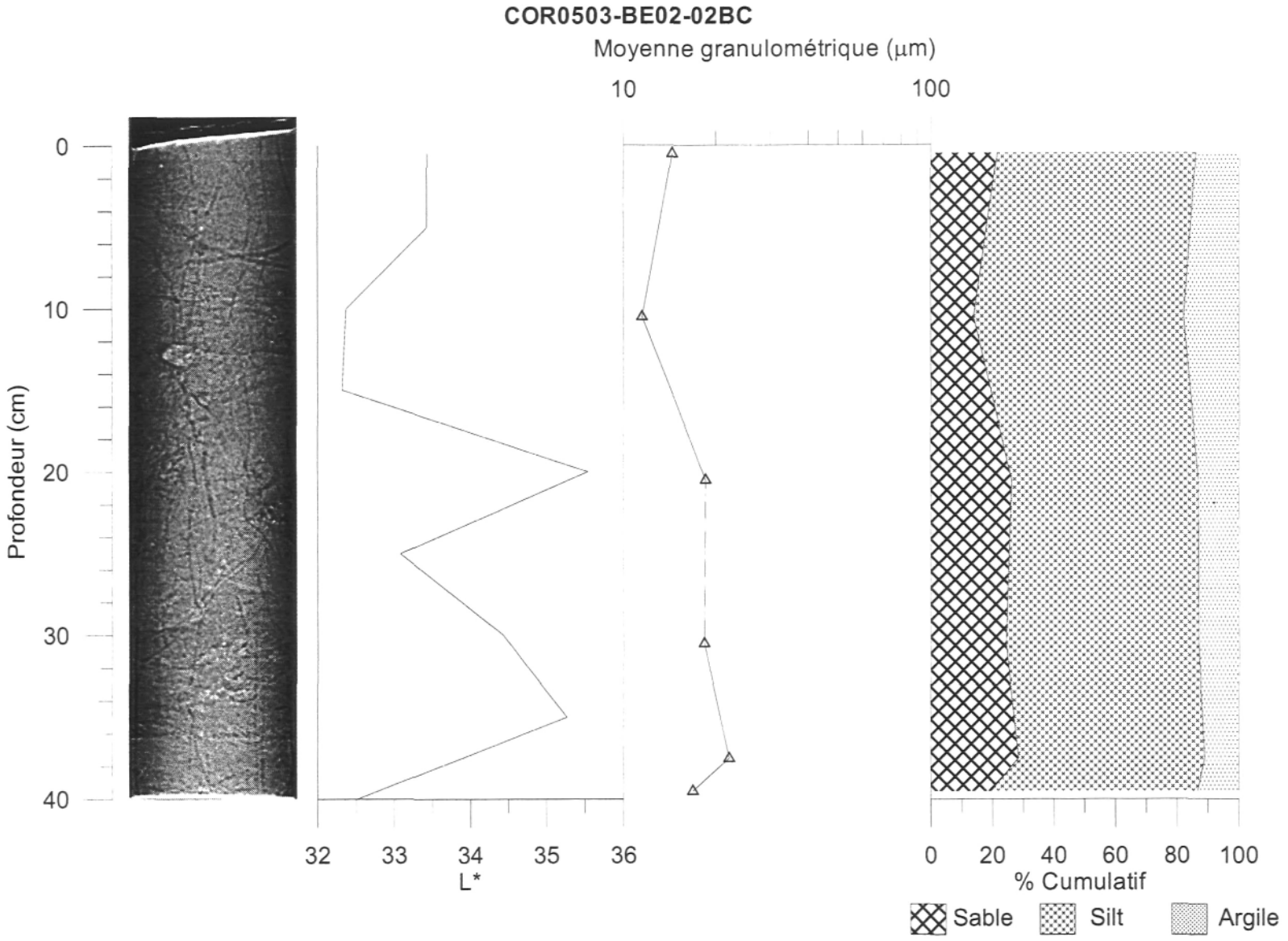
COR0503-BE02-02BC
Moyenne granulométrique (µm)
10
100
0
10
20
30
40
Profondeur (cm)
32
33
34
35
36
L*
0
20
40
60
80
100
% Cumulatif
Sable
Silt
Argile

COR0503-BE02-02BC

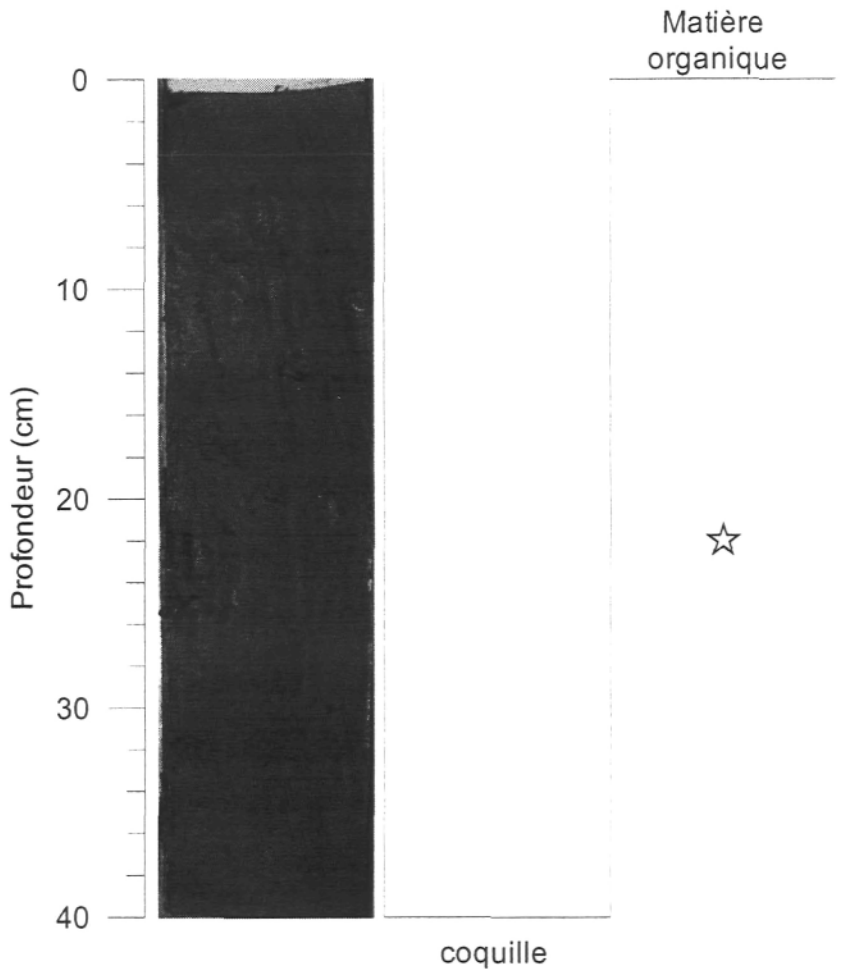

Date: 11/25/2005
Observateurs: GCV - G.St-Onge
Échantillon: COR0503-BE02-BC02
Section: AB
Longueur: 40 cm
Profondeur: 0-40 cm

Intervalle	Structure	Granulo	Description
0-3		Si A	Zone sans présence de bioturbation
3-36		Si A	Zone bioturbée avec plusieurs tubes de ver, petites laminations noires où elles sont en plus grands quantité entre 7 et 17 cm
	22		Petit morceau de bois, environ 1 cm
	36		Lit de sable, visible au cat-scan
36-40			Matériau plus noir avec lamination

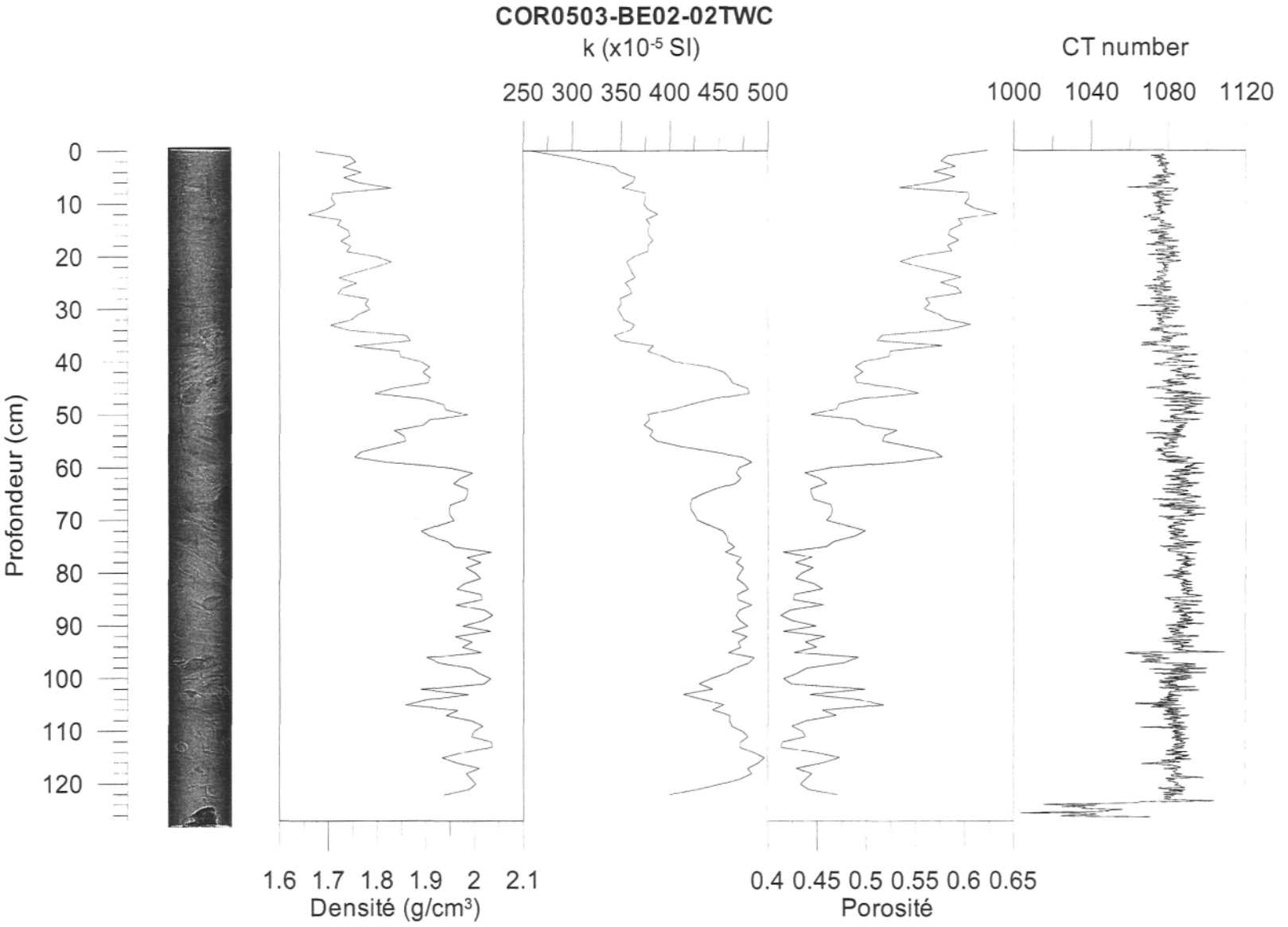
COR0503-BE02-02TWC
k (x10-5 SI)
250 300 350 400 450 500
CT number
1000 1040 1080 1120
Profondeur (cm)
0
10
20
30
40
50
60
70
80
90
100
110
120
1.6 1.7 1.8 1.9 2 2.1
Densité (g/cm3)
0.4 0.45 0.5 0.55 0.6 0.65
Porosité

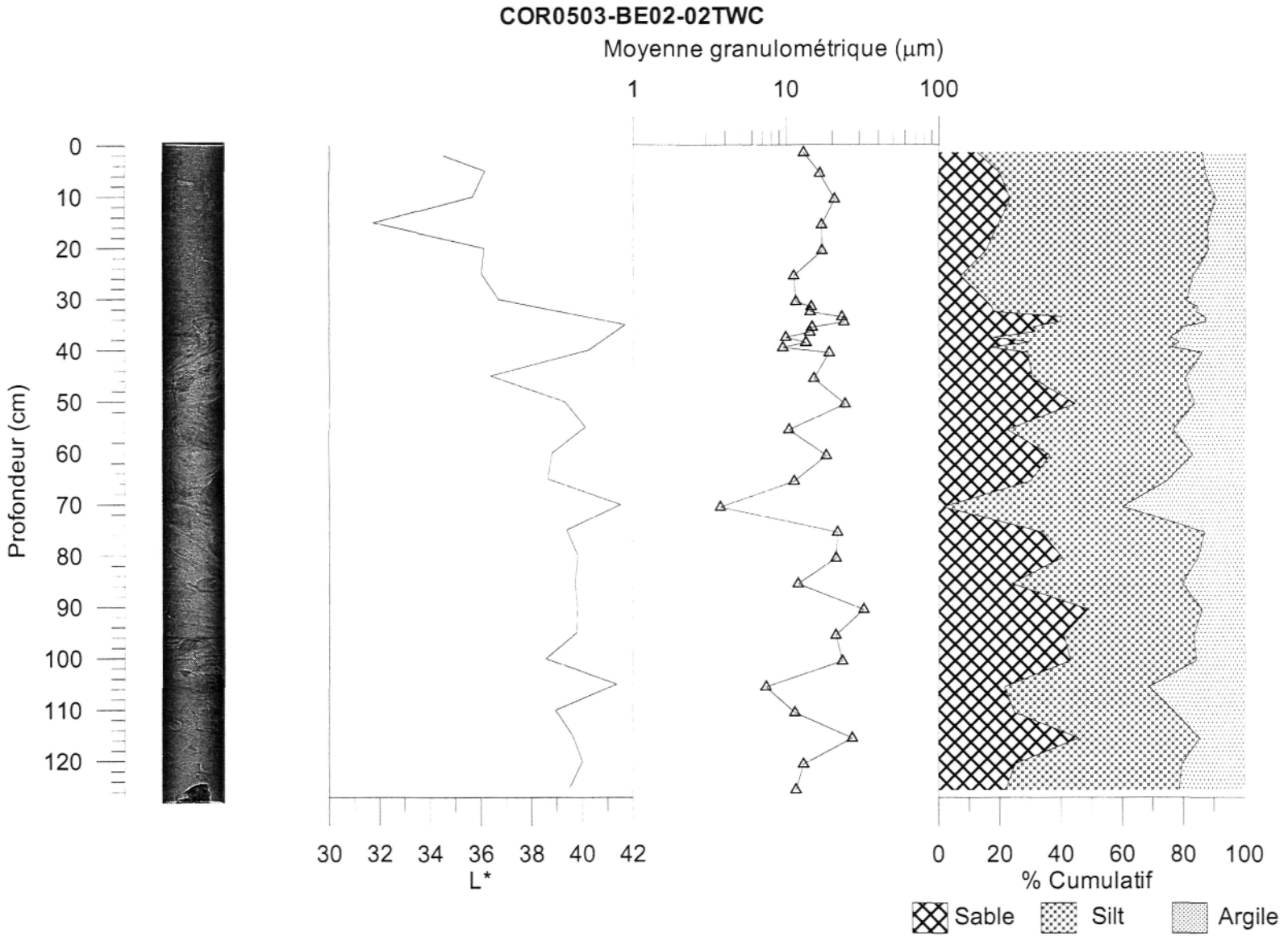
COR0503-BE02-02TWC
Moyenne granulométrique (µm)
1
10
100
Profondeur (cm)
0
10
20
30
40
50
60
70
80
90
100
110
120
30
32
34
36
38
40
42
L*
0
20
40
60
80
100
% Cumulatif
Sable
Silt
Argile

COR0503-BE02-02TWC

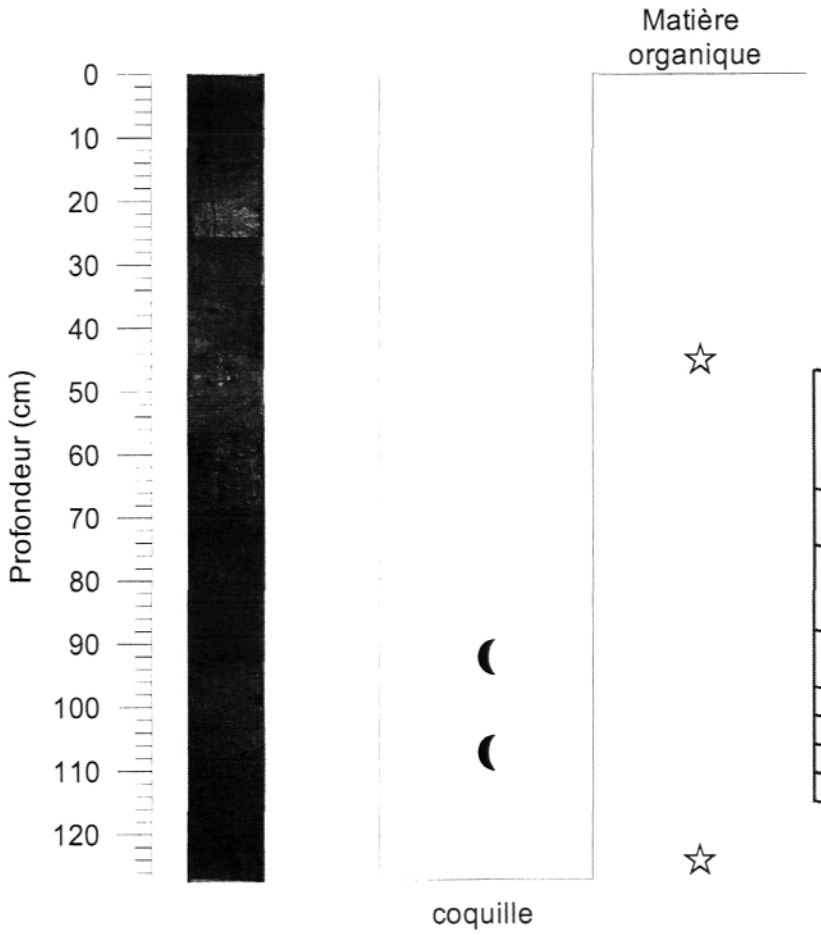

Date: 11/23/2005
Observateurs: GCV - G.St-Onge
Échantillon: COR0503-BE02-02TWC
Section: AB
Longueur: 127 cm
Profondeur: 1-127 cm

Intervalle	Structure	Granulo	Description
0-30		A Si	Argile silteuse bioturbée, avec tubes de ver, traces noires
30-127		Si A	Débris; Matrice: silt argileux présence de minéraux noirs, pas de trace de bioturbation, Galet: argile silteuse, plus homogène.
	45		Morceau de bois défait, ne se tient pas, environ 2 x 2 cm
	92		Bivalve brisée, 1 x 2 cm
	107		Fragment de coquille, 1 cm
	111		Couche d'argile plus agglomérée
	124		Petite racine intacte, 2.5 mm, 2mm diamètre

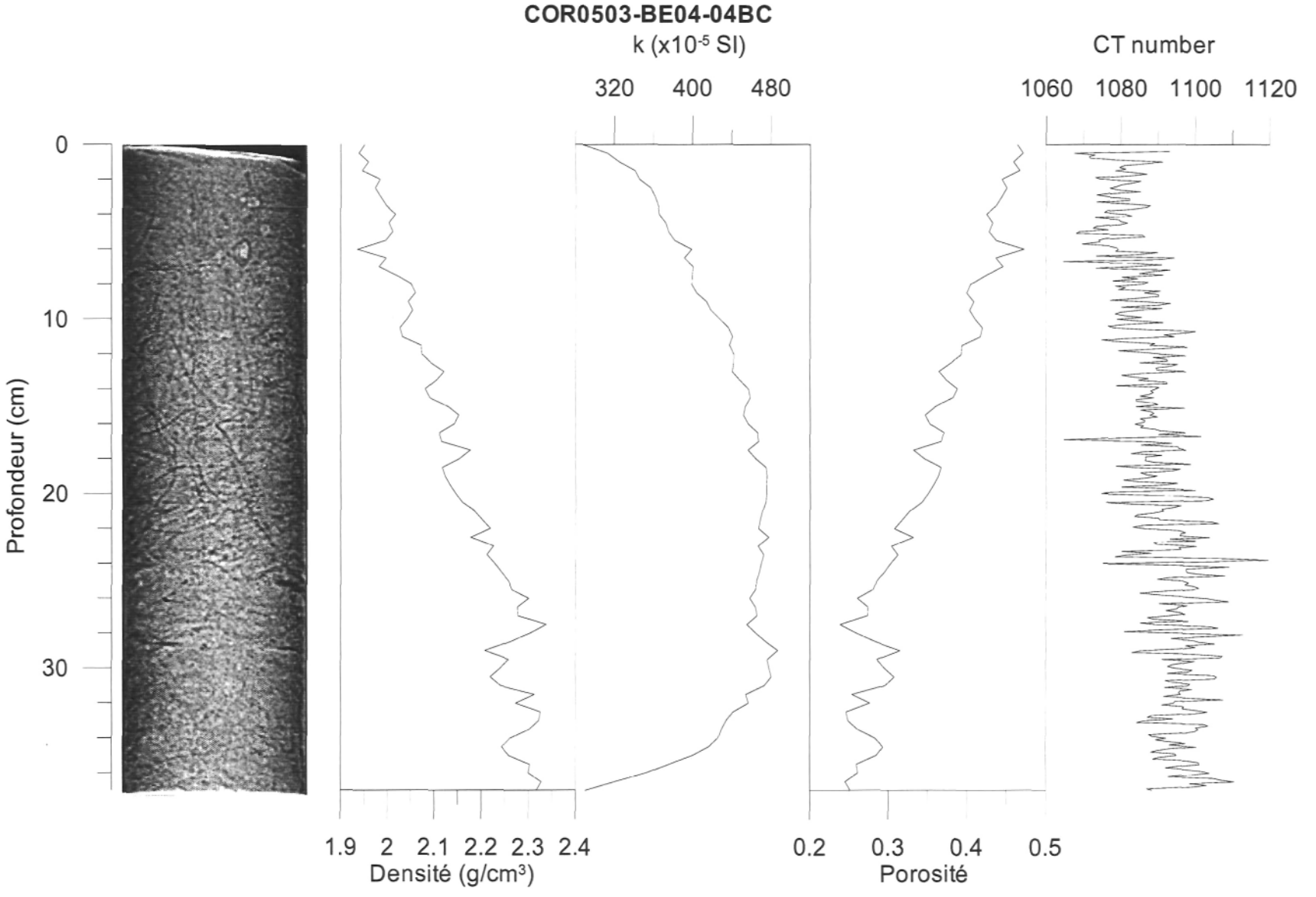
COR0503-BE04-04BC
k (x10-5 SI)
320
400
480
CT number
1060
1080
1100
1120
0
10
20
30
Profondeur (cm)
1.9
2
2.1
2.2
2.3
2.4
Densité (g/cm3)
0.2
0.3
0.4
0.5
Porosité

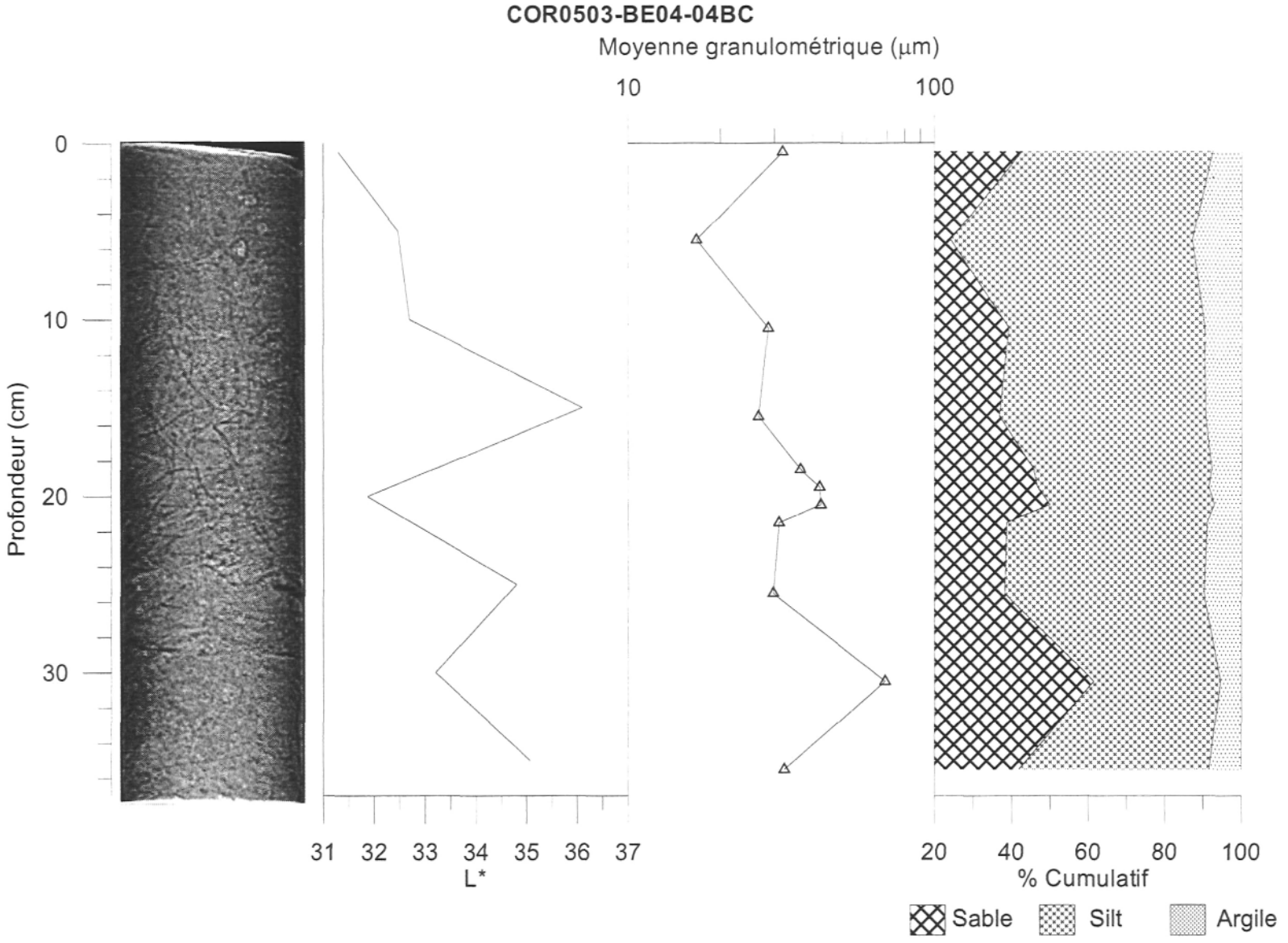
COR0503-BE04-04BC
Moyenne granulométrique (µm)
10
100
0
10
20
30
Profondeur (cm)
31
32
33
34
35
36
37
L*
20
40
60
80
100
% Cumulatif
Sable
Silt
Argile

COR0503-BE04-04BC

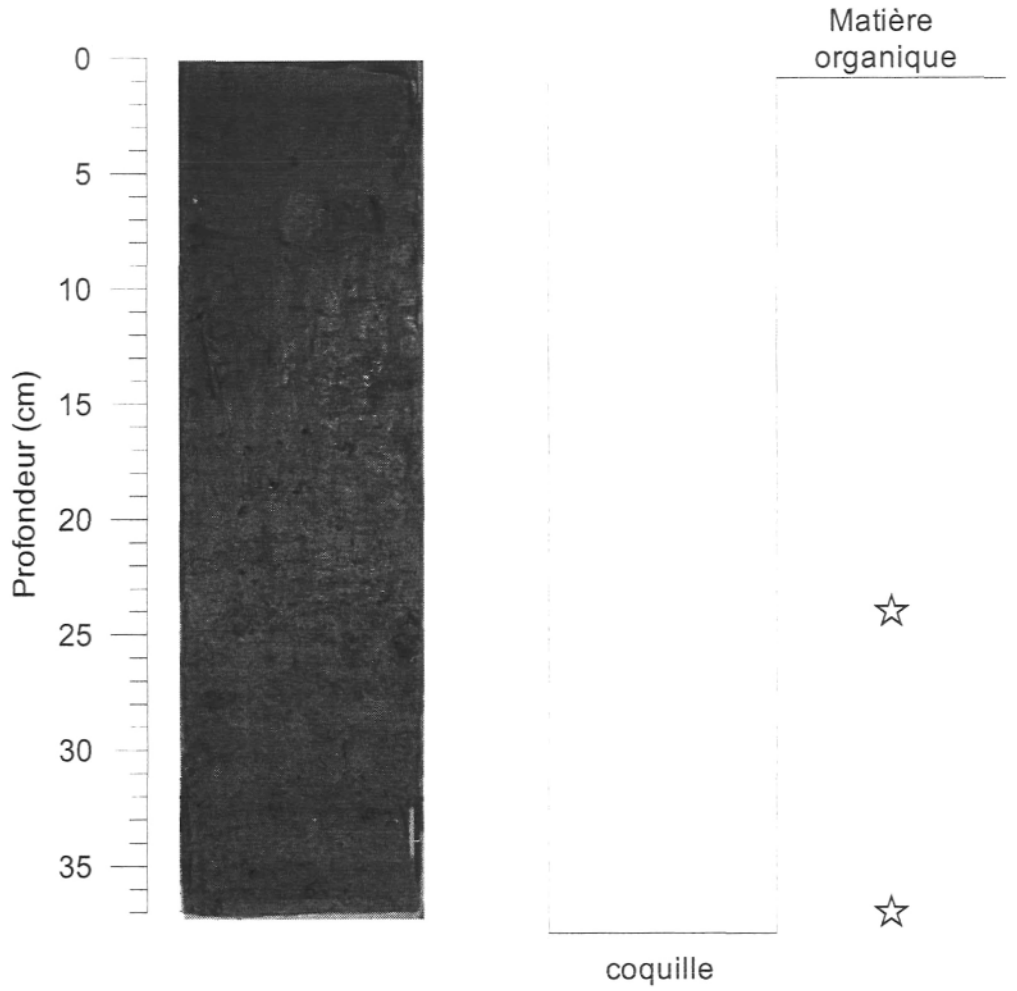

Date: 11/25/2005
Observateurs: GCV - G.St-Onge
Échantillon: COR0503-BE04-BC04
Section: AB
Longueur: 37 cm
Profondeur: 0-37 cm

Intervalle	Structure	Granulo	Description
0-22		Si A	Silt argileux, traces de bioturbation, tubes de ver
	24		Deux morceaux de bois, 1 cm^3
22-37		MS	coulée de débris, roches, sable, argile, présence de morceau de bois. Pas de bioturbation
	37		Micro-reste de quelque chose d'organique
36-37			Couche de sable très compact avec une faible teneur en eau

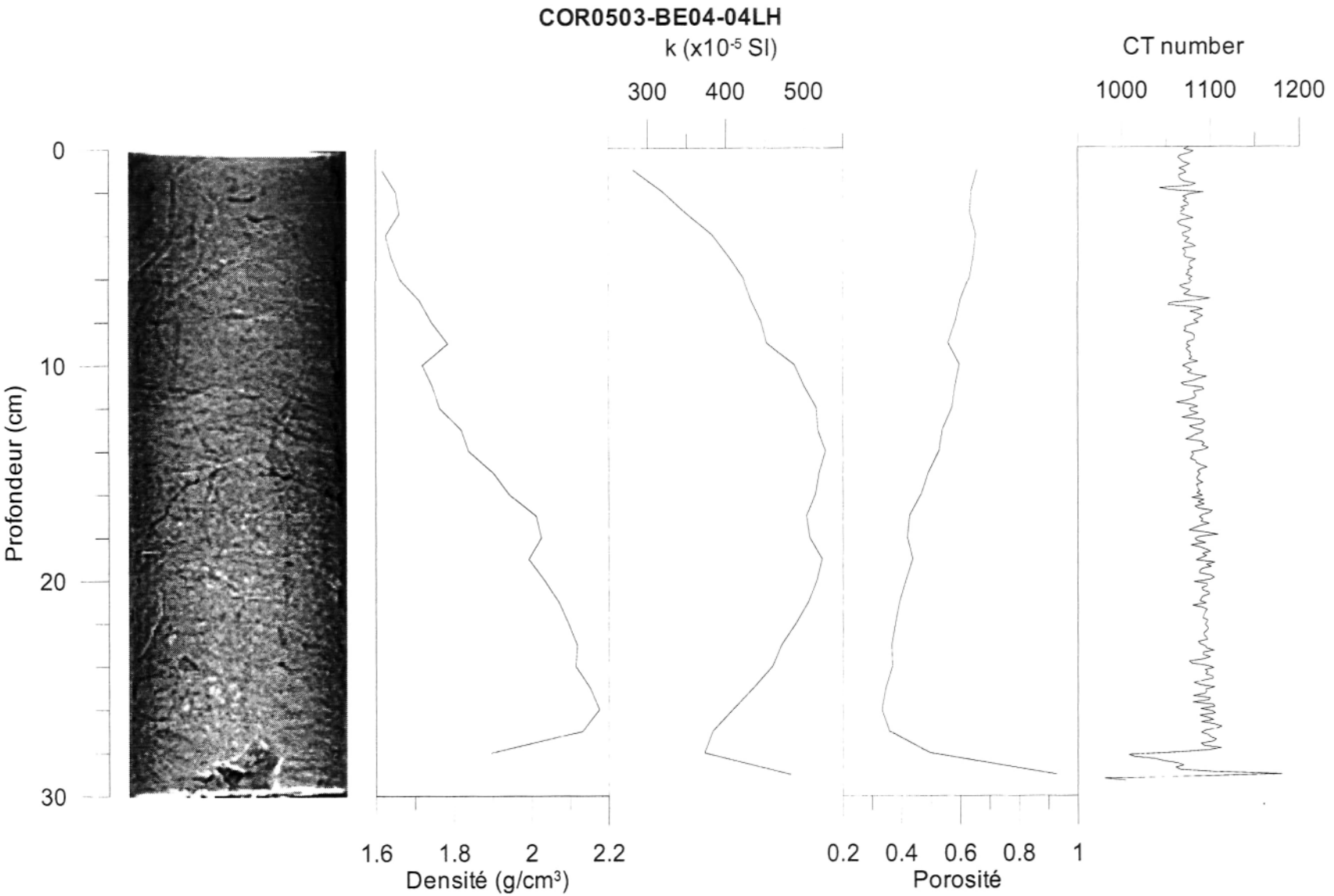
COR0503-BE04-04LH
k (x10-5 SI)
300
400
500
CT number
1000
1100
1200
0
10
20
30
Profondeur (cm)
1.6
1.8
2
2.2
Densité (g/cm3)
0.2
0.4
0.6
0.8
1
Porosité

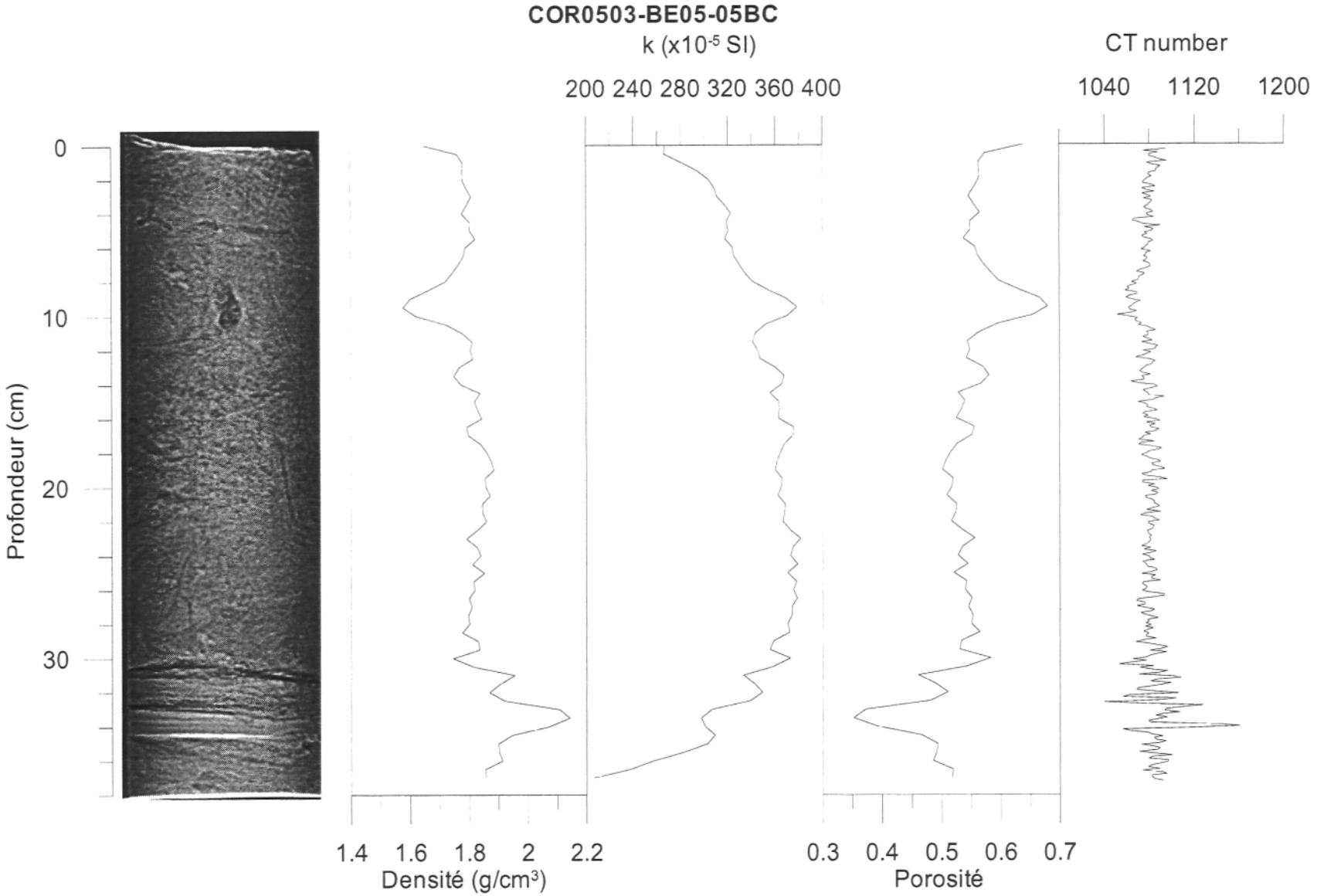
COR0503-BE05-05BC
k (x10-5 SI)
200 240 280 320 360 400
CT number
1040 1120 1200
Profondeur (cm)
0
10
20
30
1.4 1.6 1.8 2 2.2
Densité (g/cm3)
0.3 0.4 0.5 0.6 0.7
Porosité

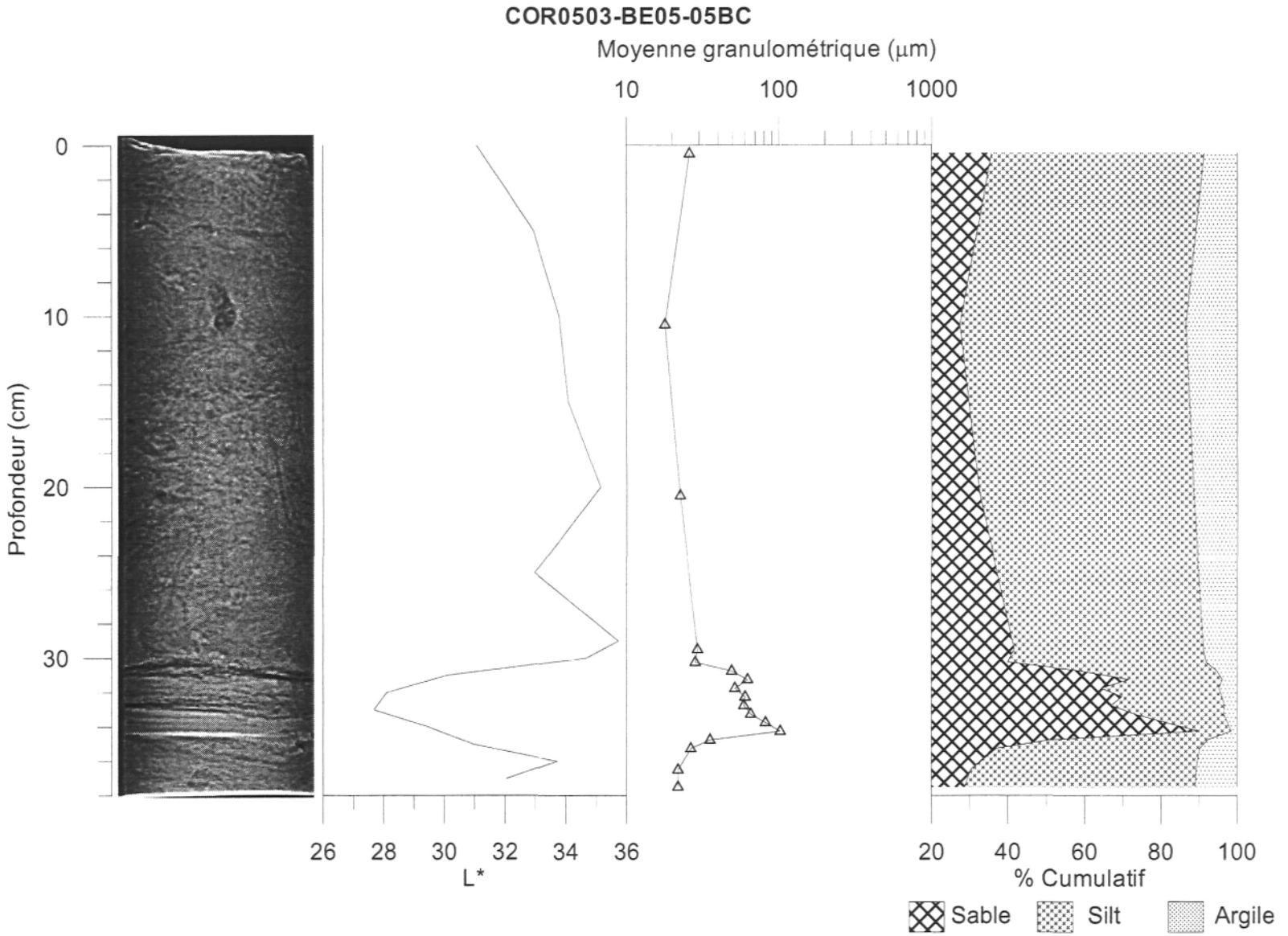
COR0503-BE05-05BC
Moyenne granulométrique (µm)
10
100
1000
0
10
20
30
Profondeur (cm)
26
28
30
32
34
36
L*
20
40
60
80
100
% Cumulatif
Sable
Silt
Argile

COR0503-BE05-05BC

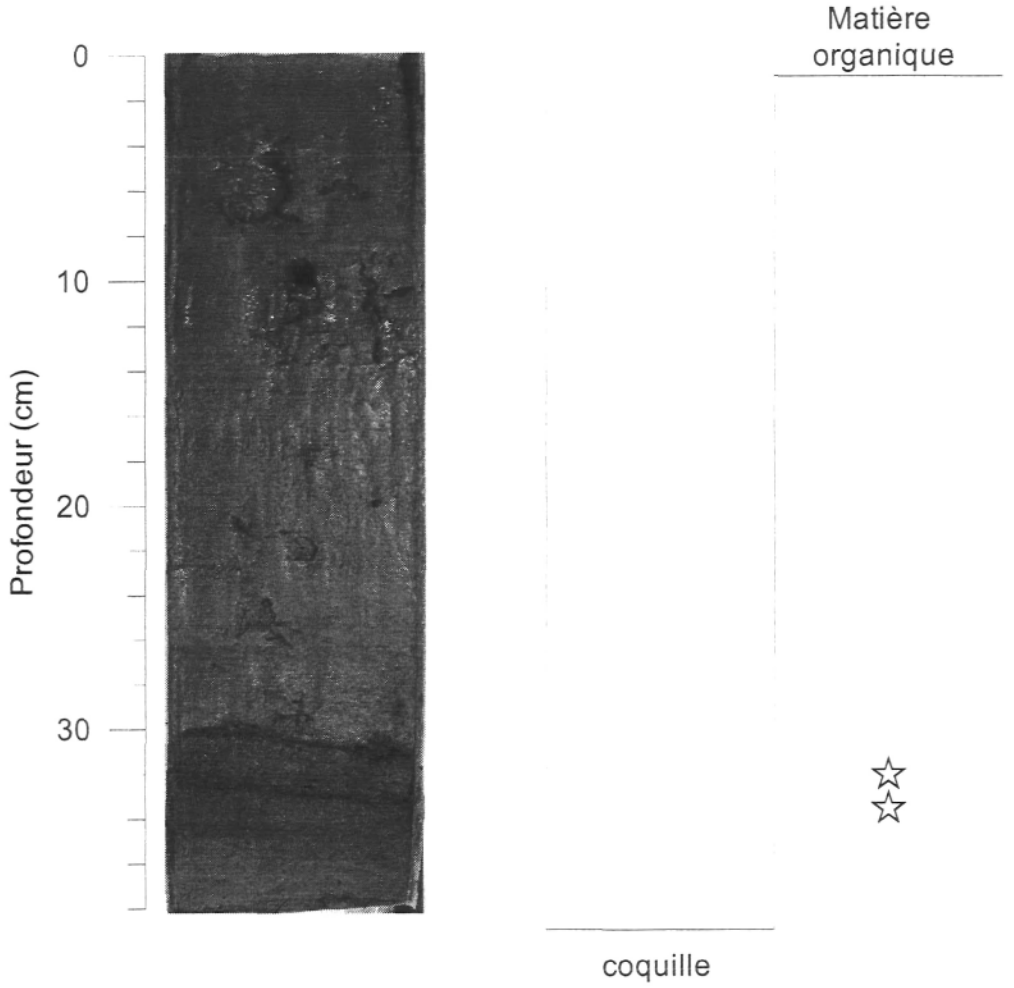

Date: 11/25/2005
Observateurs: GCV - G.St-Onge
Échantillon: COR0503-BE05-BC05
Section: AB
Longueur: 38 cm
Profondeur: 0-38 cm

Intervalle	Structure	Granulo	Description
0-31		Si A	Silt argileux bioturbé, avec présence de tubes de ver
	10		trou de biotubation, diamètre de 1 cm
30-33.5		Sa	Couches anormales
	30	MO	Couche avec présence de filament organique
30-32			Sable fin, présence de silt et argile
	32	MO	Deuxième couche de matière organique
32-33.5		Sa	Deuxième couche de sable (avec présence de silt et d'argile)
	33.5		Couche de sable beaucoup plus foncée, mais sans présence de sable apparante, plus de minéraux noirs
33.5-38			Sédimentation normale de silt argileux

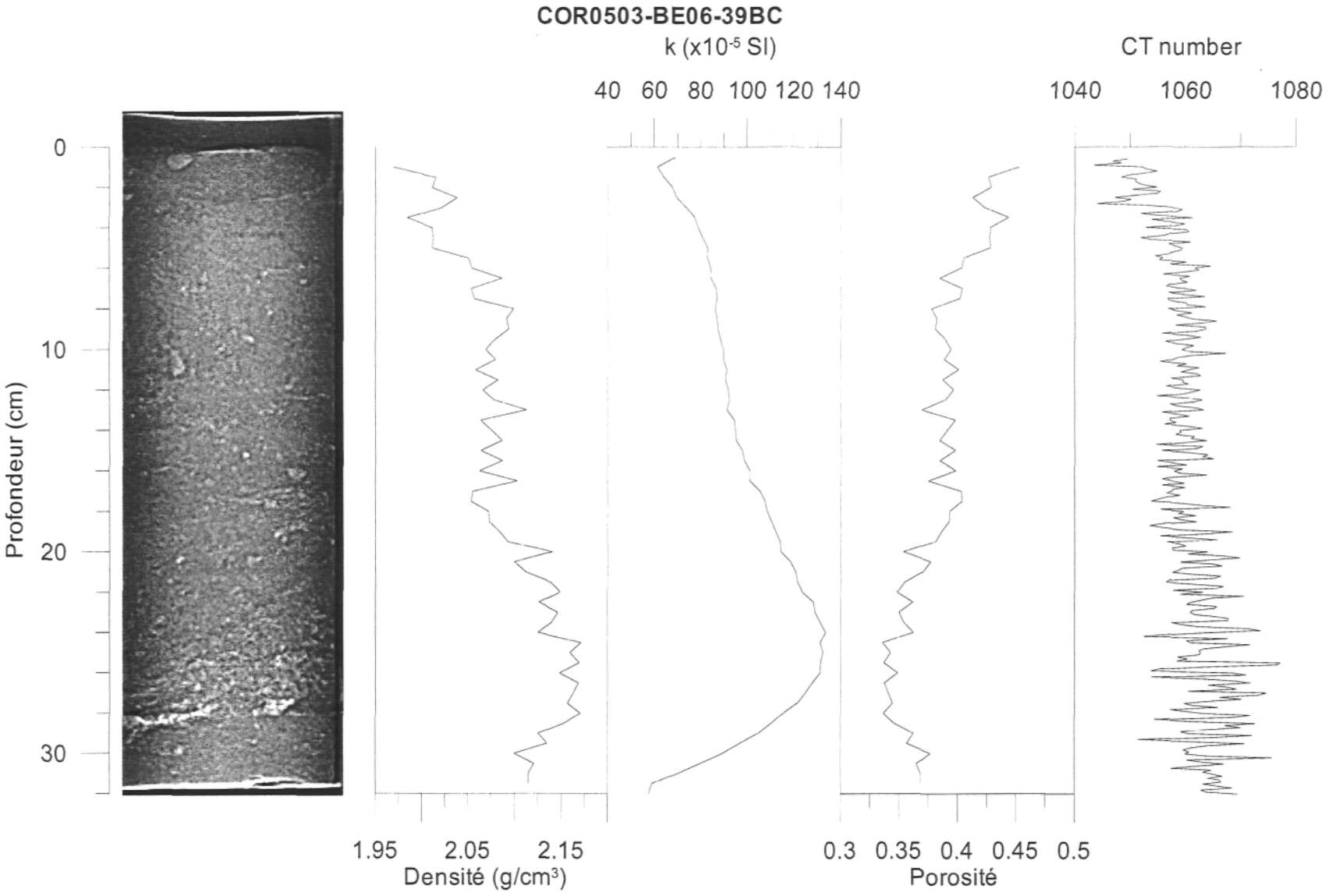
COR0503-BE06-39BC
k (x10-5 SI)
CT number
40 60 80 100 120 140
1040 1060 1080
0
10
20
30
Profondeur (cm)
1.95 2.05 2.15
Densité (g/cm3)
0.3 0.35 0.4 0.45 0.5
Porosité

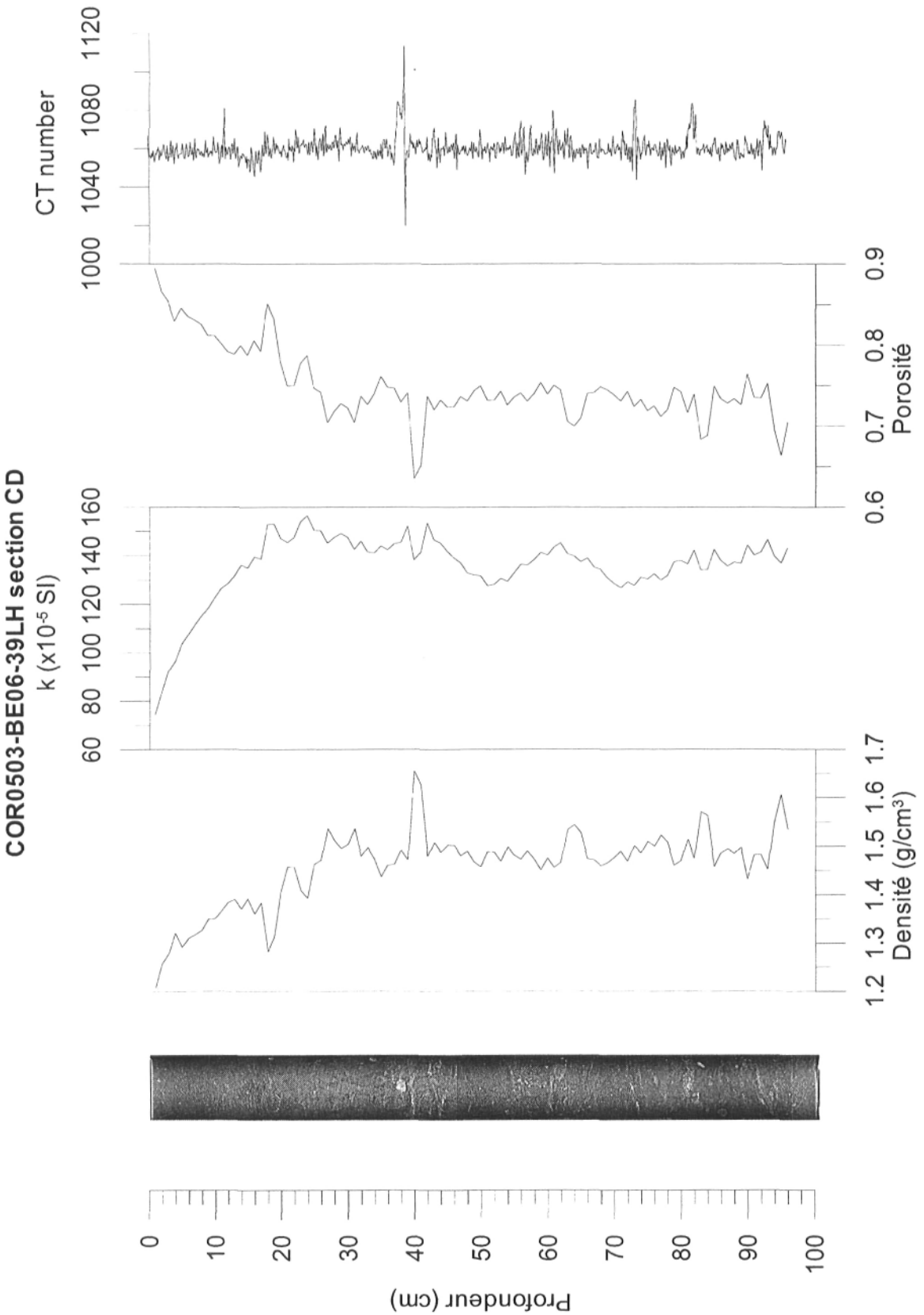
COR0503-BE06-39LH section CD
CT number
1000 1040 1080 1120
k (x10-5 SI)
60 80 100 120 140 160
Porosité
0.6 0.7 0.8 0.9
Densité (g/cm3)
1.2 1.3 1.4 1.5 1.6 1.7
Profondeur (cm)
0 10 20 30 40 50 60 70 80 90 100

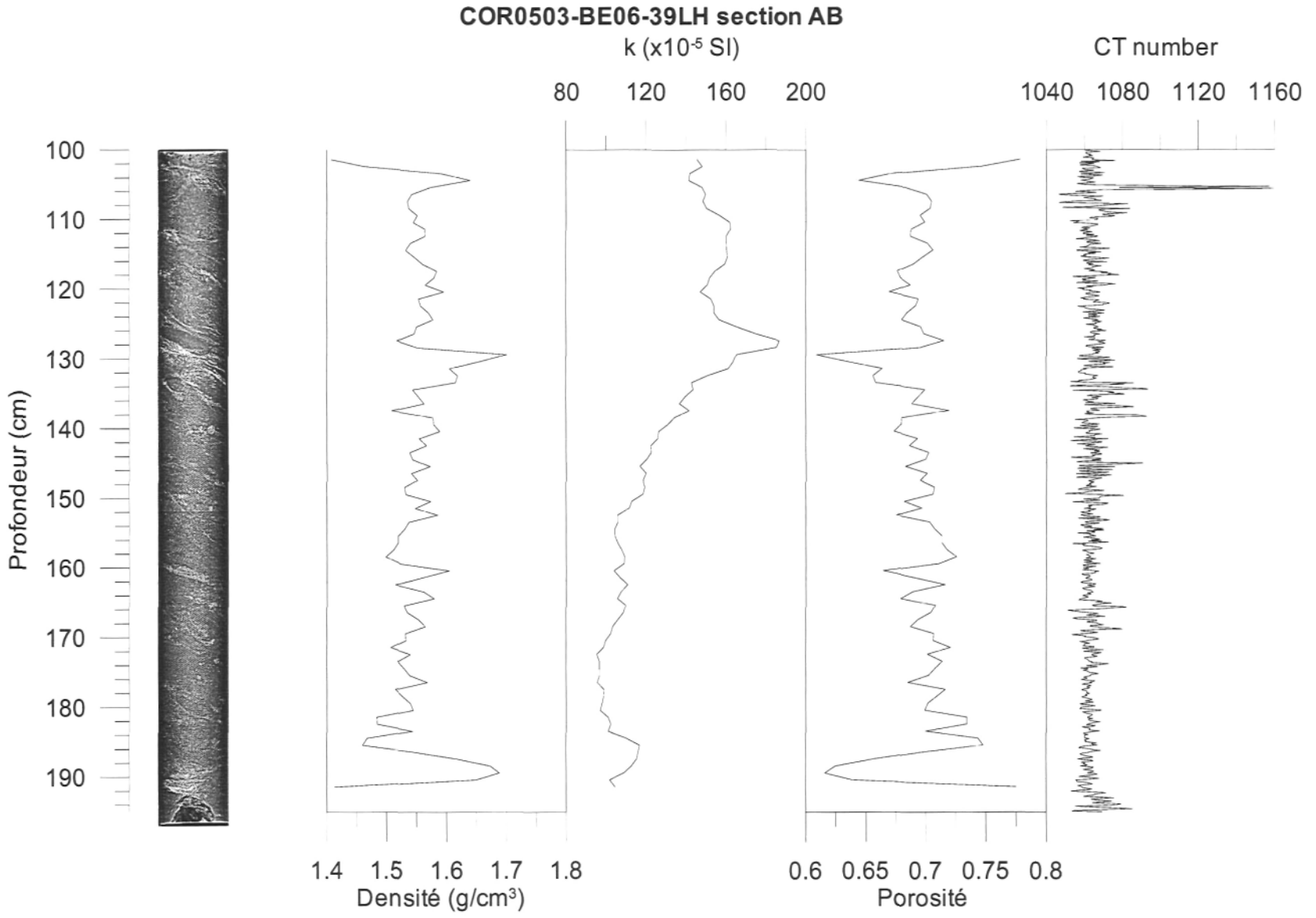
COR0503-BE06-39LH section AB
k (x10-5 SI)
80 120 160 200
CT number
1040 1080 1120 1160
Profondeur (cm)
100 110 120 130 140 150 160 170 180 190
1.4 1.5 1.6 1.7 1.8
Densité (g/cm3)
0.6 0.65 0.7 0.75 0.8
Porosité

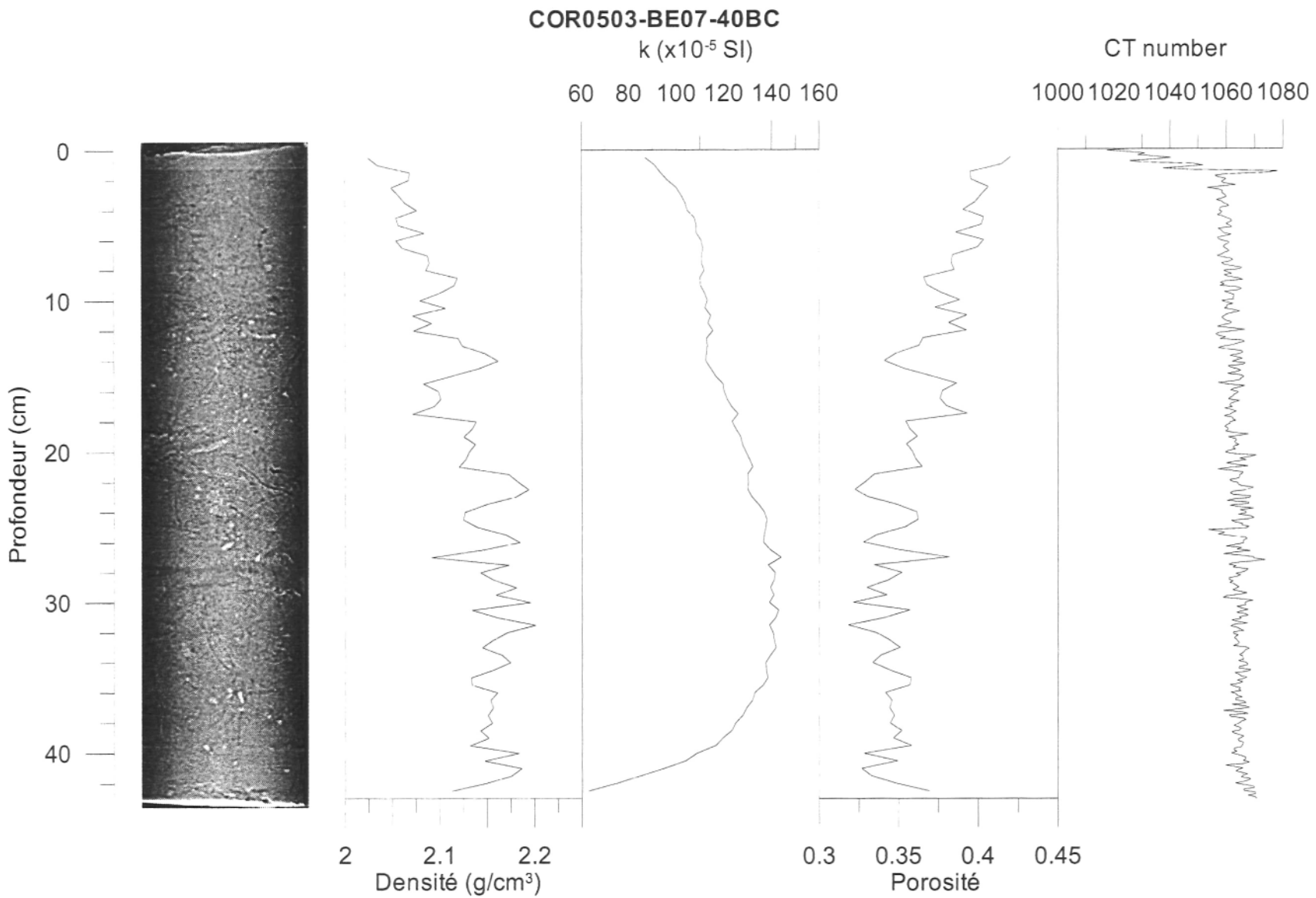
COR0503-BE07-40BC
k (x10-5 SI)
60 80 100 120 140 160
CT number
1000 1020 1040 1060 1080
Profondeur (cm)
0
10
20
30
40
2 2.1 2.2
Densité (g/cm3)
0.3 0.35 0.4 0.45
Porosité

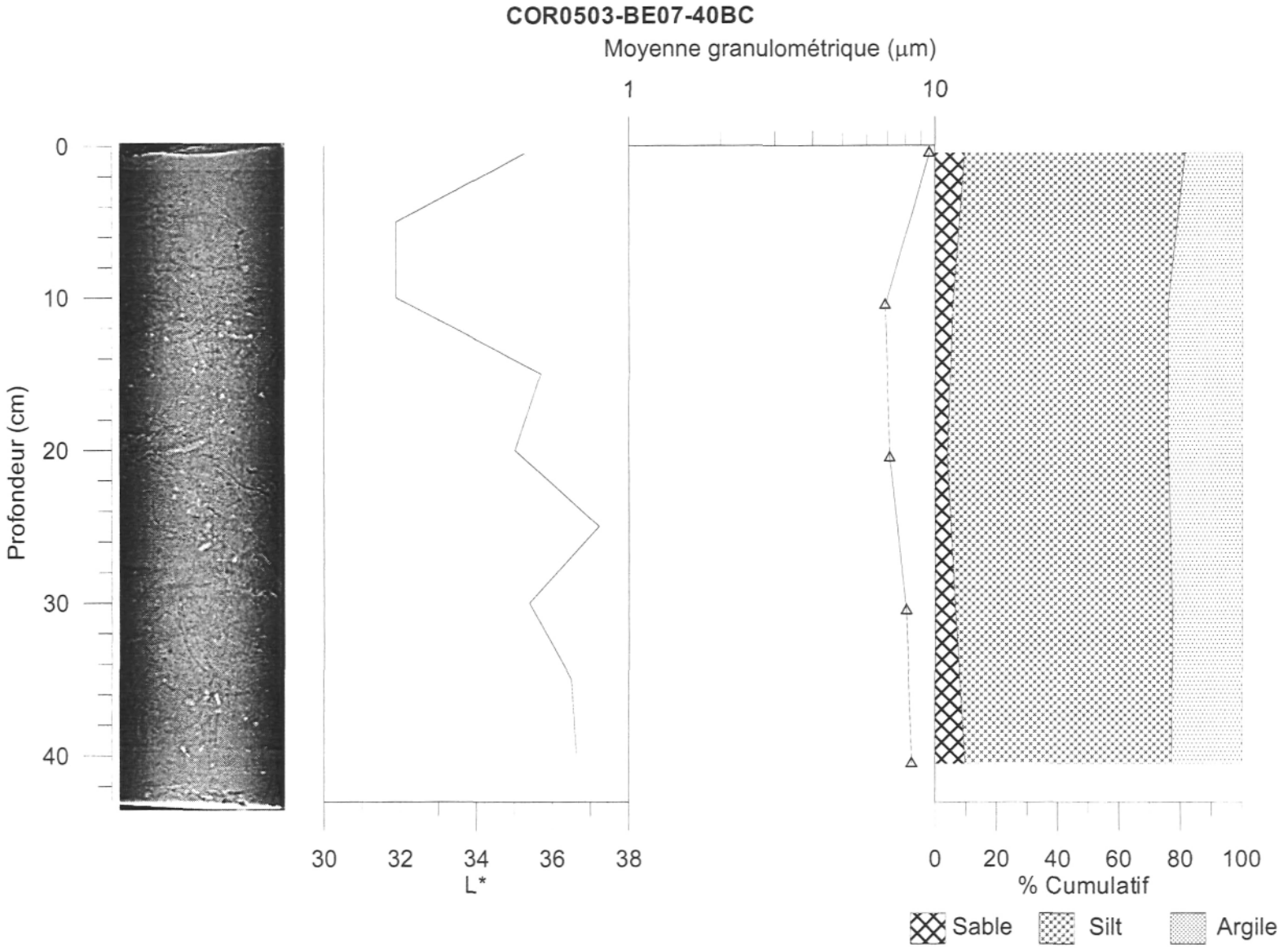
COR0503-BE07-40BC
Moyenne granulométrique (µm)
1
10
0
10
20
30
40
Profondeur (cm)
30
32
34
36
38
L*
0
20
40
60
80
100
% Cumulatif
Sable
Silt
Argile

COR0503-BE07-40BC

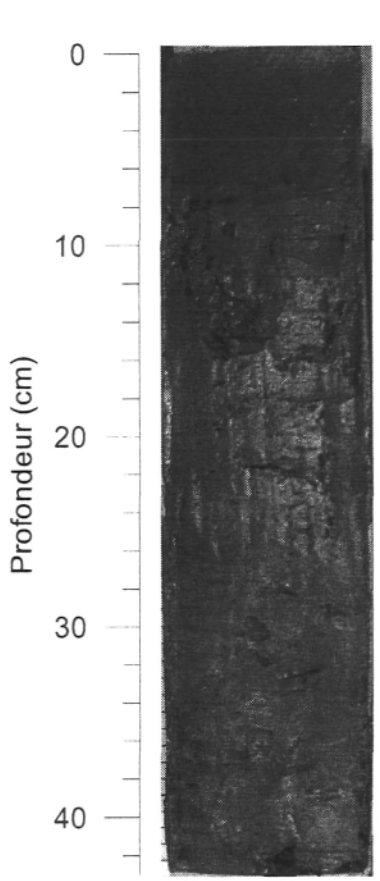

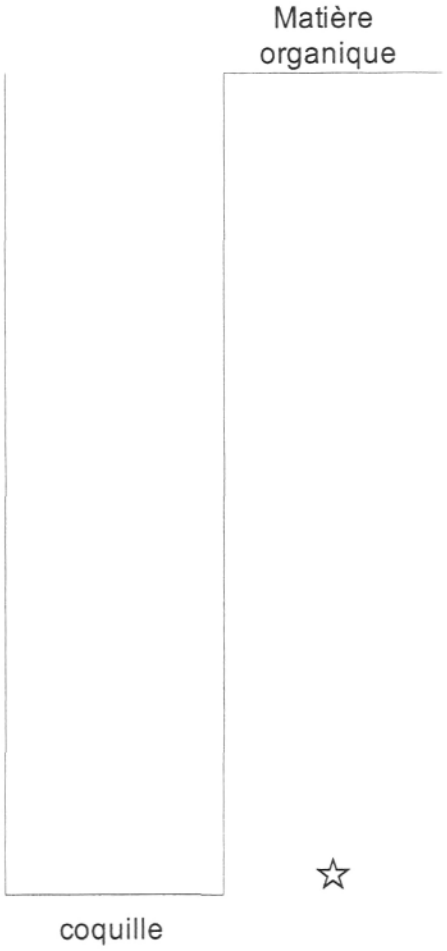

Date: 11/25/2005
Observatrice: GCV
Échantillon: COR0503-BE07-BC40
Section: AB
Longueur: 43 cm
Profondeur: 0-43 cm

Intervalle	Structure	Granulo	Description
0-4		A Si	Argile silteuse sans présence apparante de bioturbation, pas de mouchetures noires
4-43		A Si	Argile silteuse fortement bioturbée, tubes de ver, mouchetures noires, présence de grain de silt et de sable ici et là
	30	Sa	Petite pochette de sable sur le côté droit, visible sur le cat-scan
	43		Morceau de bois, environ 1 x 2 cm

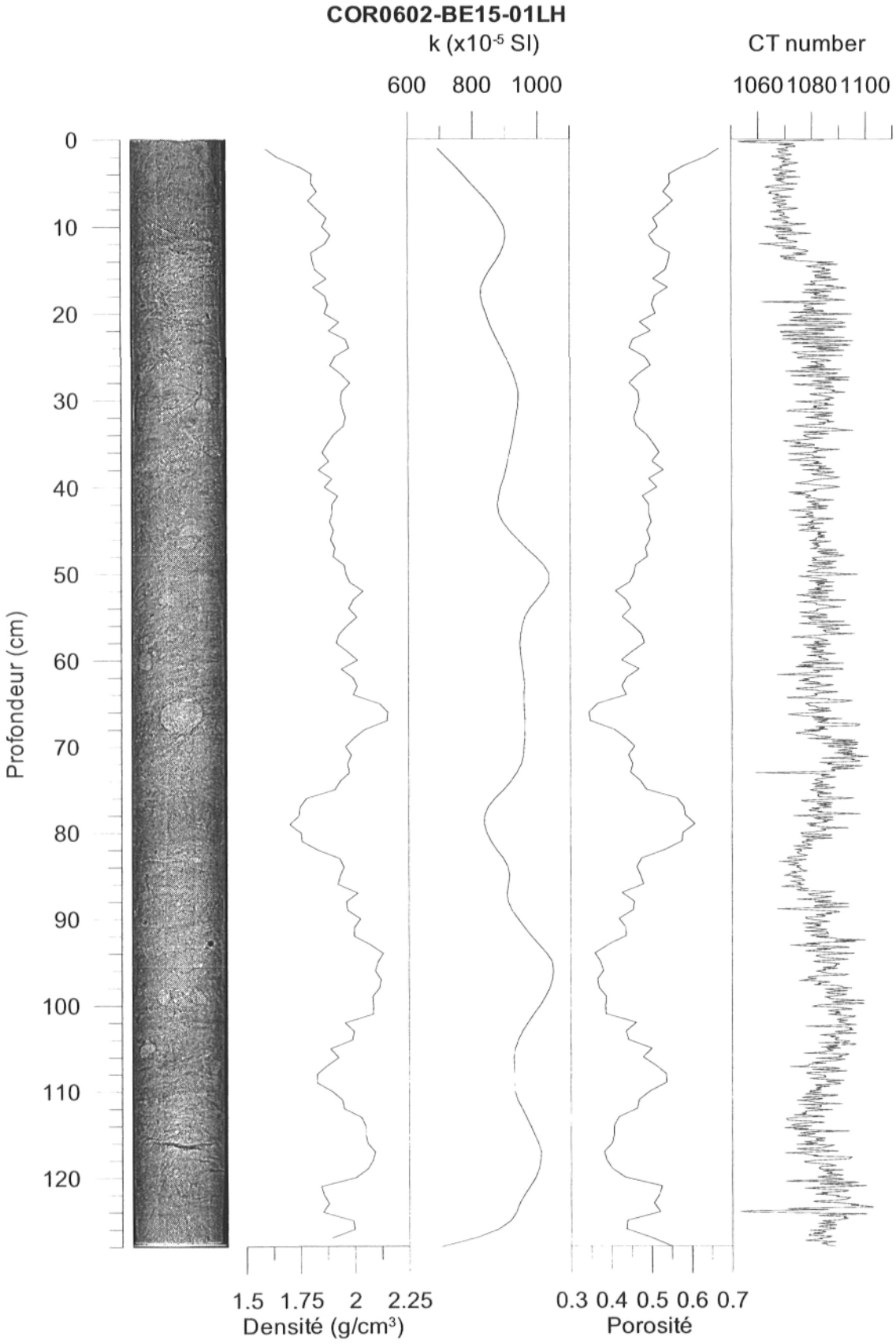
COR0602-BE15-01LH
k (x10-5 SI)
600 800 1000
CT number
1060 1080 1100
Profondeur (cm)
0
10
20
30
40
50
60
70
80
90
100
110
120
1.5 1.75 2 2.25
Densité (g/cm3)
0.3 0.4 0.5 0.6 0.7
Porosité

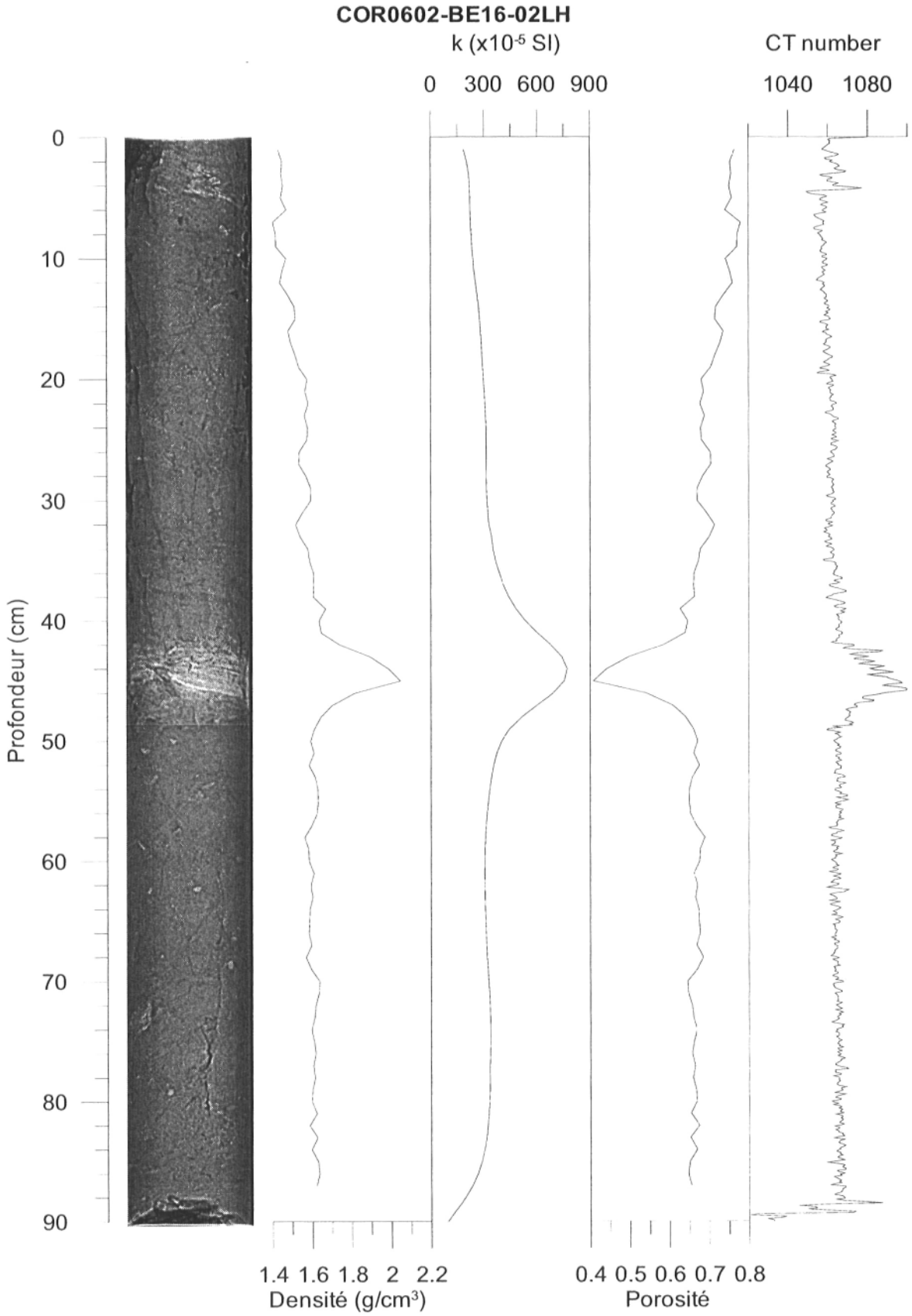
COR0602-BE16-02LH
k (x10-5 SI)
0 300 600 900
CT number
1040 1080
Profondeur (cm)
0
10
20
30
40
50
60
70
80
90
1.4 1.6 1.8 2 2.2
Densité (g/cm3)
0.4 0.5 0.6 0.7 0.8
Porosité

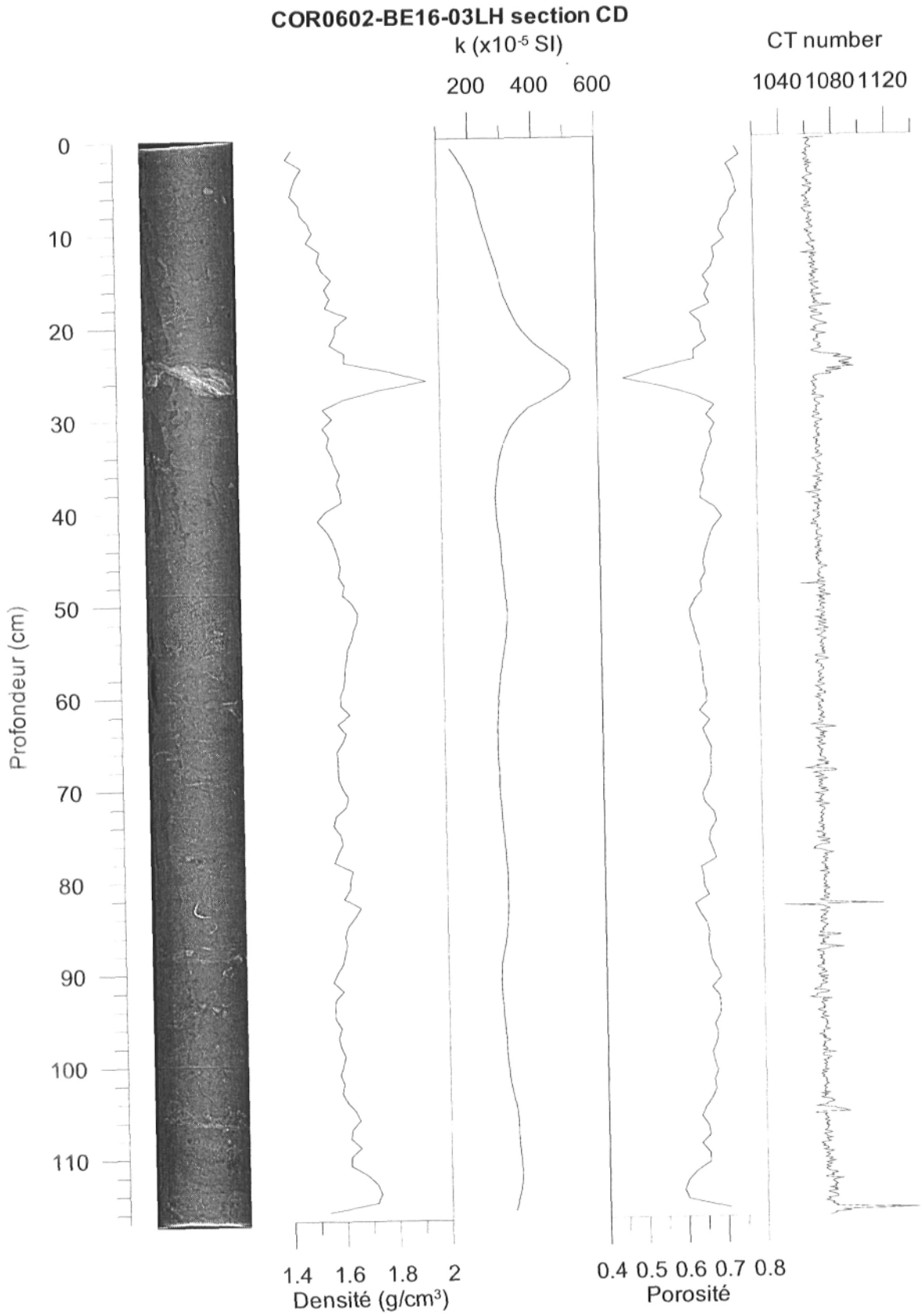
COR0602-BE16-03LH section CD
k (x10-5 SI)
200 400 600
CT number
1040 1080 1120
Profondeur (cm)
0
10
20
30
40
50
60
70
80
90
100
110
1.4 1.6 1.8 2
Densité (g/cm3)
0.4 0.5 0.6 0.7 0.8
Porosité

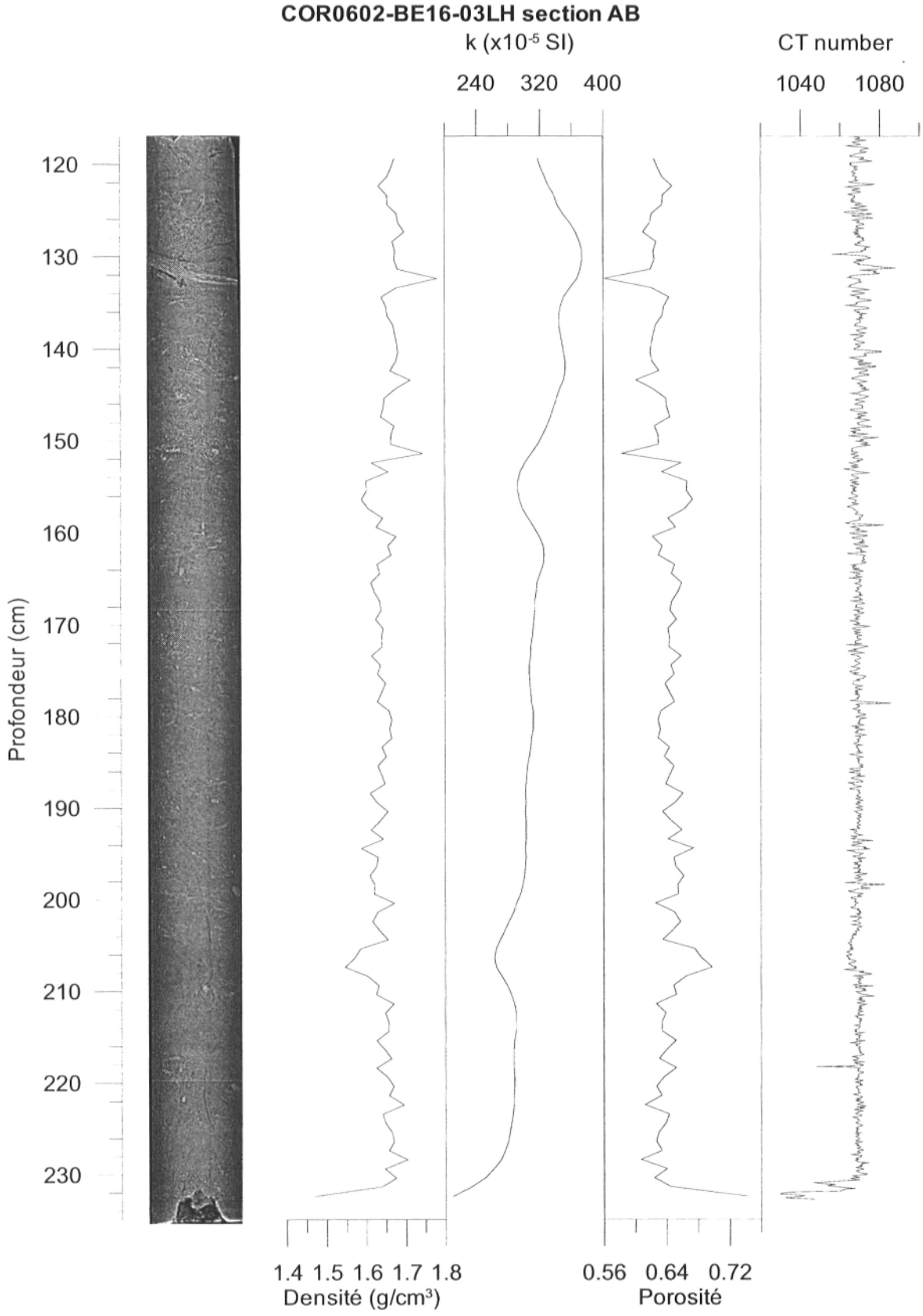
COR0602-BE16-03LH section AB
k (x10-5 SI)
240 320 400
CT number
1040 1080
Profondeur (cm)
120
130
140
150
160
170
180
190
200
210
220
230
1.4 1.5 1.6 1.7 1.8
Densité (g/cm3)
0.56 0.64 0.72
Porosité

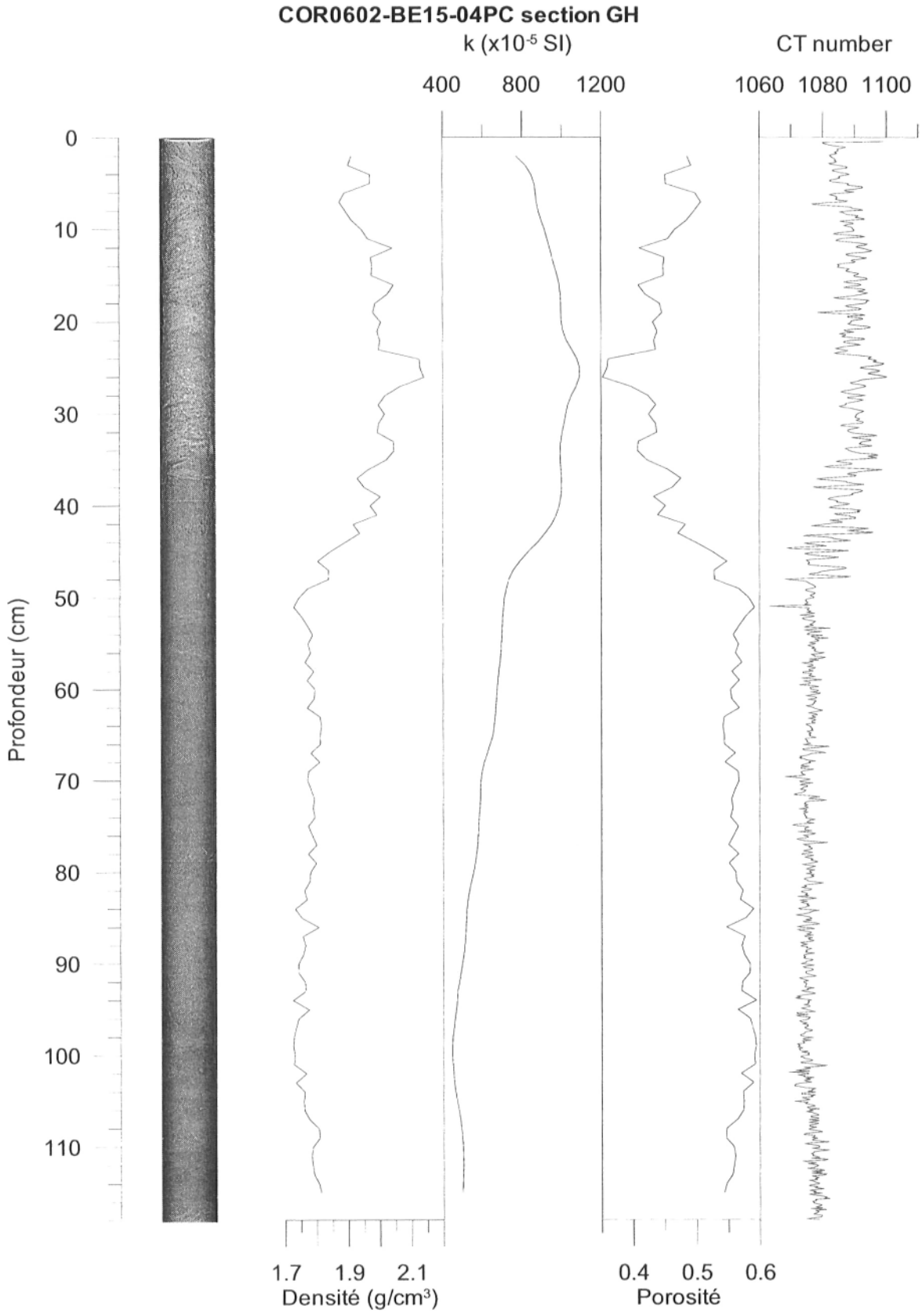
COR0602-BE15-04PC section GH
k (x10-5 SI)
400
800
1200
CT number
1060
1080
1100
0
10
20
30
40
50
60
70
80
90
100
110
Profondeur (cm)
1.7
1.9
2.1
Densité (g/cm3)
0.4
0.5
0.6
Porosité

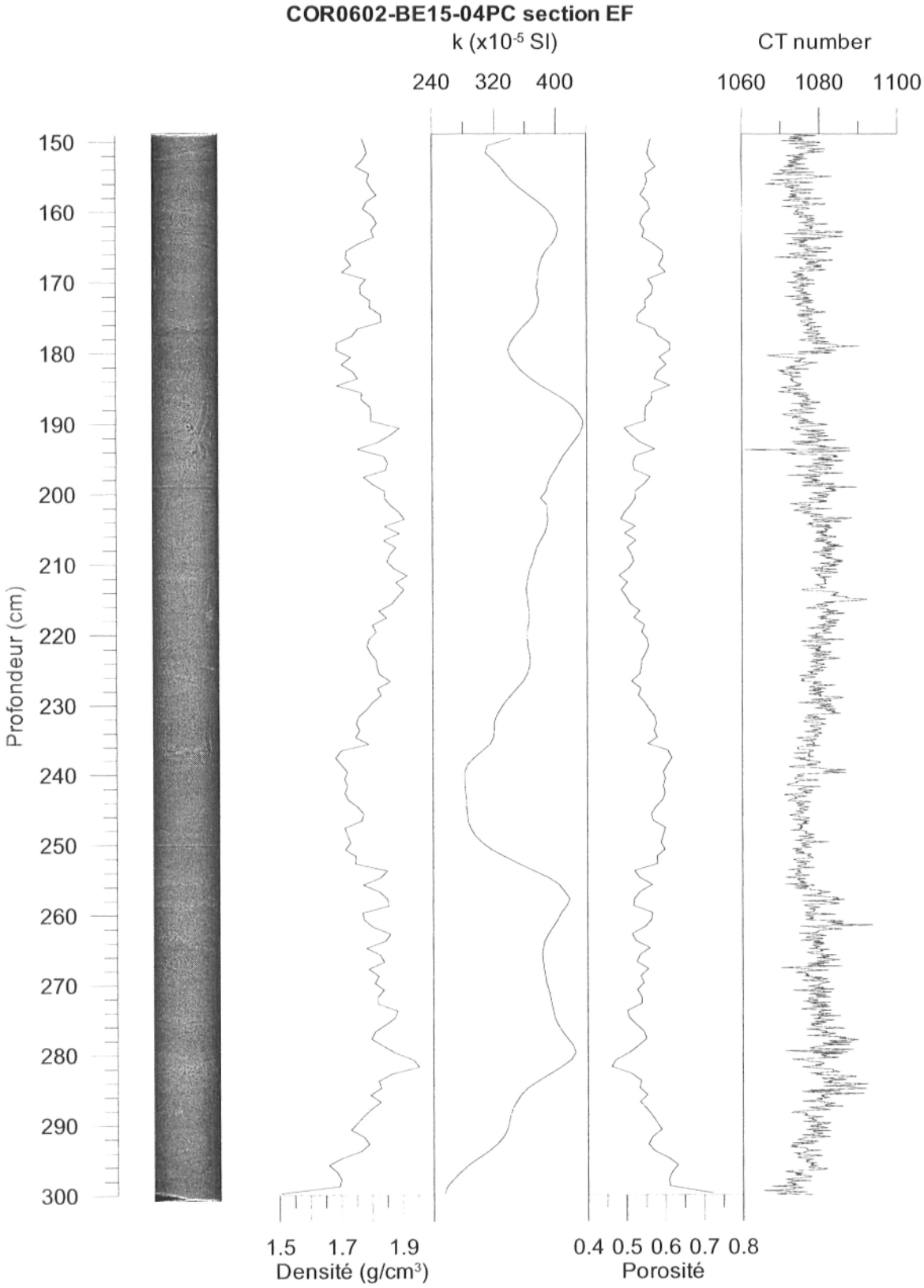
COR0602-BE15-04PC section EF
k (x10-5 SI)
240 320 400
CT number
1060 1080 1100
Profondeur (cm)
150
160
170
180
190
200
210
220
230
240
250
260
270
280
290
300
1.5 1.7 1.9
Densité (g/cm3)
0.4 0.5 0.6 0.7 0.8
Porosité

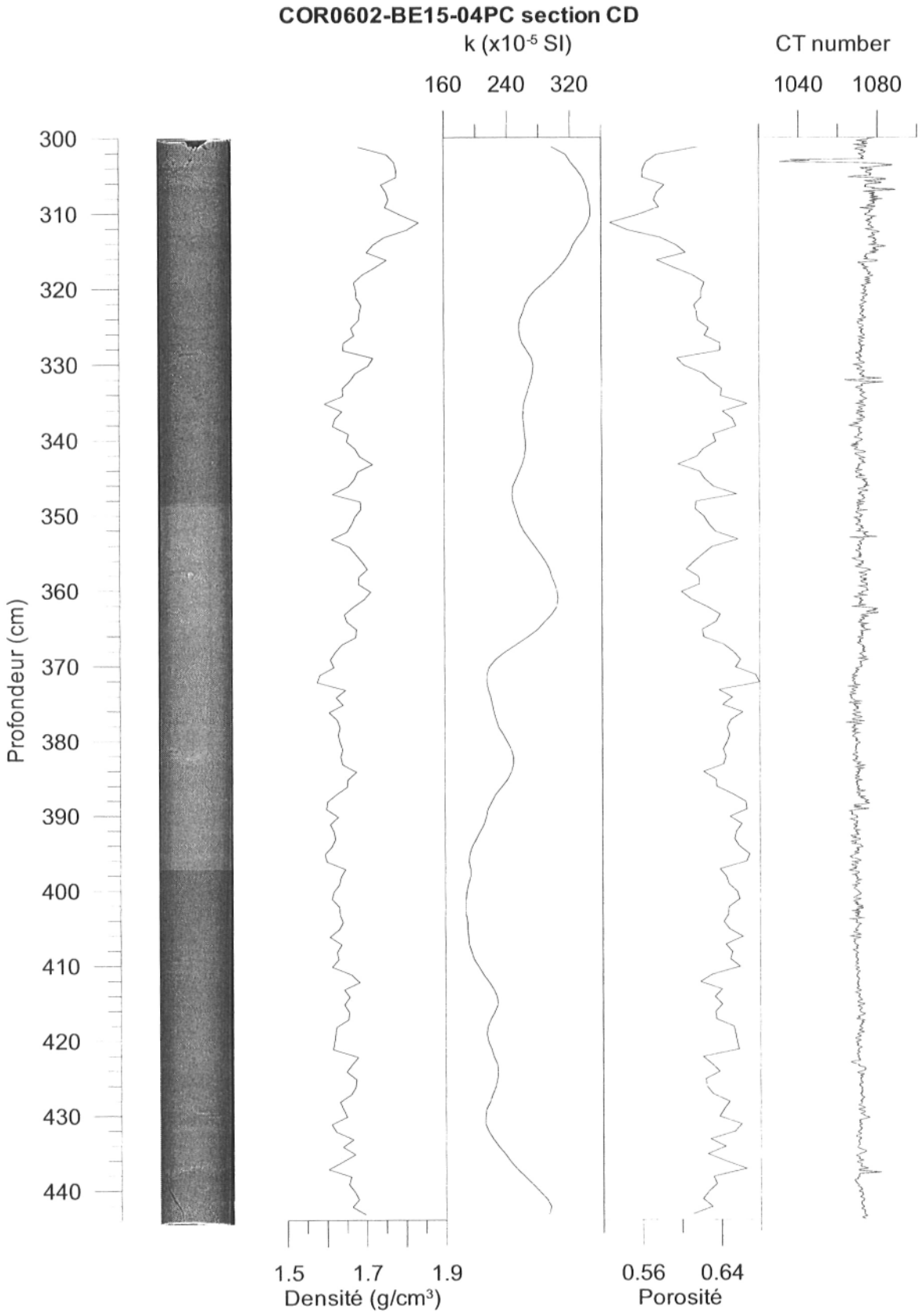
COR0602-BE15-04PC section CD
k (x10-5 SI)
160 240 320
CT number
1040 1080
Profondeur (cm)
300
310
320
330
340
350
360
370
380
390
400
410
420
430
440
1.5 1.7 1.9
Densité (g/cm3)
0.56 0.64
Porosité

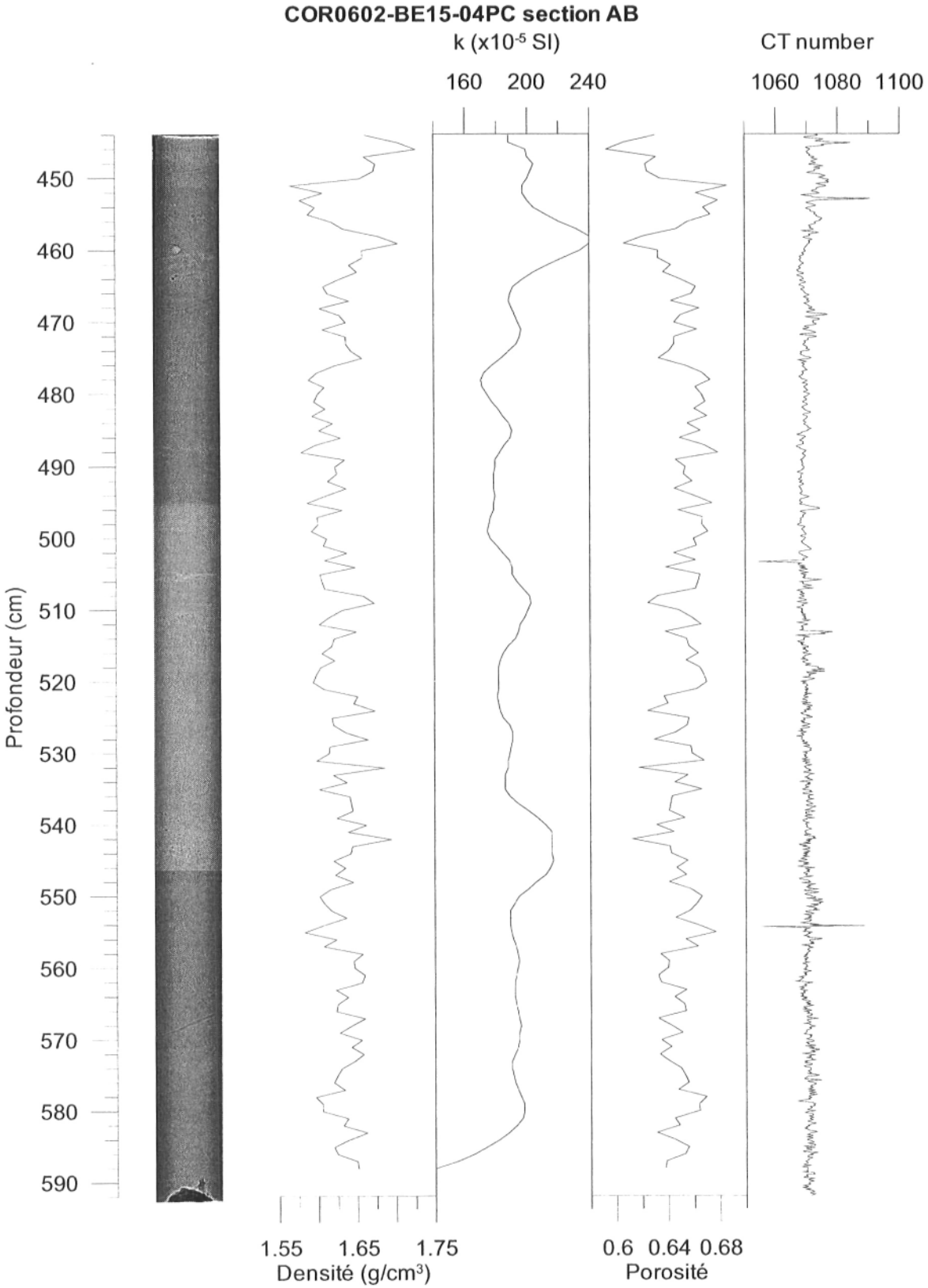
COR0602-BE15-04PC section AB
k (x10-5 SI)
160 200 240
CT number
1060 1080 1100
Profondeur (cm)
450
460
470
480
490
500
510
520
530
540
550
560
570
580
590
1.55 1.65 1.75
Densité (g/cm3)
0.6 0.64 0.68
Porosité

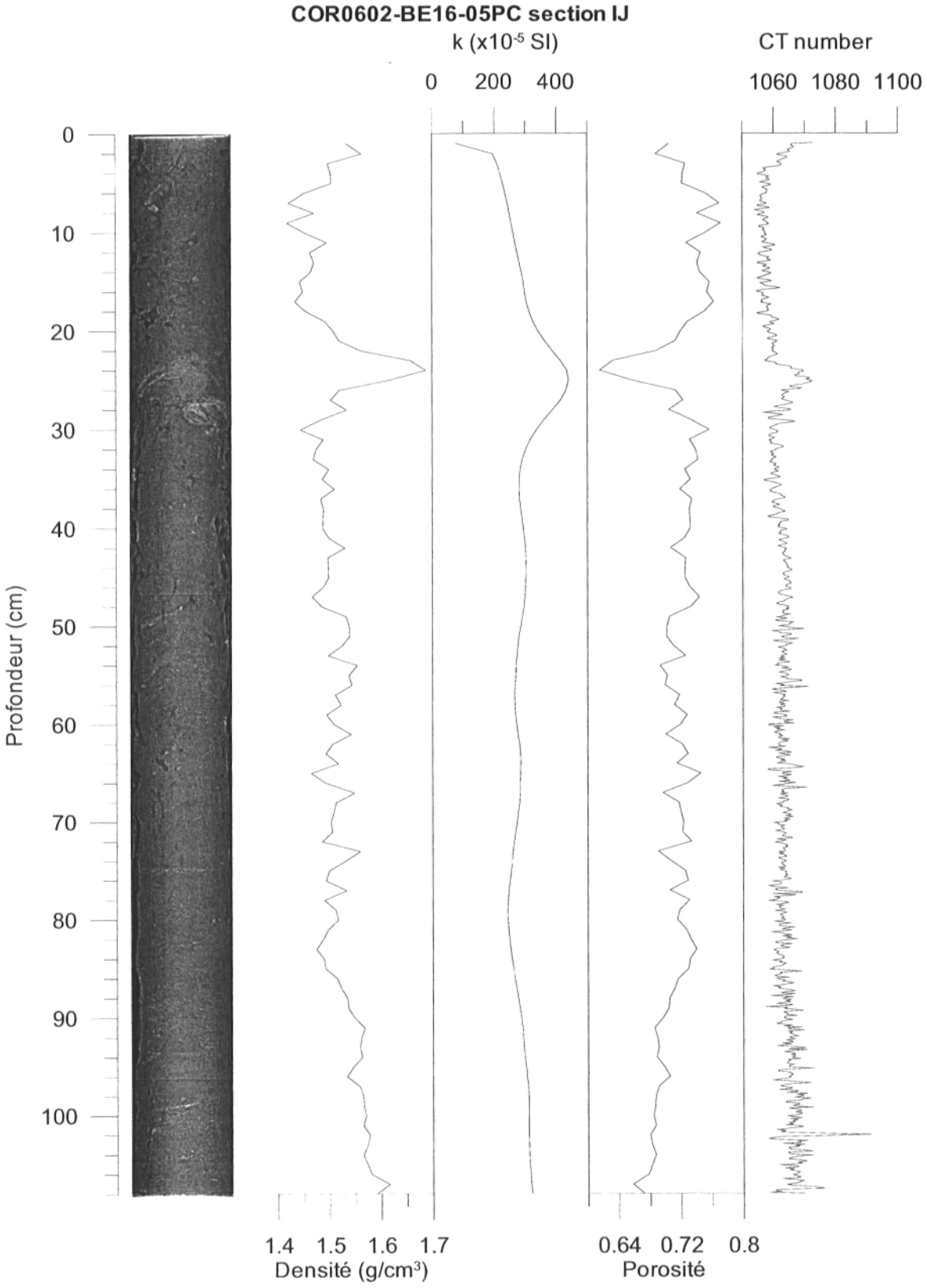
COR0602-BE16-05PC section IJ
k (x10-5 SI)
0 200 400
CT number
1060 1080 1100
Profondeur (cm)
0
10
20
30
40
50
60
70
80
90
100
1.4 1.5 1.6 1.7
Densité (g/cm3)
0.64 0.72 0.8
Porosité

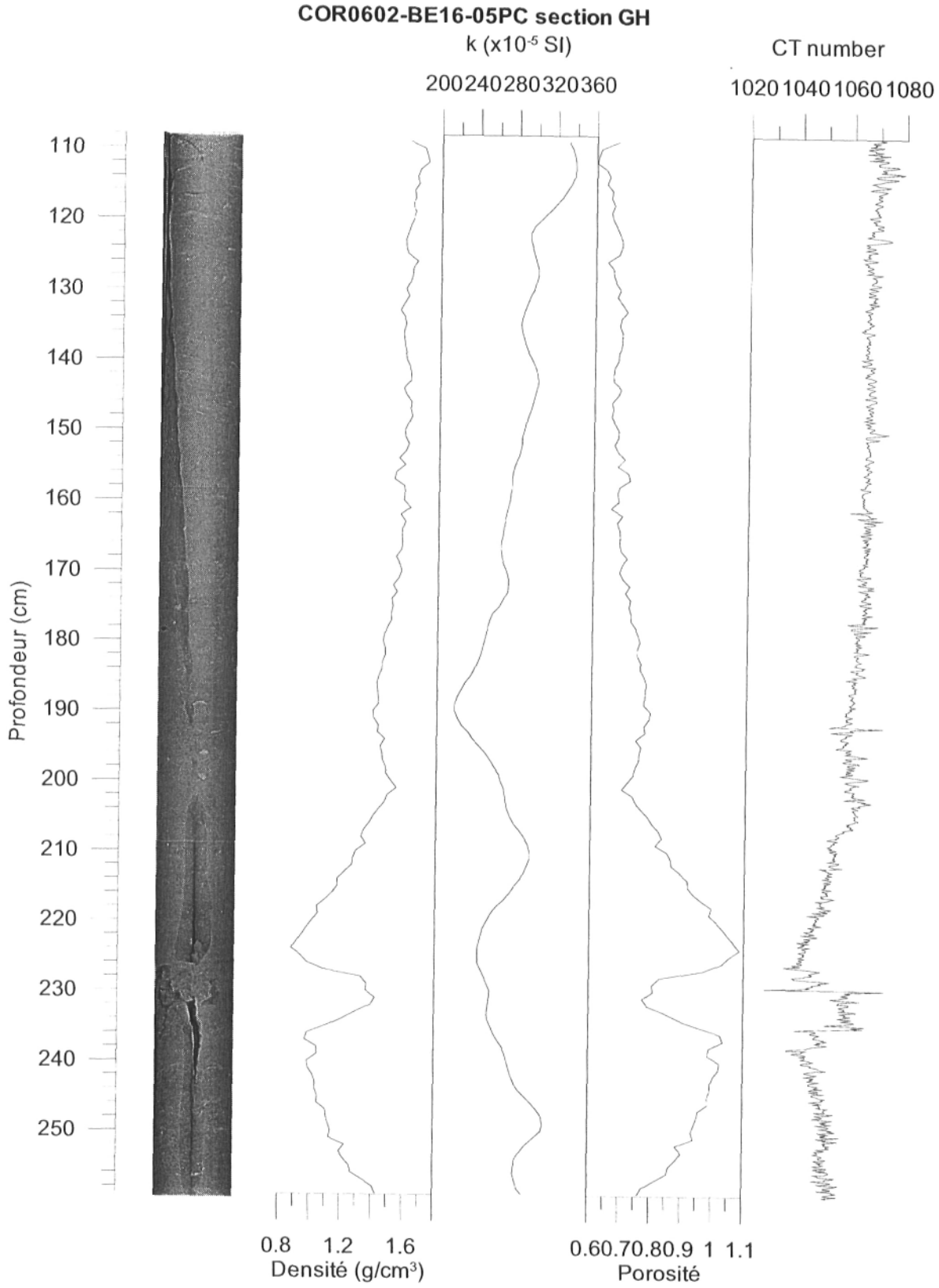
COR0602-BE16-05PC section GH
k (x10-5 SI)
200240280320360
CT number
1020 1040 1060 1080
Profondeur (cm)
110
120
130
140
150
160
170
180
190
200
210
220
230
240
250
0.8 1.2 1.6
Densité (g/cm3)
0.60.70.80.9 1 1.1
Porosité

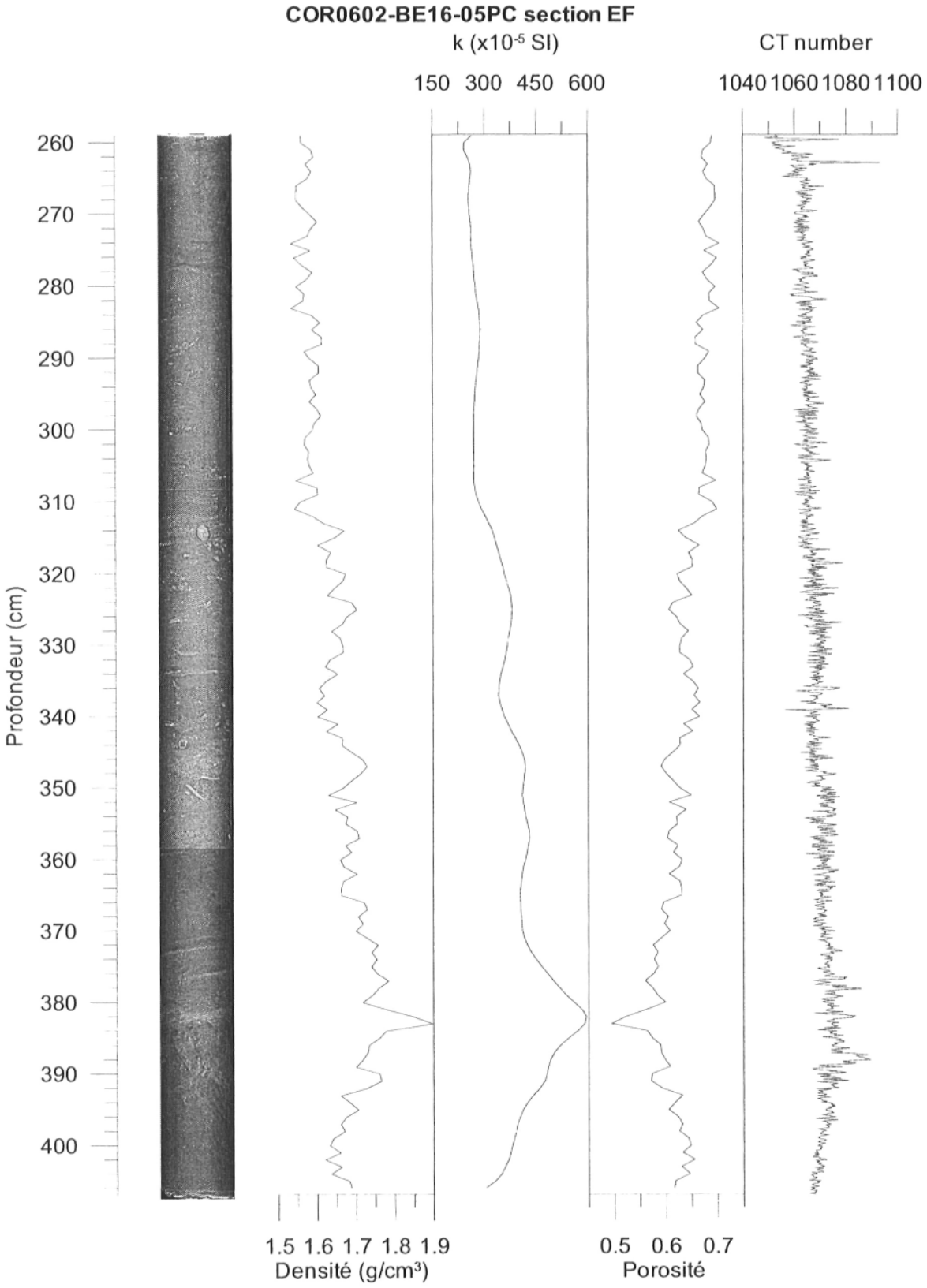
COR0602-BE16-05PC section EF
k (x10-5 SI)
150 300 450 600
CT number
1040 1060 1080 1100
Profondeur (cm)
260
270
280
290
300
310
320
330
340
350
360
370
380
390
400
1.5 1.6 1.7 1.8 1.9
Densité (g/cm3)
0.5 0.6 0.7
Porosité

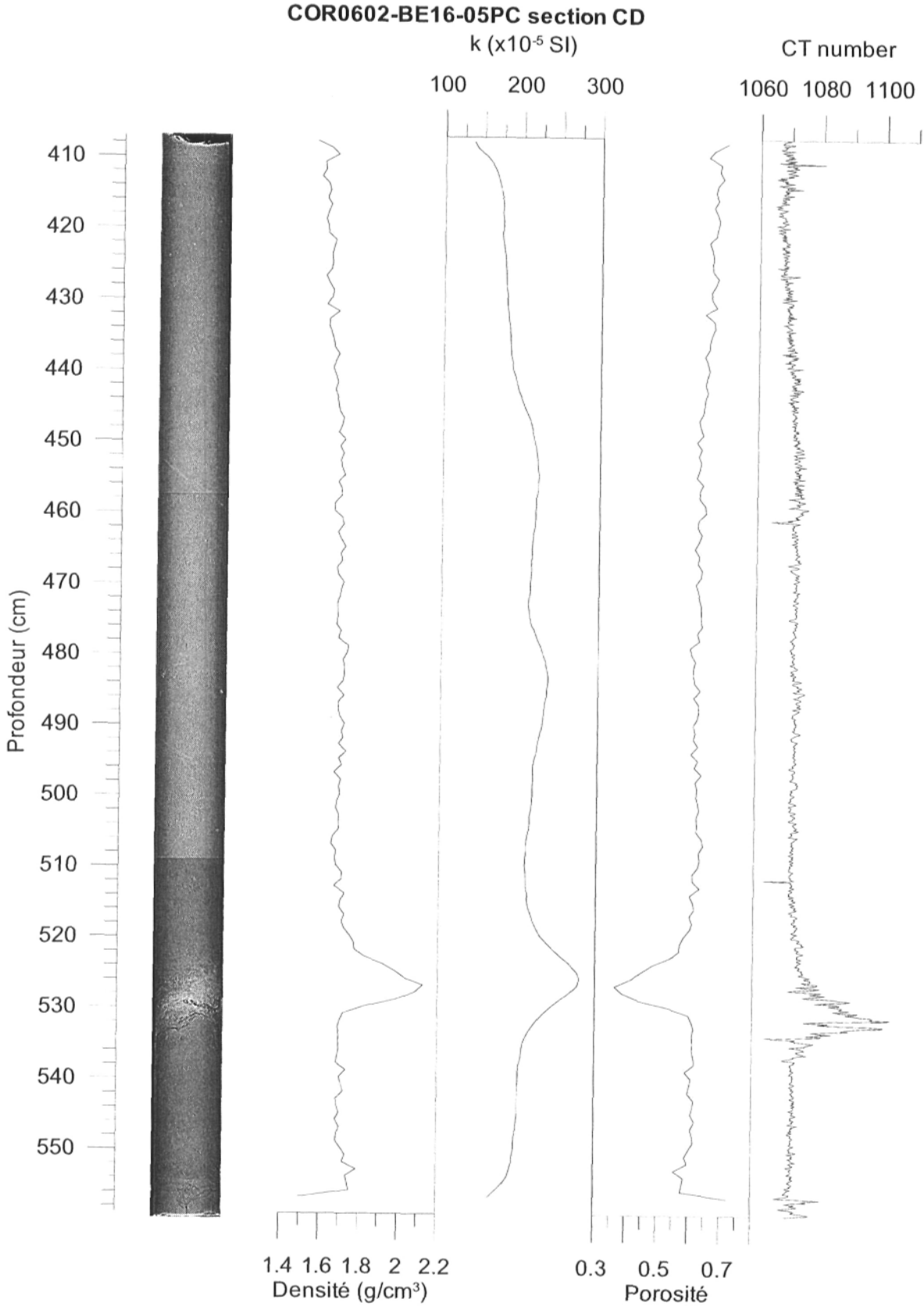
COR0602-BE16-05PC section CD
k (x10-5 SI)
100 200 300
CT number
1060 1080 1100
Profondeur (cm)
410
420
430
440
450
460
470
480
490
500
510
520
530
540
550
1.4 1.6 1.8 2 2.2
Densité (g/cm3)
0.3 0.5 0.7
Porosité

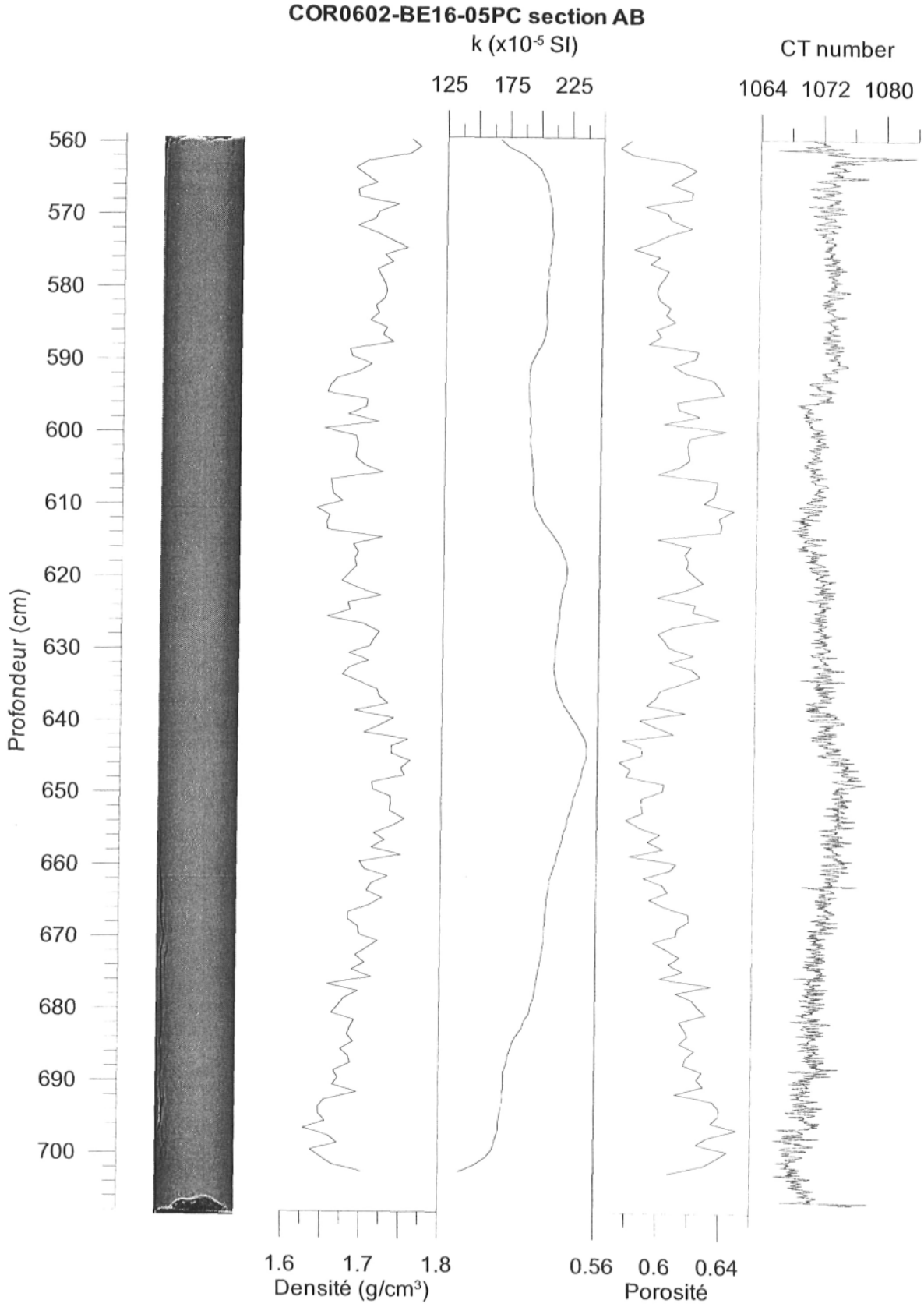
COR0602-BE16-05PC section AB
k (x10-5 SI)
125 175 225
CT number
1064 1072 1080
Profondeur (cm)
560
570
580
590
600
610
620
630
640
650
660
670
680
690
700
1.6 1.7 1.8
Densité (g/cm3)
0.56 0.6 0.64
Porosité

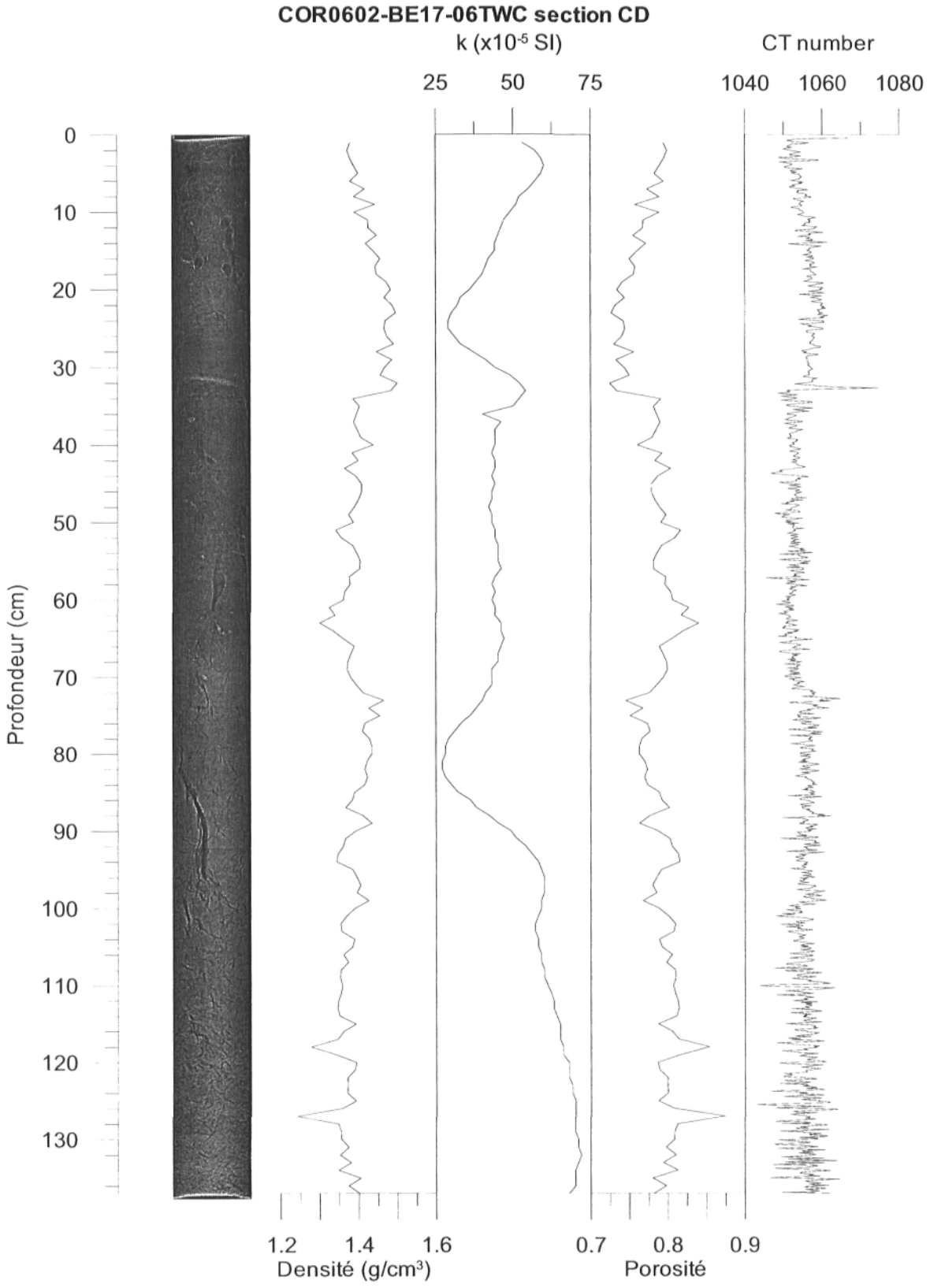
COR0602-BE17-06TWC section CD
k (x10-5 SI)
25
50
75
CT number
1040
1060
1080
Profondeur (cm)
0
10
20
30
40
50
60
70
80
90
100
110
120
130
1.2
1.4
1.6
Densité (g/cm3)
0.7
0.8
0.9
Porosité

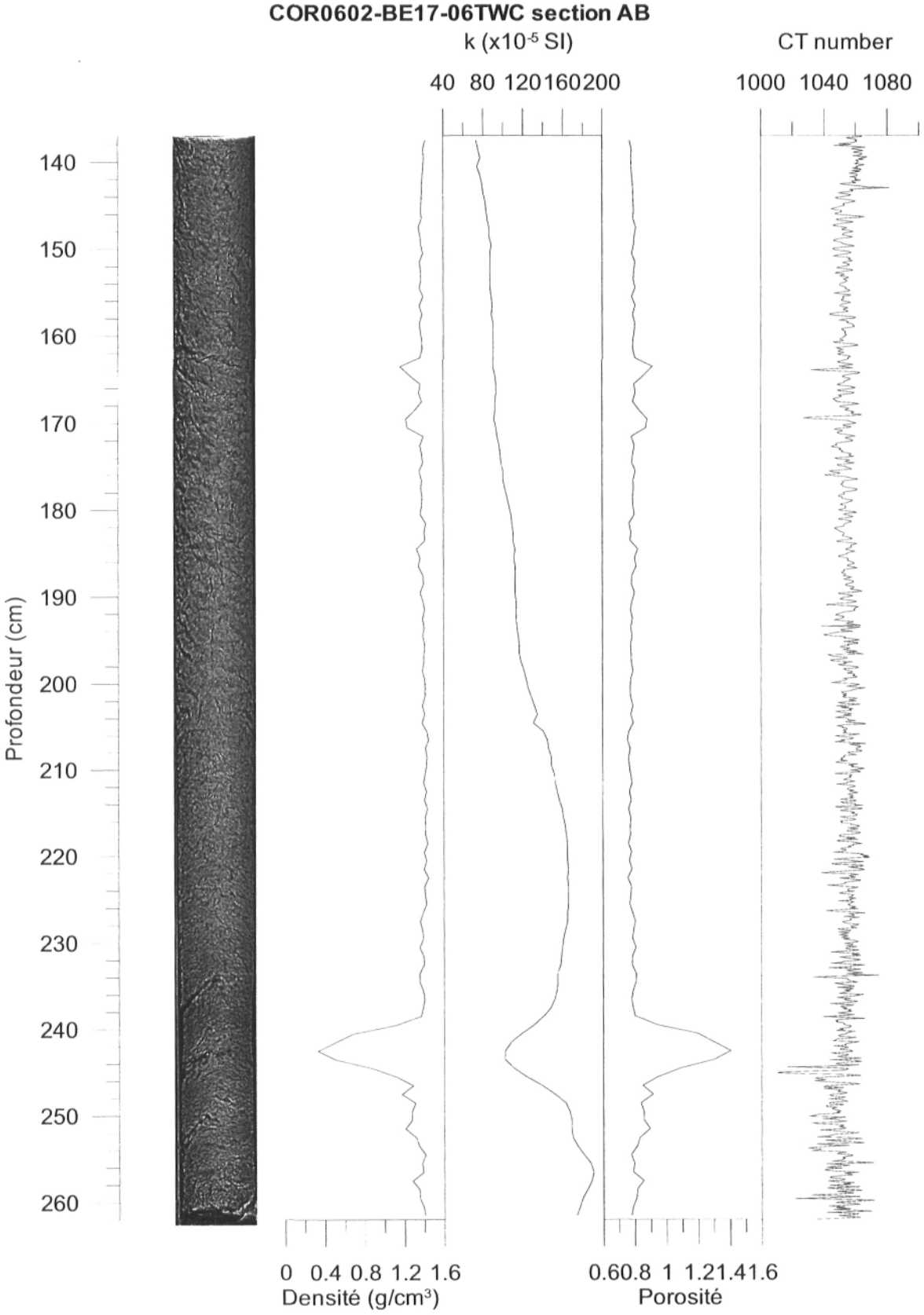
COR0602-BE17-06TWC section AB
k (x10-5 SI)
40 80 120160200
CT number
1000 1040 1080
Profondeur (cm)
140
150
160
170
180
190
200
210
220
230
240
250
260
0 0.4 0.8 1.2 1.6
Densité (g/cm3)
0.60.8 1 1.21.41.6
Porosité

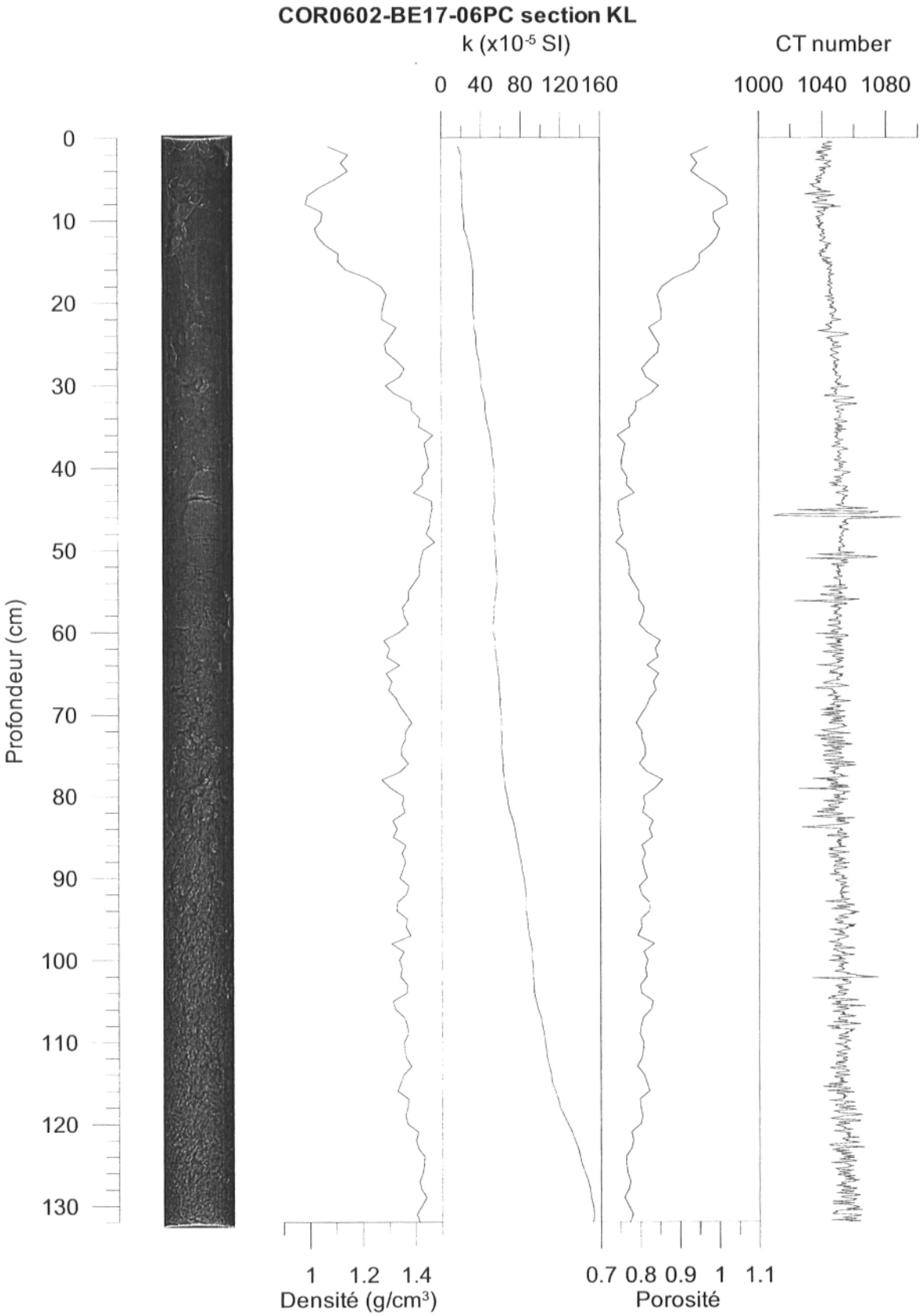
COR0602-BE17-06PC section KL
k (x10-5 SI)
0 40 80 120 160
CT number
1000 1040 1080
Profondeur (cm)
0
10
20
30
40
50
60
70
80
90
100
110
120
130
1 1.2 1.4
Densité (g/cm3)
0.7 0.8 0.9 1 1.1
Porosité

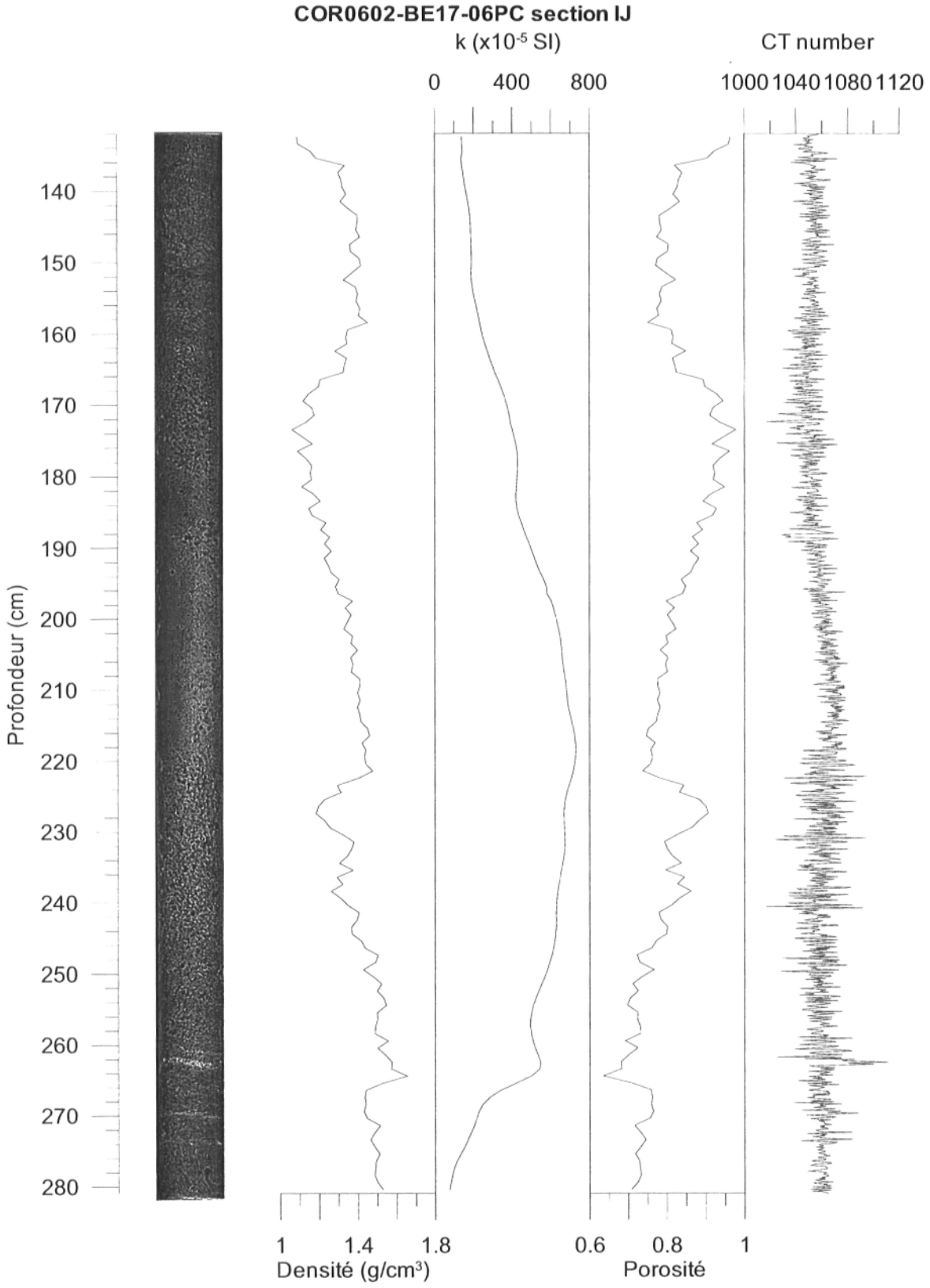
COR0602-BE17-06PC section IJ
k (x10-5 SI)
0
400
800
CT number
1000
1040
1080
1120
Profondeur (cm)
140
150
160
170
180
190
200
210
220
230
240
250
260
270
280
1
1.4
1.8
Densité (g/cm3)
0.6
0.8
1
Porosité

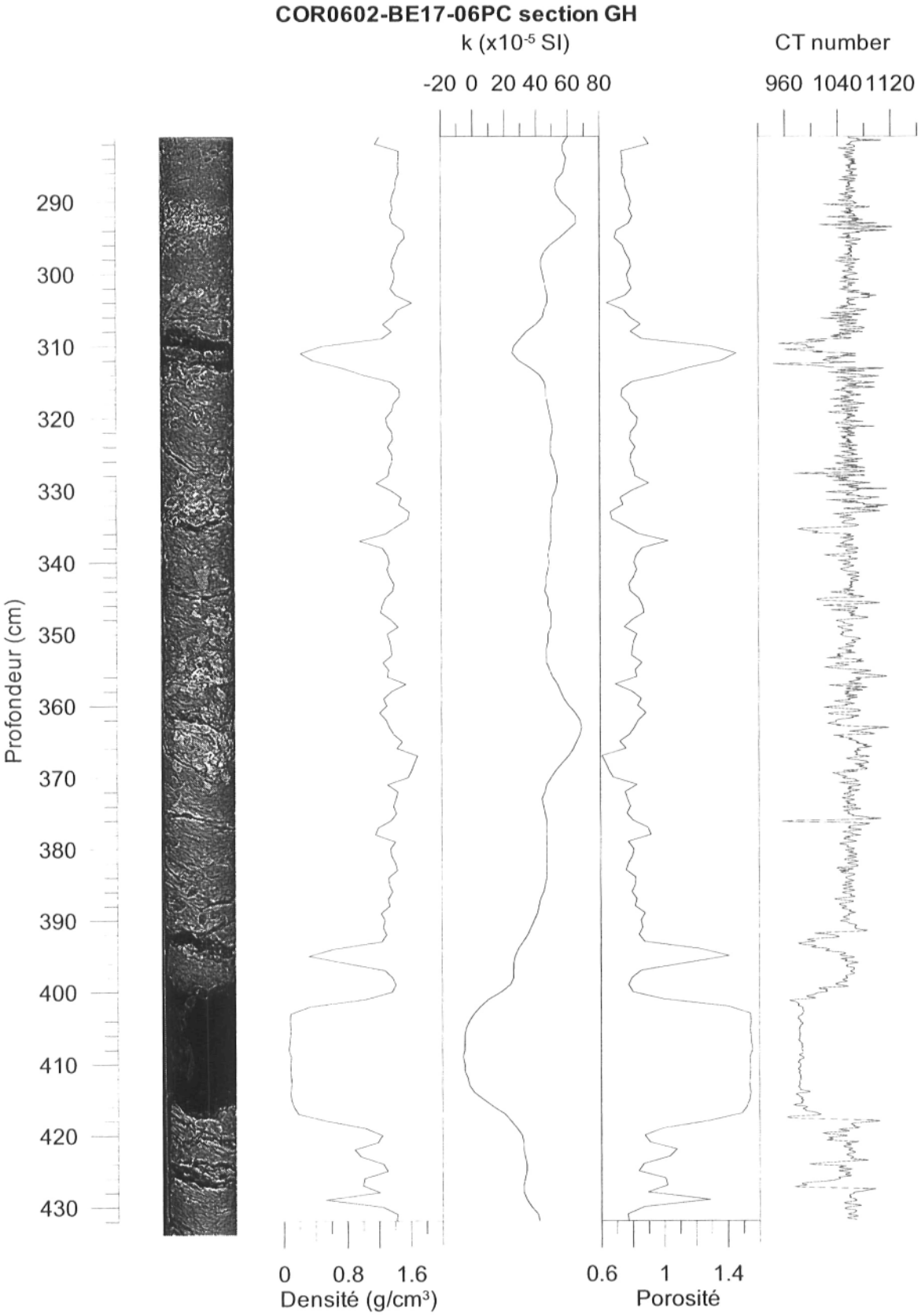
COR0602-BE17-06PC section GH
k (x10-5 SI)
-20 0 20 40 60 80
CT number
960 1040 1120
Profondeur (cm)
290
300
310
320
330
340
350
360
370
380
390
400
410
420
430
0 0.8 1.6
Densité (g/cm3)
0.6 1 1.4
Porosité

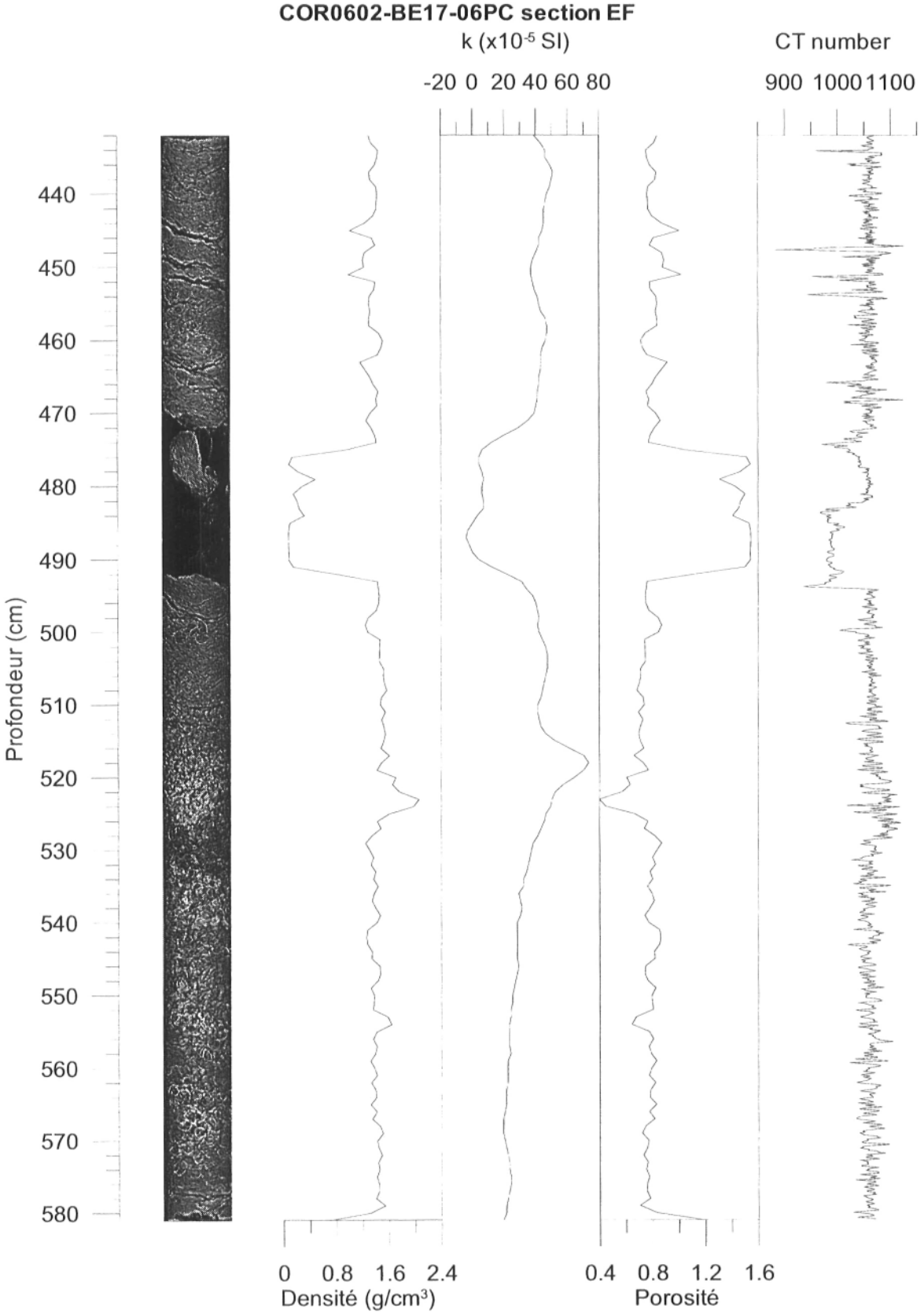
COR0602-BE17-06PC section EF
k (x10-5 SI)
-20 0 20 40 60 80
CT number
900 1000 1100
Profondeur (cm)
440
450
460
470
480
490
500
510
520
530
540
550
560
570
580
0 0.8 1.6 2.4
Densité (g/cm3)
0.4 0.8 1.2 1.6
Porosité

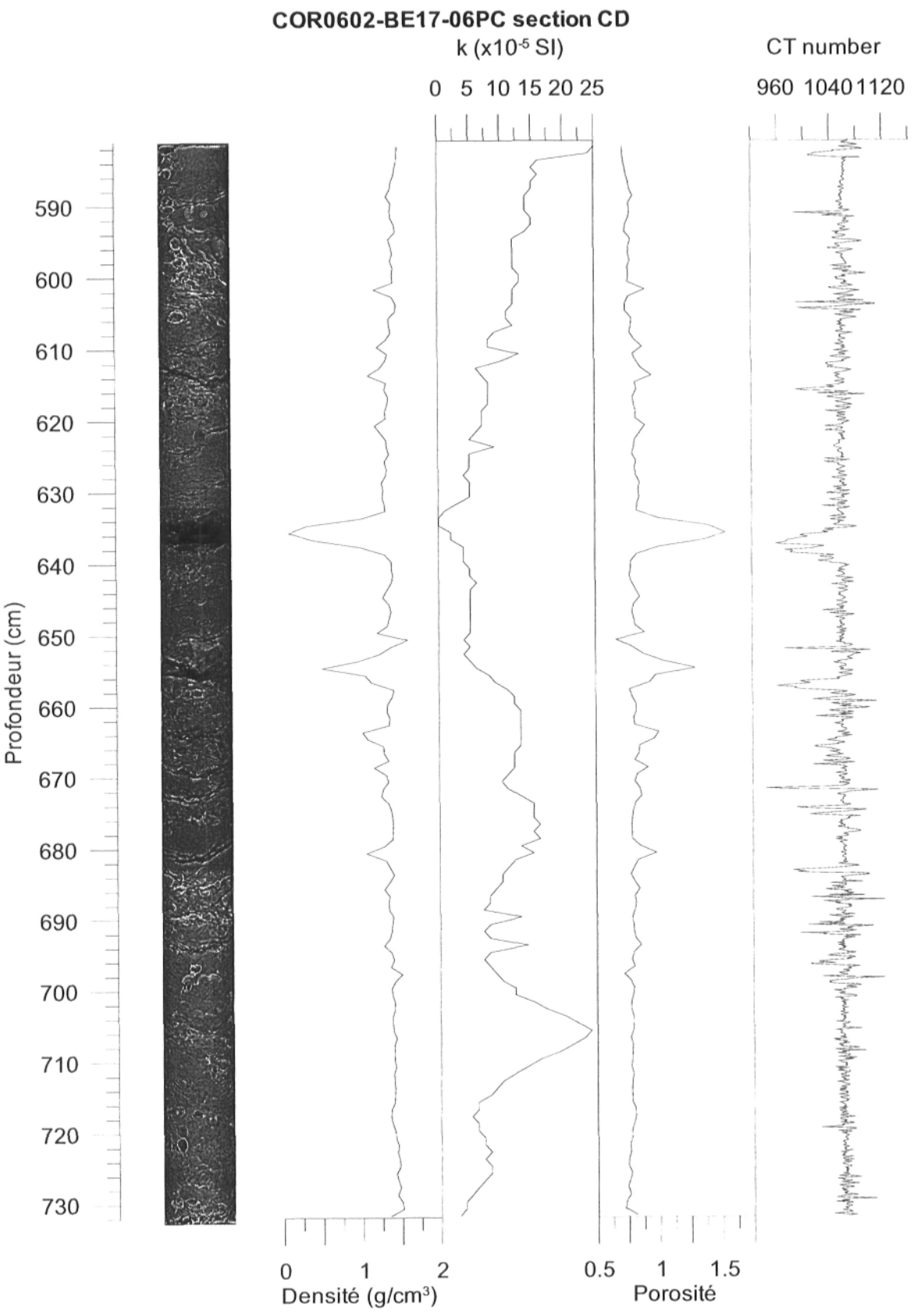
COR0602-BE17-06PC section CD
k (x10-5 SI)
0 5 10 15 20 25
CT number
960 1040 1120
Profondeur (cm)
590
600
610
620
630
640
650
660
670
680
690
700
710
720
730
0 1 2
Densité (g/cm3)
0.5 1 1.5
Porosité

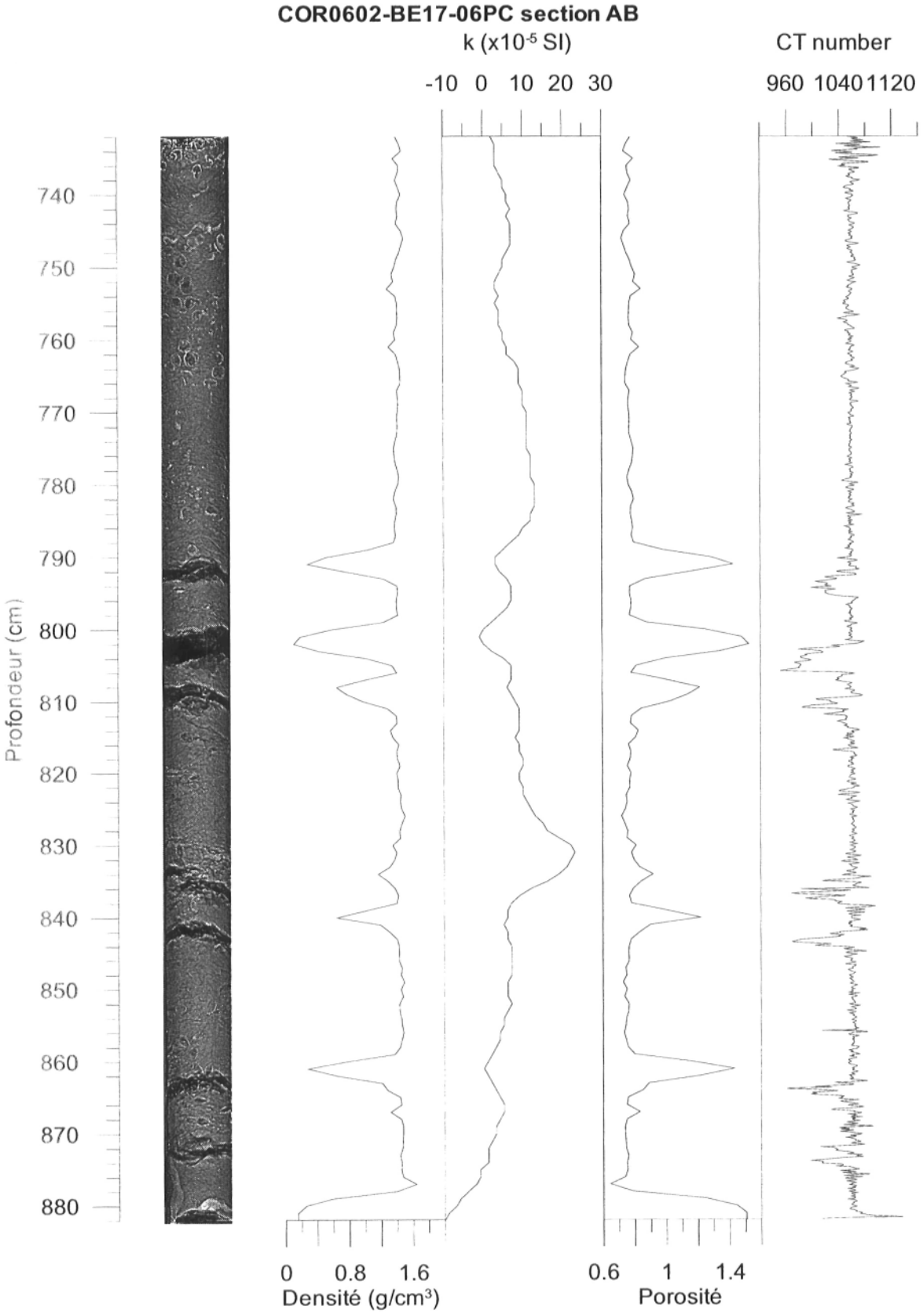
COR0602-BE17-06PC section AB
k (x10-5 SI)
-10 0 10 20 30
CT number
960 1040 1120
Profondeur (cm)
740
750
760
770
780
790
800
810
820
830
840
850
860
870
880
0 0.8 1.6
Densité (g/cm3)
0.6 1 1.4
Porosité

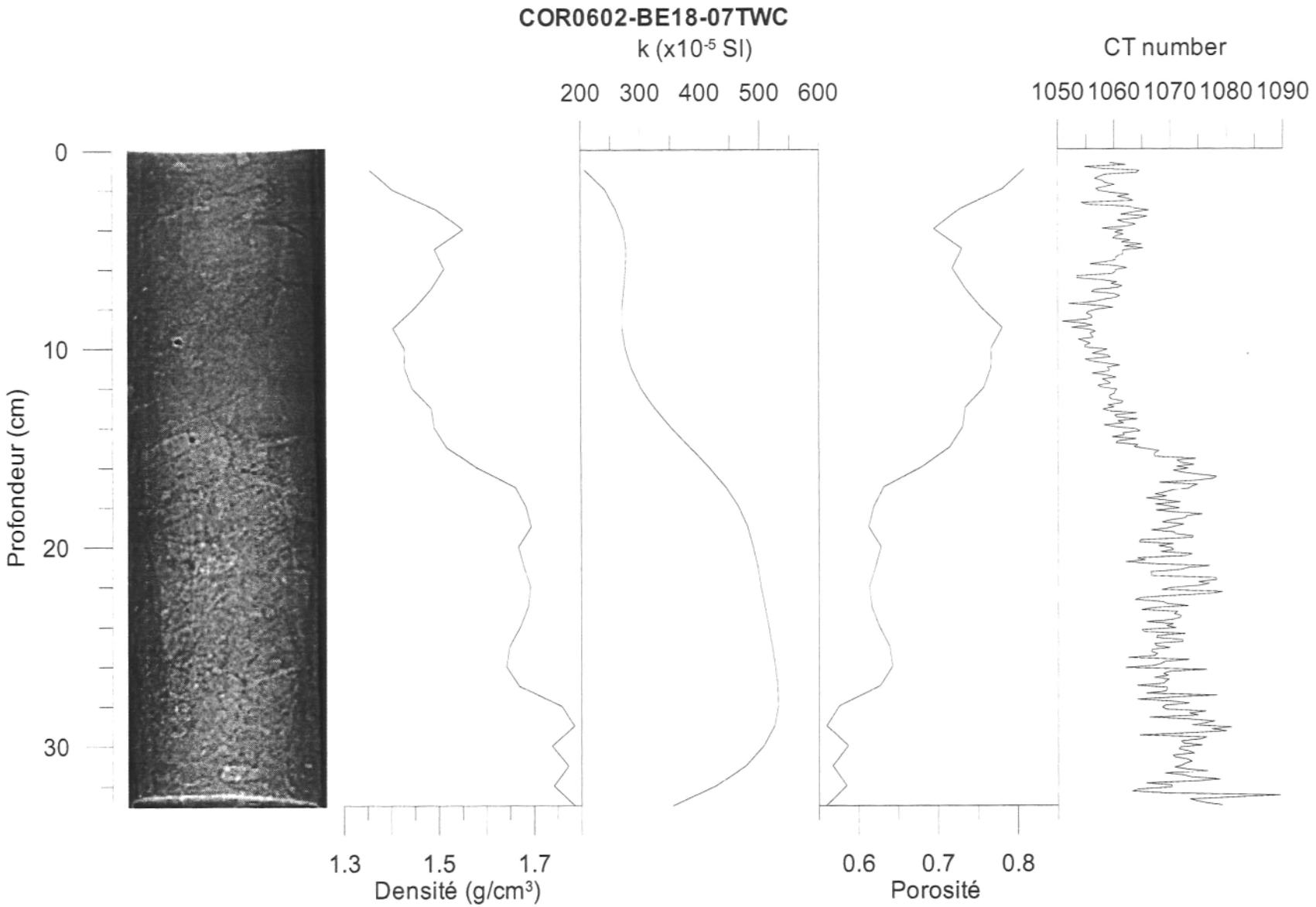
COR0602-BE18-07TWC
k (x10-5 SI)
200 300 400 500 600
CT number
1050 1060 1070 1080 1090
0
10
20
30
Profondeur (cm)
1.3 1.5 1.7
Densité (g/cm3)
0.6 0.7 0.8
Porosité

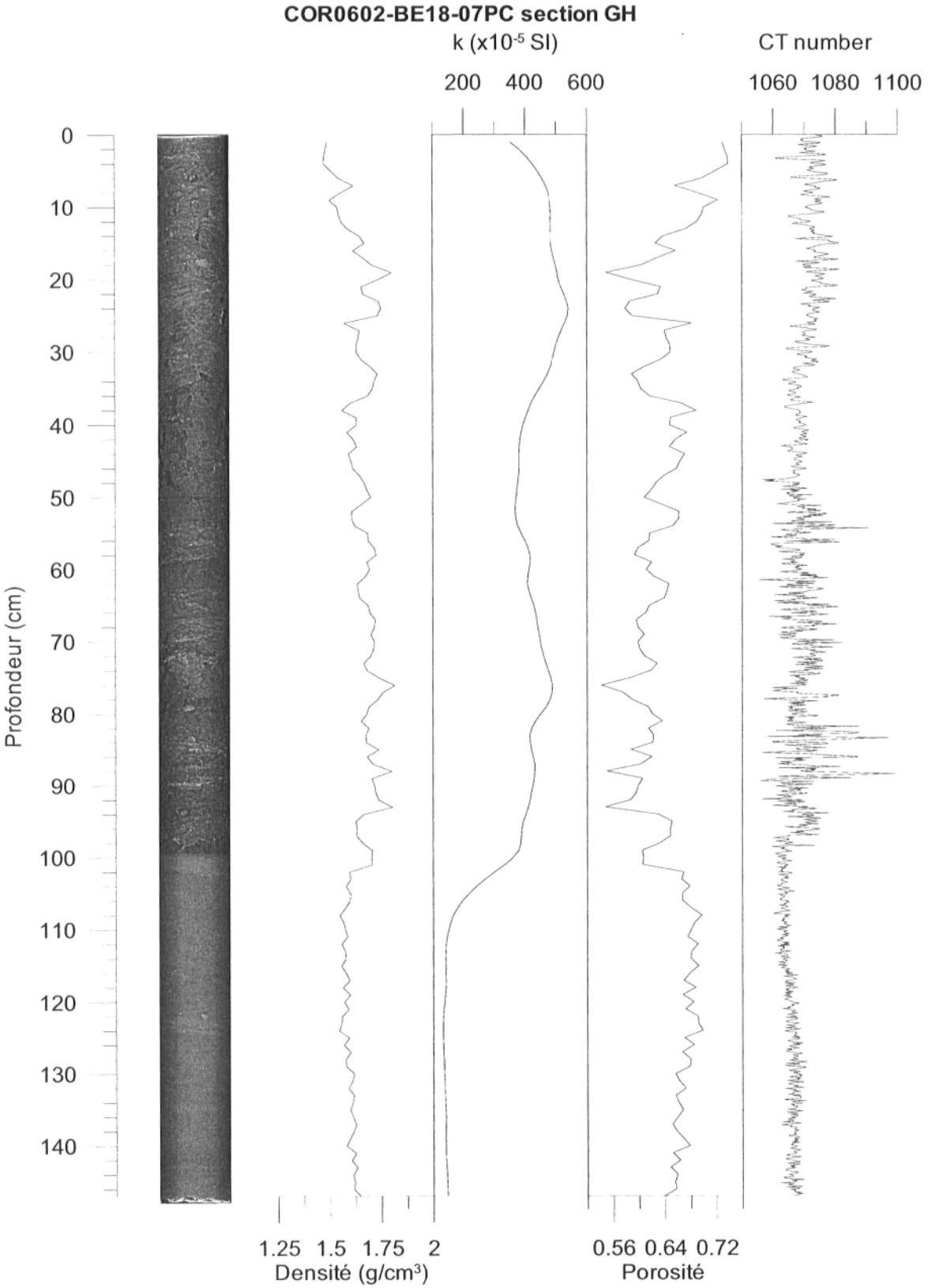
COR0602-BE18-07PC section GH
k (x10-5 SI)
200 400 600
CT number
1060 1080 1100
0
10
20
30
40
50
60
70
80
90
100
110
120
130
140
Profondeur (cm)
1.25 1.5 1.75 2
Densité (g/cm3)
0.56 0.64 0.72
Porosité

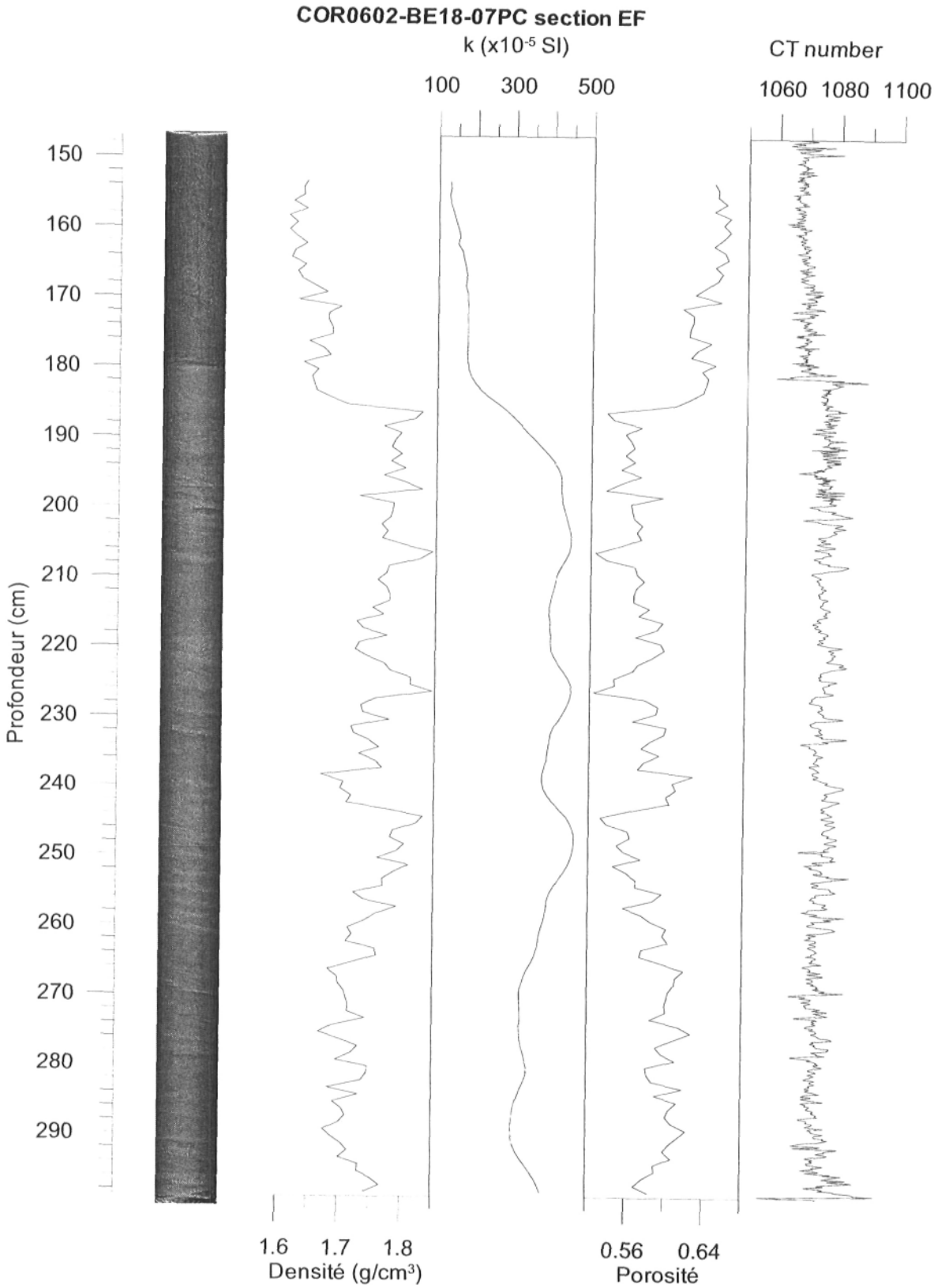
COR0602-BE18-07PC section EF
k (x10-5 SI)
100
300
500
CT number
1060
1080
1100
150
160
170
180
190
200
210
220
230
240
250
260
270
280
290
Profondeur (cm)
1.6
1.7
1.8
Densité (g/cm3)
0.56
0.64
Porosité

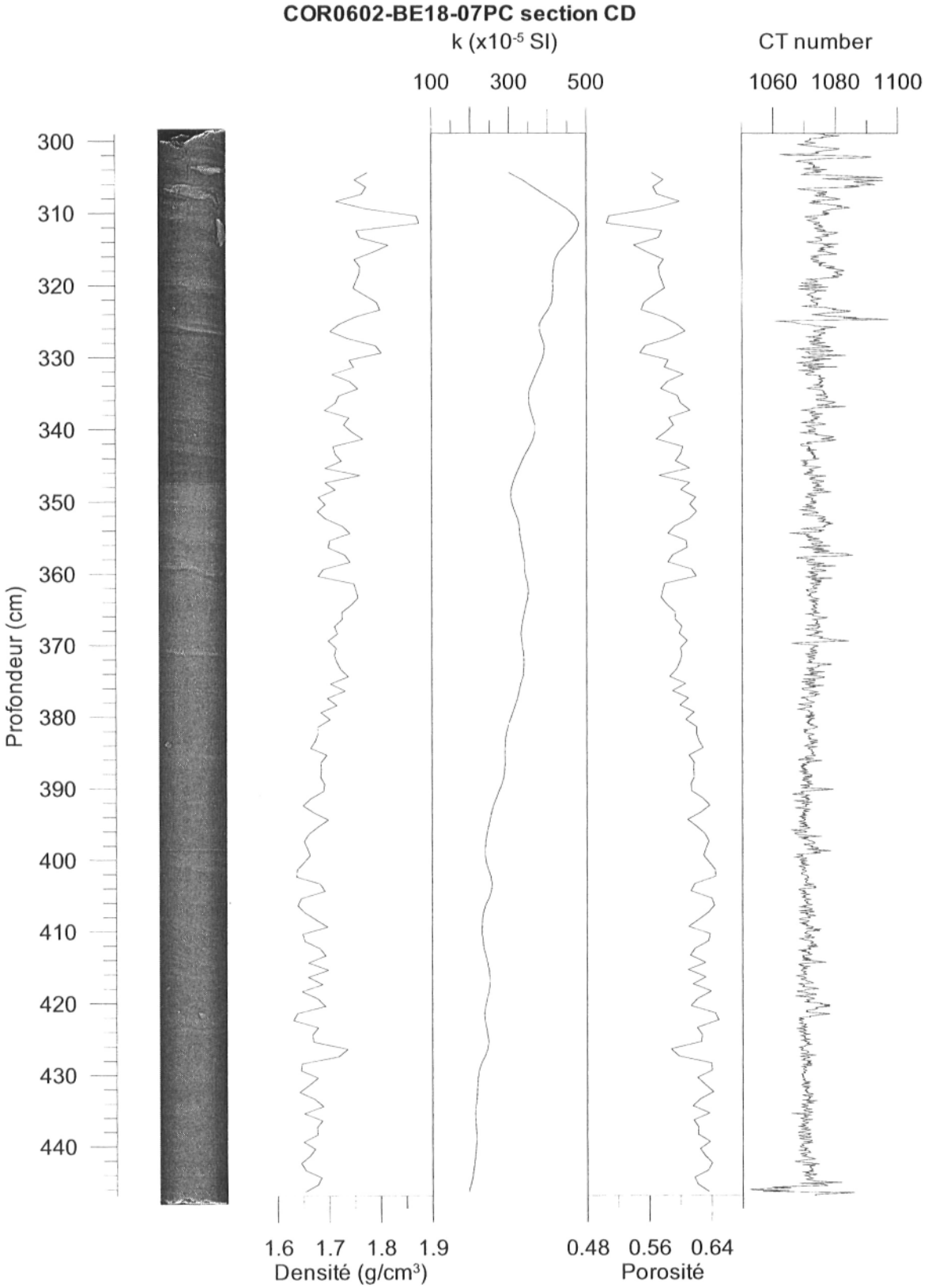
COR0602-BE18-07PC section CD
k (x10-5 SI)
100 300 500
CT number
1060 1080 1100
Profondeur (cm)
300
310
320
330
340
350
360
370
380
390
400
410
420
430
440
1.6 1.7 1.8 1.9
Densité (g/cm3)
0.48 0.56 0.64
Porosité

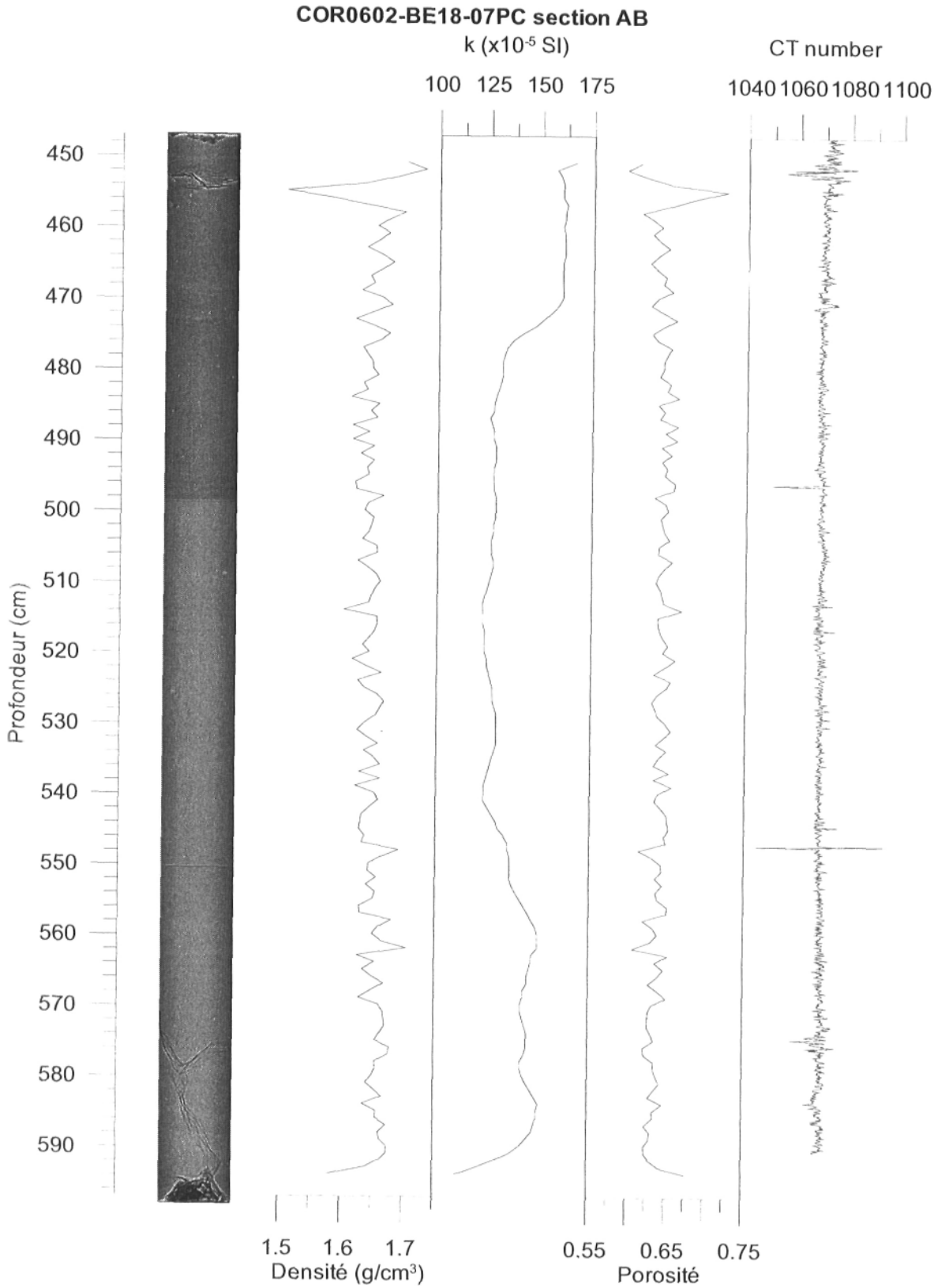
COR0602-BE18-07PC section AB
k (x10-5 SI)
100 125 150 175
CT number
1040 1060 1080 1100
Profondeur (cm)
450
460
470
480
490
500
510
520
530
540
550
560
570
580
590
1.5 1.6 1.7
Densité (g/cm3)
0.55 0.65 0.75
Porosité

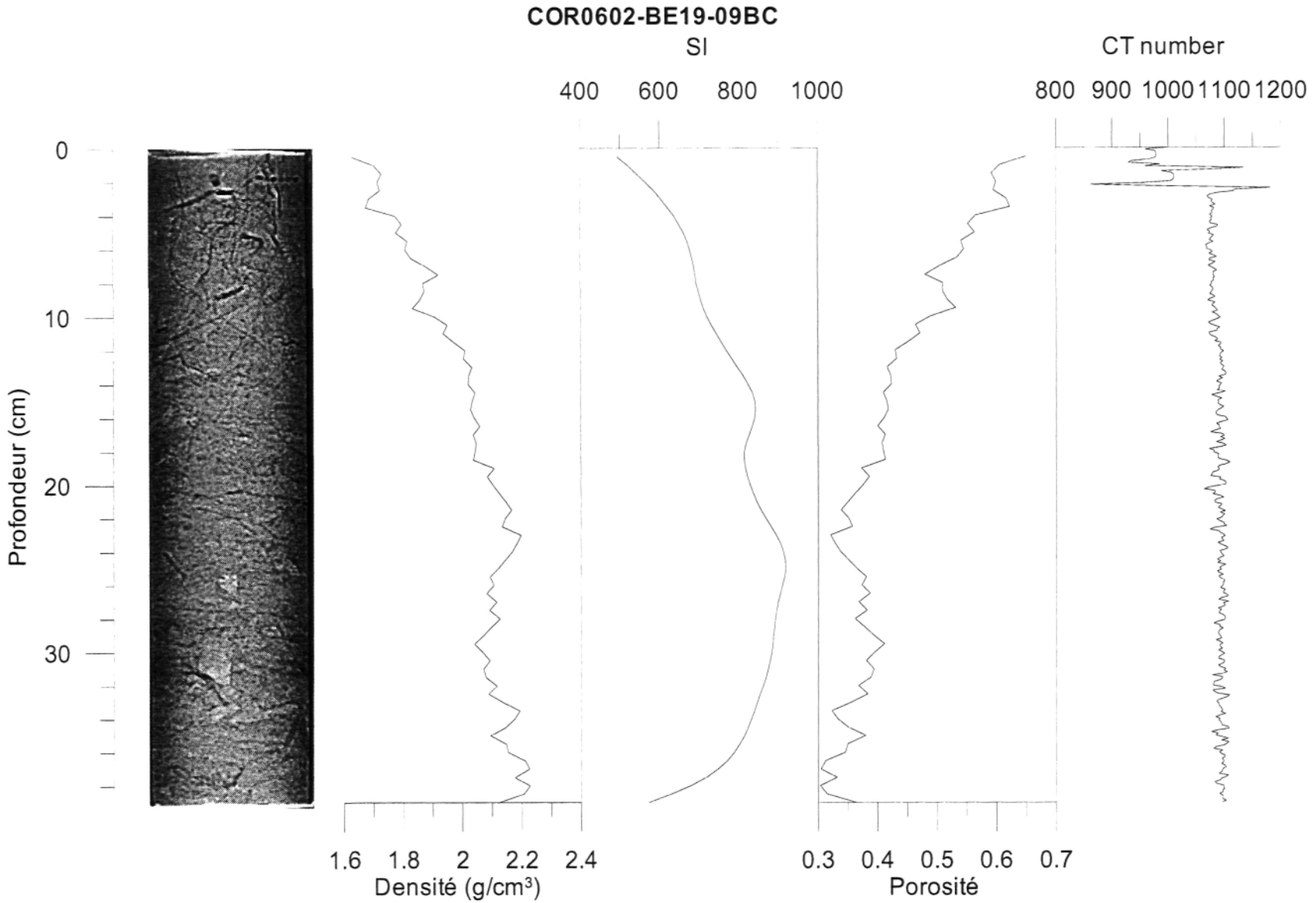
COR0602-BE19-09BC
SI
400 600 800 1000
CT number
800 900 1000 1100 1200
0
10
20
30
Profondeur (cm)
1.6 1.8 2 2.2 2.4
Densité (g/cm³)
0.3 0.4 0.5 0.6 0.7
Porosité

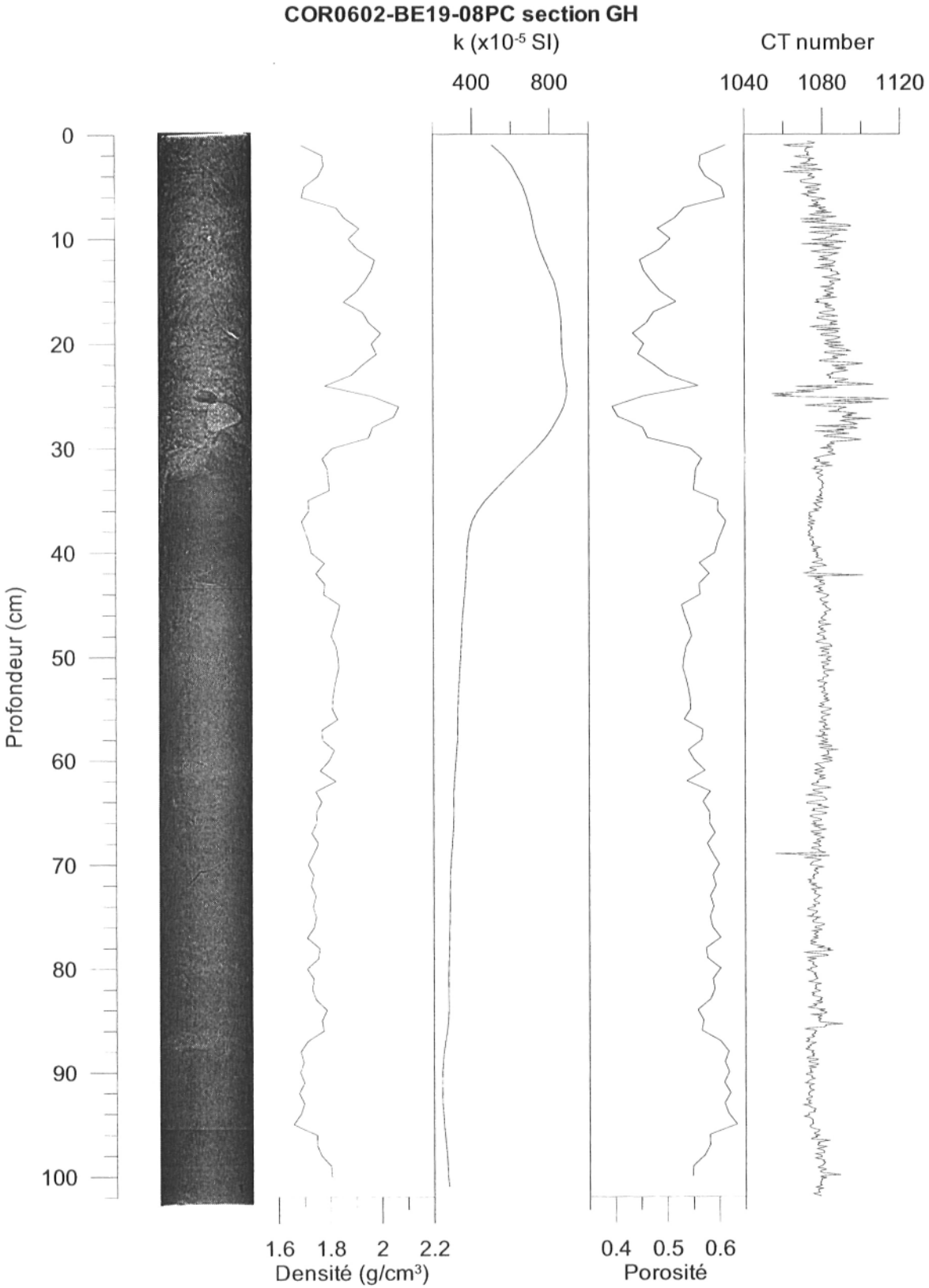
COR0602-BE19-08PC section GH
k (x10-5 SI)
400
800
CT number
1040
1080
1120
0
10
20
30
40
50
60
70
80
90
100
Profondeur (cm)
1.6
1.8
2
2.2
Densité (g/cm3)
0.4
0.5
0.6
Porosité

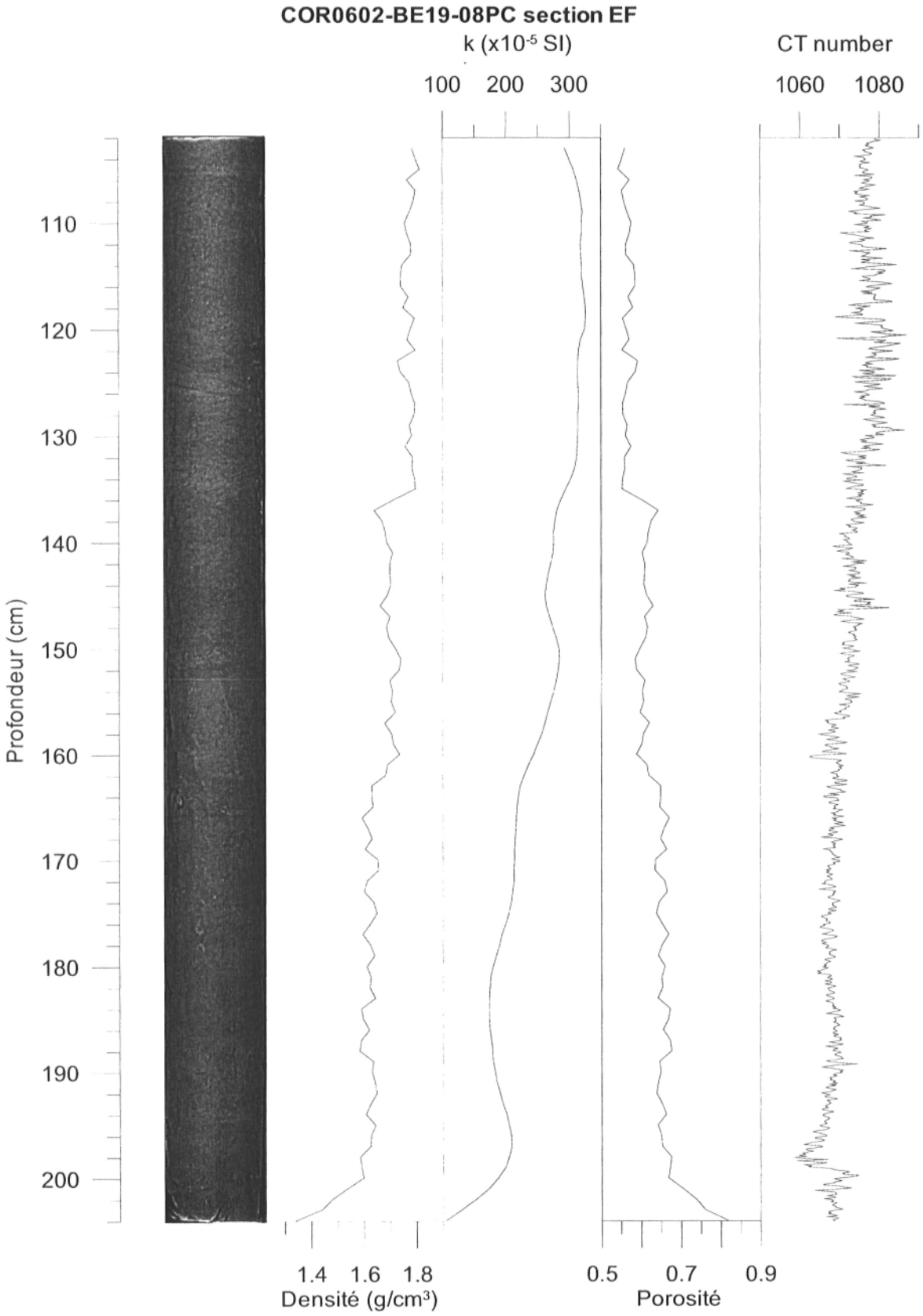
COR0602-BE19-08PC section EF
k (x10-5 SI)
100 200 300
CT number
1060 1080
Profondeur (cm)
110
120
130
140
150
160
170
180
190
200
1.4 1.6 1.8
Densité (g/cm3)
0.5 0.7 0.9
Porosité

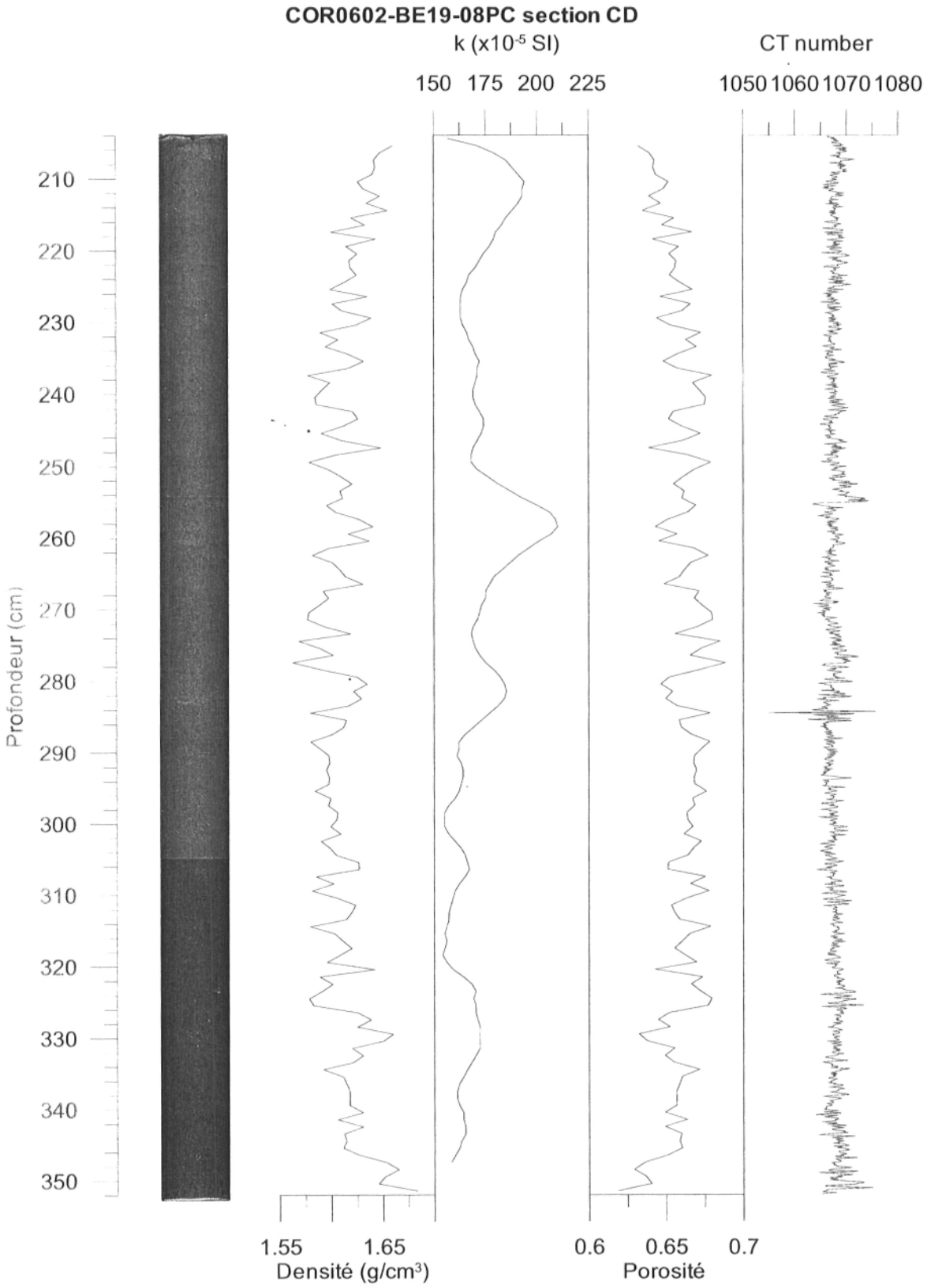
COR0602-BE19-08PC section CD
k (x10-5 SI)
150 175 200 225
CT number
1050 1060 1070 1080
Profondeur (cm)
210
220
230
240
250
260
270
280
290
300
310
320
330
340
350
1.55 1.65
Densité (g/cm3)
0.6 0.65 0.7
Porosité

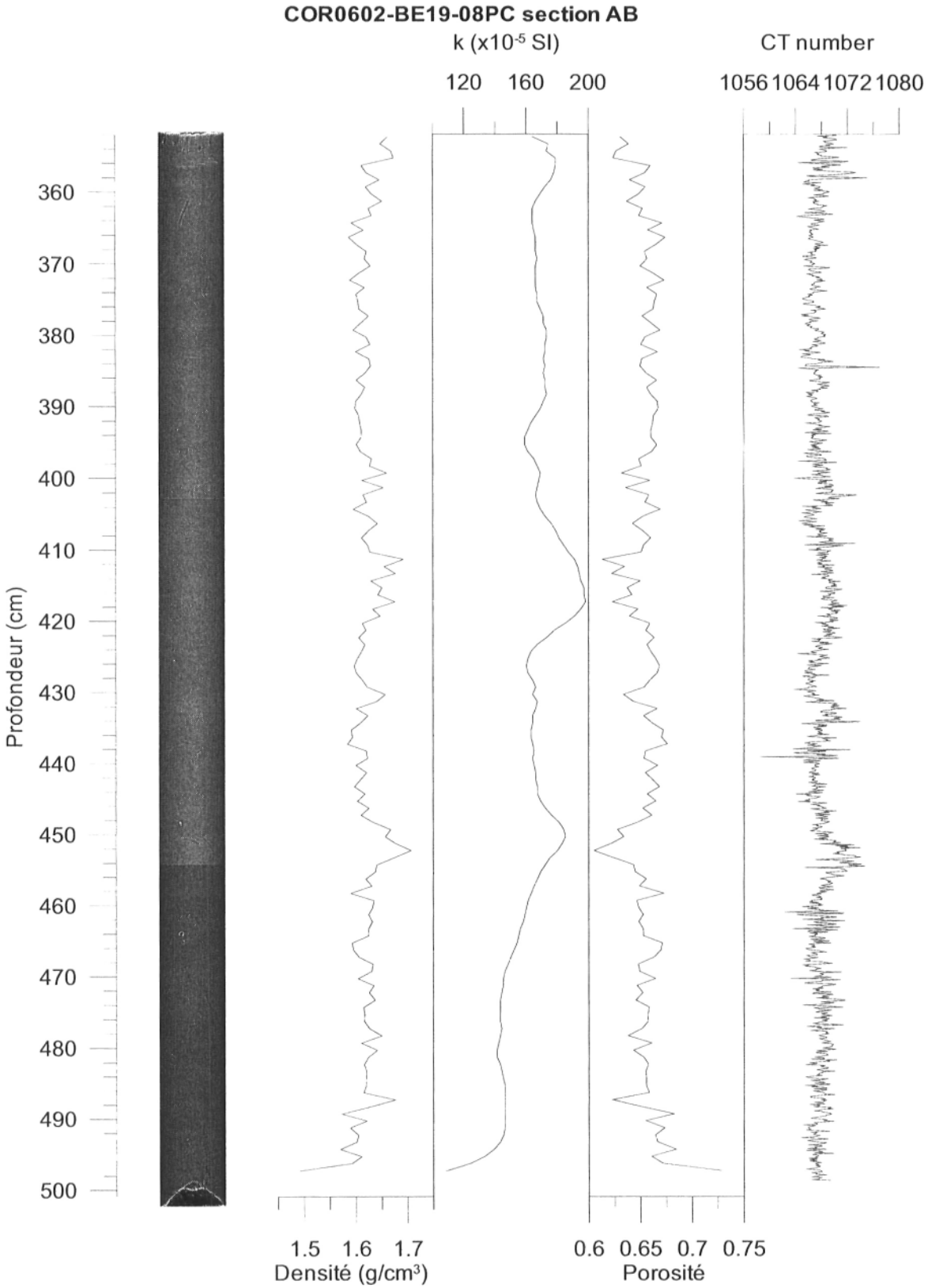
COR0602-BE19-08PC section AB
k (x10-5 SI)
120 160 200
CT number
1056 1064 1072 1080
Profondeur (cm)
360
370
380
390
400
410
420
430
440
450
460
470
480
490
500
1.5 1.6 1.7
Densité (g/cm3)
0.6 0.65 0.7 0.75
Porosité

ANNEXE C : Courbes granulométriques cumulatives

Courbes granulométrique cumulatives pour les échantillons :

COR0307-BE01-40PC
COR0307-BE01-47BC
COR0307-BE12-52BC
COR0307-BE12-53LH
COR0503-BE02-02BC
COR0503-BE02-02TWC
COR0503-BE04-04BC
COR0503-BE05-05BC
COR0503-BE07-40BC

COR0307-BE01-40PC

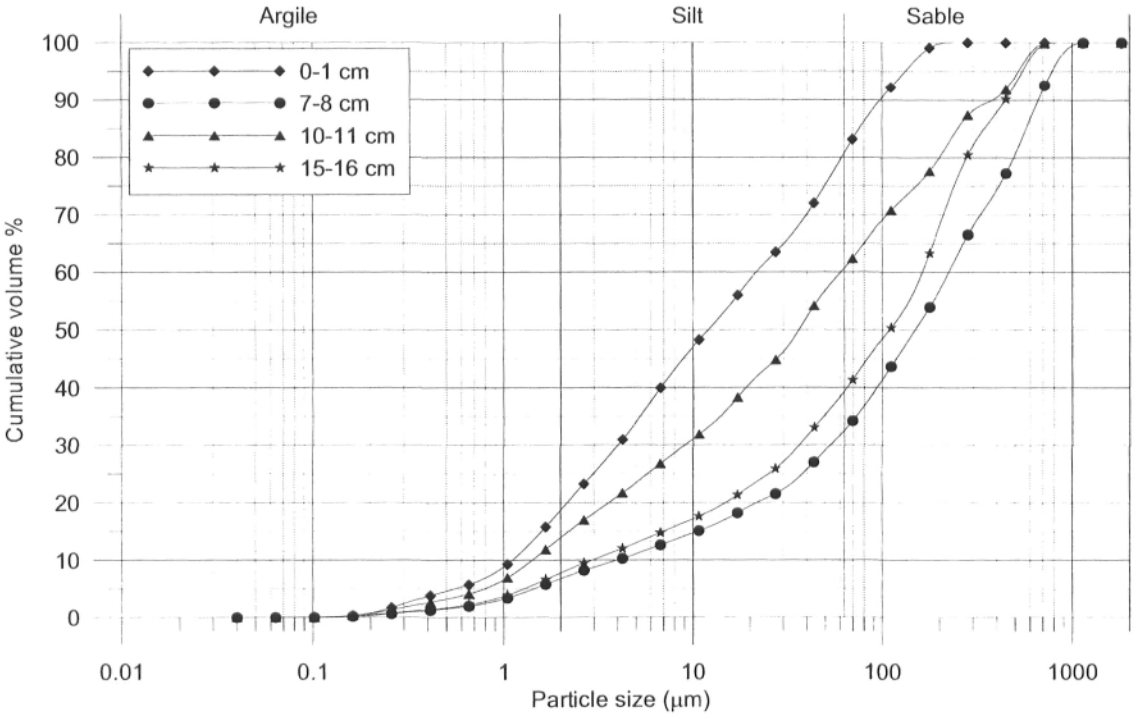

COR0307-BE01-40PC

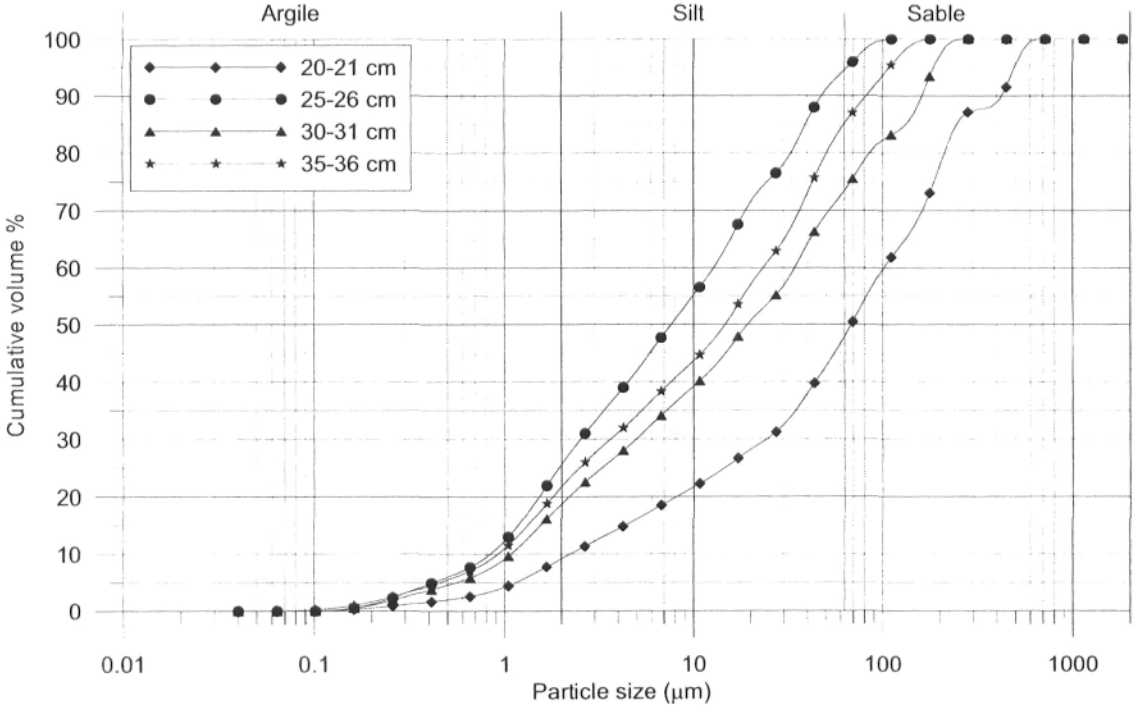

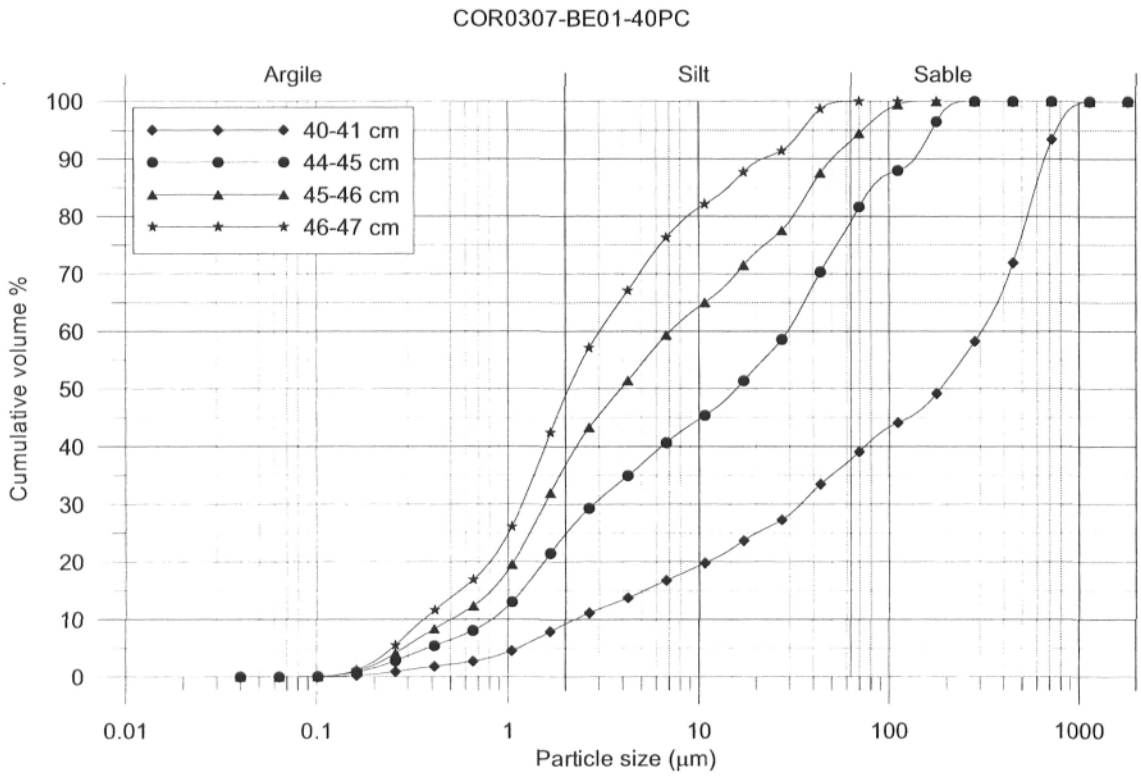
COR0307-BE01-40PC
Argile
Silt
Sable
40-41 cm
44-45 cm
45-46 cm
46-47 cm
Cumulative volume %
Particle size (µm)
0.01
0.1
1
10
100
1000

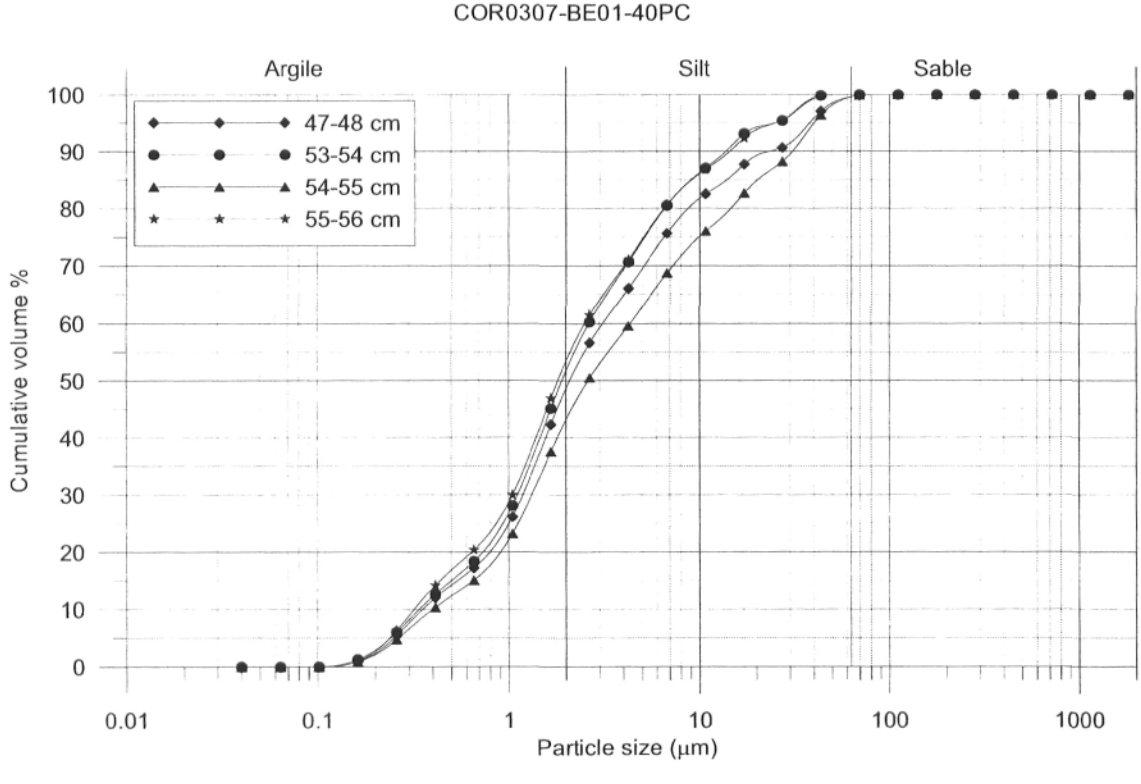
COR0307-BE01-40PC
Argile
Silt
Sable
47-48 cm
53-54 cm
54-55 cm
55-56 cm
Cumulative volume %
Particle size (µm)
0.01
0.1
1
10
100
1000

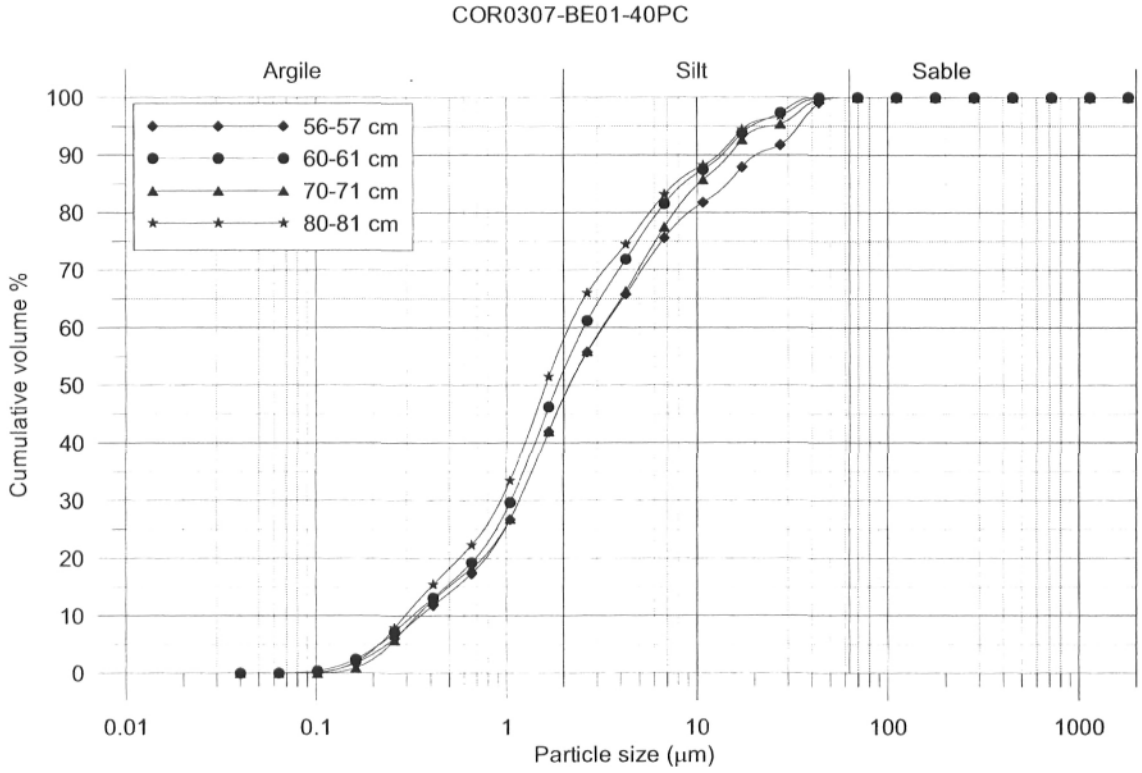
COR0307-BE01-40PC
Argile
Silt
Sable
56-57 cm
60-61 cm
70-71 cm
80-81 cm
Cumulative volume %
Particle size (µm)
0.01
0.1
1
10
100
1000

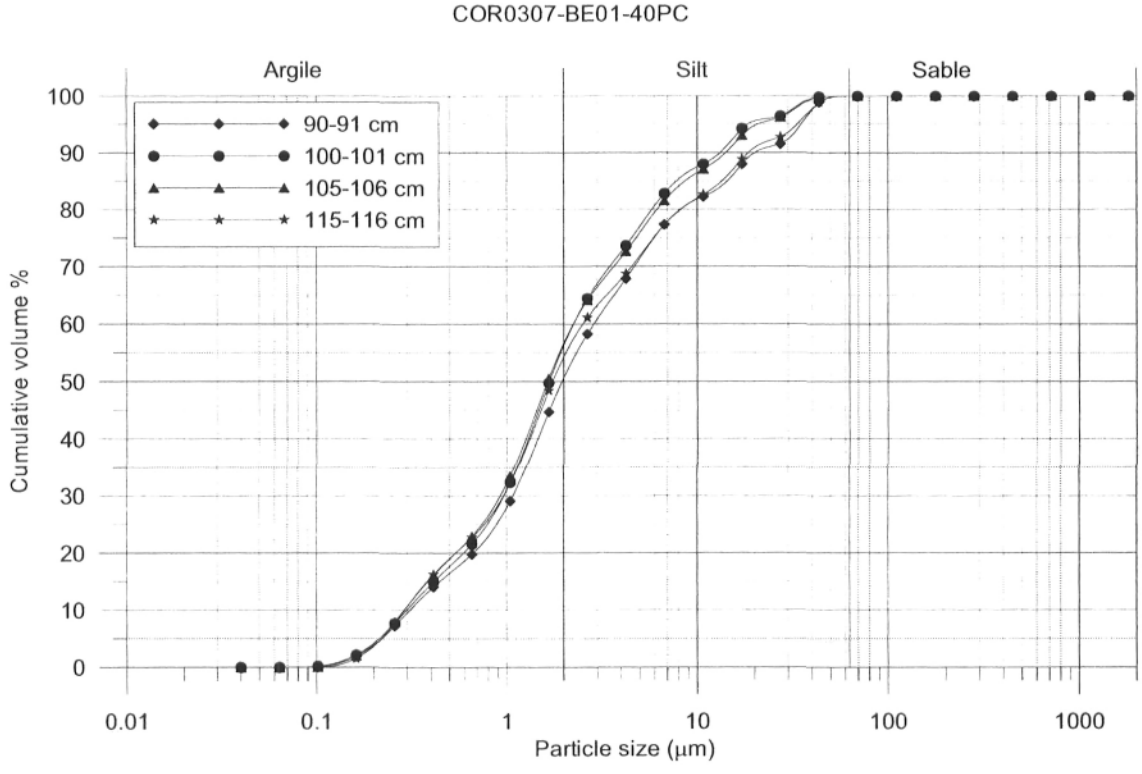
COR0307-BE01-40PC
Argile
Silt
Sable
90-91 cm
100-101 cm
105-106 cm
115-116 cm
Cumulative volume %
Particle size (µm)
0.01
0.1
1
10
100
1000

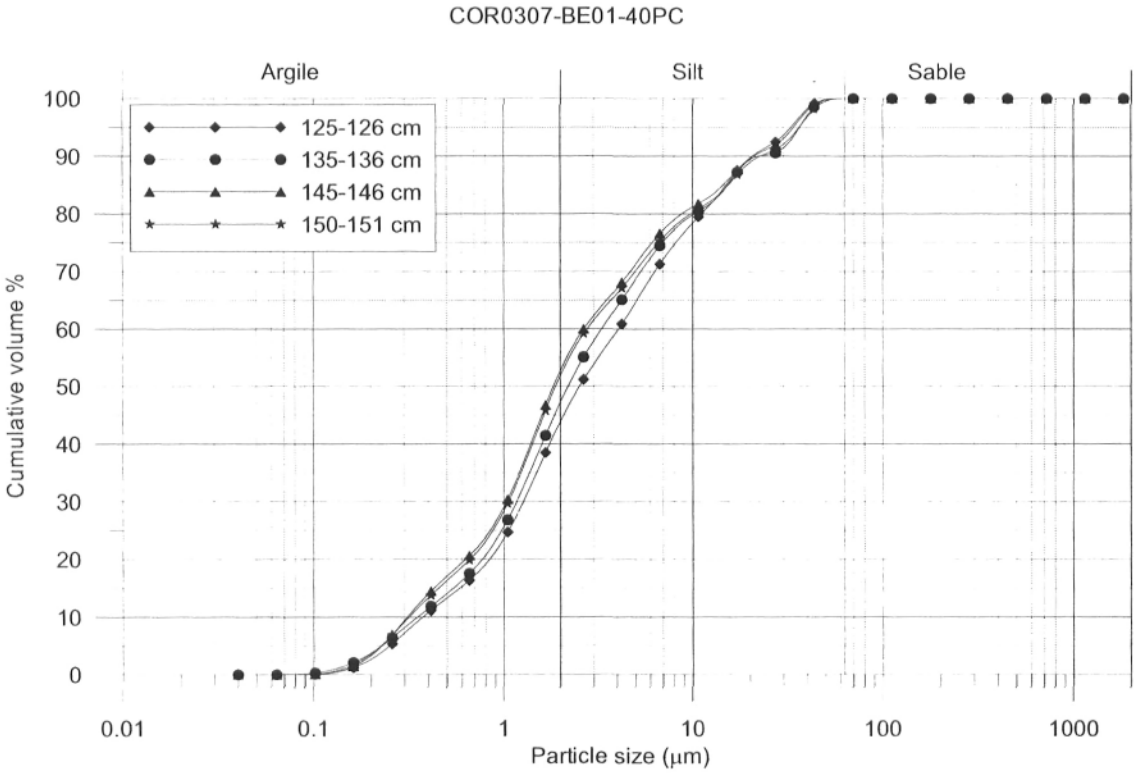
COR0307-BE01-40PC
Argile
Silt
Sable
125-126 cm
135-136 cm
145-146 cm
150-151 cm
Cumulative volume %
Particle size (µm)
0.01
0.1
1
10
100
1000

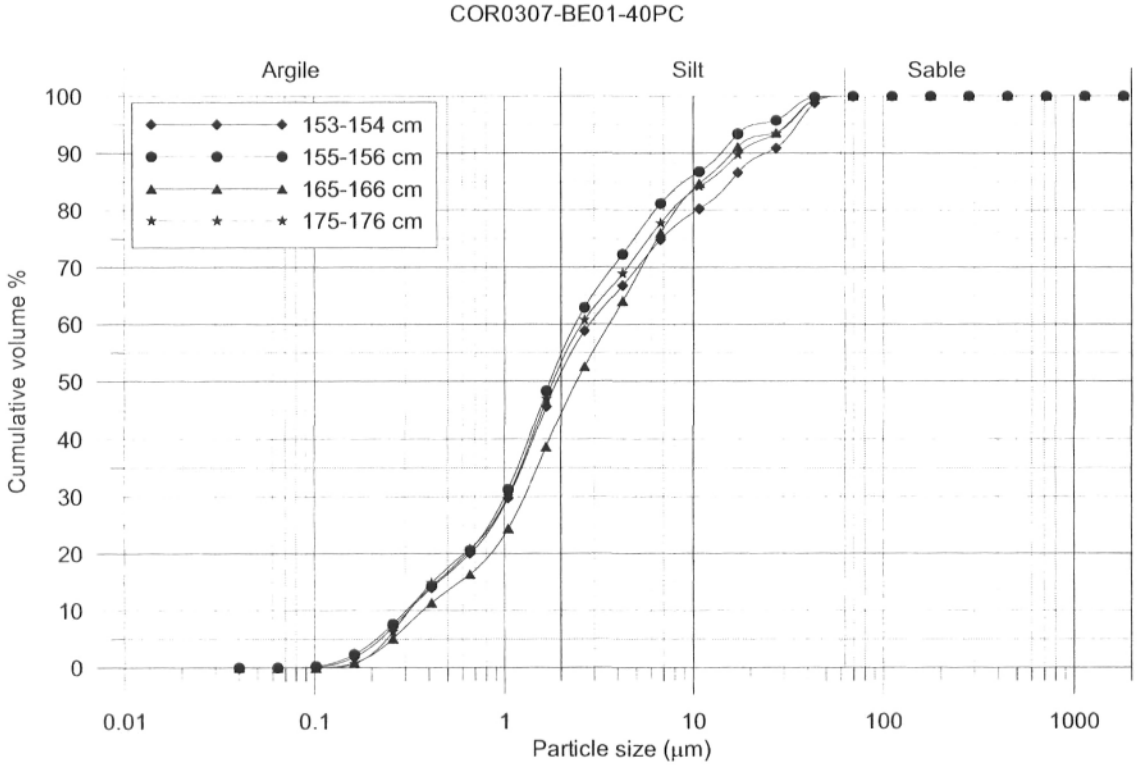
COR0307-BE01-40PC
Argile
Silt
Sable
153-154 cm
155-156 cm
165-166 cm
175-176 cm
Cumulative volume %
Particle size (µm)
0.01
0.1
1
10
100
1000

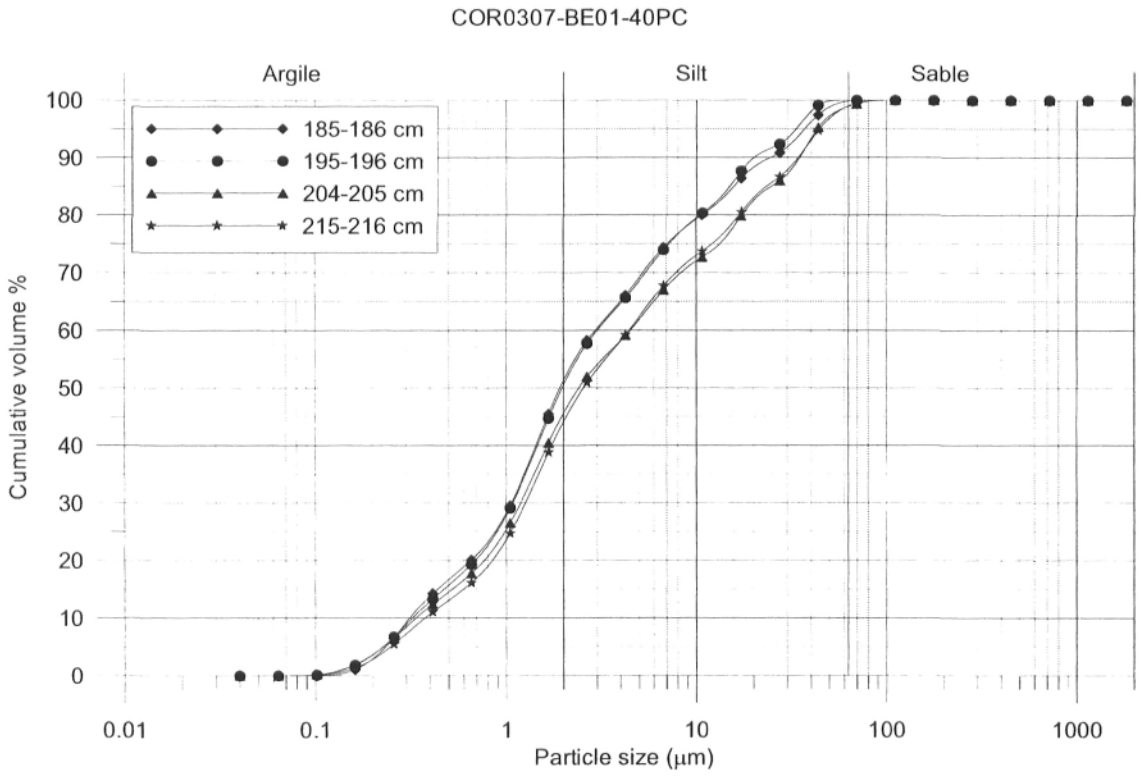
COR0307-BE01-40PC
Argile
Silt
Sable
185-186 cm
195-196 cm
204-205 cm
215-216 cm
Cumulative volume %
Particle size (µm)
0
10
20
30
40
50
60
70
80
90
100
0.01
0.1
1
10
100
1000

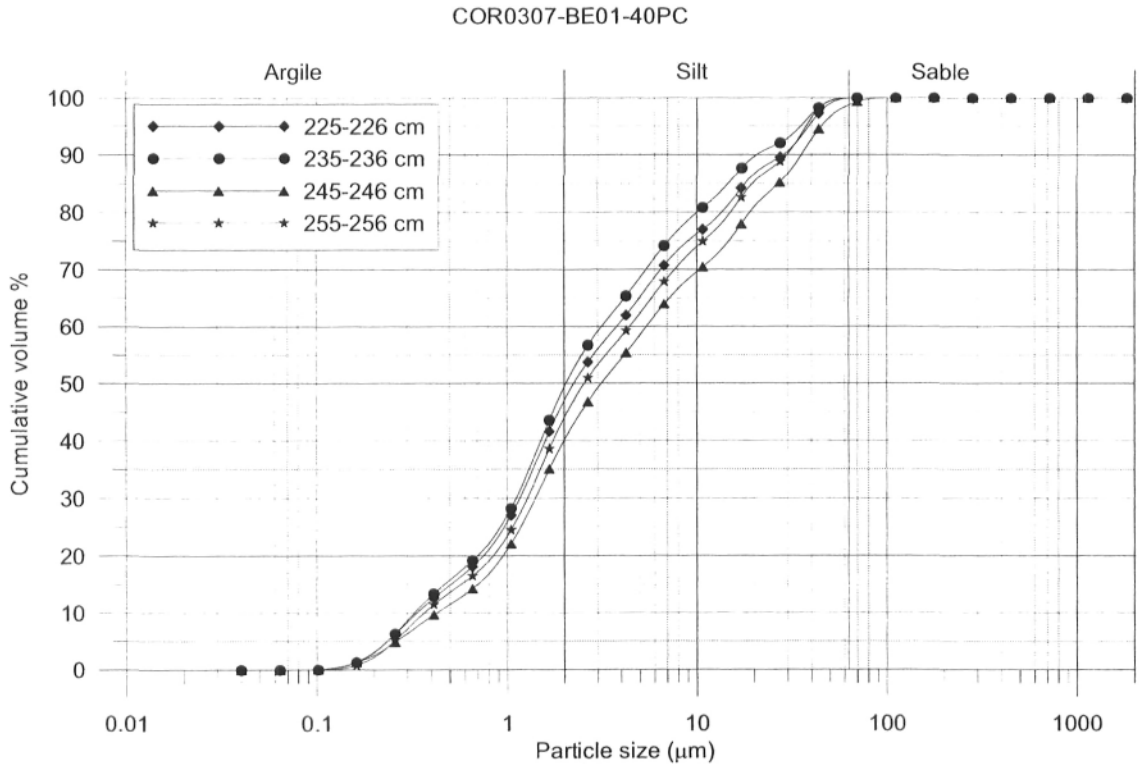
COR0307-BE01-40PC
Argile
Silt
Sable
225-226 cm
235-236 cm
245-246 cm
255-256 cm
Cumulative volume %
Particle size (µm)
0
10
20
30
40
50
60
70
80
90
100
0.01
0.1
1
10
100
1000

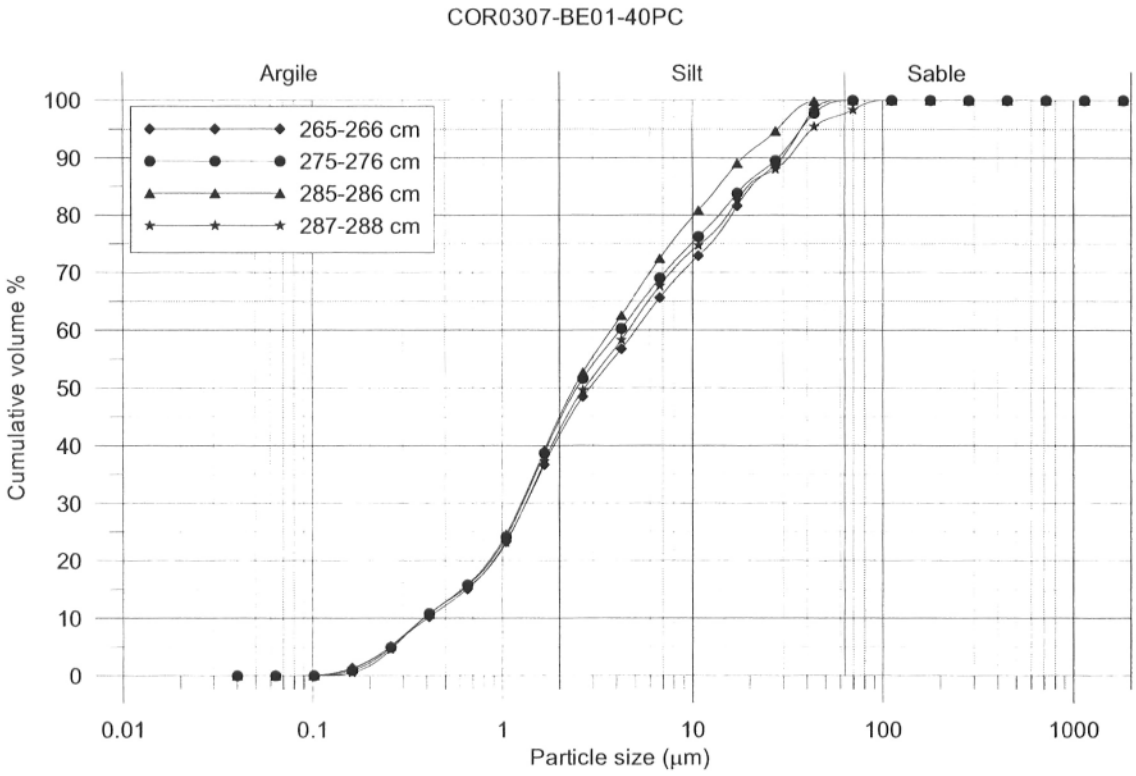
COR0307-BE01-40PC
Argile
Silt
Sable
265-266 cm
275-276 cm
285-286 cm
287-288 cm
Cumulative volume %
Particle size (µm)
0.01
0.1
1
10
100
1000

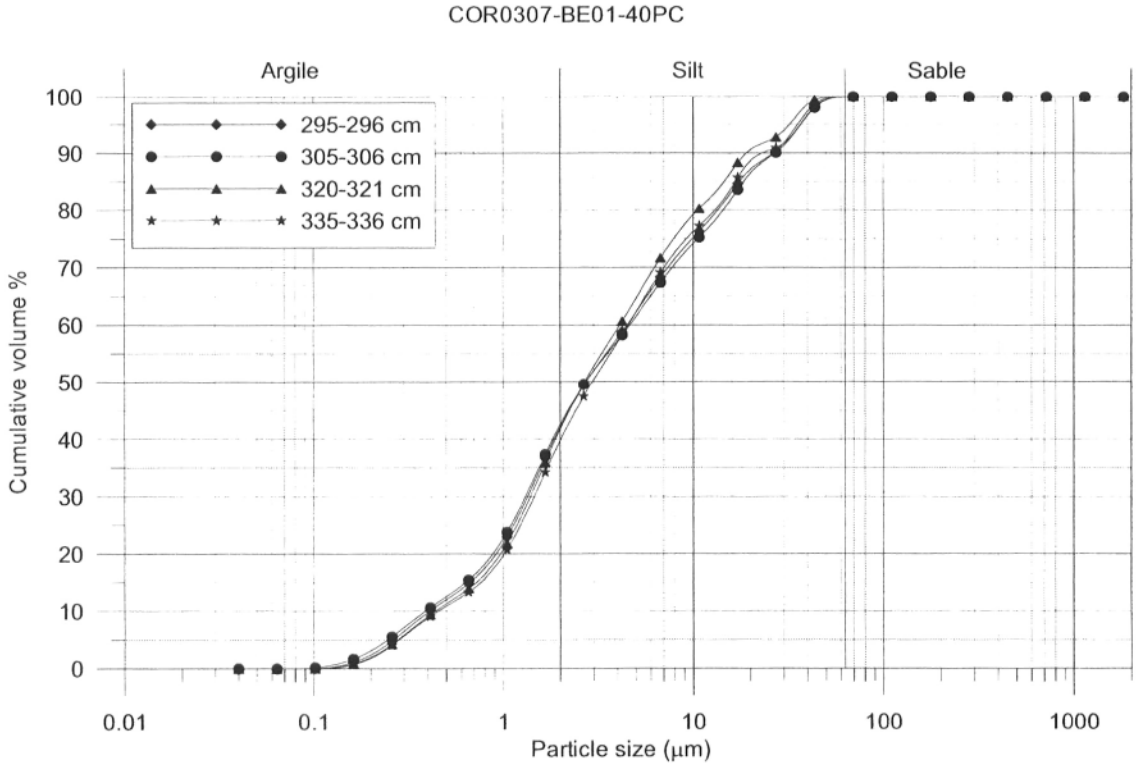
COR0307-BE01-40PC
Argile
Silt
Sable
295-296 cm
305-306 cm
320-321 cm
335-336 cm
Cumulative volume %
Particle size (µm)
0.01
0.1
1
10
100
1000

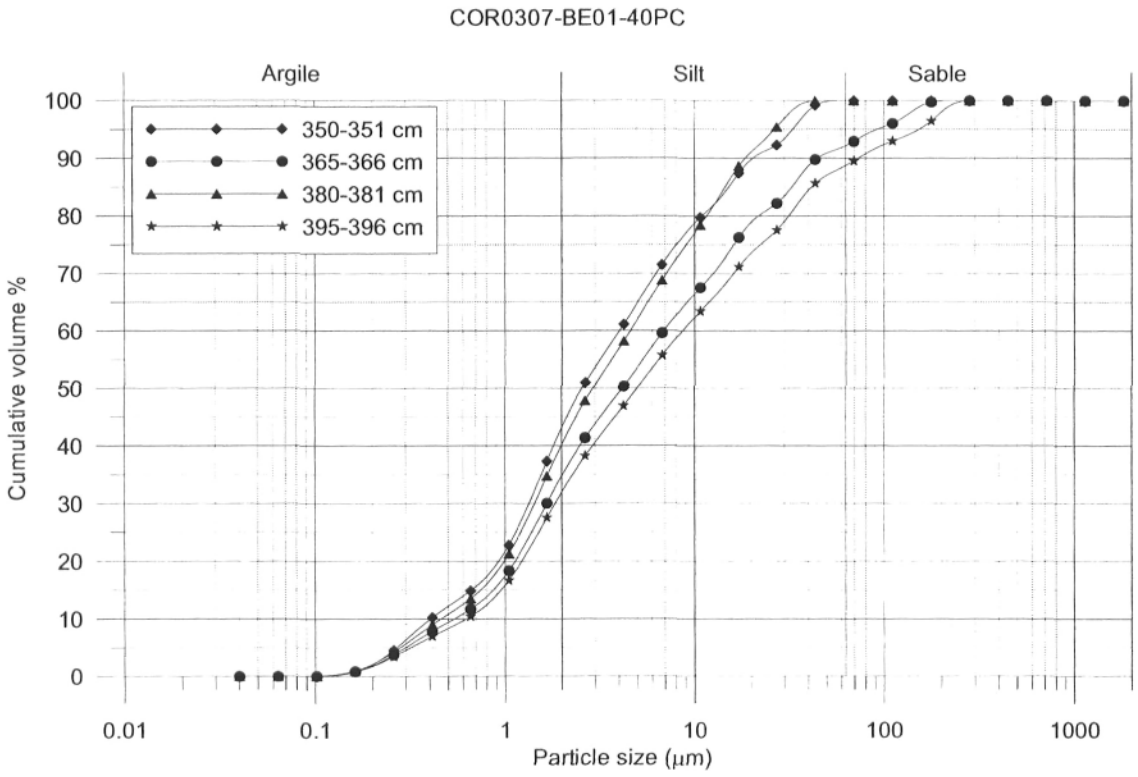
COR0307-BE01-40PC
Argile
Silt
Sable
350-351 cm
365-366 cm
380-381 cm
395-396 cm
Cumulative volume %
Particle size (µm)
0.01
0.1
1
10
100
1000

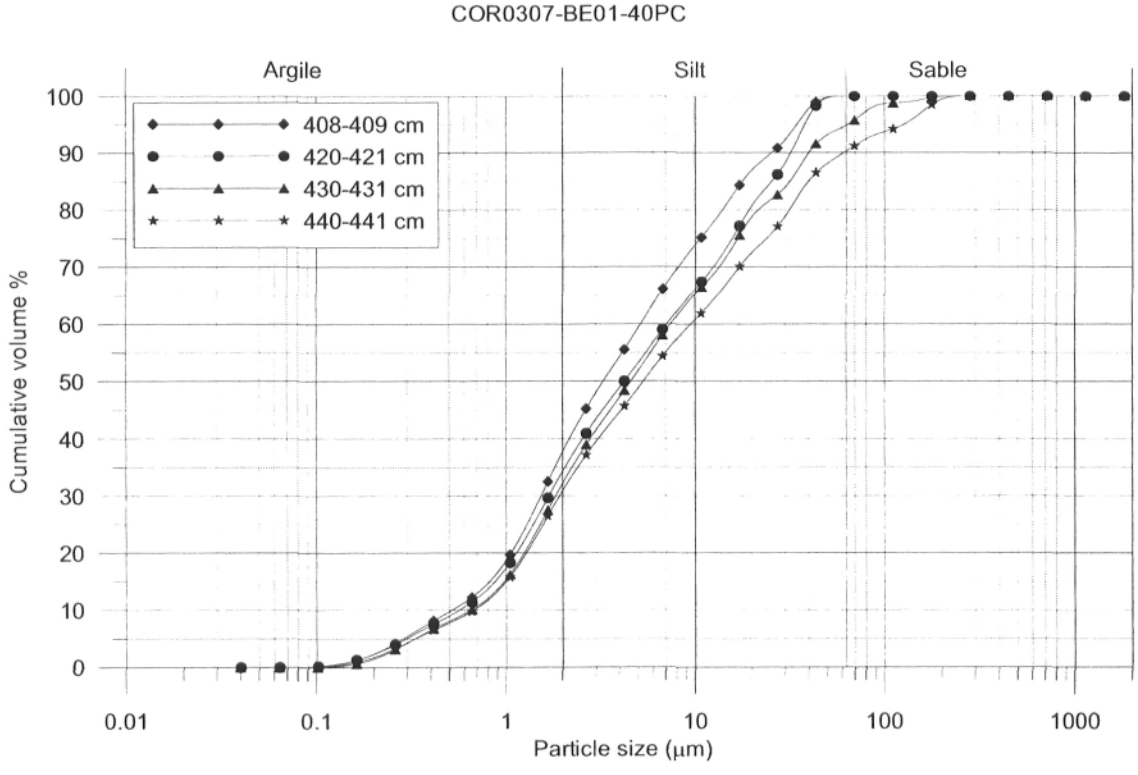
COR0307-BE01-40PC
Argile
Silt
Sable
408-409 cm
420-421 cm
430-431 cm
440-441 cm
Cumulative volume %
Particle size (µm)
0.01
0.1
1
10
100
1000

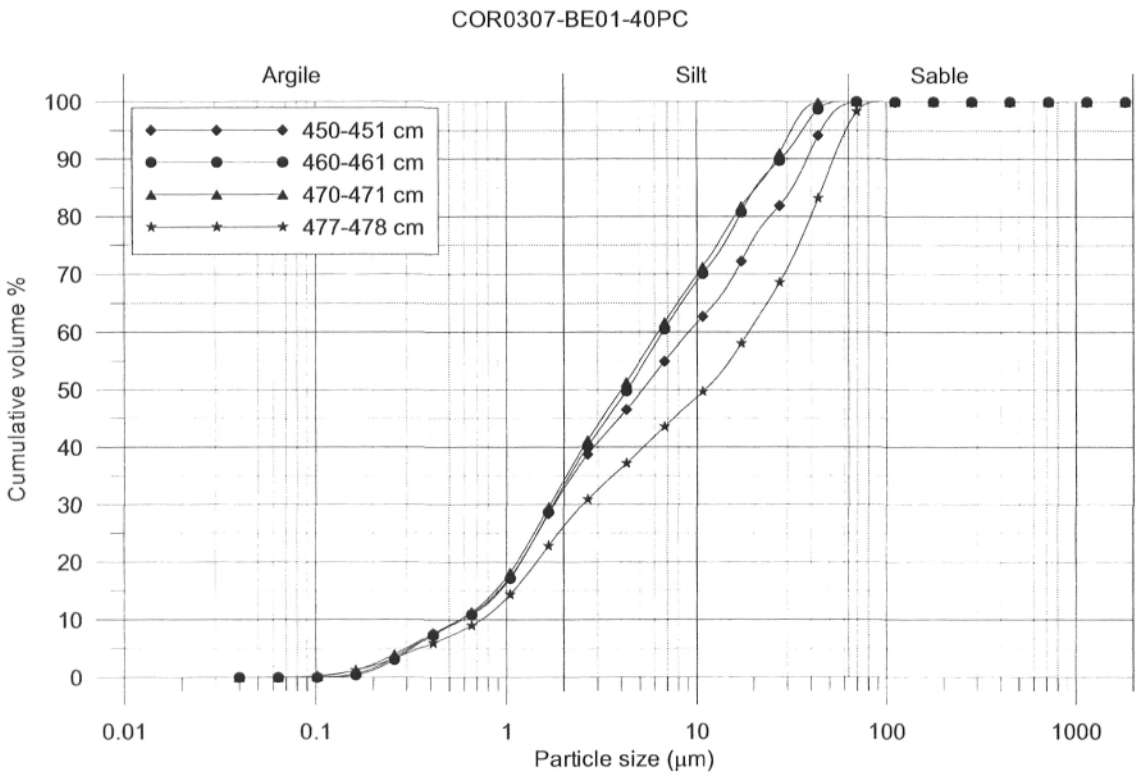
COR0307-BE01-40PC
Argile
Silt
Sable
450-451 cm
460-461 cm
470-471 cm
477-478 cm
Cumulative volume %
Particle size (µm)
0.01
0.1
1
10
100
1000

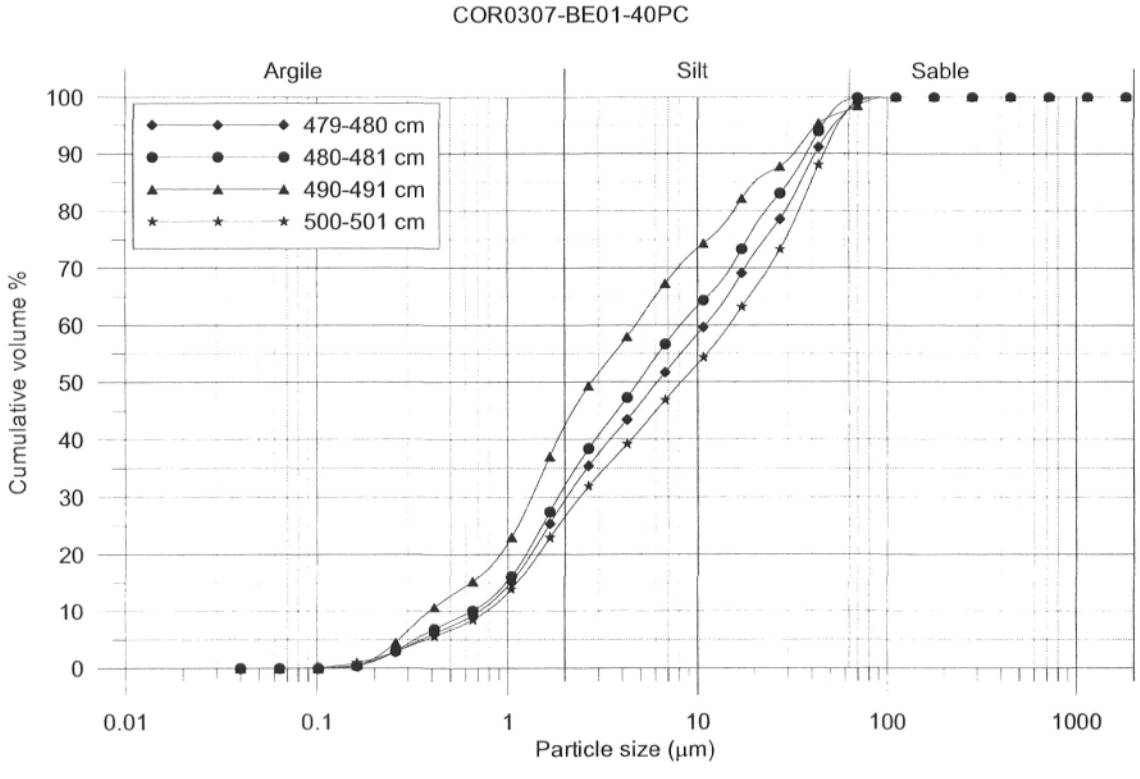
COR0307-BE01-40PC
Argile
Silt
Sable
479-480 cm
480-481 cm
490-491 cm
500-501 cm
Cumulative volume %
Particle size (µm)
0.01
0.1
1
10
100
1000

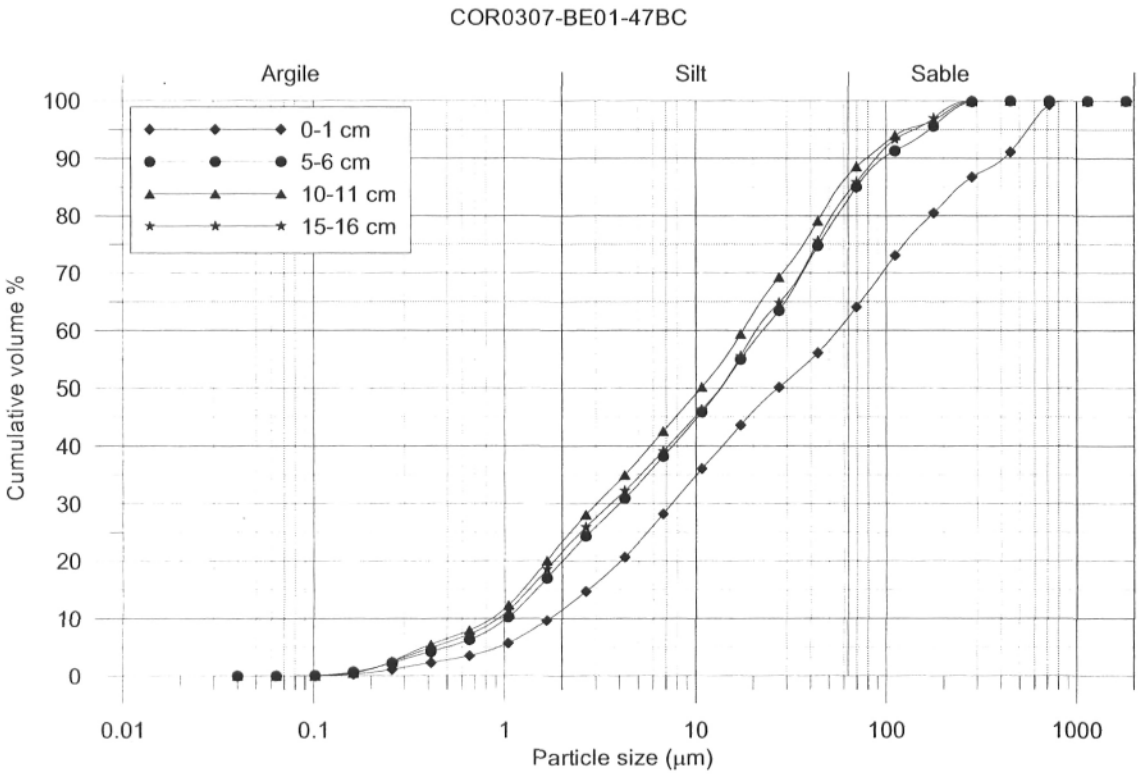
COR0307-BE01-47BC
Argile
Silt
Sable
0-1 cm
5-6 cm
10-11 cm
15-16 cm
Cumulative volume %
Particle size (µm)
0.01
0.1
1
10
100
1000

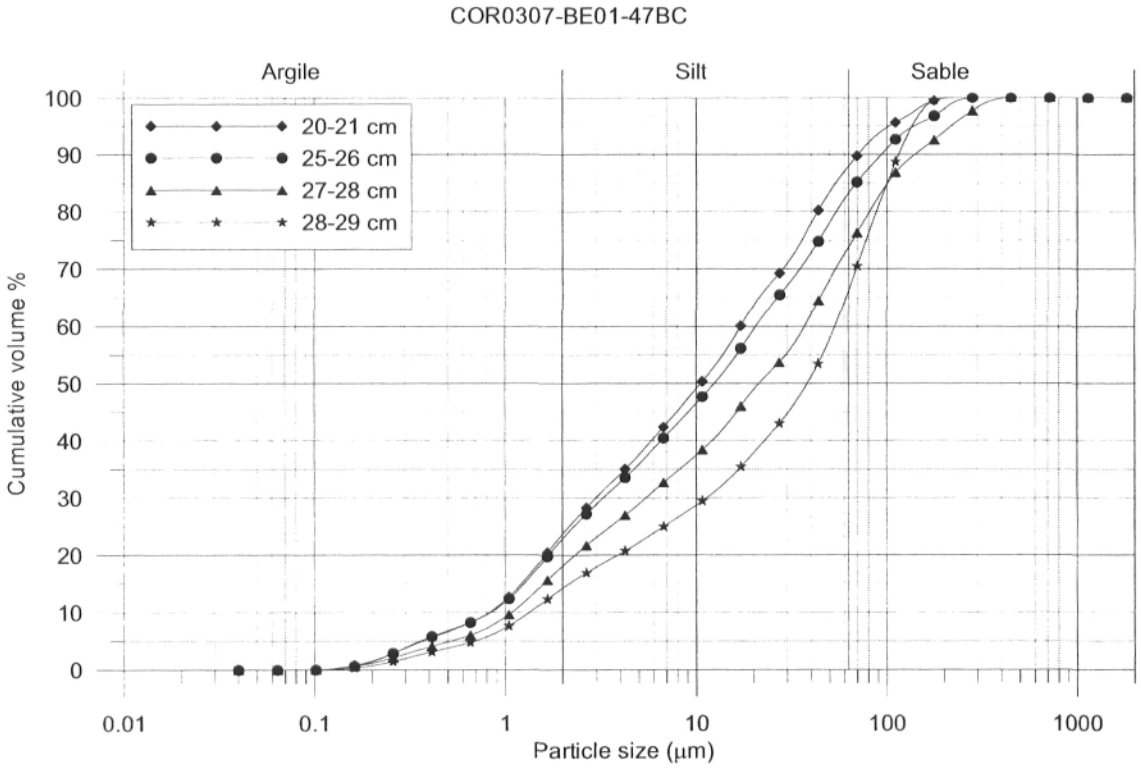
COR0307-BE01-47BC
Argile
Silt
Sable
20-21 cm
25-26 cm
27-28 cm
28-29 cm
Cumulative volume %
Particle size (µm)
0.01
0.1
1
10
100
1000

COR0307-BE01-47BC

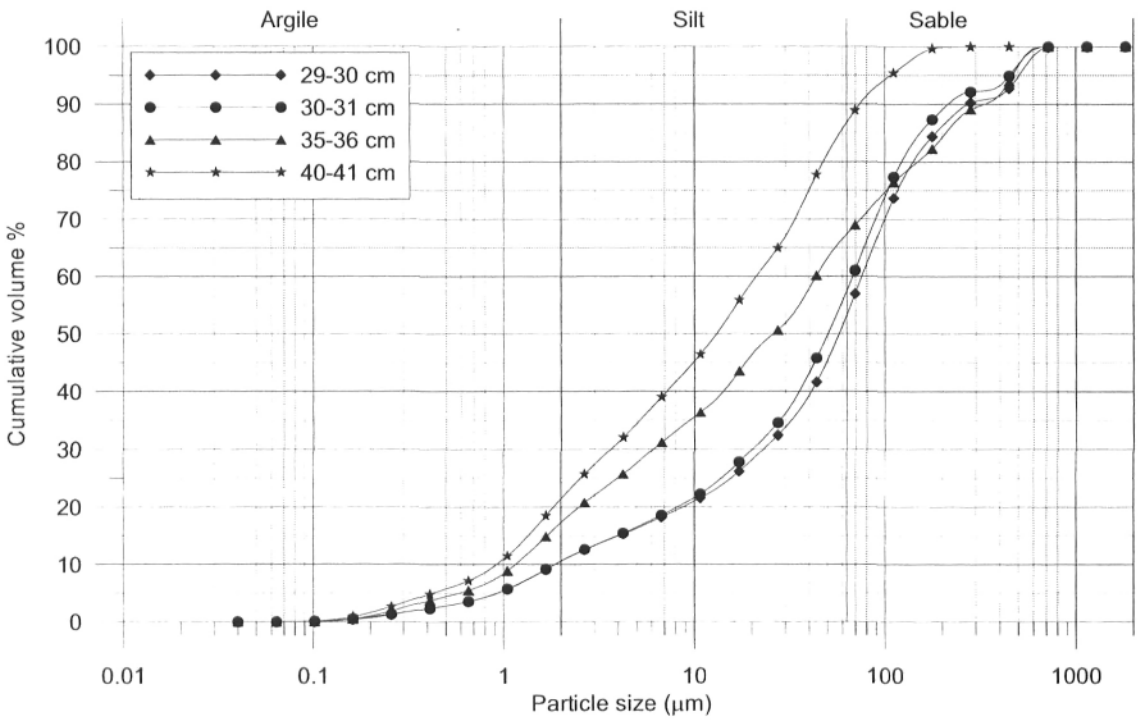

COR0307-BE12-52BC

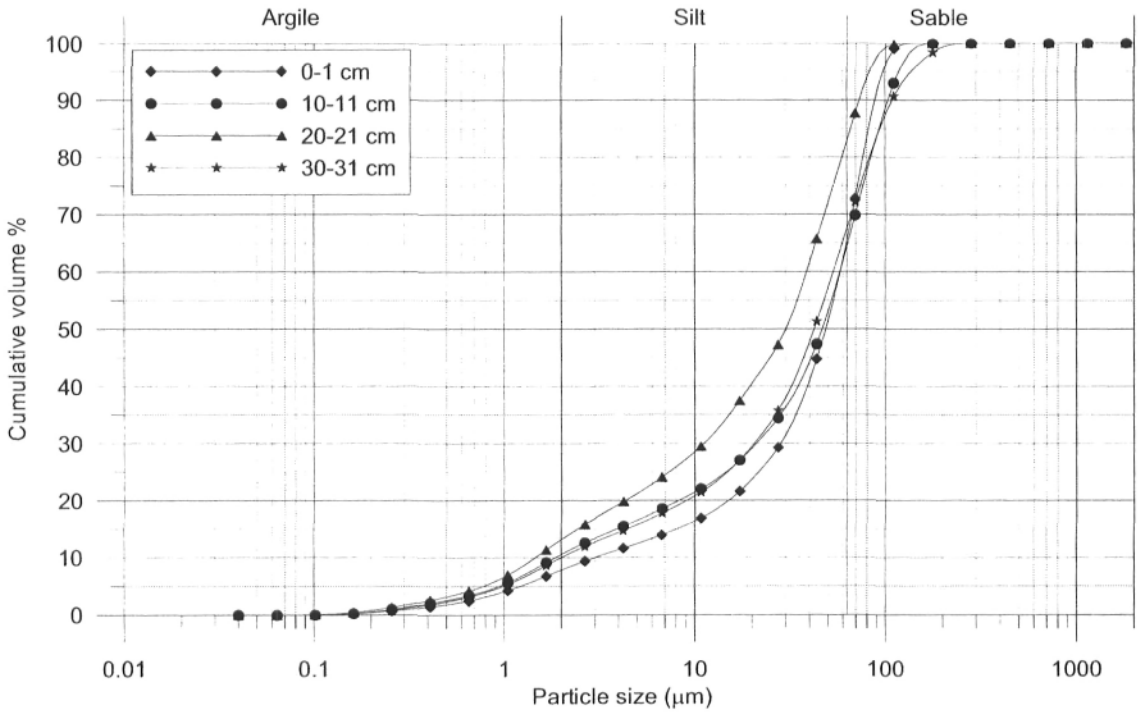

COR0307-BE12-52BC

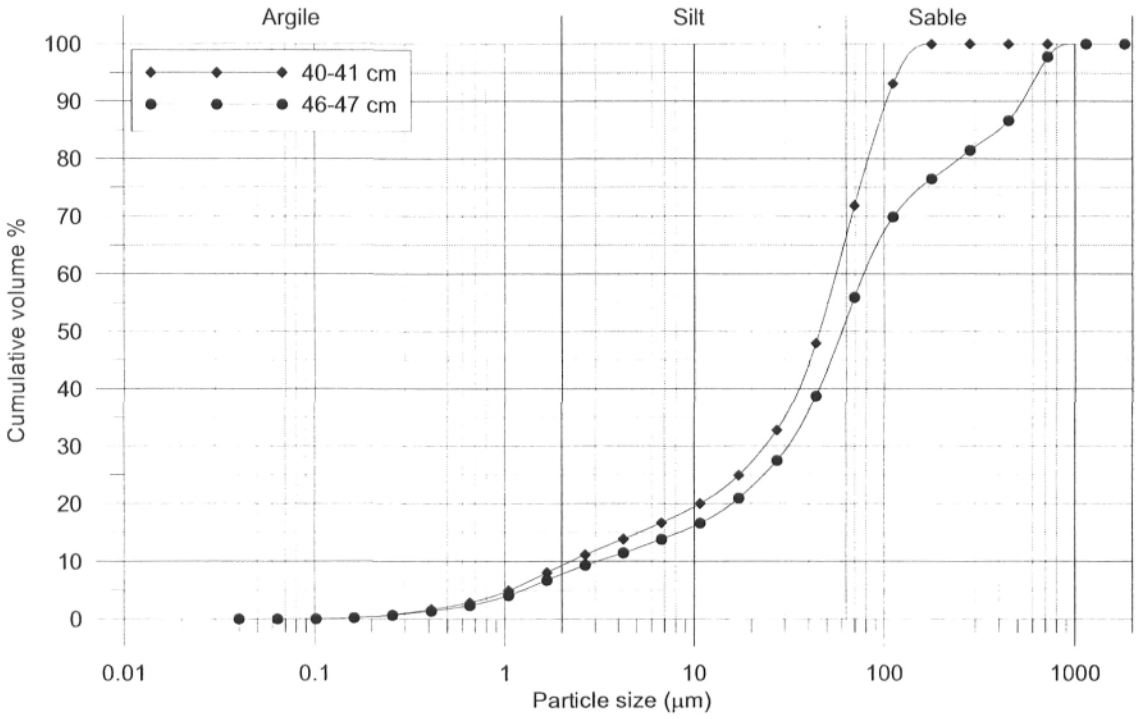

COR0307-BE12-53LH

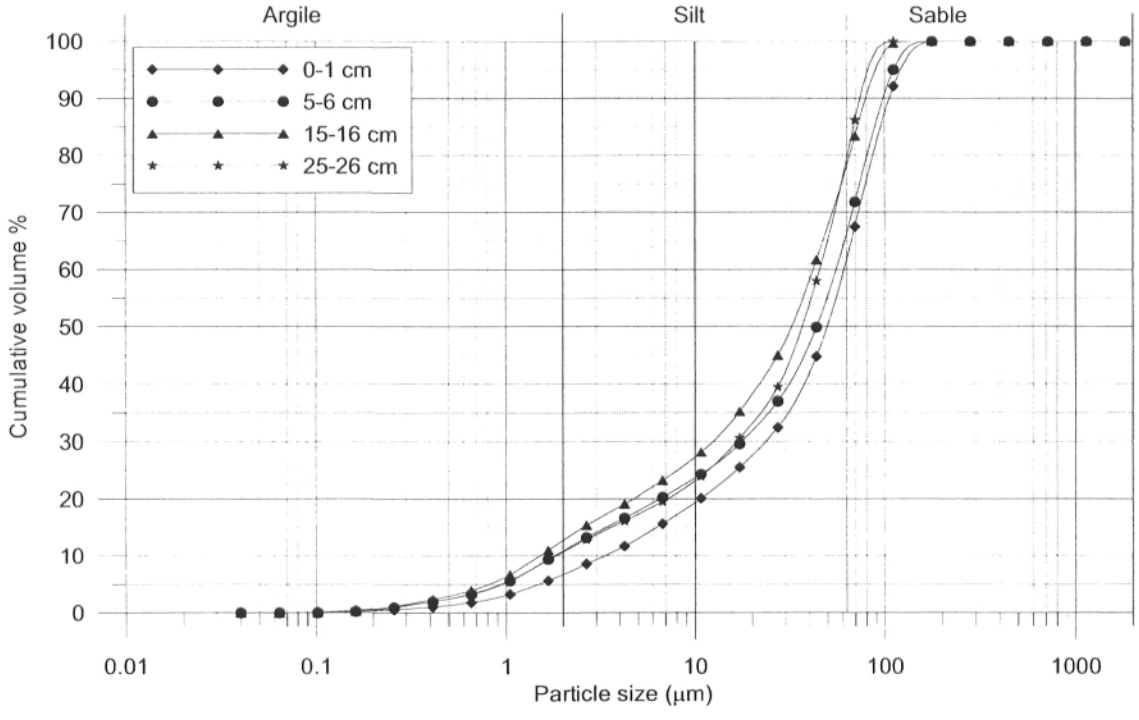

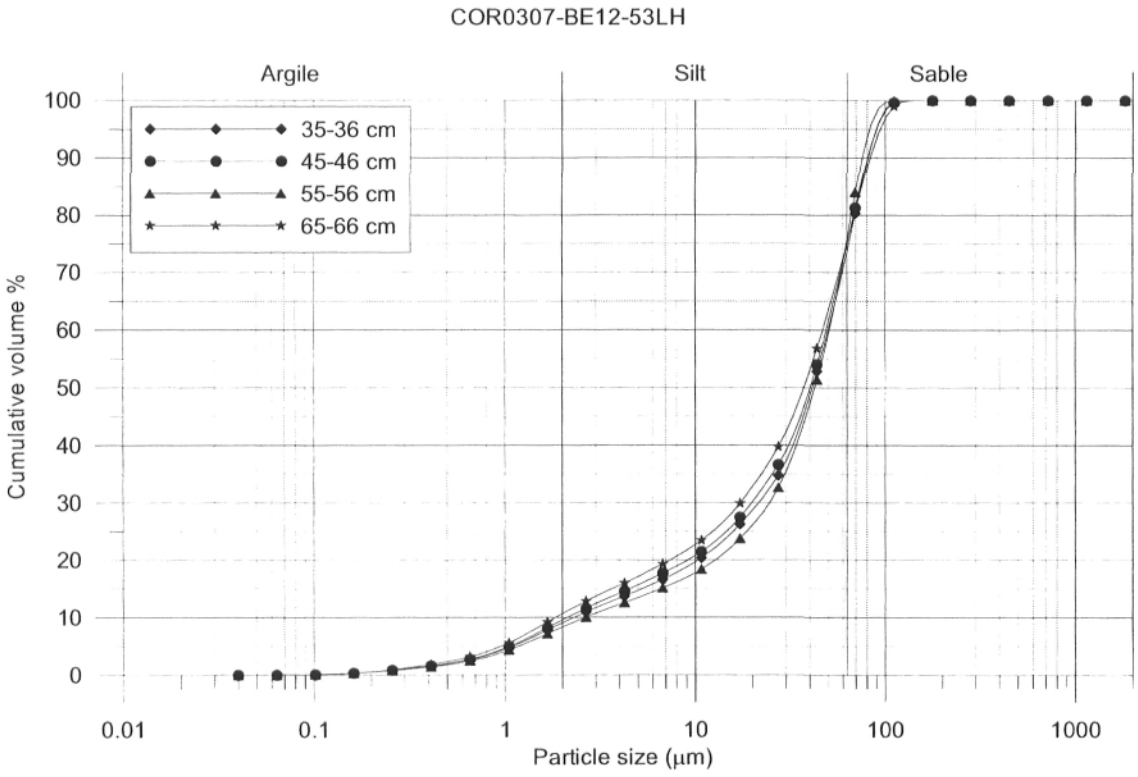
COR0307-BE12-53LH
Argile
Silt
Sable
35-36 cm
45-46 cm
55-56 cm
65-66 cm
Cumulative volume %
Particle size (µm)
0.01
0.1
1
10
100
1000

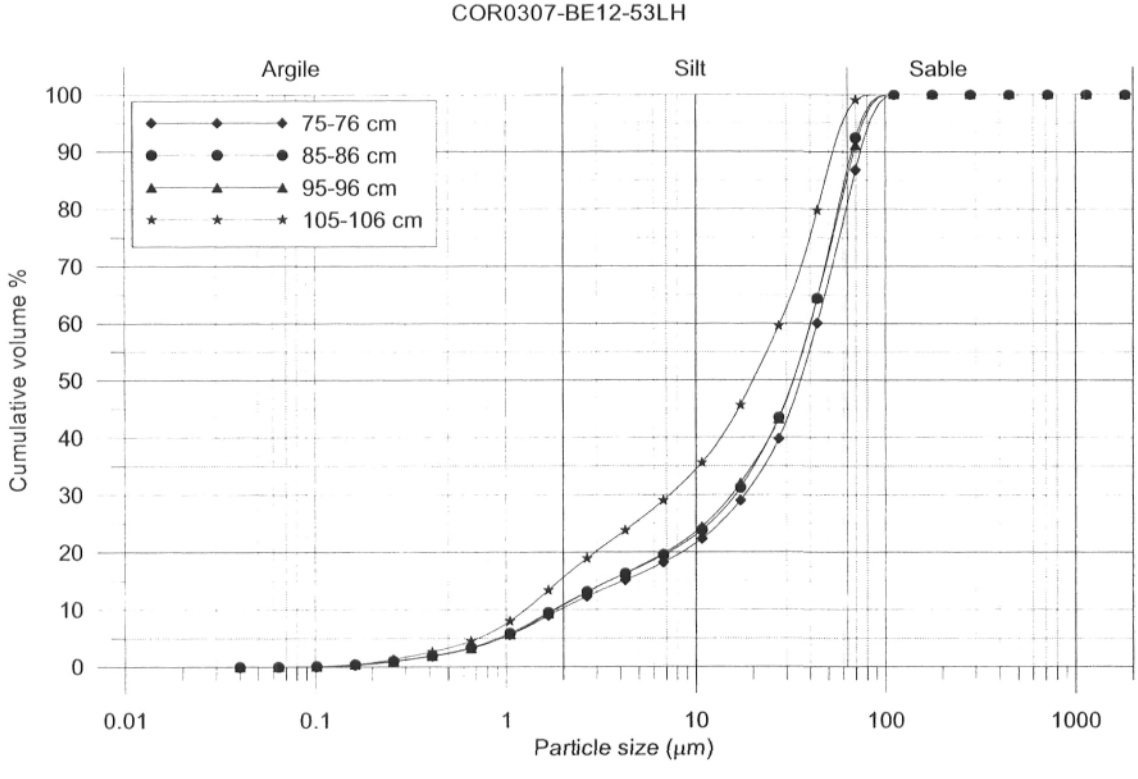
COR0307-BE12-53LH
Argile
Silt
Sable
75-76 cm
85-86 cm
95-96 cm
105-106 cm
Cumulative volume %
Particle size (µm)
0.01
0.1
1
10
100
1000

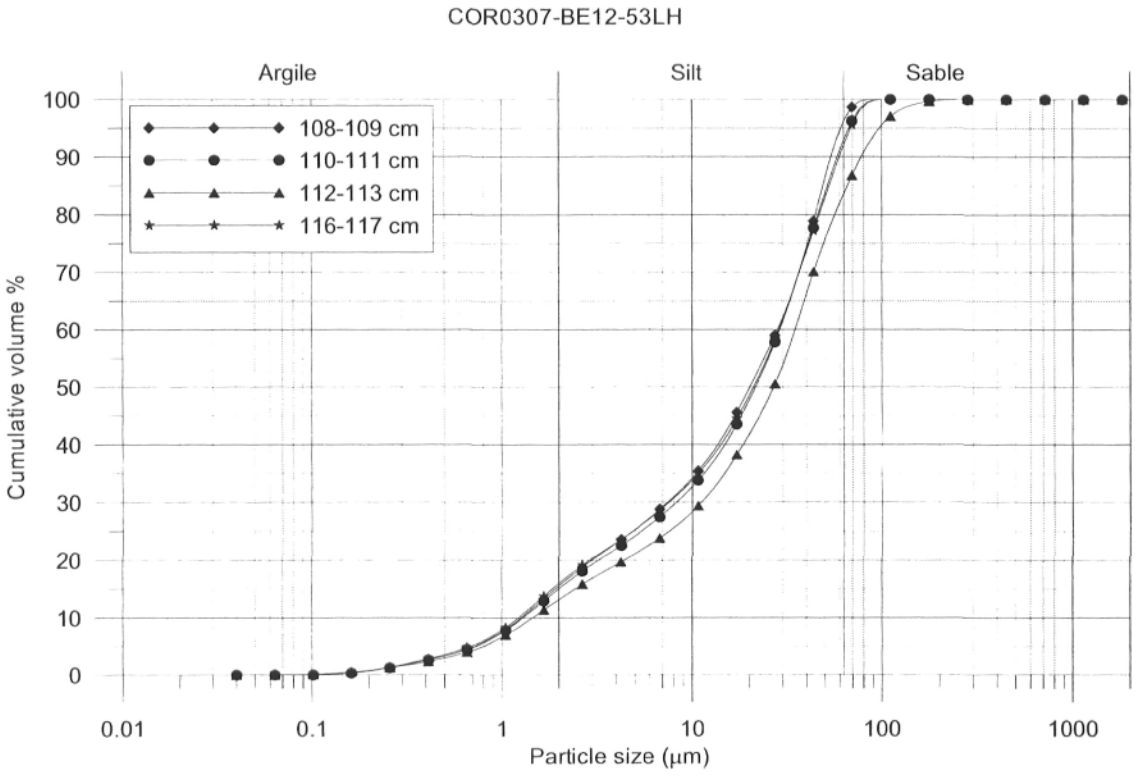
COR0307-BE12-53LH
Argile
Silt
Sable
108-109 cm
110-111 cm
112-113 cm
116-117 cm
Cumulative volume %
Particle size (µm)
0.01
0.1
1
10
100
1000

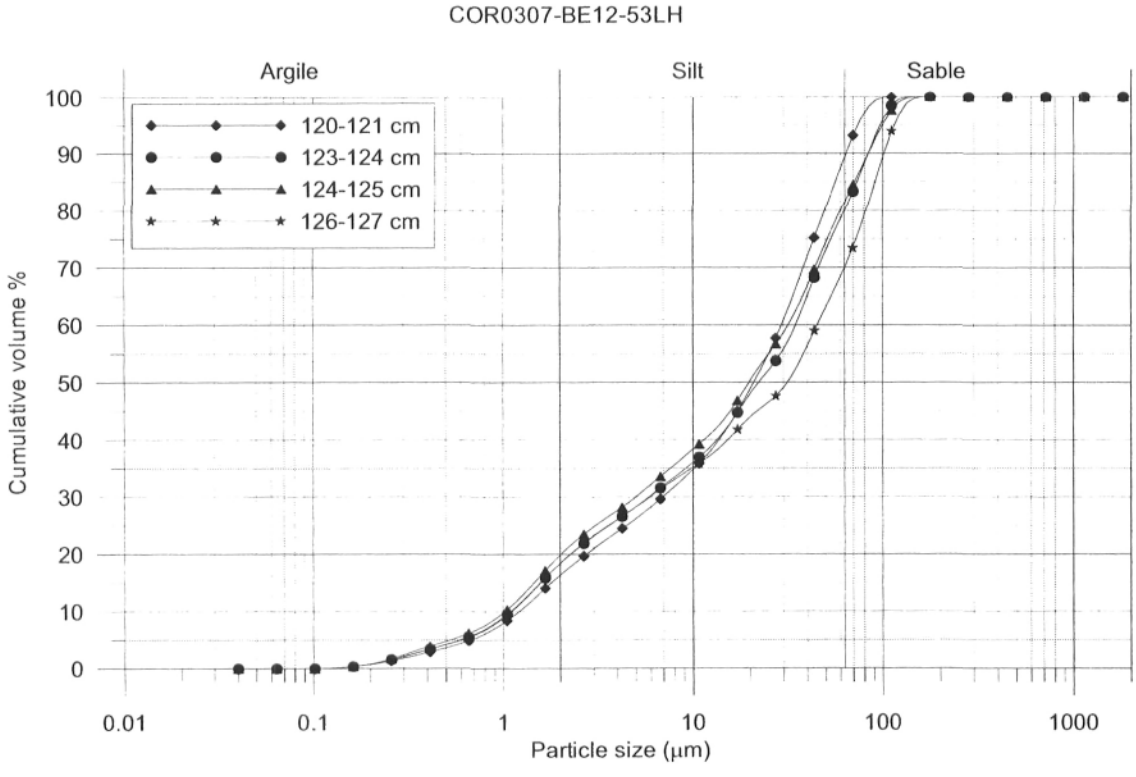
COR0307-BE12-53LH
Argile
Silt
Sable
120-121 cm
123-124 cm
124-125 cm
126-127 cm
Cumulative volume %
Particle size (µm)
0.01
0.1
1
10
100
1000

COR0307-BE12-53LH

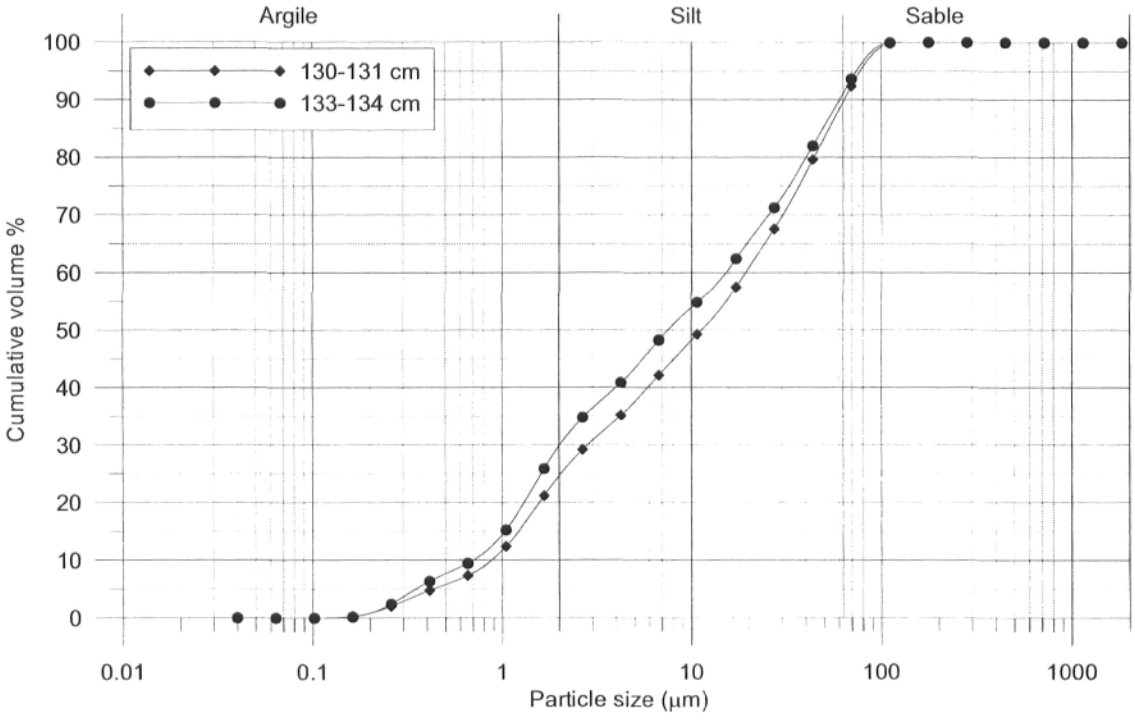

COR0503-BE02-02BC

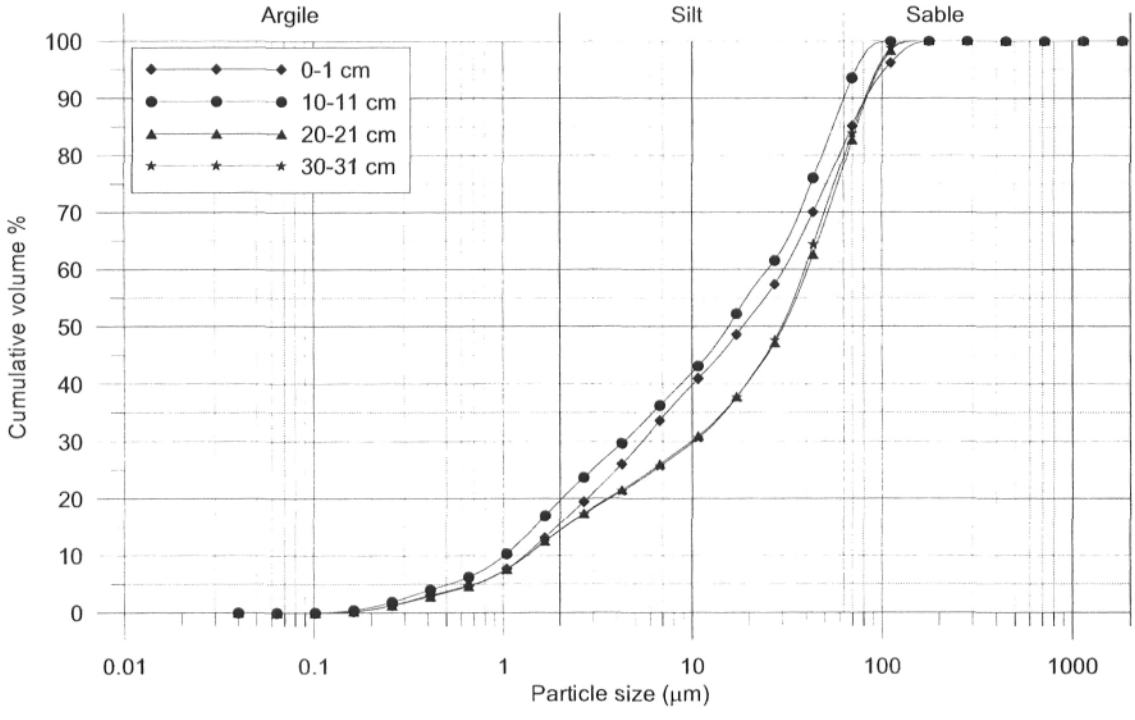

COR0503-BE02-02BC

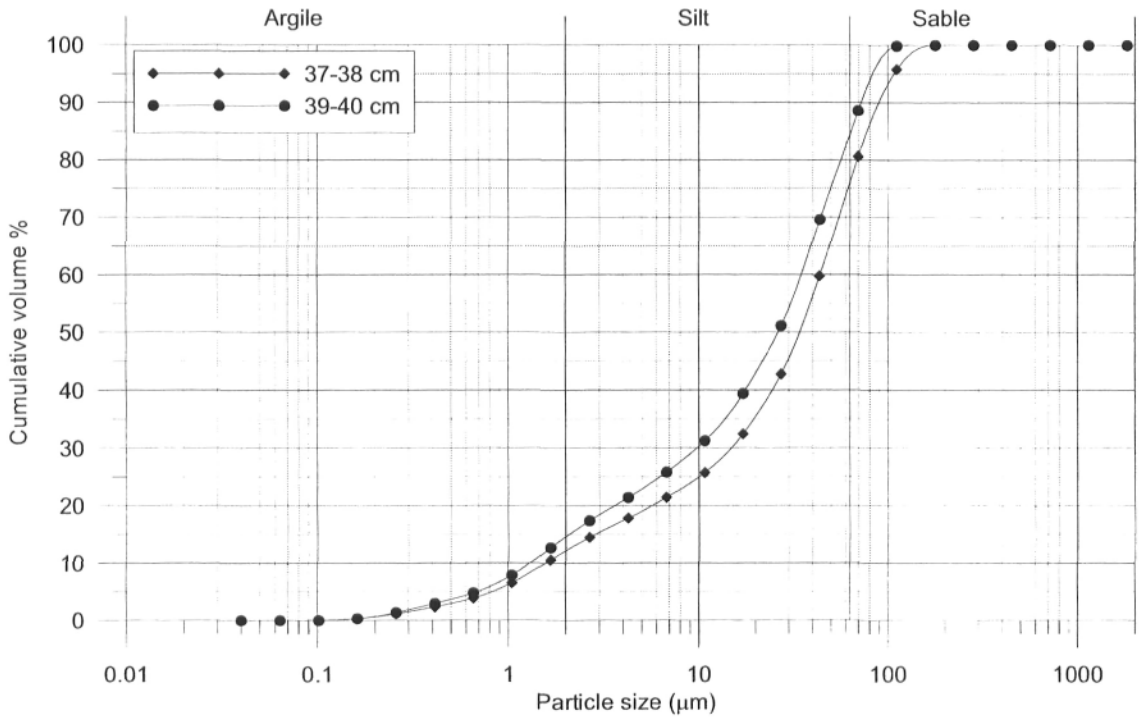

COR0503-BE02-02TWC

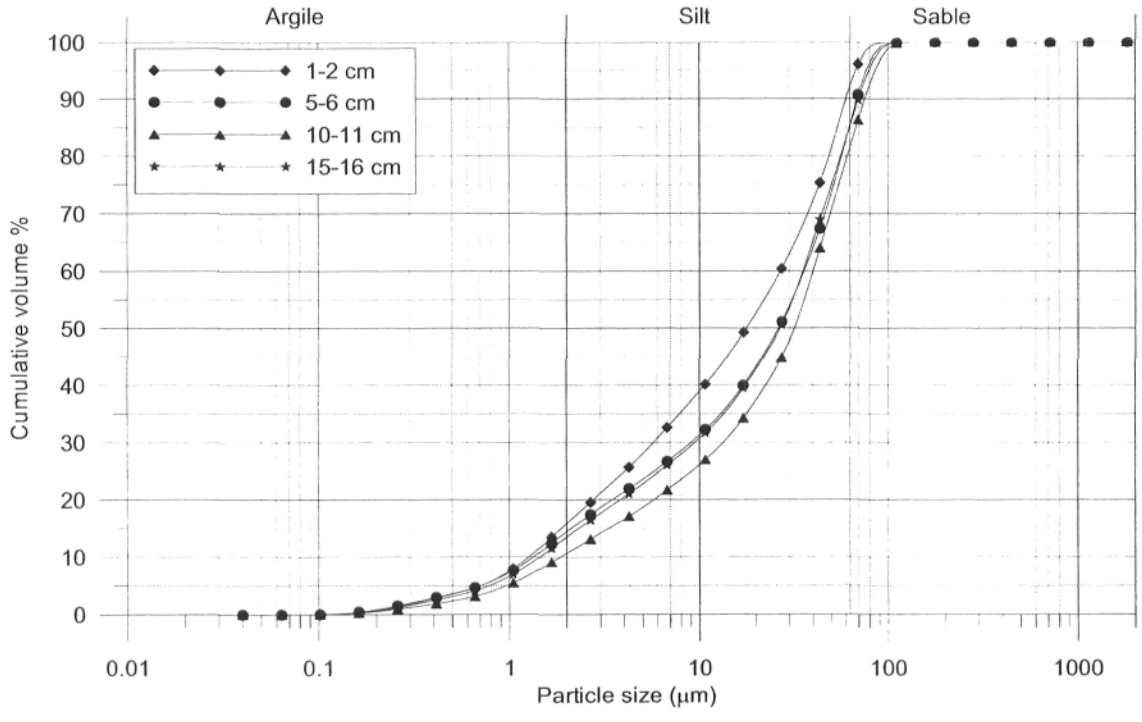

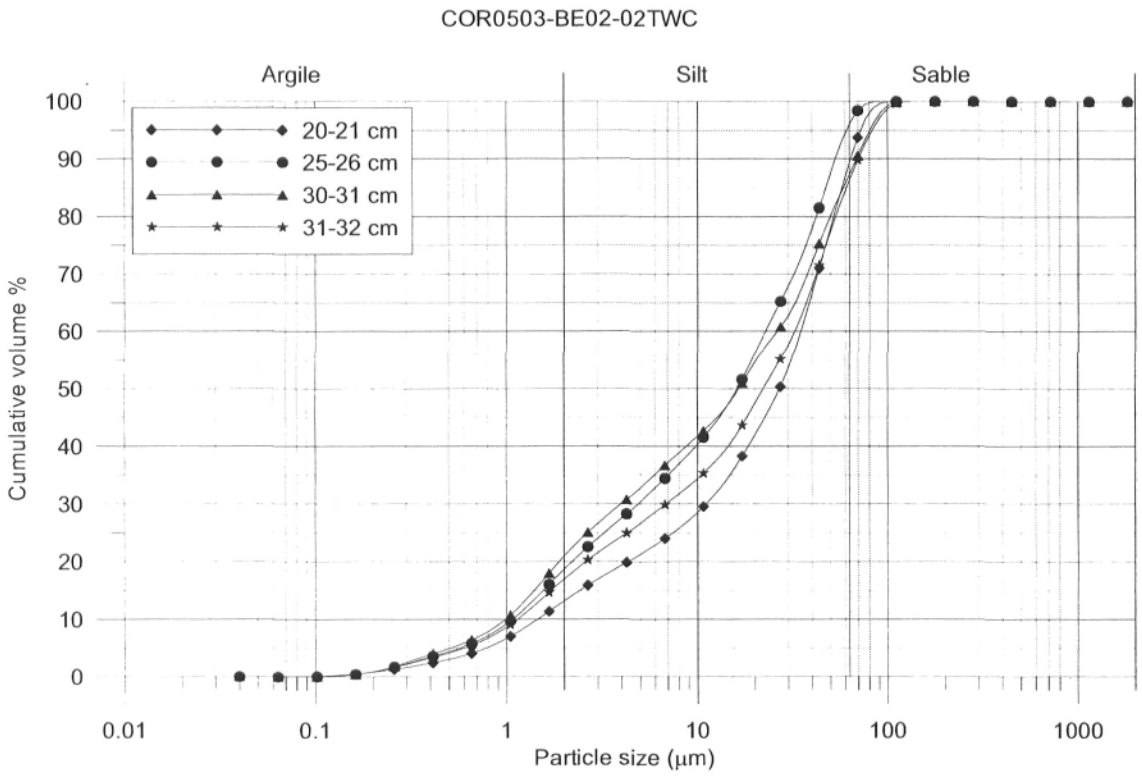
COR0503-BE02-02TWC
Argile
Silt
Sable
20-21 cm
25-26 cm
30-31 cm
31-32 cm
Cumulative volume %
Particle size (µm)
0
10
20
30
40
50
60
70
80
90
100
0.01
0.1
1
10
100
1000

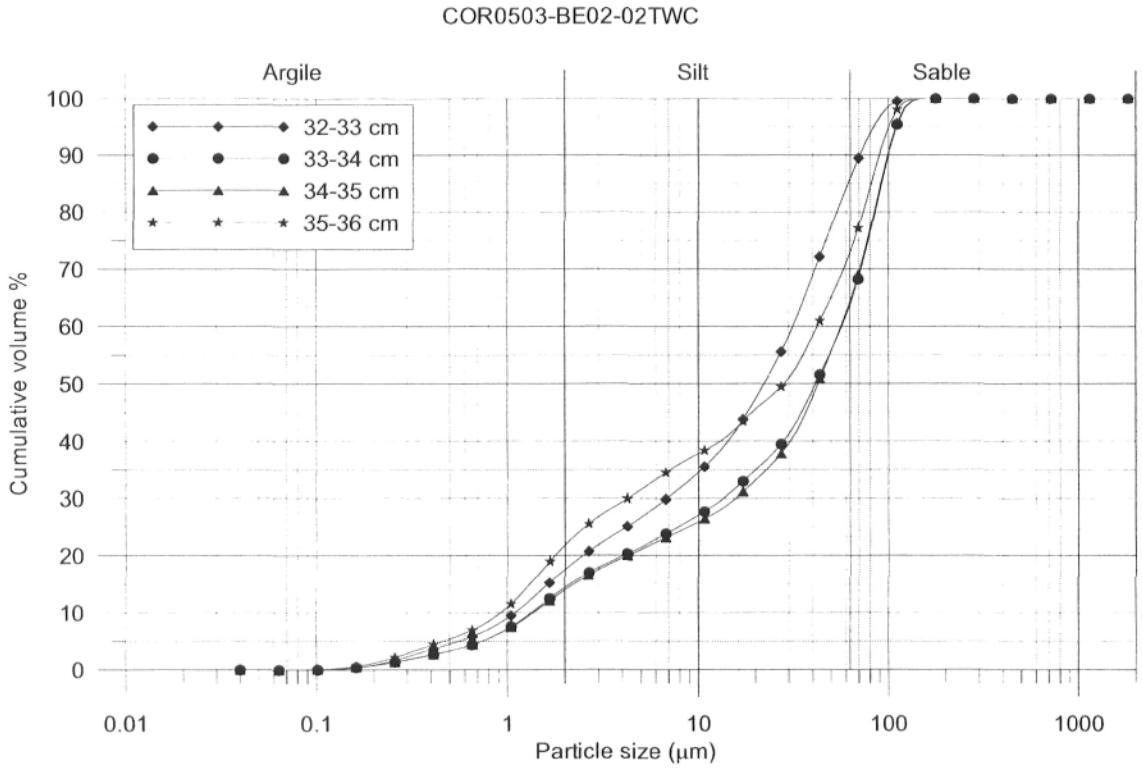
COR0503-BE02-02TWC
Argile
Silt
Sable
32-33 cm
33-34 cm
34-35 cm
35-36 cm
Cumulative volume %
Particle size (µm)
0
10
20
30
40
50
60
70
80
90
100
0.01
0.1
1
10
100
1000

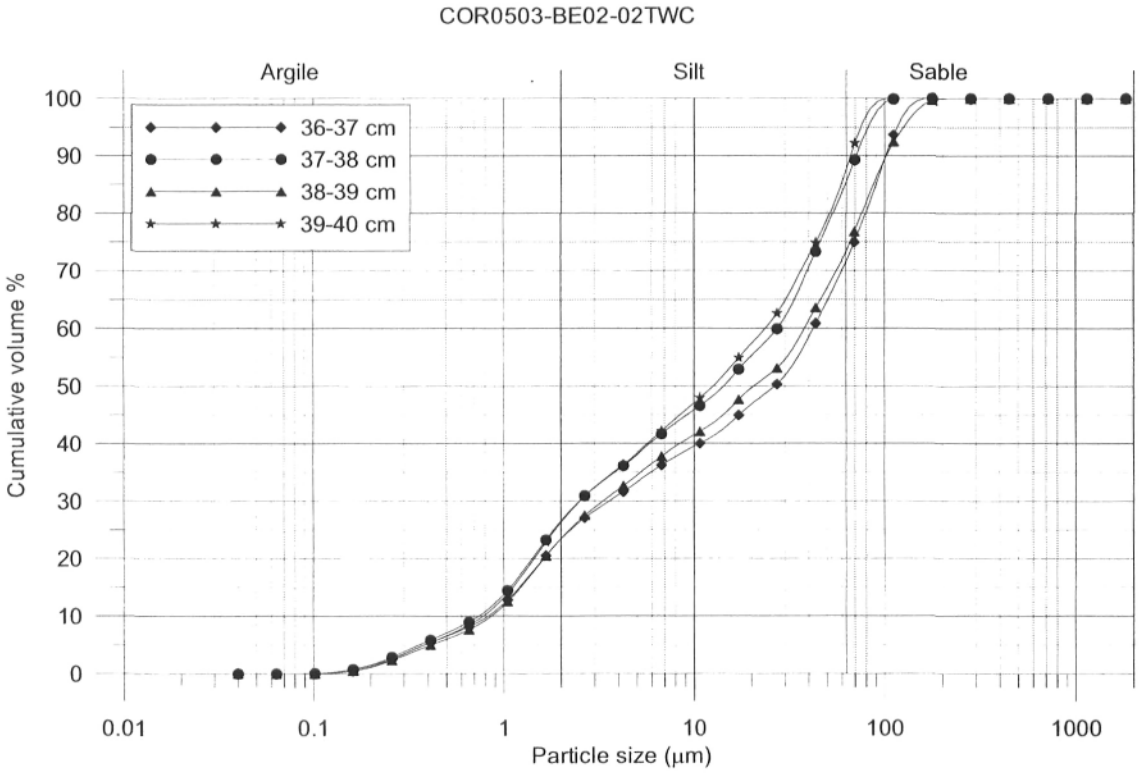
COR0503-BE02-02TWC
Argile
Silt
Sable
36-37 cm
37-38 cm
38-39 cm
39-40 cm
Cumulative volume %
Particle size (µm)
0.01
0.1
1
10
100
1000

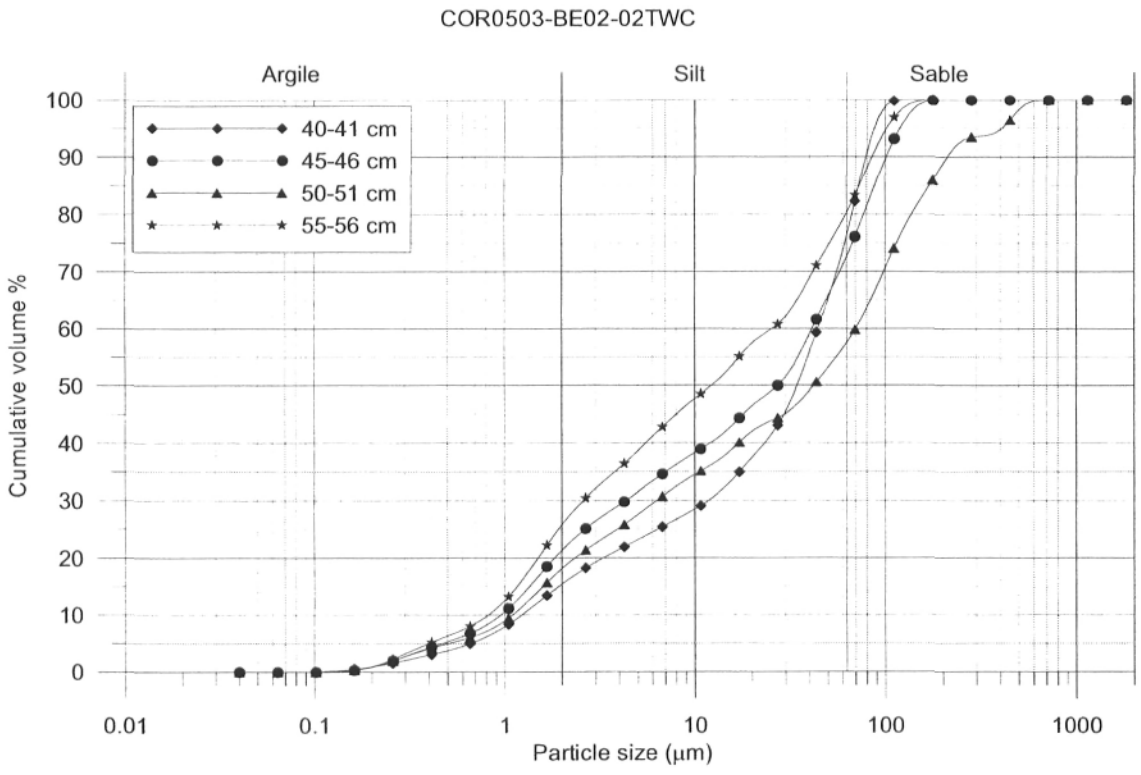
COR0503-BE02-02TWC
Argile
Silt
Sable
40-41 cm
45-46 cm
50-51 cm
55-56 cm
Cumulative volume %
Particle size (µm)
0.01
0.1
1
10
100
1000

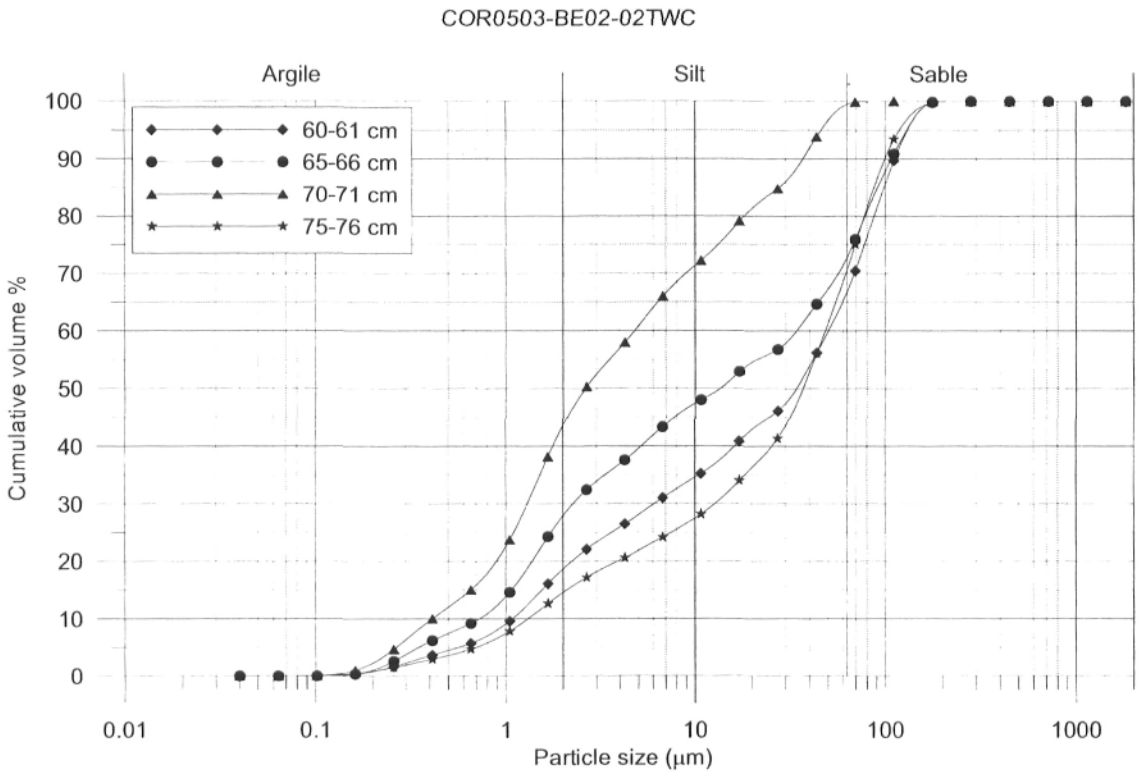
COR0503-BE02-02TWC
Argile
Silt
Sable
60-61 cm
65-66 cm
70-71 cm
75-76 cm
Cumulative volume %
Particle size (µm)
0.01
0.1
1
10
100
1000

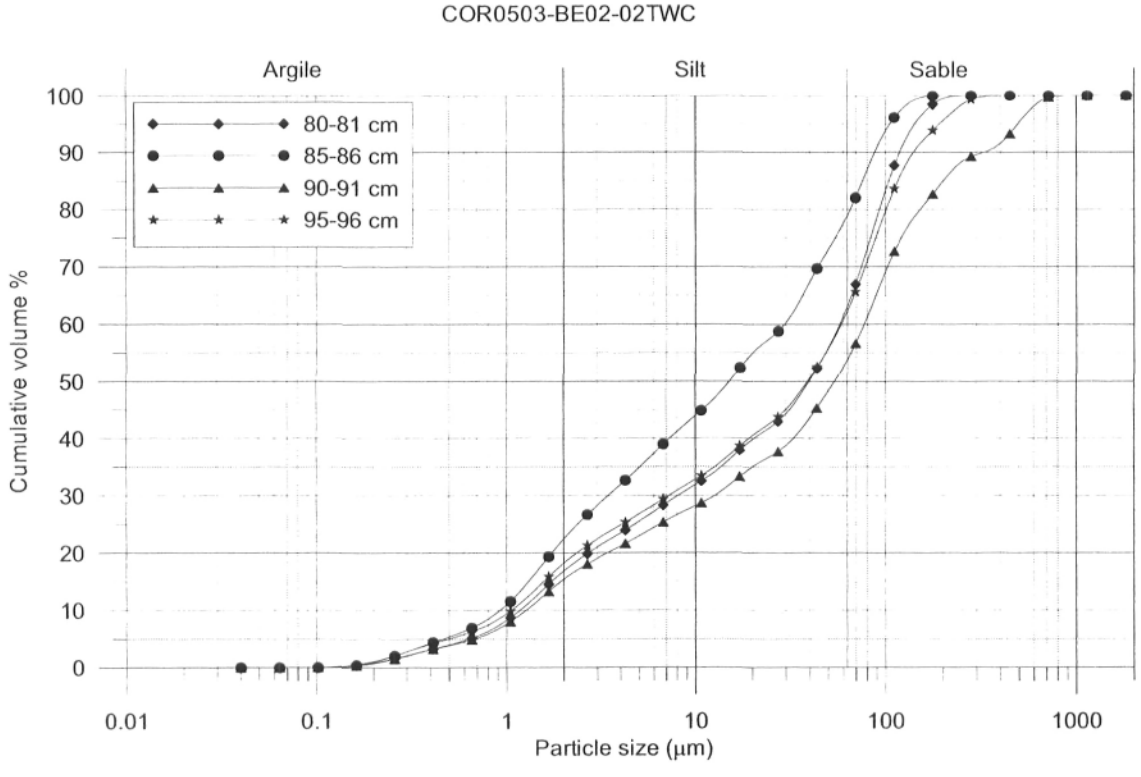
COR0503-BE02-02TWC
Argile
Silt
Sable
80-81 cm
85-86 cm
90-91 cm
95-96 cm
Cumulative volume %
Particle size (µm)
0.01
0.1
1
10
100
1000

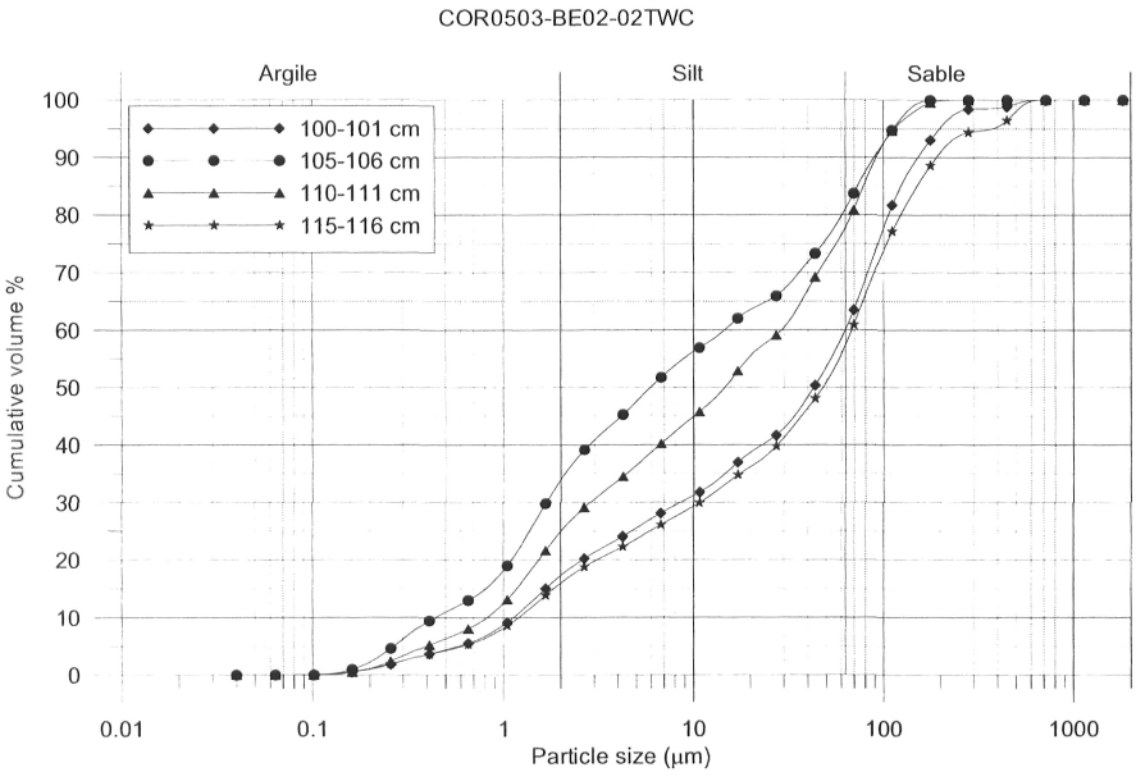
COR0503-BE02-02TWC
Argile
Silt
Sable
100-101 cm
105-106 cm
110-111 cm
115-116 cm
Cumulative volume %
Particle size (µm)
0.01
0.1
1
10
100
1000

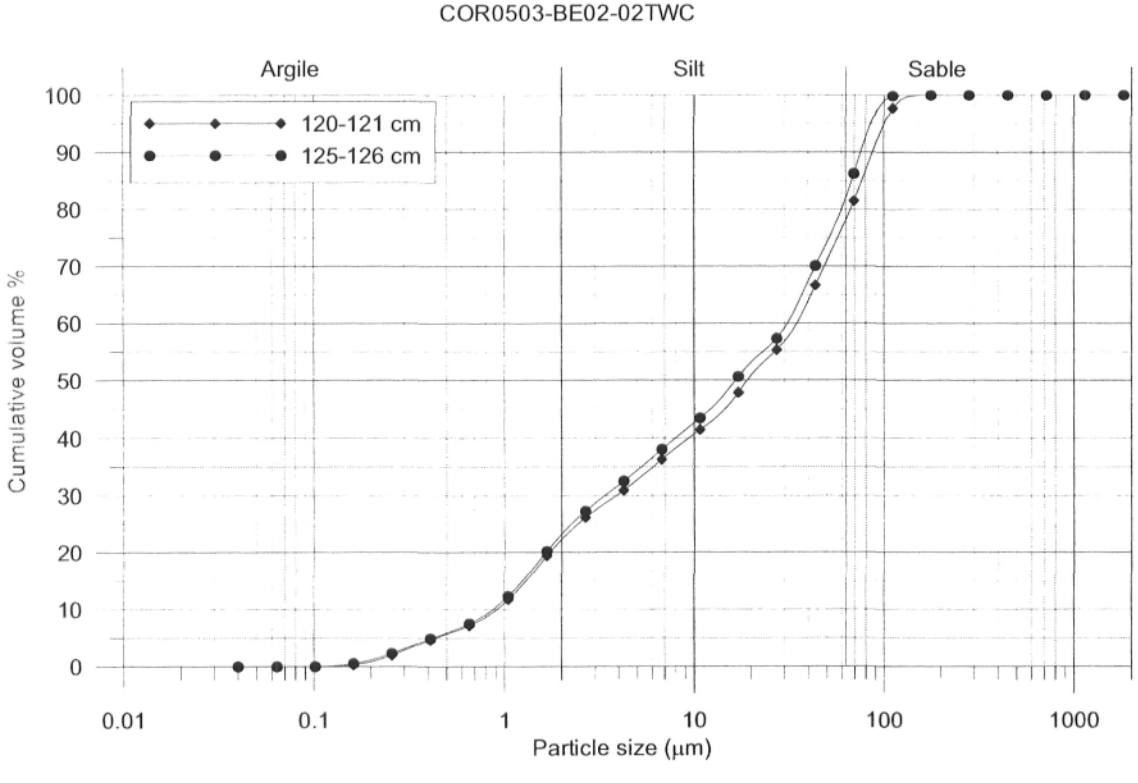
COR0503-BE02-02TWC
Argile
Silt
Sable
120-121 cm
125-126 cm
Cumulative volume %
Particle size (µm)
0.01
0.1
1
10
100
1000

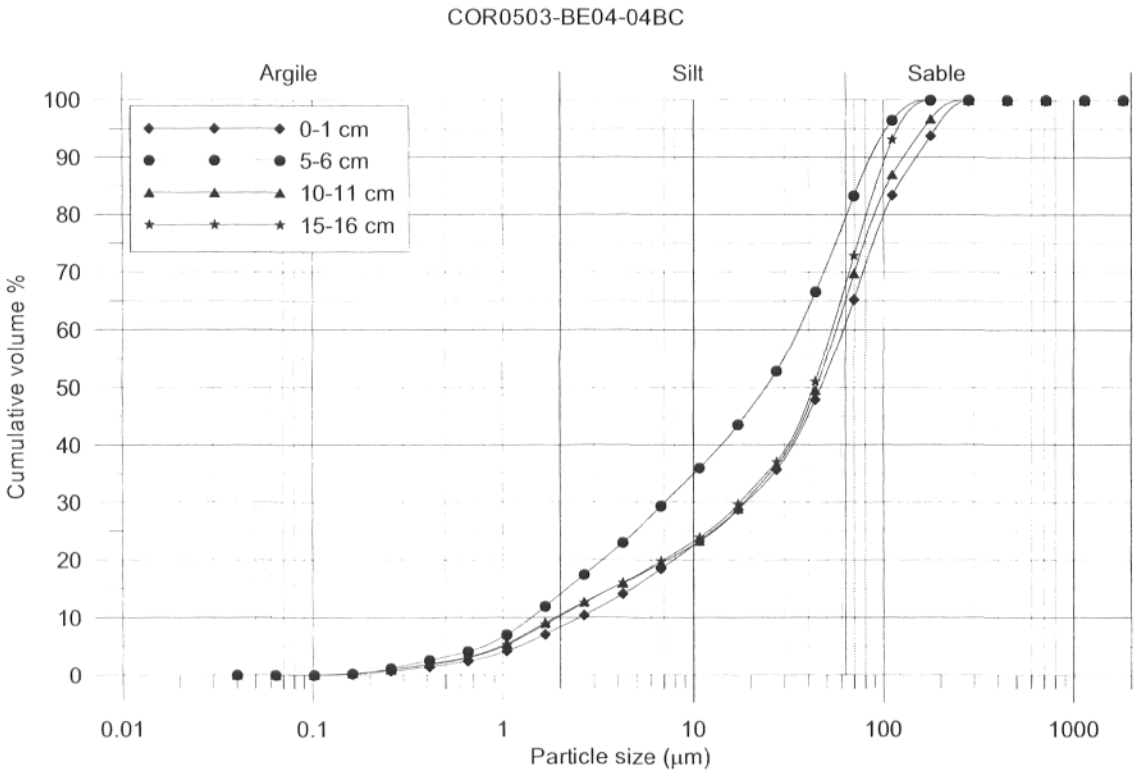
COR0503-BE04-04BC
Argile
Silt
Sable
0-1 cm
5-6 cm
10-11 cm
15-16 cm
Cumulative volume %
Particle size (µm)
0.01
0.1
1
10
100
1000

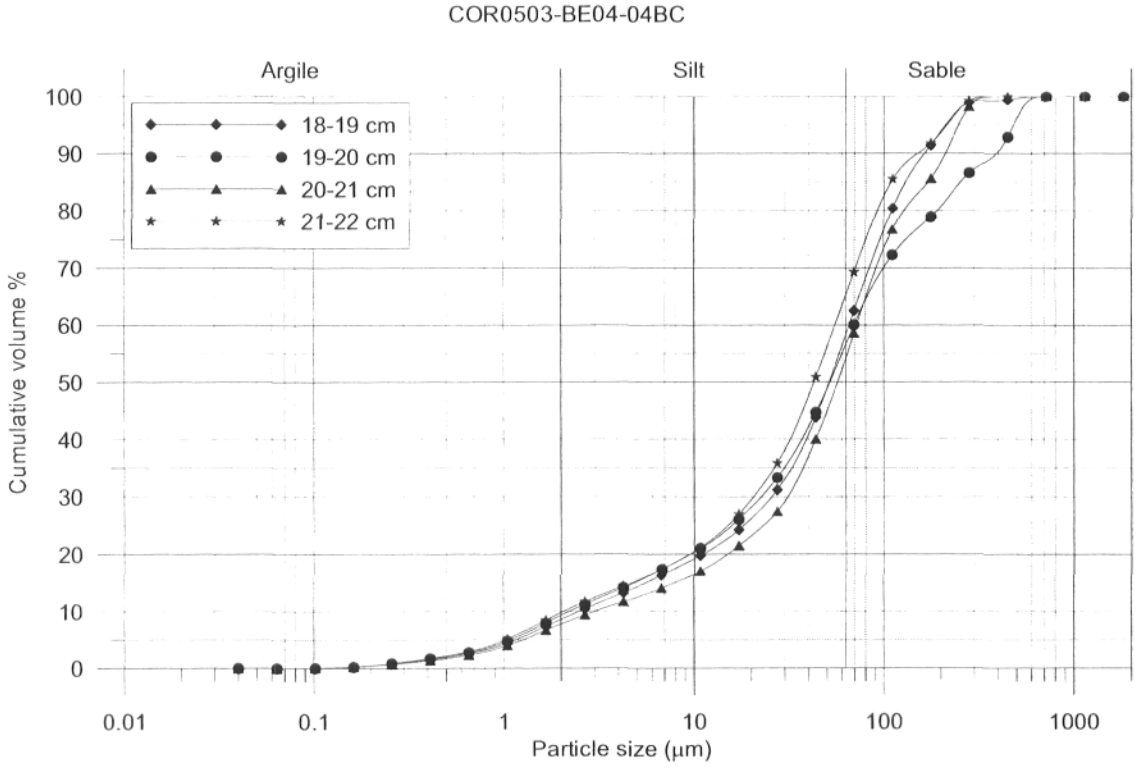
COR0503-BE04-04BC
Argile
Silt
Sable
18-19 cm
19-20 cm
20-21 cm
21-22 cm
Cumulative volume %
Particle size (µm)
0.01
0.1
1
10
100
1000

COR0503-BE04-04BC

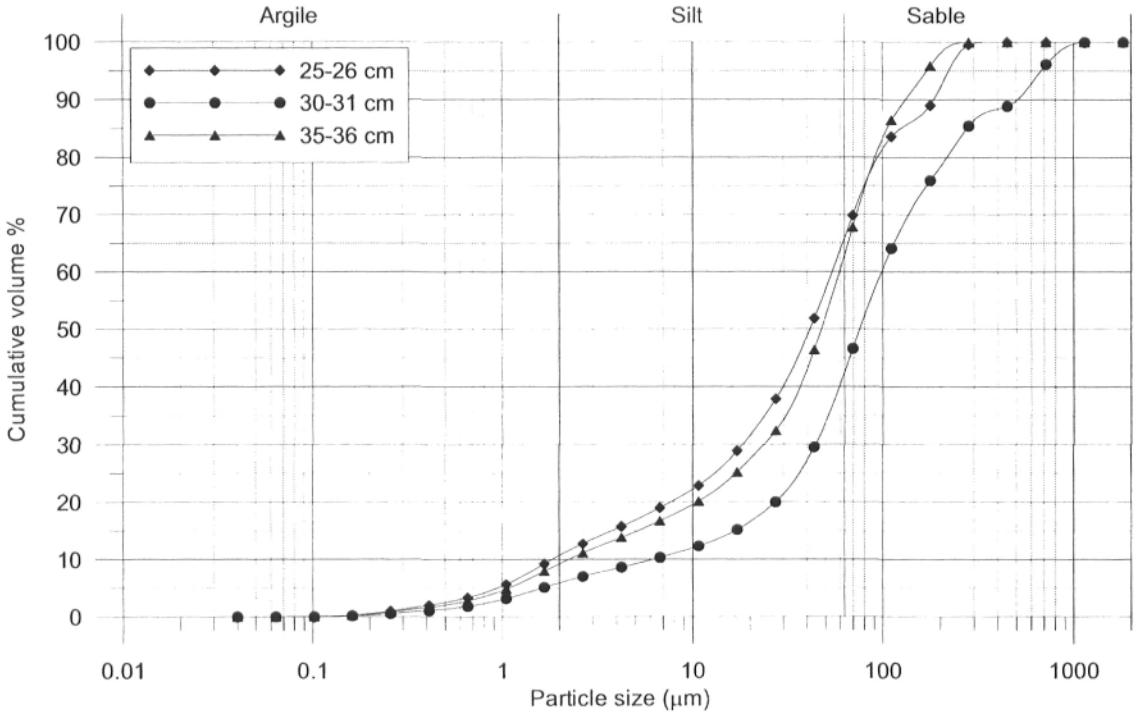

COR0503-BE05-05BC

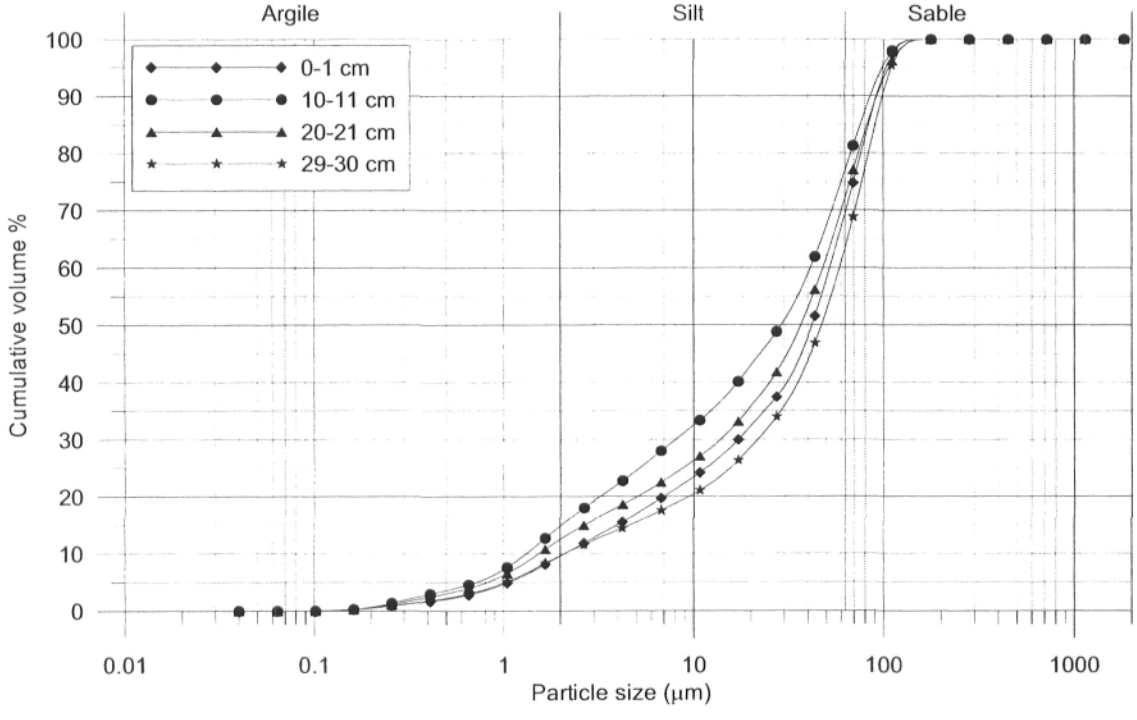

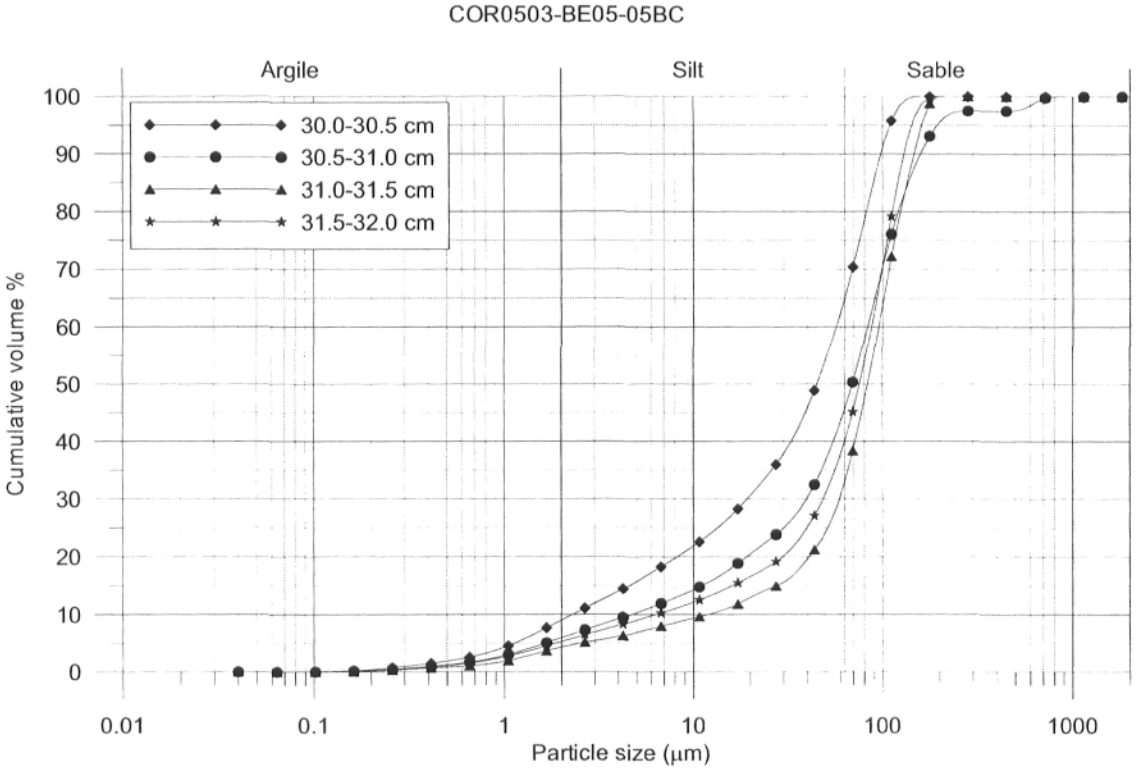
COR0503-BE05-05BC
Argile
Silt
Sable
30.0-30.5 cm
30.5-31.0 cm
31.0-31.5 cm
31.5-32.0 cm
Cumulative volume %
Particle size (µm)
0.01
0.1
1
10
100
1000

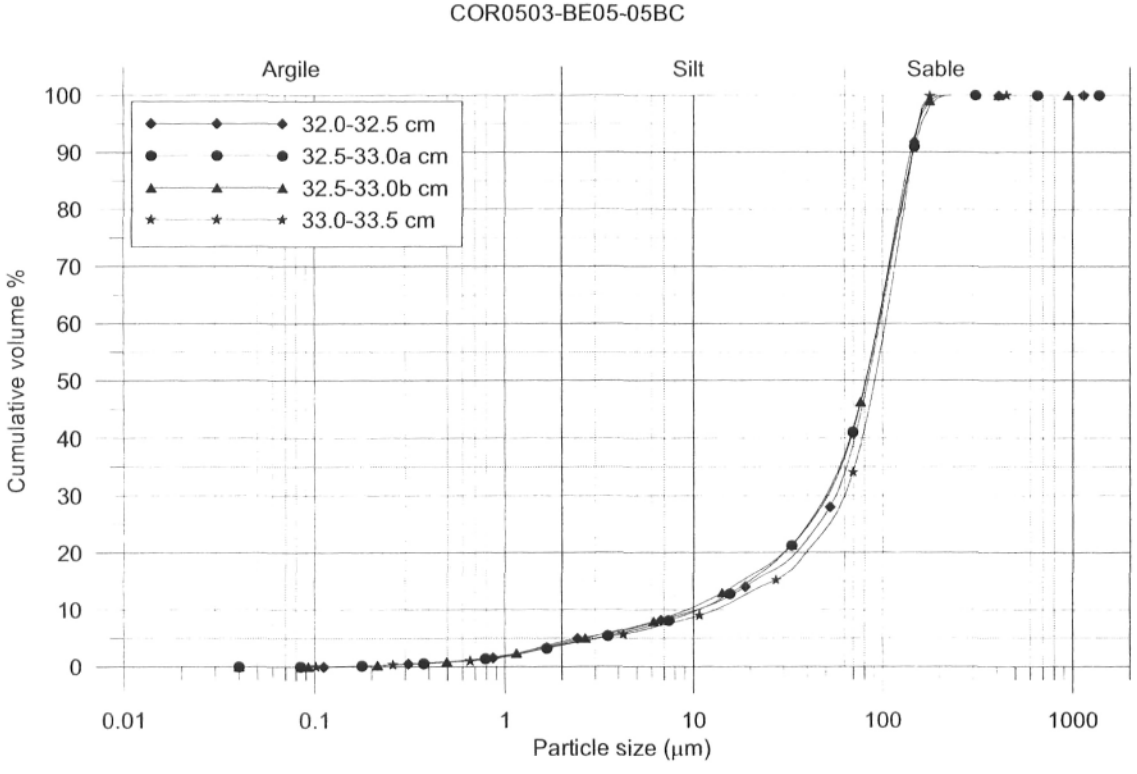
COR0503-BE05-05BC
Argile
Silt
Sable
32.0-32.5 cm
32.5-33.0a cm
32.5-33.0b cm
33.0-33.5 cm
Cumulative volume %
Particle size (µm)
0.01
0.1
1
10
100
1000

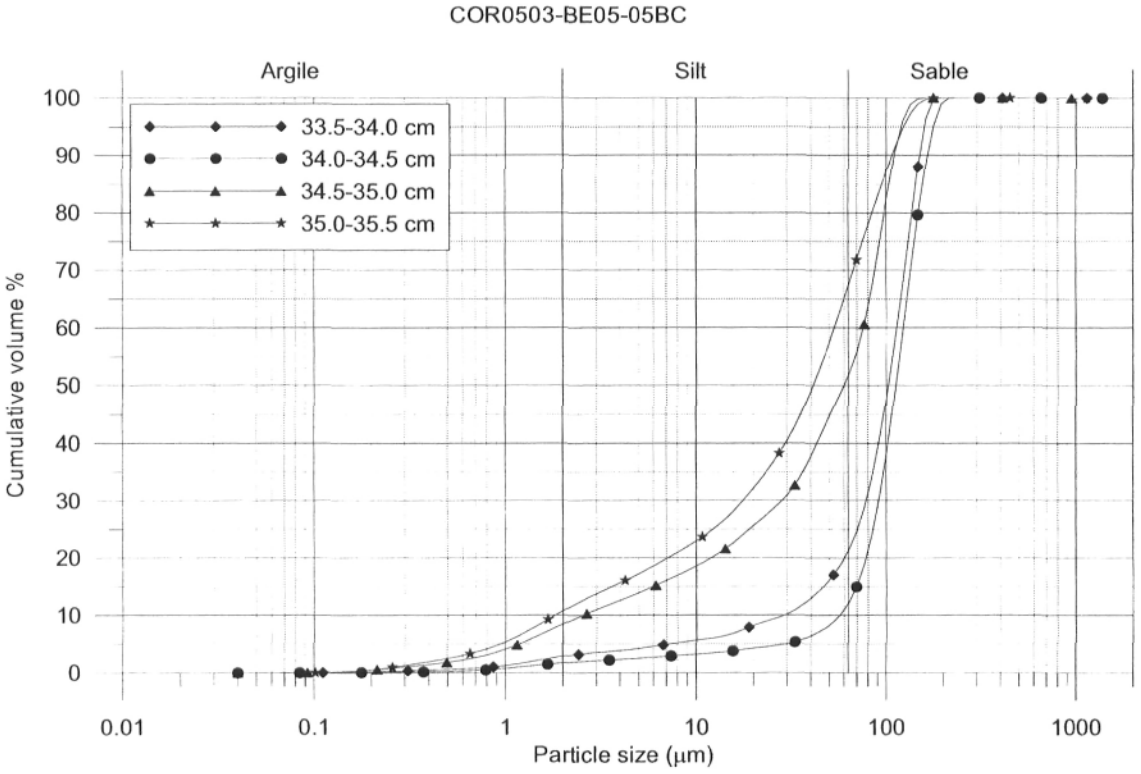
COR0503-BE05-05BC
Argile
Silt
Sable
33.5-34.0 cm
34.0-34.5 cm
34.5-35.0 cm
35.0-35.5 cm
Cumulative volume %
Particle size (µm)
0.01
0.1
1
10
100
1000

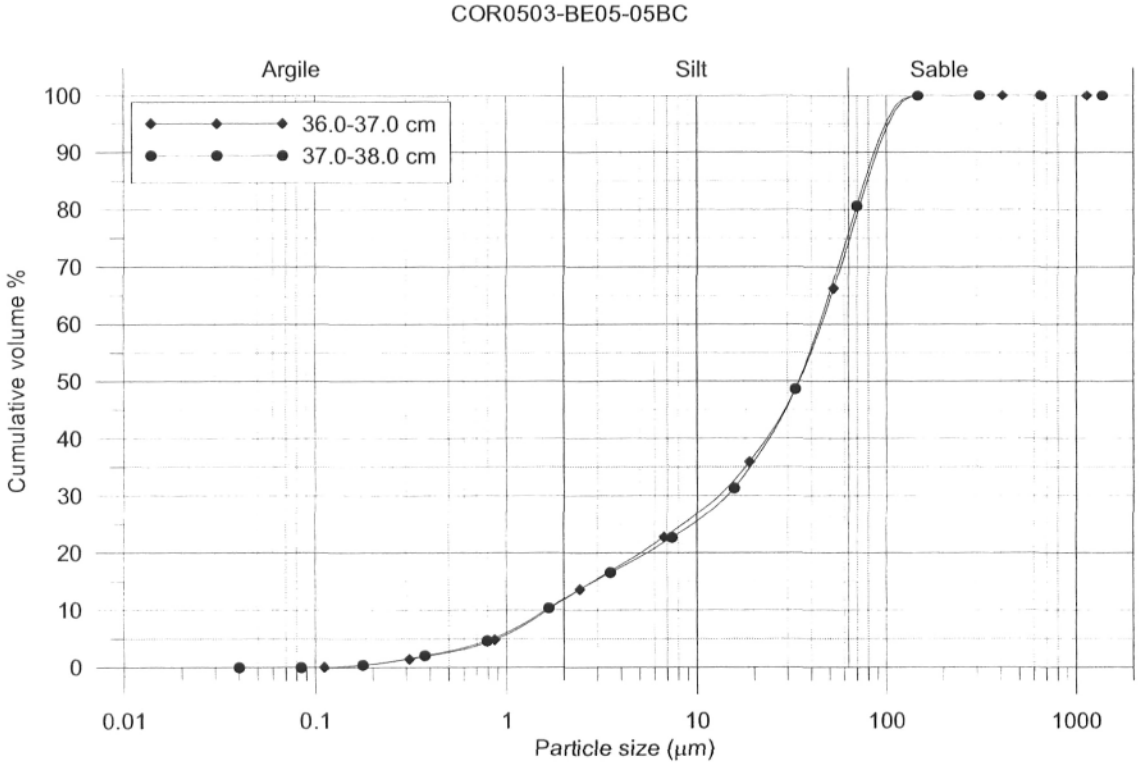
COR0503-BE05-05BC
Argile
Silt
Sable
36.0-37.0 cm
37.0-38.0 cm
Cumulative volume %
Particle size (µm)
0.01
0.1
1
10
100
1000

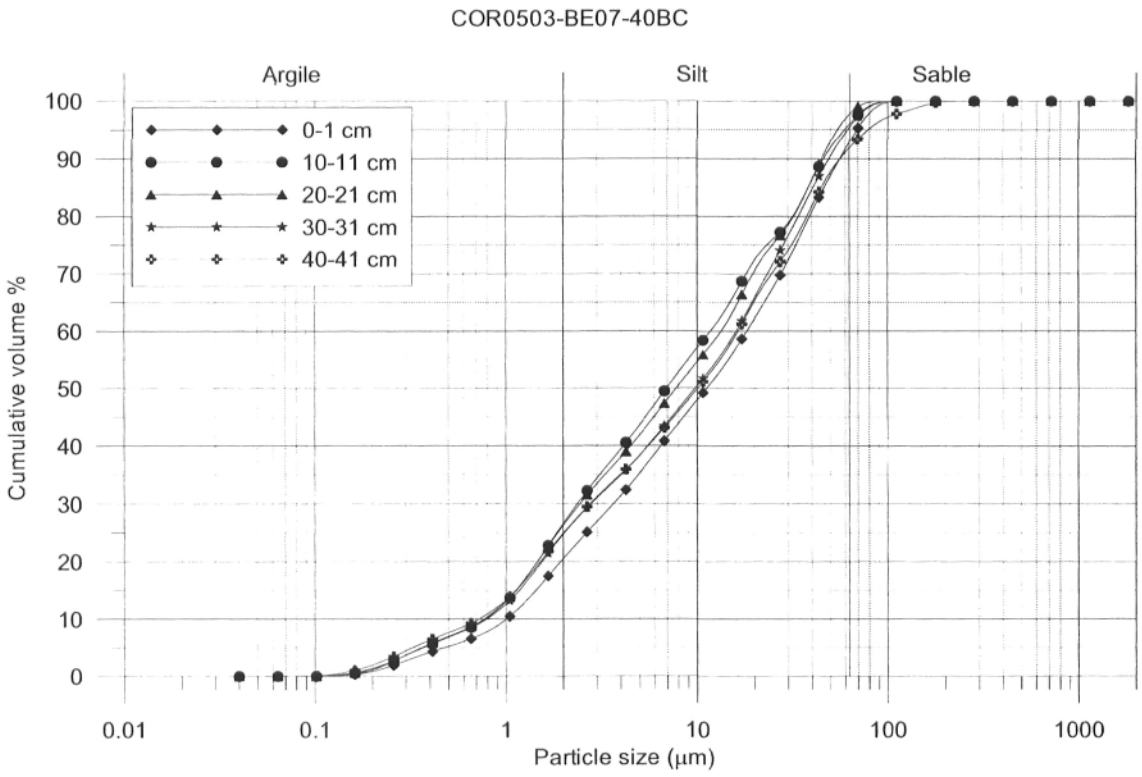
COR0503-BE07-40BC
Argile
Silt
Sable
0-1 cm
10-11 cm
20-21 cm
30-31 cm
40-41 cm
Cumulative volume %
Particle size (µm)
0
10
20
30
40
50
60
70
80
90
100
0.01
0.1
1
10
100
1000